UNIVERSITÀ
DEGLI STUDI
DI PADOVA

UNIVERSITÀ DEGLI STUDI DI PADOVA

DIPARTIMENTO DI FISICA E ASTRONOMIA "GALILEO GALILEI"

CORSO DI DOTTORATO DI RICERCA IN ASTRONOMIA
Ciclo XXXV

THE IMPACT OF STELLAR MASS ON THE FORMATION OF PLANETS

Tesi redatta con il contributo finanziario dell'Istituto Nazionale di Astrofisica

Coordinatore: Ch.mo Prof. Giovanni Carraro
Supervisore: Ch.mo Prof. Raffaele Gratton
Co-Supervisore: Ch.ma Prof. Valentina D'Orazi

Dottorando: Vito Squicciarini

Contents

Abstract

Having recently reached the impressive milestone of 5000 confirmed extrasolar planets, the exoplanetary field has attained in less than 30 years a remarkable degree of maturity. While a purely detection-oriented phase is giving way to a subtler and more intense characterization phase, the quest for statistical trends connecting the observed properties of the exoplanet population is rapidly emerging as the next big step forward for the field. Unveiling the physical processes lurking behind the multifaceted hues of observed planetary architectures -– and the limits outside which these processes no longer work — is indeed the ultimate purpose of *exoplanet demographics*.

Still, the role played by the central star in carving these processes, and hence in shaping its own planetary system, is not completely understood. Disks around more massive stars are known to be more massive, shorter-lived and more prone to fragmentation; several formation mechanisms, differing in the accretion timescale and in the resulting mass distribution, have been proposed. In this tension between *matter*, *time* and *gravity* lies the kismet of planet formation for stars with increasing mass, at the borderline between becoming more efficient and being abruptly halted.

This thesis revolves around the *B-Star Exoplanet Abundance STudy* (BEAST), an ongoing direct-imaging survey that is searching for a wide-orbit giant planet population around B-type ($2.4\ M_{\odot} \lesssim M \lesssim 16\ M_{\odot}$) members of the young ($5 - 30$ Myr) Scorpius-Centaurus association. Previous radial velocity (RV) and direct imaging campaigns have mostly focused on less massive targets; the few existing RV-based indications suggest a turnoff in the occurrence frequency of giant planets at about $M \sim 2M_{\odot}$, consistent with the early disk dissipation predicted by *core accretion*; the argument does not apply to *gravitational instability*, whose wide-orbit massive products may have escaped detection in RV surveys that are virtually insensitive to orbital periods $\gtrsim$ 20 yr. By targeting the outer regions around young B stars, BEAST is ideally positioned to investigate the frontiers of planet formation.

As a first step in preparation for forthcoming detections, we focused our efforts in constraining a stellar property that is crucial to companion characterization: namely, age. In order to circumvent the well-known issues of direct age determination for B stars, we explored an indirect technique which hinges upon the membership of BEAST targets to small groups of stars within the association. By computing group ages through isochronal fitting, we were able to refine the age estimates for the majority of the targets.

This kinematic analysis, enabled by the extreme precision of data delivered by the Gaia satellite, was later extended to encompass the whole Upper Scorpius (US), one of the three subregions in which Scorpius-Centaurus is classically divided. Impressed with the prominent degree of substructuring

discernible in the subregion, we developed a trace-back model to understand whether US still retained traces of its initial velocity structure. We discovered that about one half of US appears composed of many smaller entities, which were in a more compact configuration in the past. The presence of a kinematic duality is reflected into an age spread between this younger clustered population and an older diffuse population, in turn confirmed by a different fraction of disk-bearing stars. Star formation in US appears to have lasted more than 10 Myr and proceeded in small groups that, after a few Myr, dissolve in the field of the older population but retain for some time memory of their initial structure.

Prompted by the necessity to evaluate isochronal ages for large lists of stars in a fast and robust way, we began developing a tool, MADYS, to automatize the entire process. The tool gathers from the literature a large set of stellar evolutionary models and puts them in a unified framework, allowing extensive customization of input parameters. With an eye on the study of star-forming regions and the other on directly imaged substellar objects such as those expected from BEAST, we assembled the list of models to encompass substellar evolutionary models as well. In this way, the versatility of MADYS turned it into the ideal tool to determine the physical parameters of direct-imaged substellar companions based on measured contrasts to their parent stars.

While BEAST is still in progress, its provisional results are already intriguing. A $10.9 \pm 1.6\ M_J$ object was found around the $6 - 10 M_\odot$ binary b Centauri, setting the record for the most massive planet-bearing system to date. Shortly thereafter, when analyzing high-contrast images of μ^2 Scorpii, we found evidence of a comoving substellar companion at a projected separation of 290 ± 10 au. In order to precisely determine the properties of this companion, we first undertook a complete reassessment of the properties of the star. Based on kinematic information, we established its membership to a small group of stars and hence constrained its distance, which in turn allowed us to refine the precision on the remaining stellar parameters. We determined the mass of the companion to be $14.4 \pm 0.8\ M_\mathrm{J}$, slightly above the deuterium-burning limit that classically marks the transition between planets and brown dwarfs. Lurking beneath the glaring light of the star, a second companion candidate was tentatively spotted at an extremely small separation ($0.12'' \approx 20$ au). If confirmed, its luminosity and age would be consistent with a mass $M = 18.5 \pm 1.5 M_\mathrm{J}$.

The nature of these objects is uncertain, and challenges our current view of planet formation. While their masses are near the deuterium burning limit, their properties better resemble those of giant planets around less massive stars and are better reproduced by assuming that they formed under a planet-like, rather than a star-like scenario. When putting this finding in the

context of core accretion and gravitational instability formation scenarios, we conclude that the current modeling of both mechanisms is not able to produce this kind of companion and needs being extended to higher stellar masses.

The BEAST survey has already shown that B stars can possess planetary — or at least planet-like – systems, challenging many of our prior expectations. In the next few years, we will know how frequent these systems are, and the combination of thorough follow-up efforts and dedicated models will hopefully shed light on their elusive origin.

Sommario

Superato di recente il considerevole traguardo del 5000^o pianeta extrasolare confermato, si può affermare che gli studi esoplanetari abbiano raggiunto in meno di 30 anni un notevole grado di maturità. Mentre la semplice fase di rivelazione cede il passo a una fase di più intensa e minuziosa caratterizzazione, la ricerca di relazioni statistiche in grado di connettere le proprietà osservate della popolazione di esopianeti si sta rapidamente affermando quale prossimo grande obiettivo per il settore. Portare alla luce i processi fisici nascosti dietro la multiforme varietà delle architetture planetarie – e i limiti al di fuori dei quali tali processi smettono di operare – è, difatti, il fine ultimo della *demografia esoplanetaria*.

Eppure, il ruolo della stella centrale nel plasmare questi processi, e dunque nel dare forma al proprio sistema planetario, non è ancora completamente compreso. È risaputo che i dischi attorno a stelle più massicce sono a loro volta più massicci, meno longevi e più inclini a frammentazione; i diversi meccanismi di formazione proposti differiscono fortemente riguardo ai tempi scala dell'accrescimento e alla distribuzione finale di massa. É in questa tensione tra *materia*, *tempo* e *gravità* che si esplicano le sorti della formazione planetaria per stelle via via più massicce, sospesa tra il divenire più efficiente e l'interrompersi bruscamente.

Questa tesi è incentrata sullo *studio dell'abbondanza di pianeti attorno a stelle B* (BEAST): basato sulla tecnica del *direct imaging*, esso sta cercando prove dell'esistenza di una popolazione di pianeti giganti nelle regioni esterne attorno a stelle B ($2.4\ M_\odot \lesssim M \lesssim 16\ M_\odot$) appartenenti alla giovane ($5-30$ milioni di anni) associazione Scorpius-Centaurus. Le campagne osservative di velocità radiali e direct imaging del passato si sono per lo più concentrate su stelle meno massicce; i pochi indizi esistenti, basati su studi di velocità radiali, suggeriscono un massimo nella frequenza di pianeti giganti a circa $M \sim 2 < M_\odot$, in accordo con la rapida dissipazione del disco prevista dal meccanismo di *core accretion*; l'argomento non si applica alla *gravitational instability*, che predice la formazione di oggetti massicci e lontani dalla stella che possono essere sfuggiti agli studi di velocità radiali (sostanzialmente insensibili a periodi orbitali $\gtrsim 20$ anni). Rivolgendosi alle regioni esterne attorno a stelle B, BEAST fornisce un punto di vista privilegiato per indagare i limiti della formazione planetaria.

Passaggio necessario in vista delle potenziali scoperte, ci siamo concentrati anzitutto sulla determinazione di un parametro cruciale per la caratterizzazione dei compagni: l'età. Onde evitare di incorrere nei noti problemi che affliggono la determinazione diretta delle età stellari per le stelle B, abbiamo sviluppato una tecnica indiretta, basata sull'appartenenza delle stelle di BEAST a piccoli gruppi di stelle all'interno dell'associazione. Attraverso

la stima delle età di gruppo ottenuta per confronto con le isocrone, siamo riusciti a migliorare le stime di età per la maggior parte delle stelle.

Tale analisi cinematica, resa possibile dalla grande precisione dei dati forniti dal satellite Gaia, è stata in seguito estesa all'intero Scorpione Superiore (US), una delle tre sottoregioni in cui si suole dividere Scorpius-Centaurus. Motivati dalla presenza pronunciata e visibile di sottostrutture spaziali nella sottoregione, abbiamo sviluppato un modello di ricostruzione temporale per comprendere se US conservi ancora traccia della sua struttura di velocità spaziale. Abbiamo trovato che circa metà di US si compone di molte unità più piccole che si trovavano in passato in una configurazione più compatta. La presenza di una bimodalità cinematica trova riflesso in una differenza di età tra questa popolazione "raggruppata", più giovane, e una popolazione diffusa, più vecchia; differenza di età confermata da una diversa frazione di stelle con dischi protoplanetari. La formazione stellare in US è durata più di 10 milioni di anni ed è avvenuta all'interno di piccoli gruppi che, dopo pochi milioni di anni, si dissolvono nel campo stellare della popolazione più antica, pur conservando per un po' di tempo l'informazione cinematica iniziale.

Spinti dalla necessità di determinare le età stellari per un gran numero di stelle nella maniera più veloce e robusta possibile, abbiamo iniziato a sviluppare un programma, MADYS, capace di automatizzare l'intero processo. Il programma mette insieme una larga collezione di modelli di letteratura in una cornice omogenea, permettendo inoltre un controllo completo su numerosi parametri di input. Avendo in mente da un lato lo studio delle regioni di formazione stellare e dall'altro quello di oggetti substellari scoperti tramite *direct imaging* (quali quelli attesi in BEAST), abbiamo incluso nella lista dei modelli anche alcuni modelli evolutivi substellari. In questo modo, la versatilità di MADYS lo rende particolarmente adatto a determinare i parametri fisici dei compagni substellari scoperti tramite *imaging* partendo dai contrasti misurati rispetto alle loro stelle.

Sebbene BEAST sia ancora in corso, i suoi risultati preliminari sono già estremamente interessanti. Un oggetto di $10.9 \pm 1.6\ M_J$ è stato scoperto nel sistema binario ($M = 6 - 10 M_\odot$) b Centauri, stabilendo il record del sistema planetario più massiccio noto ad oggi. Poco dopo, analizzando le immagini ad alto contrasto di μ^2 Scorpii, abbiamo trovato evidenze dell'esistenza di un compagno stellare comovente a una separazione proiettata di 290 ± 10 au. Per determinare precisamente le proprietà di questo compagno, abbiamo innanzitutto provveduto a ricalcolare le proprietà della stella. Sulla base di informazioni cinematiche abbiamo stabilito la sua appartenenza a un piccolo gruppo di stelle e dunque la sua distanza, che ci ha permesso a sua volta di migliorare la precisione sugli altri parametri stellari. Abbiamo così determinato la massa del compagno: $M = 14.4 \pm 0.8\ M_\mathrm{J}$, poco sopra il limite di bruciamento del deuterio usato per distinguere tra pianeti e nane brune.

Nascosto dall'intensa luce stellare, abbiamo probabilmente osservato un secondo candidato compagno a una separazione molto ridotta ($0.12'' \approx 20$ au). Se confermato, la sua luminosità e la sua età sarebbero consistenti con una massa $M = 18.5 \pm 1.5 M_{\rm J}$.

La natura di questi oggetti è incerta e mette parzialmente in discussione l'attuale concezione della formazione planetaria. Se da una parte questi oggetti sono vicini al limite di bruciamento del deuterio, dall'altra le loro proprietà ricordano quelle dei pianeti giganti attorno a stelle meno massicce e sono riprodotte più facilmente assumendo che si siano formati in uno scenario simil-planetario piuttosto che in uno scenario simil-stellare. Mettendo queste considerazioni nel contesto dei modelli di formazione di *core accretion* e *gravitational instability*, concludiamo che l'attuale modellizzazione di entrambi i meccanismi non è ancora in grado di produrre questo tipo di compagni e necessita pertanto di un'estensione a masse stellari maggiori.

La survey BEAST ha già dimostrato che le stelle B possono possedere sistemi planetari — o almeno simil-planetari –, mettendo in discussione molte delle nostre aspettative iniziali. Nei prossimi anni sapremo quanto sono frequenti questi sistemi, e la combinazione di minuziosi studi di follow-up e di nuovi modelli potrà fare chiarezza sulla loro sfuggevole origine.

Thesis outline

This Thesis is organized as follows: in Chapter 1 we introduce the scientific problem of giant planet formation, with a special focus on the role played by the mass of the central star. After presenting the main formation channels proposed in the literature, we will focus on the existing observational constraints. The limitations inherent to each detection technique will be discussed, justifying the need for a direct-imaging study dedicated to B-stars. Chapter 2 will then describe in detail the BEAST survey: its stellar sample, the large-scale stellar environment in which the targets are embedded, and the kind of companions amenable to detection given the performance of SPHERE instruments. We will describe our efforts toward obtaining precise and reliable stellar ages for our sample, and present the results of our analysis. MADYS, the epitome of our isochronal age determination technique, will be introduced in Chapter 3, devoting particular emphasis on the variety of its possible applications. Chapter 4 presents the results of our combined kinematic and isochronal analysis of Upper Scorpius and its implications for the star-formation history of the association. The focus will shift back to BEAST in Chapter 5, describing the early results of the survey; particular attention will be devoted to the analysis of the μ^2 Scorpii system. The implications of BEAST's early results on our view of giant planet formation around B stars will be discussed in Chapter 6, together with the stimulating questions that it raises and some possible directions for the field.

Chapter 3, Chapter 4 and Section 5.3 are based on my three first-author papers published in refereed journals. Chapter 6 expands and builds upon the discussion presented in the paper about the μ^2 Scorpii system. The first paper of the BEAST series, which our efforts for target age determination constitute an important part of, is the basis for Chapter 2. Finally, scientific applications of MADYS featured in published papers are provided as an appendix to Chapter 3.

Dissemination of the results of this Thesis

The main results described in this Thesis have been published in the following peer-reviewed articles:

Squicciarini V., Gratton R., Bonavita M., et al., *Unveiling the star formation history of the Upper Scorpius association through its kinematics,* MNRAS,507,1381 (2021)

Squicciarini, V. & Bonavita, M., *Introducing MADYS: the Manifold Age Determination for Young Stars*, A&A in press (2022; preprint: arXiv:2205.02279)

Squicciarini, V., Gratton, R., Janson, M., et al., *A scaled-up planetary system around a supernova progenitor*, A&A, 664, A9 (2022)

while additional scientific results, referenced throughout the dissertation, have contributed to the content of the following papers:

Janson M., **Squicciarini V.**, Delorme P., et al., *BEAST begins: sample characteristics and survey performance of the B-star Exoplanet Abundance Study*, A&A, 646, A164 (2021)

Janson M., Gratton R., Rodet L., et al, including **Squicciarini V.**, *A wide-orbit giant planet in the high-mass b Centauri binary system*, Nature, 600, 231 (2021)

Bonavita M., Gratton R., Desidera S., et al., including **Squicciarini V.**, *New binaries from the SHINE survey,* A&A, 663, A144 (2022)

Bonavita, M., Fontanive, C., Gratton, R., et al., including **Squicciarini V.**, *Results from The COPAINS Pilot Survey: four new brown dwarfs and a high companion detection rate for accelerating stars*, MNRAS, 513, 5588 (2022)

Ray, S., Hinkley, S., Sallum, S., et al., including **Squicciarini V.**, *Detecting planetary mass companions near the water frost-line using JWST interferometry*, under review on MNRAS (2022)

Additionally, our findings have been presented during the following international astronomy meetings or invited talks:

- ISM 2021 -– Structure, characteristic scales, and star formation – Beirut, Lebanon
- NASA 2021 Sagan Exoplanet Summer Virtual Workshop – Pasadena, US
- Journal Club – The Royal Observatory, Edinburgh – Edinburgh, UK
- Star Clusters: the Gaia Revolution – Barcelona, Spain
- From Clouds to Discs: A Tribute to the Career of Lee Hartmann – Dublin, Ireland
- ESO Workshop: The Star-Planet Connection – virtual event
- ESO Hypatia Colloquium 2022 – Garching, Germany

- The Sharpest Eyes on the Sky – Exeter, UK
- PSF Coffee – Max Planck Institute for Astronomy – Heidelberg, Germany
- COSPAR 2022 – 44^{th} Scientific Assembly – Athens, Greece
- NASA 2022 Sagan Exoplanet Summer Virtual Workshop – Pasadena, US
- Europlanet Science Congress 2022 – Granada, Spain

Symbols and acronyms

Physical and astronomical constants/units	
$M_\oplus$	terrestrial mass = 5.972×10^{24} kg
M_J	Jovian mass = 1.898×10^{27} kg
$M_\odot$	solar mass = 1.98892×10^{30} kg
$R_\oplus$	terrestrial radius = 6.3781×10^{6} m
R_J	Jovian radius = 7.1492×10^{7} m
$R_\odot$	solar radius = 6.957×10^{8} m
$L_\odot$	solar luminosity = 3.828×10^{26} W
au	astronomical unit = $1.495978707 \times 10^{11}$ m
G	gravitational constant = 6.6743×10^{-11} m^3 kg^{-1} s^{-2}
mas	milliarcsecond = 1/1000 arcsec(ond) = $1/3.6 \cdot 10^{-6}$ deg(ree)
Myr	1 million years
Commonly used variables	
α, δ	right ascension, declination [deg]
l, b	galactic longitude, galactic latitude [deg]
ϖ	annual parallax [mas]
μ^*_α	proper motion along $\alpha \equiv \mu_\alpha \cdot \cos\delta$ [mas yr^{-1}]
μ_δ	proper motion along δ [mas yr^{-1}]
L	luminosity [$L_\odot$]
T_eff	effective temperature [K]
[Fe/H]	iron abundance $\equiv \log_{10}\left(\frac{N_\mathrm{Fe}}{N_\mathrm{H}}\right)_* - \log_{10}\left(\frac{N_\mathrm{Fe}}{N_\mathrm{H}}\right)_\odot$
M_*	stellar mass [$M_\odot$]
M_p	planetary/companion mass [M_J]
q	companion-to-star mass ratio
s	companion-primary angular separation [arcsec]
PA	position angle, measured westward from the North [deg]
f_p	giant planet occurrence frequency
S/N	signal-to-noise ratio
MJD	modified Julian date [d]
Abbreviations	
ADI	angular differential imaging
AO	adaptive optics
CA	core accretion model
CC	companion candidate

DI	direct imaging
DIT	detector integration time
ESO	European Southern Observatory
FAP	false alarm probability
FoV	field of view
GI	gravitational instability model
IAU	International Astronomical Union
IMF	(stellar) initial mass function
KDE	kernel-density estimate
MS	main sequence
PMS	pre-main sequence
RV	radial velocity
SDI	spectral differential imaging
TLOCI	Template Locally Optimized Combination of Images
VLT	Very Large Telescope

Chapter 1

Introduction

1.1 Historical background

The contemplation of the night sky has been inspiring awe and wonder since the dawn of human history. Dim points of lights piercing through the enveloping darkness, stars were the compass of seafarers and the golden threads of mythological tapestries woven by poets and bards. Their cyclical annual return reflected and marked the return of the seasons, hence shaping the very idea of time and the first religious and philosophical attempts to understand the ineffable mystery of the universe.

Defying the notion of a perfectly ordered cosmos[1], five bright objects appeared to ramble through the constellations, sometimes whirling in disquieting squiggles, as if endowed with their own will: the Greeks used to call them πλανήται (planétai), literally *wanderers*, and we still refer to them as *planets*. Whether autonomous deities or mere means to communicate messages from heaven, Mercury, Venus, Mars, Jupiter and Saturn were deemed to establish a connection between the Earth and the Heavens: it is no secret, therefore, that the study of their positions was thoroughly pursued over millennia, by means of patient and reiterated observations, by countless civilizations around the world[2] (Evans 1998).

Despite the extreme precision in the mathematical description of planetary motions reached during antiquity – condensed in what would become the guidebook for Arab and European astronomers for more than one thousand years, i.e. Ptolemy's Almagest –, investigating their origin was deemed as a question beyond the aims of astronomy (Evans 1998, chap. 5.3); as regards their physical nature, the vague Aristotelian surmise of ethereal globes embedded in crystalline spheres ended up taking over due to the insurmountable limitations of naked-eye astronomy[3]. In order to reconcile the intricacy of apparent planetary motions with the need to build mathematical models capable of increasing predictive power, while saving at once circular orbits and Earth's stillness, Ptolemy and his continuators were forced to introduce ad-hoc stratagems such as epicycles, eccentrics and equants; the attempt to get rid of this burdensome arsenal, timidly initiated by Nicolaus Copernicus (1473-1543) and permanently concluded by Johannes Kepler (1571-1630), turned out to be

[1] The phrase would appear uselessly pleonastic to an ancient Greek, as the prime meaning of κόσμος (kosmos) is "order".

[2] To cite a few of them: Sumerians, Babylonians, Egyptians, Greeks, Persians, Arabs, Indians, Chinese and Mayans.

[3] But interestingly enough, the Persian polymath Abū 'Alī Ibn Sīnā (Avicenna; 980-1037) writes in his commentary on the Almagest: "I say that I saw Venus as a spot on the surface of the sun". As a transit indeed occurred during Ibn Sīnā's lifetime, on 24 May 1032 AD, his naked-eye observation has been indicated as the first recorded evidence for a planet to be an opaque physical body with a definite angular size (Kapoor 2013). This happened six centuries before Pierre Gassendi's (1592–1655) observation of a Mercury transit (1632); the French scientist was bewildered by the smallness of the planet's disk.

the missing ingredient to get planet formation into the realm of scientific investigation (Koestler & Butterfield 1968).

First enthusiastically outlined by the philosopher Giordano Bruno (1548-1600) in *De l'infinito universo et mondi* (1584), a corollary of the heliocentric theory was the twofold realization that the Sun is a star, and the Earth is a planet. Suddenly expanding the size of the universe to unfathomable distances beyond the orbit of Saturn[4], this idea of cosmic pluralism slowly began diffusing throughout the intellectual world in the following century, as testified by the *Conversations on the Plurality of Worlds* by Bernard Le Bovier de Fontenelle (1686): if the stars are distant suns, they should be surrounded by their own planetary systems.

Leaving aside the practical impossibility of confirming the existence of extrasolar planetary systems, the realization that the planets are earths and that their orbits are much simpler than previously thought gave impetus to the first scientific efforts to explain the formation of what started to be rightfully called "the Solar System". In particular, two facts had to be explained:

1. the farther a planet to the Sun, the lower its orbital speed;

2. the orbits of all the planets are almost perfectly aligned along the ecliptic plane.

Galileo Galilei (1564-1642), the father of modern astronomy, was the first to undertake such an effort (Sambursky 1962). First in the *Dialogo sopra i due massimi sistemi del mondo* (1632) and later in the *Discorsi e dimostrazioni matematiche intorno a due nuove scienze* (1638) he applied his law of falling bodies to the planets by supposing that they originated in a single place located at a distance farther from the Sun than Saturn's orbit; then,

> "if [a planet] were to start from rest at this particular height and to fall with naturally accelerated motion along a straight line, and were later to change the speed thus acquired into uniform motion, the size of its orbit and its period of revolution would be those actually observed."

In their descent toward the Sun, the planets would behave like balls rolling down an inclined plane, the acceleration being always equal to *natural acceleration*, alias g. From a physical standpoint, defining R as the distance between the Sun and the original location and r their current heliocentric distance, conservation of mechanical energy yields a velocity v:

$$v \propto \sqrt{R - r} \tag{1.1}$$

in stark contrast with Kepler's third law of planetary motion:

$$v \propto \sqrt{\frac{1}{r}} \tag{1.2}$$

which had already been published in 1619. While laudable in its seminal attempt to apply physical laws determined on Earth to an astronomical problem, what this first physical model of planetary formation successfully proves is, ironically, Galileo's complete carelessness toward Kepler's theoretical achievements (Russell 1964).

Unlike Equation 1.1, the remarkable feature of Equation 1.2 is that it only depends on the distance from the Sun: it's in relation to the Sun that the solution was to be sought. The discovery

[4]If the Earth moves, the impossibility for a 16^{th} century astronomer to detect the annual parallax of any star can only be explained by assuming that the stars are incredibly far away from the Solar System. Refusing a priori this possibility, Tycho Brahe (1546-1601) famously used this argument against heliocentrism (Blair 1990).

of such a relation in the form of the gravitational force did not tempt Isaac Newton (1642-1727) to put forward hypotheses regarding the origin of planetary orbits, since a solution to the second-order differential equations for their motion:

$$\ddot{r} + GM_{\odot} r^{-2} = 0 \tag{1.3}$$

is only determined if initial conditions for position and velocity are provided. Nevertheless, the Newtonian framework became the necessary premise for any model wishing to unveil how the planets assembled under the action of gravity and settled into their current orbits.

In the eighteenth century, the philosopher Immanuel Kant (1724-1804) created the first qualitatively attempt of a cosmogony based on Newtonian physics: the so called "Nebula Hypothesis". At the beginning, according to Kant, the Solar System was a large rotating nebula made of gas and dust. Prompted by its own gravitational attraction, the nebula began collapsing toward its center, creating the Sun; some smaller clumps of the nebula condensed in the outer regions, forming the cohort of planets and satellites. A few decades afterwards, Pierre Simone Laplace (1749-1827) worked out finer details of this scenario, including the loss of angular momentum of the nebula – turning it into a disk – and the formation of rings where planet formation occurred (Williams & Cremin 1968; Woolfson 2000).

Though studded with plenty of difficulties[5], this scenario developed to become the basis for the current view of planet formation in the Solar System. Following seminal work in the 1960s (Safronov 1972) that benefited from various kinds of evidence (chemical and physical properties of meteorite samples, the study of cratering records, isotopic composition of planets), the main elements of the core accretion theory were developed and refined in the early 1980s (see Section 1.5.1): the settling of dust grains in the mid-plane of the disk, the collision-induced accretion of macroscopic objects ($d \sim 0.01 - 10$ m), the formation of planetesimals ($d \sim 1 - 100$ km), the formation and the runaway growth of planetary embryos ($d > 100$ km) by means of mergers (Wetherill 1990; Kokubo & Ida 1996), until four of them attained large enough masses ($\sim 10 - 30 M_{\oplus}$) to accrete gas from the disk, originating Jupiter, Saturn, Uranus and Neptune (Pollack 1984; Bodenheimer & Pollack 1986). A key aspect of the planet formation paradigm in vogue in the 1980s was its static nature: namely, the idea that the current planetary orbits very closely resemble the locations of the respective planetary embryos (Hayashi 1981a). Under this view, the general tendency for a decrease in density with distance, such that the rocky planets are followed by giant planets, is naturally explained as a consequence of the initial temperature gradient in the disk itself (Hayashi et al. 1985), while the increasing timescale of embryo accretion is reflected into the decreasing trend of gas reservoir from Jupiter outward (Nakazawa & Nakagawa 1981).

Being at that time the sample size of planetary systems equal to one, the foundations of the theory were retrospectively not as solid as it was believed. Indeed, the properties of the first exoplanets come, in a sense, as a bolt from the blue.

[5]According to the Nebula Hypothesis, most of the angular momentum of the Solar System should lie in the Sun; observations instead show that our star, despite containing the 99.86% of the total system mass, only carries $\sim 0.5\%$ of the total angular momentum. This Achilles' heel, which gave rise to many concurring hypothesis – see Woolfson (2000) for a review – was solved only in the last decades thanks to the finding that stellar angular momentum is lost due to coupling between stellar wind and magnetic field (Weber & Davis 1967; Gallet & Bouvier 2013; Güdel 2020).

1.2 The exoplanet revolution

Since its inception in the early 1990s, the so-called *exoplanetary field* has profoundly shaken key aspects of planet formation theories that had been developed, as we have seen in the previous section, purely based on our Solar System.

The first signal of an exoplanet originated from one of the least promising environments for exoplanet searches: the millisecond pulsar PSR1257+12 (Wolszczan & Frail 1992). The peculiar system of PSR1257+12 is composed of at least three planets (two terrestrial planets with $M \approx 4M_\oplus$ and a Moon-sized object with $M \approx 0.02M_\oplus$), whose feeble gravitational pulls induce distinctive periodic variations on the timing of stellar pulses (Wolszczan 1994). Likely assembled from the disk of materials surrounding the pulsar after supernova explosion (Currie & Hansen 2007), systems of this kind were found to be quite uncommon (Kerr et al. 2015): a first striking example of the crucial difference existing between detection ease and occurrence frequency.

In the same years, the *radial velocity* technique – also known as *Doppler spectroscopy* – was attaining high enough sensitivity to detect planetary-mass objects around main-sequence stars (Campbell et al. 1988). The closer a planet to its star, the higher its signal (see Section 1.4.1); but the first confirmed exoplanet around a main-sequence star, 51 Pegasi b (Mayor & Queloz 1995), was so uncomfortably close to its star that it completed one orbit in just 4.2 days. A vibrant discussion sparked within the astronomical community (Deeg & Belmonte 2018, chap. 1): on the one hand, theoretical efforts thoroughly investigated whether migration could explain the observed orbital parameters (Lin et al. 1996), on the other hand an alternative explanation of the signal as due to exotic stellar pulsations was promptly put forward (Gray 1997). The detection of similar RV signals over the following years undermined the latter scenario, until the discovery of the first transiting planets (Charbonneau et al. 2000; Henry et al. 2000) put an end to the debate: 51 Pegasi b was the archetype of a whole new family of planets, the *Hot Jupiters*.

Despite its later appearance, the transit method (Struve 1952) was soon able to carve out an important role in the field; after the launch of the Kepler satellite (Borucki et al. 2010), it surpassed RV to become the most successful detection technique, a primacy that still maintains today (Figure 1.1). The first exoplanet detection via *microlensing* and *direct imaging* date back to 2004 (Bond et al. 2004; Chauvin et al. 2004); taken together, these two techniques are responsible for the $\sim 4\%$ of the present-day exoplanet population[6].

Our generation is the first in human history that knows the answer to a longstanding philosophical question: the existence of other worlds. The exoplanet revolution has unfolded before our eyes at an extremely fast pace: the number of confirmed detections, recently exceeding 5000, has increased – until 2016 – in an exponential fashion with doubling time ~ 27 months[7]. Year after year, the ever-growing diversity of observed exoplanet architectures – planets on extremely eccentric orbits (Udry & Santos 2007), with significant misalignment from the equatorial plane of their stars (e.g., Winn et al. 2009), water and lava worlds (Chao et al. 2021), evaporating Hot Jupiters (e.g., Lecavelier Des Etangs et al. 2010), resonant chains of tightly packed worlds (Luger et al. 2017) – has profoundly changed our view of planet formation and evolution (Winn & Fabrycky 2015). Moreover, the previously unknown class of super-Earths, composed of planets with intermediate mass between the Earth and Neptune and showing a large density spread, was found to be fairly common (Batalha et al. 2013).

After initial disorientation, astronomers have started to collect a fair amount of pieces of the intricate jigsaw puzzle of planetary systems; thirty years of earnest exoplanet searches make us now glimpse some detail of the underlying picture. In order to obtain an adequate representation of

[6] For a comprehensive review of planet detection techniques, see Deeg & Belmonte (2018), chap. 4.

[7] This trend is colloquially known as Mamajek's law (https://twitter.com/EricMamajek/status/790786565496680449).

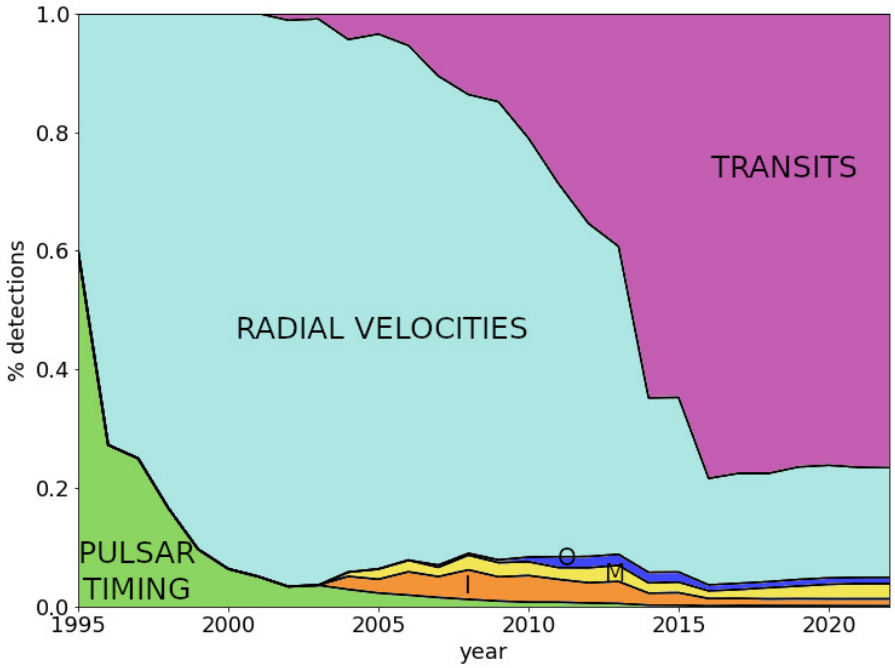

Figure 1.1: Fractional contribution of different detection methods to the population of known exoplanets (1995-2022). 'I' (orange) = imaging; 'M' (yellow) = microlensing; 'O' (blue) = other methods. Adapted from Deeg & Belmonte (2018) using data from the NASA Exoplanet Archive.

such a picture, and the Solar System's location amidst it, substantial efforts have been undertaken to statistically assess the properties of the emerging exoplanet population: this is the purpose of a recent branch of the exoplanet field, known as *exoplanet demographics*.

1.3 Exoplanet demographics

As a consequence of the extreme diversity of the discovered companions[8], the very definition of exoplanet has been the subject of extensive debate (see, e.g., Basri & Brown 2006; Chabrier et al. 2014). According to the current definition adopted by the IAU (Lecavelier des Etangs & Lissauer 2022):

> Objects with true masses below the limiting mass for thermonuclear fusion of deuterium (currently calculated to be 13 Jupiter masses for objects of solar metallicity) that orbit stars, brown dwarfs or stellar remnants and that have a mass ratio with the central object below the L4 / L5 instability ($\frac{M}{M_{central}} < \frac{2}{25+\sqrt{621}} \approx 1/25$) are "planets", no matter how they formed. The minimum mass/size required for an extrasolar object to be considered a planet should be the same as that used in our Solar System, which is a mass sufficient both for self-gravity to overcome rigid body forces and for clearing the neighborhood around the object's orbit.

[8]We will use the word "companion" to refer to any stellar or substellar object bound to a more massive primary, and the phrase "substellar companions" to indicate both planets and brown dwarfs.

With respect to previous formulations, the current definition of planet has introduced a dynamical criterion by means of the mass ratio: a first indirect recognition of the importance of stellar mass in shaping the properties of its companions. On the other hand, formation mechanisms are still not used as a criterion to distinguish planets and brown dwarfs, since they are operationally difficult to assess. We notice that the new scheme, while particularly suited to cope with companions to low-mass ($M \lesssim 0.3 M_{\odot}$) primaries, comes down to the traditional mass-based criterion for more massive stars (see discussion in Section 6.3).

Having defined the object of our study, we might still note that the definition encompasses a plethora of objects in terms of masses (from sub-Earth mass up to the deuterium burning limit), semimajor axes (from 0.01 AU to 1000 AU), and other orbital (period, eccentricity, inclination) and stellar (mass, age, activity) properties as well. The vastness of such a parameter space can not be currently explored by a single detection technique, and a significant portion of it is still completely unexplored. The combination of all the existing techniques is therefore essential to study the properties of the exoplanet population (Gaudi et al. 2021).

Figure 1.2 is perhaps the most widely used diagram in exoplanet sciences, and can be thought as the planetary version of the stellar Hertzsprung-Russell diagram. The distribution of points across the diagram is far from being uniform: indeed, several clumps, corresponding to different classes of planets, can be observed. Continuing our HR analogy, planets can – like stars – modify to a certain extent their position in the diagram over time. The foundations of exoplanet demographics lie in this very idea, namely that the distribution of exoplanets as a function of their physical, orbital and stellar-host properties, has been thoroughly crafted by physical processes related to their formation and subsequent evolution.

However, the picture is complicated by the fact that a comprehensive and unbiased census of the planetary population is still missing: as evidenced by the kernel-density estimates (KDE) in Figure 1.2, the observed distribution of exoplanets in the parameter space is heavily affected and distorted by detection biases inherent to the employed techniques. We might notice, for instance, that:

- $\sim 90\%$ of the confirmed exoplanets lie closer to their stars than the Earth is to the Sun;
- 99.3% of the confirmed exoplanets orbit around stars with $M < 2 M_{\odot}$; given that about 96% of the stars have $M < 2 M_{\odot}$ according to Chabrier's initial mass function (Chabrier 2003), $M > 2 M_{\odot}$ stars are underrepresented by a factor six.

It is therefore clear that a careful assessment of the sensitivity of a certain survey to all the parameters of interest, i.e. the survey completeness, an adequate description of the initial stellar sample, and an earnest report of all the cases resulting in nondetections, should be considered vital steps before undertaking any quantitative interpretation of its results; only through such an assessment it is possible to attempt a synthesis of the results obtained by different surveys and techniques and to sketch a complete picture of exoplanet demographics, which in turn provides the constraints that every candidate theory must respect.

1.4 The frontiers of planet formation

Having outlined the state of the art of the exoplanetary field, we introduce in this Section the scientific question lying at the heart of this PhD project:

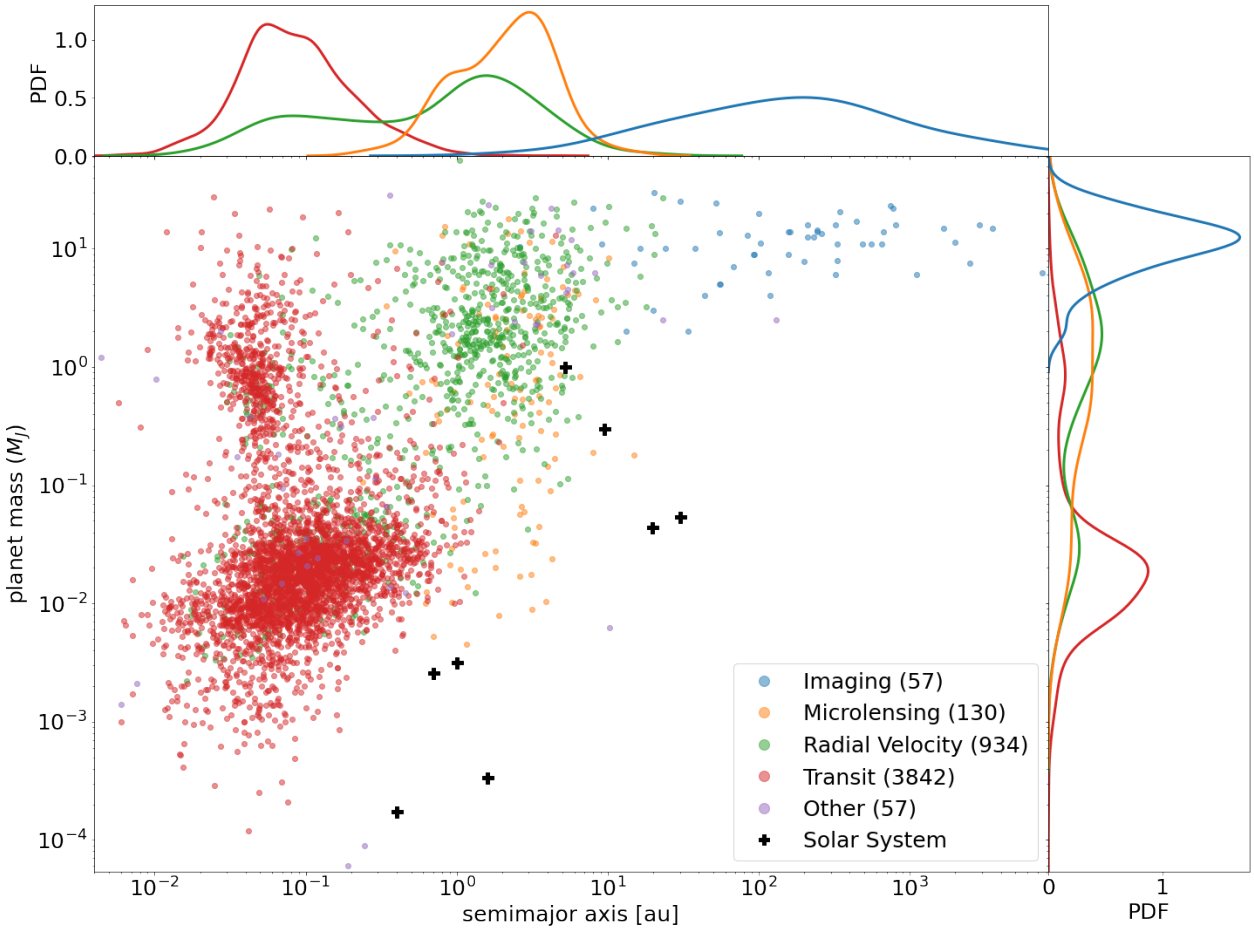

Figure 1.2: Mass vs semimajor axis of confirmed exoplanets (8^{th} July 2022). Each planet is labeled according to its detection method: transits in green, radial velocity in red, microlensing in orange and direct imaging in blue. Kernel-density estimates of the underlying distributions are provided in the upper and right-hand side subplots. Source: NASA Exoplanet Archive.

> Is the dearth of exoplanets around high-mass stars ($M \gtrsim 2M_{\odot}$) a mere consequence of observational biases inherent to the existing exoplanet searches, or is there a physical obstacle that makes increasingly difficult – and eventually impossible – to form planets around stars of increasing mass?

Observations of young stellar objects indicate that the mass of a protoplanetary disk is positively correlated with the mass of the central star (Pascucci et al. 2016). It is natural to wonder whether an increase of the available reservoir results in more frequent companions, more massive companions, or both.

While solar-type stars and less massive stars are virtually accessible to all the four main detection methods presented in Section 1.3, understanding whether the sensitivity of the methods is still adequate to cope with more massive hosts is a non-trivial task: we will derive in Section 1.4.1 approximated scaling relations for the signal-to-noise ratio (S/N) as a function of stellar mass; after identifying the most useful techniques for our science case, we will briefly review in Section 1.4.2 the main results coming from these techniques and their current limitations; at the end of this Section, the need for a dedicated direct imaging survey targeting B stars will become clear.

We emphasize that, due to the difficulties inherent to exoplanet searches around high-mass stars, our attention will from this moment on focus on the class of planets that is the easiest to observe: the class of *giant planets* ($\sim 0.1 - 13M_{\rm J}$).

1.4.1 S/N scaling laws: comparing detection techniques

As anticipated above, this Section is aimed at comparing the sensitivity of different exoplanet detection techniques in order to identify the one that is most suitable to our science case: namely, the dependence of planet formation processes on stellar mass. The comparison will involve the four most successful planet-hunting techniques (transits, radial velocities, microlensing, direct imaging) and a fifth method, astrometry, which is expected to discover thousand of giant exoplanets during this decade (Perryman et al. 2014). Although the comparison should be looked as tentative due to the neglect of several details in the exact form of S/N, the relevant scaling relations will nevertheless unveil the strenghts and the limitations of each method.

Let M_p be the planetary mass, M_* the stellar mass, a the semimajor axis of the planet's orbit and P its orbital period. As the preferred location for giant planet formation is expected to be around, or beyond, the so-called *snow line* (see Section 1.5.1), a parametrization of the snow line location as a function of stellar mass would be extremely important for our purposes. The problem is complex, for it couples two time-dependent sources of heat, namely viscous accretion within the disk and stellar irradiation, causing in turn the snow line location to be time-dependent (see Kennedy & Kenyon 2008, and references therein). Assuming for simplicity a constant $a_{sl} \approx 3$ au in the early solar disk (Armitage 2020, chap. 1.5), the mass scaling is given by the relation:

$$a_{sl} \approx 3 \text{ au} \left(\frac{M_*}{M_{\odot}}\right)^{\beta} \tag{1.4}$$

with β ranging from ~ 1 during the PMS stage (when $L_* \propto M_*^2$) to ~ 2 during the MS stage (when $L_* \propto M_*^4$) (Ida & Lin 2005; Kennedy & Kenyon 2008). The pre-main sequence lifetime τ_{PMS} is approximately equal to the Kelvin-Helmholtz timescale:

$$\tau_{PMS} \approx 1.5 \cdot 10^7 \left(\frac{M}{M_{\odot}}\right)^2 \left(\frac{R_{\odot}}{R}\right) \left(\frac{L_{\odot}}{L}\right) \sim 10^7 \left(\frac{M}{M_{\odot}}\right)^2 \left(\frac{M_{\odot}}{M}\right) \left(\frac{M_{\odot}}{M}\right)^{-3.5} \sim 10^7 \frac{M_*}{M_{\odot}}^{-2.5}. \tag{1.5}$$

Irradiation is expected to dominate over accretion as the star enters the MS, which occurs at ~ 1 Myr, ~ 3 Myr and ~ 15 Myr for $M_* \sim 3M_\odot$, $M_* \sim 2M_\odot$ and $M_* \sim 1M_\odot$, respectively. While it is safe to assume $\beta = 1$ for stars with $M \lesssim 1.5M_\odot$ (cf. Equation 1.18), we will employ both values of β for more massive hosts in order to avoid any assumption on the timescale required by planet formation.

Transits The S/N of a transit event is related to planetary mass, stellar mass and semimajor axis (Gaudi et al. 2021):

$$S/N \propto R_p^2 \; P^{-1/3} \; M_*^{-5/3} \propto M_p \; a^{-1/2} \; M_*^{-3/2}. \tag{1.6}$$

Moreover, the geometric probability of a transit p_t is also a function of these parameters:

$$p_t \propto \frac{R_*}{a} \propto P^{-2/3} \; M_*^{2/3} \propto a^{-1} \; M_*. \tag{1.7}$$

Transits are strongly biased toward close-in planets orbiting around low-mass stars: the S/N decrease with stellar mass is particularly evident for a planet located at the snow line, for which $S/N \propto M_p M_*^{-2}$, $p_t \equiv const$ (if $\beta = 1$) or $S/N \propto M_p M_*^{-5/2}$, $p_t \propto M_*^{-1}$ (if $\beta = 2$).

An even tighter constraint against transits is given by the requirement of at least three transits during the survey duration T – a criterion commonly used to vet planet candidates[9]. For the Kepler mission, the continuous monitoring of the same patch of sky lasted $T \approx 4$ yr (Van Cleve et al. 2016); assuming a random epoch for the first transit, a 68% probability to observe three transits over 4 yr translates into $P \lesssim 0.4T \sim 1.6$ yr; we can thus combine Kepler's third law of planetary motion:

$$\left(\frac{a}{1 \text{ au}}\right)^3 = \frac{M_*}{M_\odot} \cdot \left(\frac{P}{1 \text{ yr}}\right)^2 \tag{1.8}$$

with Equation 1.4 and the constraint on P. Solving for M_*, we find the condition:

$$M_* \lesssim 0.3M_\odot, \tag{1.9}$$

having assumed $\beta = 1$ (the solution with $\beta = 2$ yields $M_* \lesssim 0.6M_\odot$ and is therefore excluded). Hence, a $T \sim 4$ yr transit survey is only able to reach the snow line around stars later than spectral type $\sim$ M3, and is completely insensitive to it when dealing with more massive hosts.

Radial velocities Assuming $i = 90°$ and a negligible eccentricity ($e \lesssim 0.5$), one can derive (Gaudi et al. 2021):

$$S/N \propto M_p \; P^{-1/3} \; M_*^{-2/3} \propto M_p \; a^{-1/2} \; M_*^{-1/2}. \tag{1.10}$$

Like transits, RV are preferentially sensitive to close-in planets orbiting around low-mass stars. As regards high-mass stars, it is known that the lack of narrow spectral lines prevents their effective study during the main sequence phase; this issue is lifted as these stars expand and cool during the post-main sequence, unleashing more numerous and narrower lines (Janson

[9]But see Herman et al. (2019) for a few examples of robustly detected planets with $P = 2 - 10$ yr with a single transit.

et al. 2021b). This is the reason behind the prevalence of post-MS stars in surveys dealing with $M \gtrsim 1.5 M_\odot$ stars (e.g., Winn & Fabrycky 2015).

For a planet located at the snow line, $S/N \propto M_p M_*^{-1}$ ($\beta = 1$), $S/N \propto M_p M_*^{-3/2}$ ($\beta = 2$). As for transits, a duration-related constraint exists, since the method is able to recover planets with periods up to the maximum length of its time series: for current surveys, $T \lesssim 20$ yr. Reasoning as in Equation 1.9, we derive, depending on β, $M_* \lesssim 1.7 - 3.8 M_\odot$. An additional obstacle is intuitively given by the decreasing amplitude of the S/N: while current long-term surveys are comfortably sensitive to a Jupiter analog around a Sun-like star ($S \sim 13$ m/s, $P \sim 12$ yr), a Saturn analog around a Sun-like star ($S \sim 3$ m/s, $P \sim 30$ yr) is already at the edge of their sensitivity (Bryan et al. 2016). Thus, (Super)-Jupiters at $\gtrsim 10$ au separations are beyond the current capabilities of the method for high-mass hosts.

Microlensing Unlike the other techniques described in this section, the S/N of microlensing cannot be easily described as a simple combination of few stellar and planetary parameters. Yet, the sensitivity of the method notoriously peaks at an optimal separation r_{opt}:

$$r_{opt} = 2.85 \text{ au} \left(\frac{M_*}{0.5 M_\odot} \right)^{1/2} \left(\frac{D_s}{4 \text{ kpc}} \right)^{1/2} \left(\frac{x(1-x)}{0.25} \right)^{1/2}, \tag{1.11}$$

where $x \equiv D_l / D_s$ and D_l and D_s are the distances of the foreground target star (the *lens*) and the background magnified star (the *source*), respectively (Gaudi et al. 2021).

The intrinsic impossibility to select the targets of a microlensing campaign strongly limits the practical applicability of this method: even optimistically assuming a constant occurrence of detectable planets across all stellar masses, the shape of a realistic initial mass function (IMF) such as Chabrier's IMF (Chabrier 2003) would require the observation of ~ 1000 microlensing events to observe a few tens of high-mass stars.

An additional complication arises from the following consideration: comparing Equation 1.11 and Equation 1.4, and setting typical numbers for D_s and D_l ($D_s \approx 4$ kpc, $D_l \approx 8$ kpc), we might notice that $r_{opt}/a_{sl} \approx a_{opt}/a_{sl} \approx 1 (M/M_\odot)^{-1/2}$ ($\beta = 1$) or $r_{opt}/a_{sl} \approx a_{opt}/a_{sl} \approx 1 (M/M_\odot)^{-3/2}$ ($\beta = 2$): as with radial velocities, the outer regions of a system are bound to fall outside the method's detectability range if the host mass increases.

Direct imaging The functional form for the signal of a direct-imaged exoplanet depends on the physical source of the observed flux; generally speaking, the major source of the outgoing radiation can be either residual formation heat or a combination of reflected stellar light and thermal emission related to the planet's equilibrium temperature. In accordance with the current capabilities of the technique (Deeg & Belmonte 2018, chap. 34), we only treat here the former case.

In the usual case of a ground-based high-contrast imaging facility equipped with a coronagraph and an adaptive optics (AO) system, such as the Spectro-Polarimetric High-contrast Exoplanet REsearch (SPHERE; Beuzit et al. 2019) instrument at the Very Large Telescope (VLT), the S/N in the presence of *speckles*, defined as static or quasi-static artifacts that vary on a timescale comparable or larger than the exposure time[10], can be written as (Deeg & Belmonte

[10] From a physical standpoint, speckle constitute residual aberrations in the point spread function that are not corrected by the AO system. We will introduce in Chapter 2 some techniques that have been develop to reduce the impact of speckles on the final images.

2018, chap. 34):

$$S/N = \frac{F_p}{F_*} \frac{1}{\epsilon_\phi^2(\mathbf{n} = \alpha_p)}, \tag{1.12}$$

where F_p and F_* are the flux coming from the planet and the star, respectively, α_p is the angular distance between the star and the exoplanet, and $\epsilon_\phi^2(\mathbf{n} = \alpha_p)$ is the power spectral density of the speckles at the spatial frequency n corresponding to the separation of the planet.

As ϵ^2 decreases with α_p, meaning that the strength of this kind of noise weakens with angular separation from the star (Soummer et al. 2007), direct imaging turns out to be preferentially sensitive to wide separations.

Shifting now our attention to the *contrast* F_d/F_*, we might estimate it, for simplicity, as the ratio between the integrated luminosities[11]; using the Stefan-Boltzmann law:

$$S/N \sim \frac{L_p}{L_*} \propto \frac{R_p^2 \; T_{\text{eff},p}^4}{R_*^2 \; T_{\text{eff},*}^4} \tag{1.13}$$

where R and T_{eff} indicate radii and the effective temperatures, respectively. In order to roughly model the decay of $T_{\text{eff},p}$ and R_p over time, we refer to the AMES-Dusty models for cool stars and substellar objects (Allard et al. 2001) in the ranges $t \in [1, 1000]$ Myr, $M_p \in [5 \cdot 10^{-4}, 1 \cdot 10^{-1}] M_\odot \approx [0.5, 100] M_J$. The temperature decay is very well fitted by the relation $T_{\text{eff}} \propto t^{-0.25}$ across the entire mass range; the radius decrease is instead not as regular, but we assume the approximate mean relation $R(t) \propto t^{-0.1}$ so that $R = R_\infty t^{-0.1}$, where $R_\infty = \lim_{t \to \infty} R(t)$. As regards the primary, recalling Equation 1.5, we might safely assume that a $M > 2M_\odot$ star is already on the MS after a few Myr, and therefore $R_* \equiv const$, $T_{\text{eff},*} \equiv const$. We may finally write:

$$S/N \propto \left(\frac{R_p}{R*}\right)^2 t^{-0.2} \; t^{-1} \approx \left(\frac{M_p}{M*}\right)^2 t^{-6/5} \tag{1.14}$$

having assumed a constant proportionality between R and M.

Direct imaging is markedly sensitive to young planets and to wide separations, placing itself in a unique niche of the exoplanet parameter space.

Astrometry The S/N of an astrometric mission can be estimated as (Gaudi et al. 2021):

$$S/N \propto M_p M_*^{-1} \; a \; d^{-1} \propto M_p P^{2/3} M_*^{2/3} d^{-1} \tag{1.15}$$

For a planet located at the snow line, $S/N \propto M_p d^{-1}$ ($\beta = 1$), $S/N \propto M_p M_* d^{-1}$ ($\beta = 2$). Interestingly enough, unlike all the other techniques explored above, astrometry is not biased against – and might be even favored for – higher mass hosts for planets located around the snow line. An implicit dependence on M_*, though, is contained in the factor d, for statistically larger distances must be probed to sample the IMF up to higher stellar masses. Another limitation of the method is the sharp decrease of its sensitivity when dealing with companions with periods greater than the survey duration T, as they induce an almost linear astrometric deviation of their host star that is easily incorporated and buried into the best-fit proper motion (Casertano

[11] It is equivalent to measuring the flux in a filter with infinite bandwidth.

et al. 2008); even if correctly identified, such a signal is insufficient to adequately constrain the orbit, resulting in a mass-period degeneracy (Andrews et al. 2019).

At the moment of writing, no exoplanet has been discovered through astrometry; however, it is worth highlighting the key role of the space-borne Gaia mission (Gaia Collaboration et al. 2016) in characterizing targets of transit, RV and DI surveys (see, e.g., Stassun et al. 2018; Berger et al. 2020), in refining the derived exoplanet properties (see, e.g., Stassun et al. 2017; Hsu et al. 2019; Brandt et al. 2019) and even in guiding the *a priori* target choice to maximize the yield of DI campaigns (Bonavita et al. 2022a; Kuzuhara et al. 2022). The prosecution of Gaia – whose latest release (DR3; Gaia Collaboration et al. 2022) covers 33 months of data – over a 10 year timespan is expected to unveil a population of $\sim 10^4 - 10^5$ brown dwarfs and, to a lesser extent, Super-Jupiters (Holl et al. 2022). For the purpose of high-mass star exoplanet demographics, we repeat the usual computation of Equation 1.9 at the snow line, imposing this time the condition $P < 10$ yr; we obtain:

$$M_* \lesssim 1.3 - 1.9 M_\odot, \tag{1.16}$$

depending on the value of β. Given the timespan covered by Gaia DR3, we might get to $a = a_{sl}$ only for stars with $M_* < 0.53 M_\odot$ or, equivalently, we might explore only the region up to $0.1 - 0.3$ a_{sl} around a $M_* \sim 3 M_\odot$ star. The maximum corresponding astrometric signal of a $10 M_\mathrm{J}$ planet at a rather typical $d = 100$ pc is $S \sim 30 - 90 \mu$as, yielding at best a detection with $S/N \sim 1 - 3$. Employing a ~ 10 yr survey duration, the S/N should increase of about a factor two. While astrometry is expected to open new exciting windows for studies related to the demographics of substellar companions and to their formation, it might be not adequate to directly probe the relevant separation range around high-mass stars.

In the light of what has been outlined in this Section, it is clear that the sensitivity of transit surveys is sharply limited to the innermost regions around high-mass stars; albeit based on different physical grounds, the same limitation applies to astrometry too. Microlensing is additionally limited by the practical struggle to collect a large enough sample of high-mass stars. While suffering from the same bias toward close-in planets, radial velocity surveys are able to adequately cover the mass range $1 M_\odot < M_* < 2 M_\odot$, bridging the gap between solar-like stars and the unexplored realm of B-type stars. The opposite detection biases of direct imaging for young wide-orbit exoplanets, on the other hand, make it the ideal technique to explore the frontiers of planet formation throughout the B-type regime.

1.4.2 Observational constraints

In this Section we will review the properties of the giant planet population found around hosts of different masses. Explaining these properties in view of theoretical formation mechanisms will be the goal of Section 1.5; particular attention will be devoted to the current knowledge about systems around high-mass stars, based on radial velocity and direct imaging studies. The limitations of the current studies will justify the need for a new direct-imaging study dedicated to our science case.

By combining Kepler and a sample of F- to M-type stars studied through RV, Fernandes et al. (2019) found that the occurrence of $0.1 M_\mathrm{J} < M < 20 M_\mathrm{J}$ companions peaks at periods $T \sim 1000 - 2000$ d, corresponding to $a \sim 2 - 3$ au. In an analysis of 719 FGKM targets of the California Legacy Survey, Fulton et al. (2021) confirmed that both $1 M_\mathrm{J} < M < 20 M_\mathrm{J}$ and $0.1 M_\mathrm{J} < M < 1 M_\mathrm{J}$ companions are more commonly found at semimajor axes $a \in [1 - 10]$ au compared to orbits interior

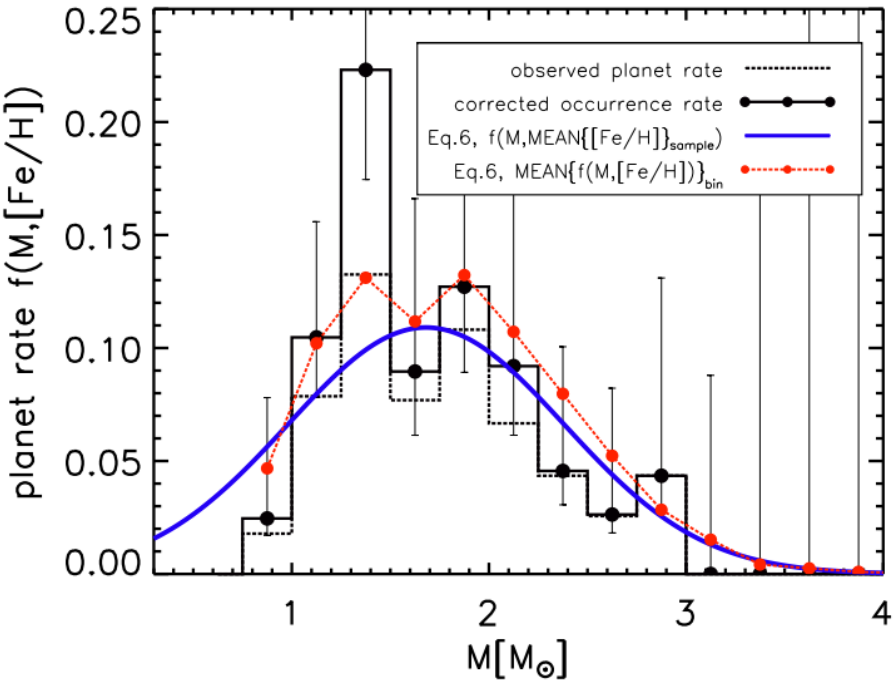

Figure 1.3: Giant planet occurrence rate as a function of stellar mass, reconstructed from a sample of 482 evolved stars studied through RV. The observed distribution of planets (black dotted histograms), when corrected for completeness, turns into the distribution indicated by solid black histograms. The blue solid line represents the best-fit normal curve fixing the metallicity to the mean value [Fe/H] $= -0.05$, while the red dots represent a correction of the best-fit curve that takes into account the mean [Fe/H] of each bin. Source: Wolthoff et al. (2022).

or exterior of this range. The occurrence frequency of the former group was estimated as $14.1^{+2.0}_{-1.8}\%$ for $a \in [2, 8]$ au, and $8.9^{+3.0}_{-2.4}\%$ for $a \in [8, 32]$ au.

It is interesting to compare the reported values with similar frequencies obtained by direct imaging studies: as DI preferentially probes orbital distances beyond the snow line, these frequencies should be much smaller. Indeed, the frequency of $0.5M_{\rm J} < M < 75M_{\rm J}$ in the separation window 20 au $< a <$ 300 au around FGK hosts is as low as $2.1^{+2.4}_{-0.6}\%$ according to Vigan et al. (2017), and comparable numbers can be found across several studies (Galicher et al. 2016; Bowler 2016; Nielsen et al. 2019; Vigan et al. 2021).

The dependence of giant planet occurrence on stellar mass has been the subject of dedicated radial velocity (RV) campaigns over the last decade. A robust result was first found by Reffert et al. (2015) by monitoring over 12 years a sample of 373 evolved stars covering the mass range $[1, 3]M_{\odot}$; a recent confirmation of their results, based on a larger stellar sample (482 stars), was recently published by Wolthoff et al. (2022). According to the latter study, the frequency of $1M_{\rm J} \lesssim M \lesssim 40M_{\rm J}$ companions is higher for larger stellar hosts up to $M_* \sim 1.7M_{\odot}$; after this peak, a turnoff is observed, until the frequency sharply drops to 0% at $M_* > 3M_{\odot}$ (Figure 1.3).

As already explained in Section 1.4.1, the increasing separation of the snow line – beyond which most giant planets are thought to form (see Section 1.5) – with stellar mass (Kennedy & Kenyon 2008), coupled with the scarce sensitivity of RV to separations larger than a few au (Figure 1.4), does not allow one to rely upon the observed trend for $M_* \gtrsim 2M_{\odot}$. Currently, only direct imaging might

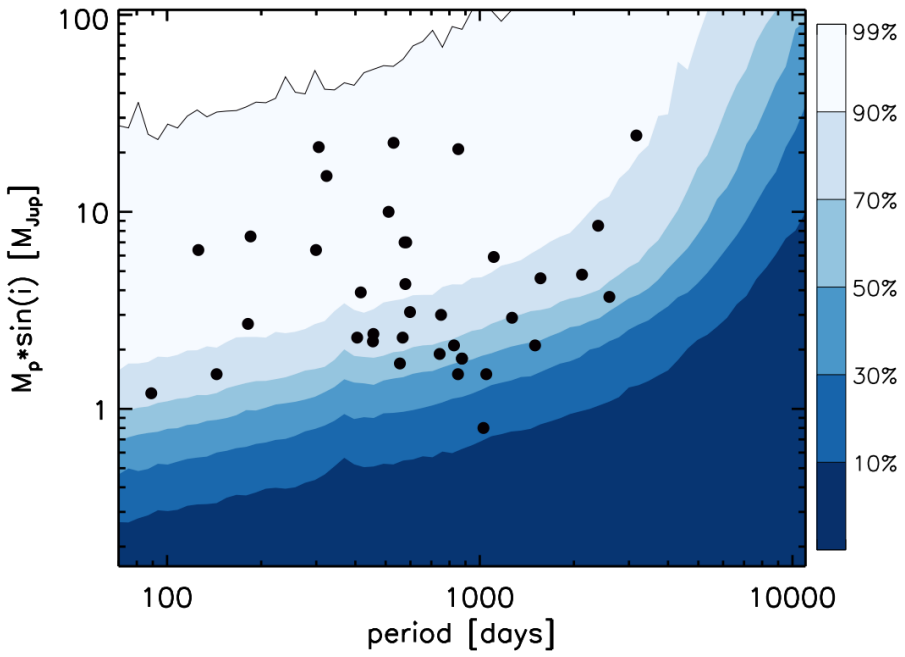

Figure 1.4: Planet detectability within the survey by Wolthoff et al. (2022). Detected planets are indicated as black dots. Planets having $M_p \cdot \sin i$ above the $n\%$ limit can be detected around $n\%$ of the targets. Source: Wolthoff et al. (2022).

clarify whether a wide-orbit population around high-mass stars has hitherto escaped detection, so that the increasing trend highlighted by RV up to $M_* \sim 2M_\odot$ continues to higher masses, or whether an upper mass limit for planet formation mechanisms exists.

The increase of the giant planet occurrence up to $M_* \sim 2M_\odot$ has been independently confirmed by direct imaging surveys (Bowler 2016; Nielsen et al. 2019; Vigan et al. 2021). In particular, the SpHere INfrared survey for Exoplanets (SHINE; Desidera et al. 2021) survey has intriguingly shown that the frequency of substellar companions is about 4 times and 2 times higher around BA stars than around FGK and M stars, respectively (Vigan et al. 2021). Unfortunately, very few stars of the sample actually belong to the B-type regime. Although B stars are seldom present in direct-imaging surveys, a few detection of $10-40M_\mathrm{J}$ companions around $M_* \sim 2.5M_\odot$ stars have sporadically been announced (Lafrenière et al. 2011; Carson et al. 2013; Cheetham et al. 2018); very little is known about more massive hosts. To date, Janson et al. (2011) have conducted the only survey dedicated to B-type stars, featuring a modest sample size (15 stars in the spectral range B2-A0). The lack of detections allowed them to place an upper limit of $< 30\%$ in the fraction of planet-hosting B stars.

In the light of the limitations of RV searches and the scarcity of past direct-imaging searches, we have stressed the need for a large DI survey dedicated to B-type stars. A survey with these properties, the B-star Exoplanet Abundance STudy (BEAST; Janson et al. 2021b), was indeed commenced in 2019 and will constitute the main focus of this dissertation.

1.5 Planet formation models

Obtaining precise constraints on the occurrence frequency of giant planets around B-type stars is, as we have seen in Section 1.3, the first step toward understanding the physical mechanisms responsible

for their formation. On the other hand, a complete lack of detections would be equally significant, for it would prove the inadequacy of the environments around B stars to sustain the formation of planets. Assuming for the moment that a population of companions indeed exists, the distribution of its orbital properties would be a key proxy of the formation mechanism at play. Even more importantly, the shape taken by its mass distribution – and its possible prosecution throughout the brown dwarf regime – is pivotal to disentangle among different formation pathways. We review in this Section the two relevant mechanisms that have been put forward in the theoretical literature: *core accretion* (Section 1.5.1) and *gravitational instability* (Section 1.5.2).

Key observational insights on planet formation processes can be garnered by studying the early stages of planetary systems. As regards our Solar System, indirect evidence coming from physical, chemical and orbital studies of minor bodies has allowed astronomers to peer into its early history (Section 1.2); the discovery of the Kuiper Belt has been equally influential (Fernandez 1980; Duncan et al. 1988; Jewitt & Luu 1993), revealing the paramount role played by dynamics in crafting the architecture of our planetary system. Complementing these findings, direct analyses of young stellar objects started in the 1980s (e.g., Smith & Terrile 1984; Strom et al. 1989; Beckwith et al. 1990) substantially helped clarify the initial conditions where planet formation occurs.

Following the collapse of a portion of a molecular cloud, the inward flow of matter toward the growing protostellar core triggers the formation of a circumstellar disk around it (Hartmann 1998). Such disks, whose existence has been first revealed by studies of T-Tauri stars (Lynden-Bell & Pringle 1974), are the cradle of planets (Goldreich & Ward 1973; Pollack et al. 1996; Williams & Cieza 2011) and usually disappear within a few Myr, due to strong stellar wind and harsh XUV radiation from the star during its T-Tauri/Herbig Ae/Be phase (e.g.,Clarke et al. 2001).

The Atacama Large Millimeter/Submillimeter Array (ALMA; Wootten & Thompson 2009), an interferometer composed of 66 12-m and 7-m antennas and capable of baselines up to 16 km, has unveiled in unprecedented detail the cradle of planets: exquisite structures such as gaps, rings and spirals, altering both the gas and the dust distribution, have often being observed (Figure 1.5), sometimes hinting at forming protoplanets (Fedele et al. 2017; Boccaletti et al. 2020; Benisty et al. 2021). Constraining the mass of protoplanetary disks – i.e., the initial reservoir available for planet formation – is, however, notoriously difficult: these masses appear to be widely spread out across Class I protostars ($M_{\rm disk} \in [0.01, 0.1] M_{\odot}$, approximately corresponding to $M_{\rm disk}/M_{*} \in [0.03, 0.4]$), and qualitatively consistent with the estimates determined for the "minimum mass Solar Nebula" in our Solar System (Weidenschilling 1977; Hayashi 1981b); theoretical works point to even higher disk masses during the Class 0 stage, with $M_{\rm disk}/M_{*} \in [0.2, 1]$ (Vorobyov 2011; Baillié et al. 2019). As regards the dependence of disk mass on stellar mass, an ALMA survey of 93 disks in the ~ 2 Myr old Chamaeleon I star-forming region (Pascucci et al. 2016) provided evidence, at least in the regime $M_{*} \in [0.03, 2] M_{\odot}$, for a steeper than linear disk-mass scaling relation:

$$M_{\rm disk} \propto M_{*}^{1.3-1.9}. \tag{1.17}$$

Equally important as the disk initial mass is the timescale of its dissipation, setting the endpoint for any planet formation pathway. By monitoring continuum and line emission in hundreds of disks at different ages, ALMA mapped the dependence of disk demographics on time; an exponential decrease of the fraction of full disks in young star populations is observed (Mamajek 2009):

$$f_D = e^{-t/\tau}. \tag{1.18}$$

Estimates of the value of τ are somewhat uncertain, sensitively depending on stellar ages determined through isochrone fitting, and range between 2.5 Myr (Mamajek 2009) and 5 Myr (Richert et al.

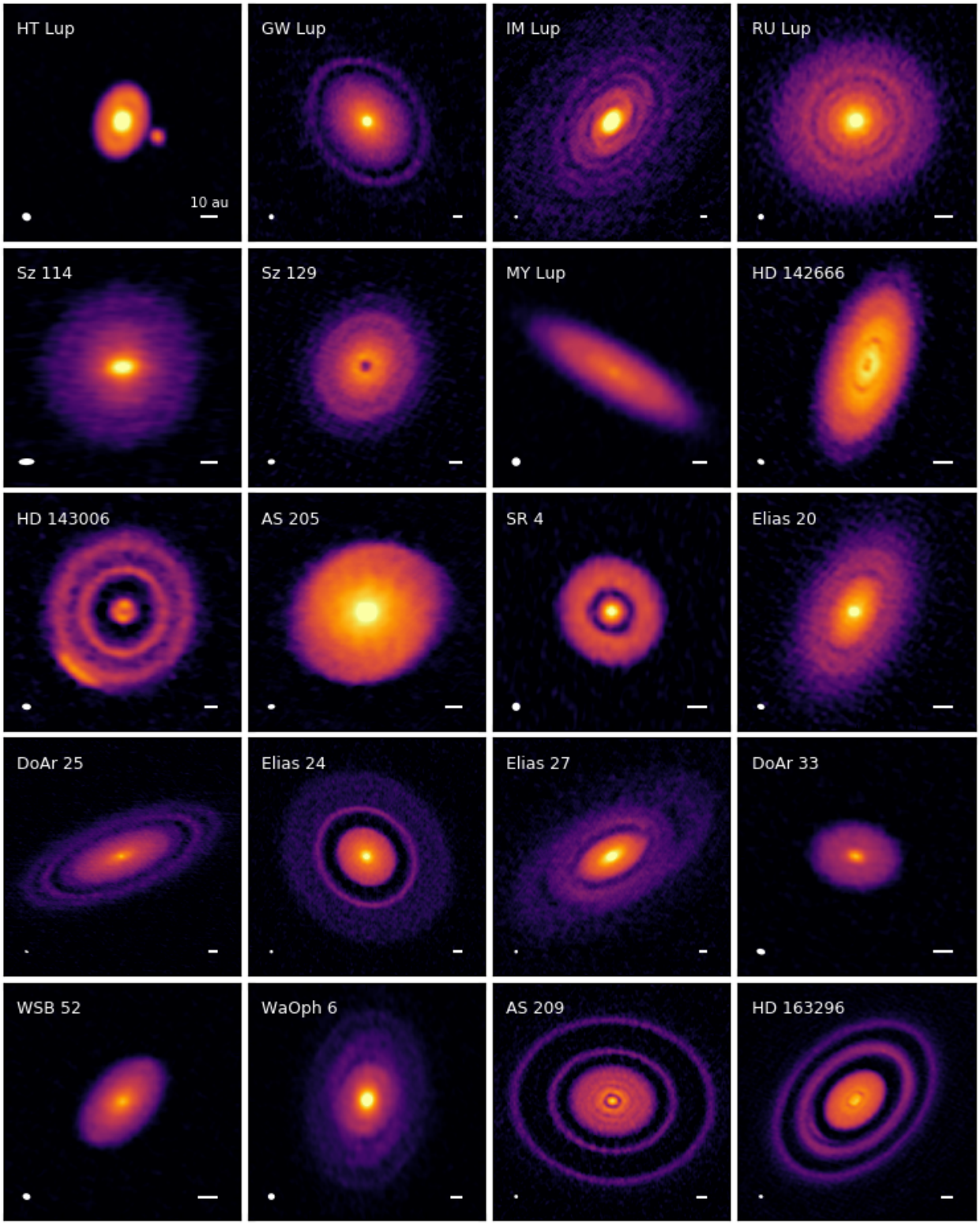

Figure 1.5: A sample of circumstellar disks as seen in continuum emission by ALMA (240 GHz ≡ 1.25 mm). The spatial scale corresponding to 10 au is indicated in the lower right corner of each panel. Source: Andrews et al. (2018).

2018); crucially for our purposes, the value has been found to depend on stellar mass because of the varying strength of XUV-induced photoevaporation: as a results, τ falls below 1 Myr for $M \gtrsim 5M_{\odot}$ (Gorti et al. 2009).

1.5.1 Core accretion

The core accretion paradigm, whose historical development has been sketched in Section 1.2, can be epitomized as the slow hierarchical assembling by successive coagulation of larger structures from dusty building blocks found in protoplanetary disks.

In the first stage ($\sim 10^3$ yr), dust grains settle in the mid-plane of the disk and simultaneously coagulate into mm-sized particles (Dullemond & Dominik 2005); their ceaseless collisions, reproduced in laboratory experiments, establish a quasi-equilibrium where coagulation, bouncing and fragmentation are balanced and the size distribution has most of its mass in mm- and cm-sized particles (Güttler et al. 2010; Birnstiel et al. 2011); the growth beyond the seemingly insurmountable *meter-size barrier* (Dominik et al. 2007), perhaps mediated by the onset of gravitational instabilities in the solid sub-disk (see, e.g., Johansen et al. 2007), should lead in $10^4 - 10^5$ yr to the formation of planetesimals (~ 1 km) (Armitage 2020, chap. 4.8). Following effective clumping in rings separated by regions of smaller density, planetesimals start colliding, initiating the runaway growth of a small number of Moon-sized planetary embryos (Kokubo & Ida 1996, 2000). Once the embryos have depleted the disk to a point when dynamical friction is no longer able to keep orbital eccentricities under control, mutual interactions initiate a $\sim 10 - 100$ Myr chaotic regime characterized by harsh collisions and scattering processes, until only a few planets are left (Raymond et al. 2006).

The picture outlined above applies both to terrestrial and giant planets. The transition between the two classes of planets occurs as soon as a critical core mass ($\sim 10M_{\oplus}$) is attained (Mizuno 1980; Mordasini et al. 2012b): a rapid runaway accretion of gas from the disk then sets in, giving origin to the massive gaseous envelopes surrounding Jovian planets (Pollack 1984; Bodenheimer & Pollack 1986; Pollack et al. 1996). In the inner regions of the disk, the feeding regions of planetary embryos do not contain enough solid material to allow for the in-situ formation of giant planets (Schlichting 2014); hence, the population of Hot Jupiters, which bewildered the astronomical community in the 1990s (Section 1.2), is assumed to be the result of an inner migration induced by torques from the gas (Baruteau et al. 2014), planet-planet scattering (Weidenschilling & Marzari 1996), cyclic secular oscillations (Naoz 2016), or chaotic secular interactions (Wu & Lithwick 2011), followed by orbital decay via tidal interactions with the host star (Essick & Weinberg 2016).

The golden spot for giant planet formation turns out to be the region immediately outward the so-called *snow line* (Mizuno 1980; Pollack 1984). The snow line, corresponding to a temperature in the disk of 150-170 K, is the region where water vapor condenses into ice, significantly increasing the surface density of solid material available for planetesimal formation (Hayashi 1981b). The location of the snow line is a function of stellar luminosity and of the accretion rate of gas through the disk, both functions of time. While theoretical works lead to a wide range of predicted snow line locations a_{sl} for the early Solar disk (0.5 au$< a_{sl} <$ 5 au; Garaud & Lin 2007), strong observational constraints have been derived from laboratory measurements of meteorite samples, placing it at about 2.7 au (Armitage 2020, chap. 1.5).

Let us now try to obtain a rough estimate of the timescale of core accretion, comparing it with the previously found timescale of disk dissipation (Equation 1.18). The accretion of planetesimals onto the core involves only a small fraction of the planetesimals entering the core's Hill sphere (Chabrier et al. 2014); assuming that their random velocity is ΩR_H, i.e. the Keplerian velocity shear across the Hill radius, a useful expression can be obtained for the temporal derivative of radius dR/dt (Dones

& Tremaine 1993):

$$\frac{dR}{dt} = \frac{\Sigma_s \Omega}{p\rho} \approx 50 \text{ m yr}^{-1} \left(\frac{r}{1 \text{ au}}\right)^{-2} \tag{1.19}$$

assuming a surface density of solids $\Sigma_s \approx 30$ g cm^{-2} at 1 AU. Here $p = (9M_*/4\pi\rho a^3)^{1/3}$, ρ is the 3D density of solids, $\Omega = \sqrt{GM/a^3}$ is the Keplerian angular velocity at $r = a$ and $R_H = (GM_p/3\Omega^2)^{1/3}$ is the Hill radius of the core.

The result corresponds to a core accretion rate of $\sim 10^{-6} M_\oplus$ yr^{-1} at the current location of Jupiter ($a = 5$), i.e. a core formation timescale of $\sim 10^7$ yr (Dodson-Robinson et al. 2009; Chabrier et al. 2014); while this scale can be reduced up to a factor 10 depending on the assumed planetesimal column density (Pollack et al. 1996), the formation of gaps around the growing embryo could act in the opposite direction (Rafikov 2003). In any case, the strong radial dependence of dR/dt strongly argues against giant planet formation beyond $10 - 20$ au, as the disk should have already dissipated before the critical mass is reached (Dodson-Robinson et al. 2009).

An interesting variation on the theme has been proposed by Rafikov (2004) and builds on the following idea. Triggered by the overwhelming gravity of a core, nearby planetesimals increase their relative velocities; their collisions are more energetic, so that destruction is favored over accretion, originating a steady-state population of $1 - 10$ m collision remnants; since objects of this size are very strongly coupled with the gas, their velocity distribution is strongly damped – especially in the vertical direction – resulting in the formation of a thin accretion disk around the core. The radius increase over time is higher than in the previous case:

$$\frac{dR}{dt} = \frac{\Sigma_s \Omega}{p^{3/2}\rho} \approx 1 \text{ km yr}^{-1} \left(\frac{r}{1 \text{ au}}\right)^{-3/2} \tag{1.20}$$

and the resulting accretion rate is high enough to allow the growth of a Neptune-sized core at $a = 30$ au in less than 10 Myr (Chabrier et al. 2014), extending the possibility of giant planet formation to 40-50 au (Rafikov 2011).

Core accretion via pebble accretion is, we might say, an even more audacious variation on the classical theme. A bottleneck in classical CA models is reached during planetesimal formation: according to the predictions of several particle growth mechanisms, effective particle growth should stop – as we have already mentioned – when they attain the cm size (Zsom et al. 2010). After forming planetary embryos through gravitational collapse of locally over-dense boulder-rich regions (Johansen et al. 2007), pebbles can efficiently be accreted from the entire Hill sphere due to their strong coupling with gas (Johansen & Lacerda 2010), allowing for 10^3 and 10^4 higher accretion rates at 5 au and 50 au, respectively (Lambrechts & Johansen 2012).

A thorough comparison between a core accretion model and the observed trends of the exoplanet population has been performed by Mordasini et al. (2012a). Their model, based on the one by Pollack et al. (1996), is coupled to two models describing the evolution of the protoplanetary disk and the orbital migration of planetary embryos triggered by angular momentum exchange with the disk (Mordasini et al. 2012b). Before runaway accretion sets in, the gas accretion rate onto the core is obtained by solving one-dimensional hydrostatic structure equations that resemble those used for stellar interiors, provided that the heating term is due to the impact of planetesimals rather than nuclear fusion (Bodenheimer & Pollack 1986). Only one core per disk is allowed in their simulations; in order to explore the wide parameter space (including core density, initial orbital location, envelope mass, accretion rate, background conditions), this population synthesis model draws thousands of initial condition sets in a Monte Carlo fashion. The resulting population of exoplanets is then "observed" with the radial velocity method, creating a synthetic exoplanet population which can be

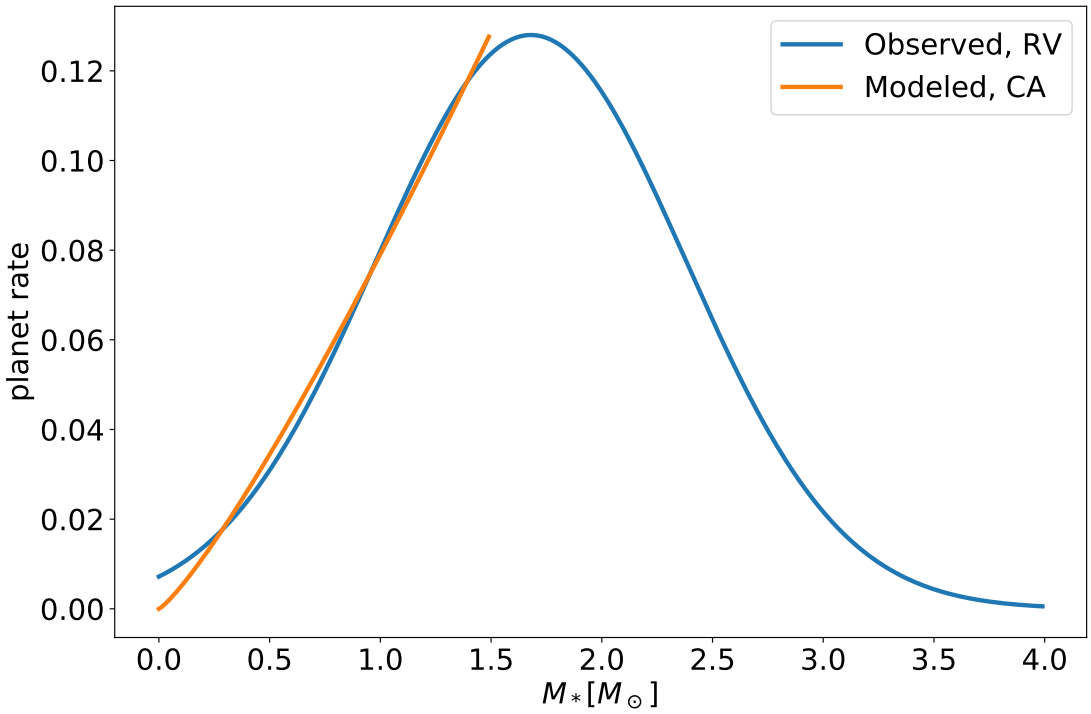

Figure 1.6: Comparison between the occurrence frequency of $1-20 M_{\rm J}$ giant planets reconstructed by Wolthoff et al. (2022) (blue curve, cp. Figure 1.3) and the core accretion predictions by Mordasini et al. (2012a) (orange curve).

finally compared to observations. Their orbital migration module, comprising both type I and type II migration, is able to produce both inward and outward movement of protoplanets (Mordasini et al. 2011). The dependence on stellar mass was explored in a previous paper of the series (Alibert et al. 2011), by varying the central stellar mass in the range $M_* \in [0.8, 2]\ M_\odot$.

The occurrence of giant planets was found to be positively correlated with stellar metallicity, as indeed observed in radial velocity studies (e.g., Reffert et al. 2015; Wolthoff et al. 2022). Disk mass is positively correlated with giant planet occurrence too, due to the increased solid reservoir: assuming $M_{\rm disk} = 0.03\ M_\odot$ for a $M_* = 1\ M_\odot$ star and $M_{\rm disk} \propto M_*^{1.3}$ (Equation 1.17), the derived giant planet occurrence frequency[12], $f_p = 0.04 \cdot (M_{\rm disk}/0.017 M_\odot)^{1.2}$, qualitatively reproduces the reconstructed best-fit expression found by Wolthoff et al. (2022) in the mass regime $[0.5\ M_\odot < M_* < 1.2\ M_\odot]$ (Figure 1.6). Another prediction of the model is that the maximum attainable planetary mass is linearly correlated with disk mass, implying a constant conversion rate of disk mass into planetary mass.

According to the model, the preferred location for giant planet formation around solar-type hosts lies at about 5 au, supposing a minimum surface density of planetesimals $\Sigma_s = 6$ g cm^{-2}. Higher

[12] Although the relation strictly refers to the fraction of stars with a giant planet, the single-planet nature of the simulation enables this semantic substitution.

densities are necessary both within and beyond this distance: to increase the low isolation mass[13], in the former case, and to decrease the long accretion timescale, in the latter case. Increasing the disk metallicity enlarges the annulus where formation can occur, so that for [Fe/H] $\gtrsim 0.4$ any orbital location $\in [1, 20]$ au becomes virtually possible. In any case, orbital migration redistributes the original a distribution by populating the inner regions up to 0.1 au: the strength of migration, increasing with [Fe/H], is reflected into the tendency of Hot Jupiter hosts to be metal-rich (Udry & Santos 2007). Conversely, very few planets are scattered to distances larger than about 10 au, in agreement with radial velocity trends and the low yield of direct imaging studies (Fernandes et al. 2019; Fulton et al. 2021; Vigan et al. 2021).

Finally, disk lifetimes τ were found to strongly affect the formation of giant planets, with $f_p \propto \tau^2$. When coupled with the steep decrease of disk lifetime around stars with $M > 3M_\odot$ (Gorti et al. 2009), this result is particularly important because it implies that core accretion is eventually halted around B stars.

1.5.2 Gravitational instability

Throughout Section 1.5.1, we have always assumed that the self-gravity of the disk is negligible with respect to the gravitational force exerted by the central star. In this case, the natural tendency of gas to form over-dense regions, or *clumps*, in the disk is thwarted by pressure and shear; if we let the mass of the disk increase, we will eventually start observing clumps, owing to the stronger disk's self-gravity.

The foundations of *gravitational instability* as a mechanism able to form planets date back to seminal intuitions by Kuiper (1951) and Cameron (1978), and were later integrated into a consistent picture by Boss (1997). Unlike in core accretion, under GI conditions planetary-mass objects are the outcome of a top-down scenario that involves the fragmentation of the gaseous disk during the early stages of its life, where self-gravity is expected to play an important role (see Section 1.5): as a result, the mechanism usually forms companions that are more massive than planets, namely brown dwarfs and low-mass stars (Wright et al. 2010).

It is possible to derive the conditions under which self-gravity is expected to dominate over the stabilizing effect of pressure and shear by requiring the collapse timescale for a clump to be shorter than the crossing timescale of a sound wave and the timescale required by shear to destroy the clump.

Let us consider an accreting clump with size Δr and mass $m \sim \pi \Delta r^2 \Sigma$. Gravitational collapse occurs on the free-fall timescale t_{ff}:

$$t_{ff} \sim \sqrt{\frac{\Delta r^3}{Gm}} \sim \sqrt{\frac{\Delta r}{\pi G \Sigma}}. \tag{1.21}$$

The time for a sound wave to cross the clump is simply given by:

$$t_p \sim \frac{\Delta r}{c_s}, \tag{1.22}$$

where c_s is the sound speed, while the shear timescale, i.e. the time in which a clump gets sheared azimuthally by an amount Δr, is:

$$t_{shear} = \frac{1}{r}\left(\frac{d\Omega}{dr}\right)^{-1} \sim \Omega^{-1}, \tag{1.23}$$

[13]The isolation mass is defined as the maximum mass that a protoplanet can reach during runaway growth after consuming all the planetesimals in its surroundings (Armitage 2020).

$\Omega = \sqrt{GM_*/r^3}$ being the Keplerian orbital frequency[14]. By imposing the equality among t_{ff}, t_p and t_{shear}, one can derive a condition for instability (Armitage 2020):

$$\pi G\Sigma \gtrsim c_s\Omega \tag{1.24}$$

that is usually expressed by defining the *Toomre Q parameter* (Toomre 1964):

$$Q \equiv \frac{c_s\Omega}{\pi G\Sigma}. \tag{1.25}$$

Local instability in a disk sets in when $Q < 1$. Given that the vertical scale height of the disk $h = c_s/\Omega$, and the disk mass can be approximated as $M_{\rm disk} \sim \pi r^2\Sigma$, Equation 1.25 can be rewritten in a global way as:

$$\frac{M_{\rm disk}}{M_*} \gtrsim \frac{h}{r}. \tag{1.26}$$

A typical value for h/r is 0.05 (Armitage 2020): the disk should be rather massive to become globally unstable against gravitational instability. Intuitively, this requirement limits the onset of GI to the early phases of young stellar objects, before the Herbig/T Tauri phase of evolution (Sheehan & Eisner 2017), when surface densities are high due to a large disk accretion rate and an inefficient angular momentum transport. Observationally, disk masses during Class II ($2-3$ Myr) are already too low in 80-90% of the time for GI to operate (Andrews et al. 2013; Kratter & Lodato 2016). Interestingly enough, there is some evidence that B stars are surrounded at birth by massive self-gravitating disks (e.g. Shepherd et al. 2001, 2004).

Colder and thinner disks are more susceptible to the action of self-gravity (Kratter & Lodato 2016). The triggering of GI creates trailing density waves that heat up the disk and increase Q; this leads to the decay of the spiral pattern, cooling down the disk that is thus prone again to instability. This cycle of spiral wave excitation and decay is known as gravitoturbulence (Gammie 2001), and leads to a marginally unstable state, with Q oscillating around the critical value (Paczynski 1978).

Fragmentation occurs if this negative feedback due to angular momentum transport breaks: if the restoring mechanism is not strong enough to counterbalance the density fluctuations, these will lead to collapsing objects embedded in the disk. The efficiency of this turbulence-driven transport is quantified by a parameter α, known as the Shakura-Sunyaev parameter (Shakura & Sunyaev 1973):

$$\alpha = \frac{64}{27}\left(\frac{\mu m_p}{k_b}\right)^2 \frac{\pi^2 Q_0 \sigma G^2}{\kappa_0}\Omega^{-3}, \tag{1.27}$$

which is related to the typical amplitude of density perturbations (Cossins et al. 2009; Rice et al. 2011):

$$\left\langle \frac{\Delta\Sigma}{\Sigma} \right\rangle \propto \sqrt{\alpha} \propto t_{cool}^{-1/2}. \tag{1.28}$$

It can be seen that, in order to produce a density perturbation that is large enough to collapse into a bound object, the local cooling time should be short enough, or the local self-gravity should be strong enough. A rough estimate of α under modeled conditions around a Sun-like stars yields:

$$\alpha \sim 0.1\left(\frac{r}{40\ \text{au}}\right)^{9/2}. \tag{1.29}$$

[14]When the disk is very massive, the angular velocity can significantly differ from the Keplerian one. A generalization of Equation 1.23 involves the *epyciclic frequency* κ – defined so that $\kappa^2 = (1/r^3)d(r^4\Omega^2)/dr$ – in place of Ω.

Therefore, as suggested by intuition, fragmentation is much easier at wide orbital distances (40 au $\lesssim a \lesssim$ 100 au) than at close separations, where the disk is not able to cool efficiently and gravitational stresses are weaker, resulting in a stable configuration (Rafikov 2005; Clarke 2009; Rafikov 2009; Rice et al. 2010). Crucially, unlike classical core accretion models, numerical models of GI consistently show that, as soon as the conditions for instability are met, fragmentation will occur within a few rotation periods, that is on a timescale of $10^3 - 10^4$ yr (Clarke 2009; Stamatellos et al. 2011; Steiman-Cameron et al. 2013; Backus & Quinn 2016).

A second interesting consideration is that the most unstable scale in a gravitational unstable disk is $\lambda \sim 2c_s^2/G\Sigma$, setting a characteristic mass for GI seeds of the order $M_p \sim \pi\lambda^2\Sigma$ (Armitage 2020, chap. 6.3). For a solar-like star, this value is approximately $M \sim 3-5M_\mathrm{J}$ (Kratter et al. 2010; Forgan & Rice 2011): a hint of the fact that GI preferentially creates very massive objects (Super Jupiters, brown dwarfs and low-mass stars). Indeed, GI is thought as the main mechanism forming binaries with separation below $\sim$ 100 au (Kratter et al. 2010), that are very common since nearly half of the stars are binaries – the fraction increasing with stellar mass (Duquennoy & Mayor 1991; Kouwenhoven et al. 2007b; Raghavan et al. 2010; Peter et al. 2012; Duchêne & Kraus 2013; Moe & Di Stefano 2017) – and the peak of the binary semimajor axis distribution is below 100 au (Duquennoy & Mayor 1991; Raghavan et al. 2010). Since accretion on the companion should be favored over accretion on the primary (Bate et al. 2002; Duffell et al. 2020; Ceppi et al. 2022), we might expect that the earlier a companion is generated by GI around a forming star, the most massive it may result (Tokovinin & Moe 2020): binary and planetary formation by GI should be seen therefore as a continuum, with planet formation occurring during the latest phases of disk instability.

Forgan et al. (2018) performed a thorough population synthesis study of objects created via gravitational instability, taking also into account the dynamical interactions between the fragments. Starting from central stellar masses $M_* \in [0.8, 1.2]M_\odot$, 1D self-gravitating disk models – assuming a uniform mix of dust and gas, with a constant dust-to-gas ratio of 0.01 – with a maximum extent of 100 au and a disk-to-star mass ratio $M_d/M_* \in [0.125, 0.375]$ were evolved until $t = 1$ Myr (or up to shorter times, if the disk dissipated due to photoevaporation).

In each simulation, fragments were added to the disk at $t = 0$; the first fragment was placed at the smallest radius where fragmentation can occur (Forgan & Rice 2011), and up to four other fragments were added at regular spacing governed by a free parameter; the choice is justified by earlier simulations showing that a single fragment is able to trigger the formation of other fragments (Vorobyov et al. 2013; Meru 2015; Hall et al. 2017). The physical evolution of the fragments, involving grain sedimentation from the disk, core formation and tidal downsizing, takes place as in Forgan & Rice (2013); in addition to Type I/Type II migration, the simulation takes into account the mutual gravitational interactions among fragments. The effect of N-body physics is profound: about 40% of the initial fragments is ejected from the system, the surviving fragments are scattered throughout the available semimajor axis space, and a significant amount of the simulations evolves toward single-body systems[15]. A prediction of their study is that – at least around solar-type stars – direct imaging surveys should preferentially find single massive objects in the outskirts of their systems; due to the negligible role played by dust, their occurrence frequency should not be correlated with stellar metallicity.

The final mass distribution of companions is shown in Figure 1.7. A multi-modal mass function is observed, with peaks at $\sim 10M_\mathrm{J}$ and $\sim 80M_\mathrm{J}$; the former shifts to about $\sim 25M_\mathrm{J}$ when taking into account dynamical evolution. Although the model neglects gas and dust accretion after fragment

[15]Interestingly enough, the over-prediction of hot Jupiters argues against GI as a major planet formation mechanism (Rice et al. 2015).

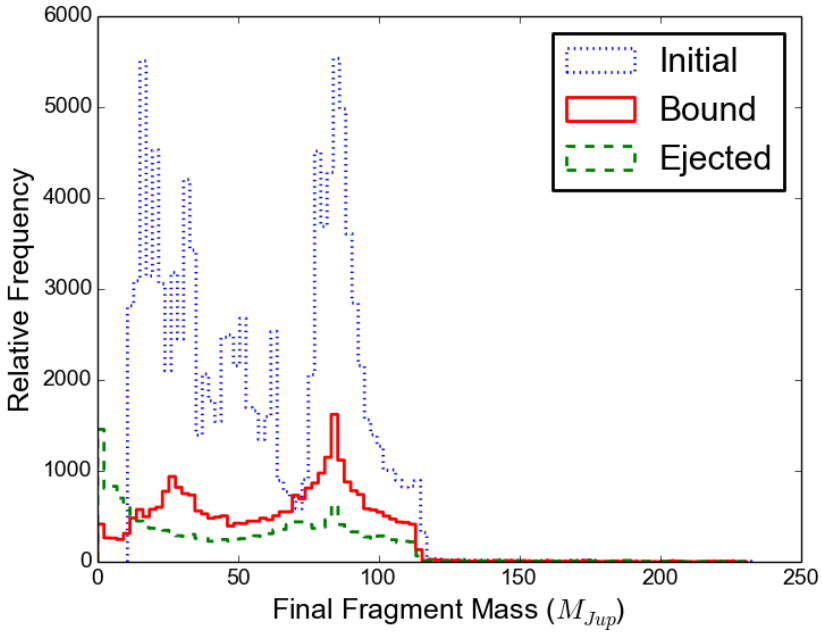

Figure 1.7: The mass distribution of initial (blue), ejected (green) and surviving (red) fragments in the gravitational instability model by Forgan et al. (2018).

formation, about 95% of the final bound companions has a mass above the deuterium-burning limit. This widespread prediction of GI simulations justifies the description of GI exoplanets as "failed binary-stars" (Kratter et al. 2010).

Direct evidence for gravitational instability in young circumstellar disks has been detected in the $\lesssim 0.15$ Myr, $\sim 1 M_{\odot}$ ternary system L1448 IRS3B, where the third object is a $M \gtrsim 0.085 M_{\odot}$ star lying within a spiral arm in the outer disk at ~ 200 au (Tobin et al. 2016), and is strongly indicated by hydrodynamical simulations as the cause for the spiral pattern seen in the ~ 1 Myr, $\sim 0.5-0.6 M_{\odot}$ star Elias 2-27 (Meru et al. 2017). On the other hand, the sensitivity of direct imaging studies to massive wide-orbit objects like those predicted by GI (Section 1.4.1) has led to the speculation that most directly imaged objects are the outcome of GI (e.g., Dodson-Robinson et al. 2009). If this is the case, wide-orbit Super Jupiters should be the tail of a population mostly composed of brown dwarfs and low-mass M-type companions (Kratter et al. 2010). While seminal statistical analysis seem indeed to show a duality in the physical and orbital distribution of DI companions with an approximate cutoff at the deuterium burning limit (Nielsen et al. 2019; Vigan et al. 2021), larger sample sizes are needed to reach more robust conclusions.

1.6 Theory vs observations: exoplanets around B stars

In Section 1.5 we have introduced the two main routes for giant planet formation that have been put forward in the theoretical literature: core accretion and gravitational instability. Observational constraints for these models are currently insufficient for B-type stars (Section 1.4.2): we have therefore compared five exoplanet detection techniques and concluded that the most suited one to disentangle among the two mechanism is direct imaging (Section 1.4.1). Here, we summarize the

predictions of both paradigms:

Core accretion The increased reservoir of disk mass – scaling with stellar mass – is naturally reflected into a greater frequency of gas giants up to $M_* = 2 - 3M_\odot$; on the other hand, the increasingly rapid dispersal of protoplanetary disks starts dominating for more massive stars, eventually leaving not enough time for giant planet formation at $M_* \gtrsim 3M_\odot$.

Gravitational instability Independent of stellar mass, wide-orbit Super Jupiters are expected to populate the outskirts ($a \sim 10s - 100s$ au) of stellar systems, albeit in smaller numbers than brown dwarfs that constitute the core of the companion population.

The companion mass distribution is expected to be significantly different in the two cases, as shown by a comparison between a CA (Emsenhuber et al. 2021) and a GI population synthesis model (Forgan et al. 2018) (Figure 1.8). Owing to their markedly distinct timescales, it is nonetheless possible – provided that the conditions are appropriate – for the two mechanisms to coexist, with GI setting the scene for subsequent CA-driven evolution in a partially depleted disk. A need for a survey with $\sim 50 - 100$ directly imaged B stars is pivotal to reach robust statistical conclusions on this points. We will introduce in the next Chapter a study designed to answer the questions posed throughout this Chapter: BEAST.

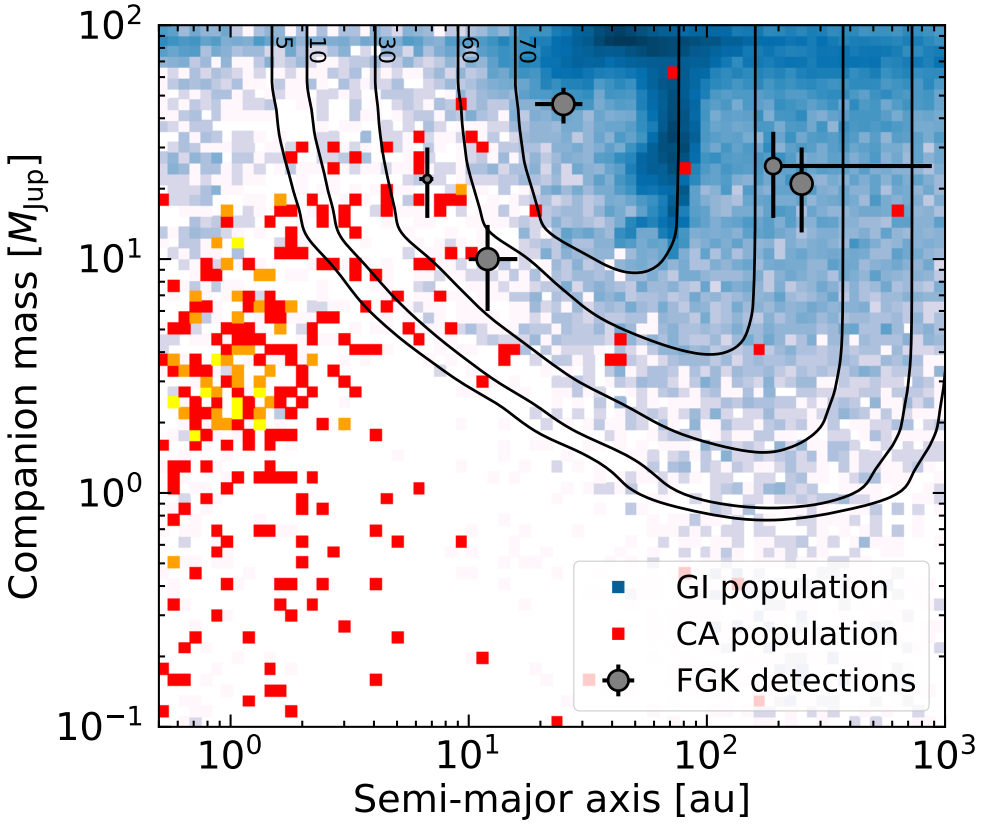

Figure 1.8: Comparison in the $a - M_p$ space between a CA model (Emsenhuber et al. 2021) and a GI model (Forgan et al. 2018). The CA companion density is represented in warm colors (red: low density; yellow: high density), while the GI companion density is coded through cool colors (white: low density; blue: high density). The detection efficiency and the detected companion of the SHINE survey (Desidera et al. 2021) are overplotted as solid lines and gray dots, respectively. Source: Vigan et al. (2021).

Chapter 2

The BEAST survey

As discussed in Chapter 1, the extension of exoplanet demographics toward the almost unexplored realm of B-type stars constitutes a key observational test for formation scenarios first developed to explain giant planet formation around lower-mass hosts. Having described the motivations underlying the choice of direct imaging as the ideal tool to shed light on this scientific case, we introduce in this section the B-star Exoplanet Abundance STudy (BEAST; Janson et al. 2021b), a survey performed through the SPHERE instrument (Beuzit et al. 2019) at the Very Large Telescope (VLT). This Chapter is mostly based upon BEAST's introductory paper (Janson et al. 2021b); my main contribution to the article consists in the derivation of precise ages for the stellar sample and is thoroughly described in Sections 2.4.2.

2.1 The stellar sample

The stellar sample of BEAST is constituted by 85 members of the Scorpius-Centaurus (Sco-Cen) association, the nearest ($\sim 100-200$ pc) star-forming region to the Sun (Section 2.2). The selection of Sco-Cen as the best-suited environment to look for stellar targets is motivated by the simultaneous requirements of proximity and youth – two parameters that strongly affect the performances of a direct imaging campaign. On the one hand, closer young moving groups to the Sun exist, but they are neither as young or as massive to possess a large sample of B-type members (Bell et al. 2015); on the other hand, younger associations and clusters are found at substantially larger distances than Sco-Cen (de Zeeuw et al. 1999). In addition, Sco-Cen is so extended ($\sim 10^5$ bona-fide members; Damiani et al. 2019) that it possesses a large (~ 100) sample of B-type stars with a small spread in age and metallicity, whose study nicely complements previous direct imaging survey addressing A- and F-type stars within the same association (Desidera et al. 2021).

The criteria employed to assemble the final sample are described in detail in the following Section 2.1.1, while a focus on the association – the subject of Chapter 4 – is placed in Section 2.2.

2.1.1 Sample selection

Stellar associations can be discerned as overdensities of sources not only in the physical space but also in the velocity space through the common motion of their members (Blaauw 1946). The starting point for the process of target selection was the list of Sco-Cen members compiled by Rizzuto et al. (2011) based on kinematic data: restricting the list to B-type stars with a $> 50\%$ membership probability, the candidate roster comprises 165 stars. 11 additional candidates with a $> 50\%$ membership probability according to the BANYAN code (Gagné et al. 2014) were retrieved

from an earlier list (de Zeeuw et al. 1999). The initial list was subsequently vetted, removing the stars that are either:

1. known binaries with separations $s \in [0.1 - 6.0]''$, that would have a negative impact on SPHERE's performances. Wide and spectroscopic binaries were instead retained, although a kinematic-based selection can be moderately biased against both groups due to astrometric perturbations of the photocenter (Kervella et al. 2019);

2. targets of previous SPHERE observations with comparable performances;

3. located in the declination range $\delta \in -24.6° + [-3°, +3°]$, since they approach so much the local zenith of Paranal to make tracking troublesome at a hour angle of $0h$, rendering angular differential imaging (ADI; Marois et al. 2006) unfeasible.

As the membership probabilities by Rizzuto et al. (2011) were based on the astrometric solution obtained by Hipparcos (van Leeuwen 2007), a re-evaluation of these values based on Gaia Data Release 2 (Gaia DR2; Gaia Collaboration et al. 2018b) was undertaken for the stars passing the previous selection by means of a more recent version of BANYAN (BANYAN Σ; Gagné et al. 2018). For a dozen targets the new analysis, both with or without the inclusion of radial velocities from the literature, yielded membership probabilities $< 40\%$. Nevertheless, they were retained in the sample due to the large uncertainty[1] on astrometric parameters.

The final sample, as already mentioned, is composed of 85 B-type stars[2] sampling an almost unexplored parameter niche with respect to other surveys (Figure 2.1). We list in Table 2.1 the main astrometric and kinematic properties of our targets, taken from Gaia DR2 or – if not present in the catalog – from Hipparcos. Membership probabilities computed as described above are reported, together with the subgroup of Sco-Cen they are most likely associated to.

Table 2.1: Final sample of BEAST with its main astrometric (α, δ, ϖ) and kinematic (μ^*_α, μ_δ) properties. Membership probabilities to the three subgroups of Sco-Cen (US, UCL, LCC) are indicated in the last column.

Target	Alt name	α (hh mm ss)	δ (dd mm ss)	ϖ (mas)	σ_ϖ (mas)	μ^*_α (mas/yr)	μ_δ (mas/yr)	Region	Prob. (%)
HIP 50847	L Car	10 22 58.15	-66 54 05.4	8.16	0.20	-22.23	12.17	LCC	79.9
HIP 52742	HR 4221	10 46 57.47	-56 45 25.9	4.98	0.23	-20.71	0.57	LCC	0.0
HIP 54767	HD 97583	11 12 45.21	-64 10 11.2	10.59	0.14	-47.32	5.46	LCC	3.9
HIP 58452	HD 104080	11 59 10.68	-45 49 56.0	7.52	0.07	-30.43	-9.03	LCC	46.8
HIP 58901	HD 104900	12 04 45.25	-59 15 11.8	9.14	0.08	-38.22	-12.04	LCC	99.3
HIP 59173	HR 4618	12 08 05.22	-50 39 40.6	9.85	0.32	-34.35	-11.51	LCC	99.1
HIP 59747	δ Cru	12 15 08.72	-58 44 56.1	11.62	0.96	-37.29	-9.97	LCC	99.6
HIP 60009	ζ Cru	12 18 26.25	-64 00 11.1	10.49	0.33	-34.96	-6.24	LCC	99.9
HIP 60379	HR 4706	12 22 49.43	-57 40 34.1	9.69	0.16	-37.25	-12.11	LCC	95.1
HIP 60710	G Cen	12 26 31.76	-51 27 02.3	7.85	0.37	-31.42	-10.41	LCC	99.0

[1]Owing to the extreme brightness of most targets ($G \lesssim 6$), the accuracy of Gaia is strongly reduced (Lindegren et al. 2018); unresolved binarity further exacerbates the problem. A parallax comparison with Hipparcos shows that the scatter around the 1-to-1 relation is 1.28 mas, much larger than the usual precision attained by both surveys.

[2]One star, HIP 79098, was originally in the target list, but later removed due to a SPHERE observation from 2015 (criterion 2). However, a reassessment of archival observations unveiled the presence of a previously unidentified substellar companion (Janson et al. 2019). We will examine this system in greater detail in Section 5.

Table 2.1: continued.

Target	Alt name	α (hh mm ss)	δ (dd mm ss)	ϖ (mas)	σ_ϖ (mas)	μ^*_α (mas/yr)	μ_δ (mas/yr)	Region	Prob. (%)
HIP 60823	σ Cen	12 28 02.38	-50 13 50.3	8.88	0.33	-32.11	-13.81	LCC	98.3
HIP 60855	u Cen	12 28 22.46	-39 02 28.2	7.40	0.24	-26.89	-7.32	LCC	4.1
HIP 61257	HD 109195	12 33 12.19	-52 04 58.2	7.99	0.07	-31.40	-12.57	LCC	99.1
HIP 61585	α Mus	12 37 11.02	-69 08 08.0	8.62	0.83	-29.37	-11.38	LCC	89.1
HIP 62058	HR 4834	12 43 09.18	-56 10 34.4	7.90	0.06	-31.56	-12.30	LCC	99.7
HIP 62327	HD 110956	12 46 22.71	-56 29 19.7	10.03	0.34	-33.53	-14.97	LCC	99.4
HIP 62434[b]	β Cru	12 47 43.27	-59 41 19.6	11.71	0.98	-42.97	-16.18	LCC	99.1
HIP 62786	HR 4879	12 51 56.93	-39 40 49.6	6.89	0.08	-25.73	-18.86	UCL	78.5
HIP 63003	μ.01 Cru	12 54 35.62	-57 10 40.5	9.63	0.36	-31.09	-14.51	LCC	98.6
HIP 63005	μ.02 Cru	12 54 36.89	-57 10 07.2	8.95	0.23	-28.16	-10.34	LCC	97.3
HIP 63210	H Cen	12 57 04.35	-51 11 55.5	7.93	0.19	-30.57	-15.50	LCC	98.9
HIP 63945	f Cen	13 06 16.70	-48 27 47.8	7.58	0.33	-30.05	-14.55	LCC	95.1
HIP 64004	ξ02 Cen	13 06 54.64	-49 54 22.5	6.70	0.29	-26.36	-10.58	LCC	95.9
HIP 65021	HD 115583	13 19 43.42	-67 21 51.6	5.76	0.05	-23.43	-13.86	LCC	0.0
HIP 65112	V964 Cen	13 20 37.83	-52 44 52.2	8.17	0.17	-30.44	-16.30	LCC	97.0
HIP 66454	HR 5121	13 37 23.47	-46 25 40.4	7.07	0.23	-29.53	-18.05	UCL	73.5
HIP 67464	ν Cen	13 49 30.28	-41 41 15.8	10.05	0.47	-27.86	-18.08	UCL	95.9
HIP 67669	VV983 Cen	13 51 49.60	-32 59 38.7	11.10	0.43	-34.70	-27.91	UCL	96.7
HIP 67703	HD 120642	13 52 04.85	-52 48 41.5	10.48	0.16	-39.04	-27.43	LCC	82.5
HIP 68245	ϕ Cen	13 58 16.27	-42 06 02.7	8.51	0.36	-25.55	-17.27	UCL	96.3
HIP 68282	υ01 Cen	13 58 40.75	-44 48 12.9	8.73	0.59	-24.02	-21.84	UCL	96.5
HIP 68862	χ Cen	14 06 02.77	-41 10 46.7	7.75	0.38	-24.60	-20.19	UCL	99.1
HIP 69011	HD 123247	14 07 40.81	-48 42 14.5	10.13	0.07	-34.20	-28.27	UCL	76.8
HIP 69618	HD 124367	14 14 57.14	-57 05 10.1	7.89	0.23	-25.10	-20.19	UCL	87.3
HIP 70300	a Cen	14 23 02.24	-39 30 42.5	10.13	0.44	-24.95	-18.61	UCL	96.5
HIP 70626	HR 5400	14 26 49.87	-39 52 26.4	6.95	0.10	-20.63	-20.86	UCL	99.8
HIP 71352[b]	η Cen	14 35 30.42	-42 09 28.2	10.67	0.21	-34.73	-32.72	UCL	99.6
HIP 71353	HR 5439	14 35 31.48	-41 31 02.8	9.38	0.34	-22.17	-20.93	UCL	99.4
HIP 71453	HD 128207	14 36 44.13	-40 12 41.7	7.00	0.16	-23.71	-22.32	UCL	99.8
HIP 71536	ρ Lup	14 37 53.23	-49 25 33.0	10.19	0.54	-28.57	-26.48	UCL	99.2
HIP 71860[b]	α Lup	14 41 55.76	-47 23 17.5	7.02	0.17	-20.94	-23.67	UCL	99.9
HIP 71865	b Cen	14 41 57.59	-37 47 36.6	10.24	0.64	-31.52	-31.50	UCL	99.8
HIP 73266	HD 132094	14 58 24.26	-37 21 44.9	5.66	0.13	-19.46	-22.69	UCL	94.5
HIP 73624	HD 132955	15 02 59.28	-32 38 35.9	6.58	0.18	-19.74	-21.57	UCL	98.9
HIP 74100	HR 5625	15 08 39.20	-42 52 04.5	6.76	0.09	-20.87	-21.65	UCL	99.9
HIP 74449	e Lup	15 12 49.59	-44 30 01.5	7.64	0.97	-22.02	-22.16	UCL	99.4
HIP 74657	HD 135174	15 15 19.64	-44 08 58.2	6.43	0.12	-19.37	-21.75	UCL	99.8
HIP 74752	HD 135454	15 16 37.15	-42 22 12.6	7.45	0.07	-22.16	-27.38	UCL	99.9
HIP 74950	VGG Lup	15 18 56.38	-40 47 17.6	6.97	0.18	-20.07	-21.58	UCL	99.9
HIP 75141	δ Lup	15 21 22.33	-40 38 51.0	8.72	0.47	-17.28	-23.15	UCL	99.6
HIP 75304[b]	ϕ02 Lup	15 23 09.35	-36 51 30.6	6.28	0.20	-18.24	-20.72	UCL	99.6
HIP 75647	HR 5736	15 27 18.13	-36 46 03.2	7.11	0.22	-19.55	-23.58	UCL	99.9
HIP 76048	HR 5753	15 31 50.23	-32 52 52.0	6.31	0.12	-17.75	-22.15	UCL	99.1

Table 2.1: continued.

Target	Alt name	α (hh mm ss)	δ (dd mm ss)	ϖ (mas)	σ_ϖ (mas)	μ^*_α (mas/yr)	μ_δ (mas/yr)	Region	Prob. (%)
HIP 76126	ζ04 Lib	15 32 55.22	-16 51 10.3	4.53	0.19	-11.50	-10.85	US	0.0
HIP 76591	HR 5805	15 38 32.64	-39 09 38.5	6.85	0.05	-19.81	-23.90	UCL	99.9
HIP 76600	τ Lib	15 38 39.37	-29 46 39.9	[c]4.14	0.76	-11.08	-22.88	UCL	2.9
HIP 76633	HD 139486	15 39 00.06	-19 43 57.2	6.19	0.06	-15.30	-18.22	US	76.7
HIP 77562	HD 141168	15 50 07.08	-53 12 35.2	10.28	0.10	-27.59	-39.27	UCL	95.2
HIP 77968	HD 142256	15 55 22.88	-44 31 33.6	5.50	0.06	-15.66	-19.65	UCL	80.7
HIP 78104	ρ Sco	15 56 53.08	-29 12 50.7	7.49	0.41	-18.08	-24.39	US	78.5
HIP 78168	HD 142883	15 57 40.46	-20 58 59.1	6.39	0.10	-10.13	-21.75	US	99.4
HIP 78207	48 Lib	15 58 11.37	-14 16 45.7	7.52	0.25	-14.92	-16.42	US	81.9
HIP 78324	HD 143022	15 59 30.88	-40 51 54.6	6.02	0.05	-16.51	-20.31	UCL	97.4
HIP 78384	η Lup	16 00 07.33	-38 23 48.2	5.99	0.41	-18.64	-28.46	UCL	97.3
HIP 78655	HR 5967	16 03 24.19	-38 36 09.2	9.23	0.47	-18.49	-28.15	UCL	99.8
HIP 78702	HD 143956	16 04 00.24	-19 46 02.9	6.56	0.07	-9.89	-21.48	US	99.8
HIP 78918	θ Lup	16 06 35.55	-36 48 08.3	8.17	0.38	-20.10	-33.42	UCL	94.4
HIP 78933	ω Sco	16 06 48.43	-20 40 09.1	7.06	0.40	-7.91	-21.06	US	99.9
HIP 78968	HD 144586	16 07 14.93	-17 56 09.7	6.62	0.08	-8.77	-21.27	US	99.7
HIP 79044	HD 144591	16 08 04.38	-36 13 54.6	7.29	0.05	-16.88	-28.04	UCL	99.7
HIP 79404	c02 Sco	16 12 18.20	-27 55 34.9	6.65	0.36	-11.81	-23.76	US	97.8
HIP 80142	HD 147001	16 21 27.03	-48 11 19.0	5.56	0.06	-12.75	-21.97	UCL	11.7
HIP 80208	HD 147152	16 22 28.00	-49 34 20.5	5.30	0.44	-11.32	-25.75	UCL	3.2
HIP 80569	χ Oph	16 27 01.43	-18 27 22.5	8.18	0.31	-4.97	-21.75	US	93.7
HIP 80911	N Sco	16 31 22.93	-34 42 15.7	7.45	0.56	-11.01	-18.08	UCL	96.8
HIP 81208	HD 149274	16 35 13.84	-35 43 28.7	6.75	0.07	-9.61	-25.70	UCL	94.9
HIP 81266	τ Sco	16 35 52.95	-28 12 57.7	6.88	0.53	-9.89	-22.83	US	77.5
HIP 81316	HD 149425	16 36 28.67	-40 18 10.9	5.23	0.06	-11.98	-20.79	UCL	36.8
HIP 81472	VV1003 Sco	16 38 26.29	-43 23 54.3	5.12	0.11	-11.05	-20.25	UCL	28.1
HIP 81474	HD 149914	16 38 28.65	-18 13 13.7	6.30	0.08	-13.91	-20.38	UCL	7.5
HIP 81891	HR 6211	16 43 38.72	-32 06 21.4	6.41	0.07	-8.79	-23.17	UCL	93.9
HIP 81914	HD 150591	16 43 54.08	-41 06 48.0	5.66	0.08	-12.95	-21.76	UCL	58.6
HIP 81972	HD 150742	16 44 42.59	-40 50 22.8	5.84	0.11	-12.44	-21.67	UCL	85.8
HIP 82514	μ.01 Sco	16 51 52.23	-38 02 50.6	[a]3.73	0.69	-0.84	-18.51	UCL	0.0
HIP 82545	μ.02 Sco	16 52 20.15	-38 01 03.1	7.92	0.55	-9.98	-19.88	UCL	96.3

[a]Unreliable value

[b]Data taken from Hipparcos

[c]The estimate was later revised to $\varpi = 6.84 \pm 0.50$ mas (see Section 6.2).

2.1.2 Masses and binarity

Albeit generally not essential to determine the properties of directly imaged companions, precise stellar masses are by definition crucial to our science case. The binary fraction of B stars has been estimated as $50 - 70\%$ (Duchêne & Kraus 2013; Guo et al. 2022) and, despite our selection cuts against binaries, is at least $\sim 35\%$ in our sample based on companion detections found in the

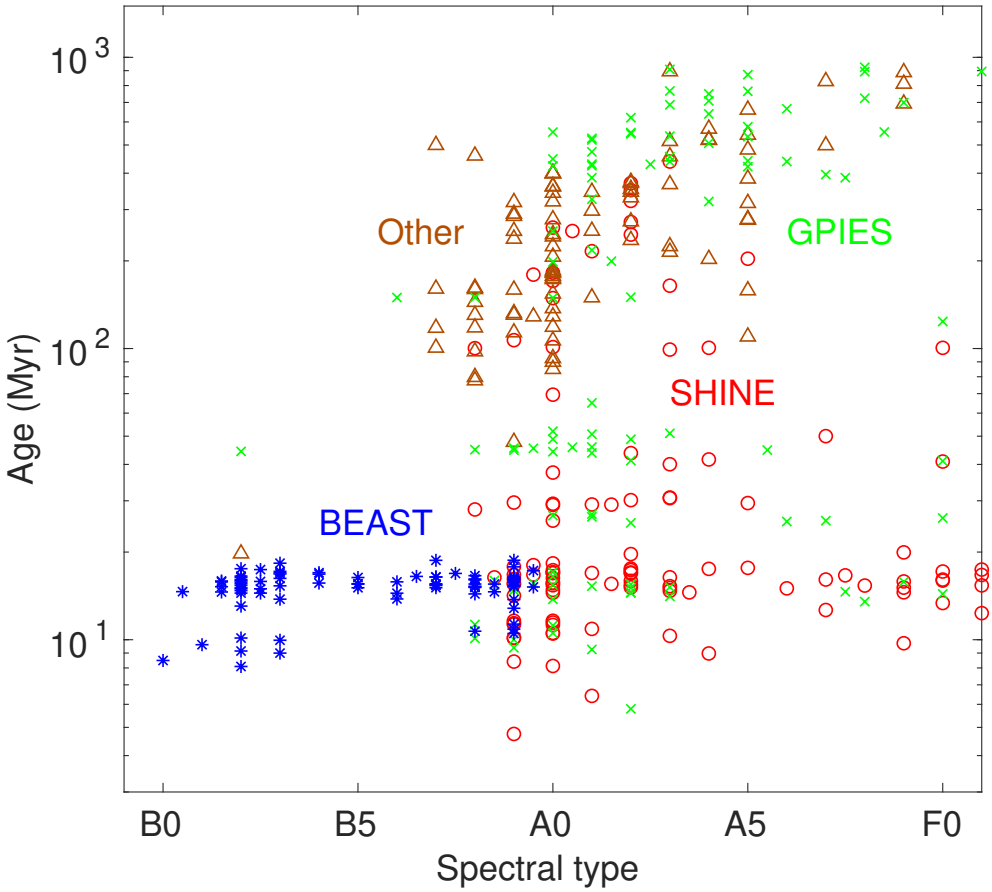

Figure 2.1: Comparison among the stellar samples of BEAST (blue asterisks), SHINE (Desidera et al. 2021) (red circles), GPIES (Nielsen et al. 2019) (green crosses), and earlier DI surveys (Janson et al. 2011; Nielsen et al. 2013). Details on the derivation of ages are provided in Section 2.3. A random alteration with standard deviation $\sigma_{age} = 1$ Myr was applied to each age for the sake of visibility. Source: Janson et al. (2021b).

literature; deriving individual masses of binary systems through isochrone fitting is not possible if the components are unresolved.

In order to estimate stellar masses, the spectral type of each system was employed as an indicator of its mass – or of the primary mass, when binary – through the relation by Lafrenière et al. (2014). The results of this analysis are shown in Table 2.2. A comparison with the three systems (HIP 74950, HIP 78168, HIP 82514) that, thanks to their twofold nature of eclipsing binaries and double-lined spectroscopic binaries, possess dynamical model-independent mass estimates (Budding et al. 2015; David et al. 2019), indicates a relative difference between 6% and 21%. Conversely, only minimal information is available about the masses of secondary components of binary systems: over the next years, dedicated follow-up exploiting radial velocities, astrometry, imaging and/or interferometry might be able to shed light on their elusive properties.

Table 2.2: Spectral types (SpT) and (primary) masses of BEAST stars. Known binaries are indicated via their detection method(s): spectroscopy (SB1: single-lined binary; SB2: double-lined binary), photometry (EB: eclipsing binary), interferometry (INT), and imaging (AO).

Target	SpT	Mass $M_\odot$	binarity	Ref.[a]
HIP 50847	B8V	2.9	SB2, AO	Q10, J21
HIP 52742	B8.5III	2.7	—	—
HIP 54767	B8V	2.9	—	—
HIP 58452	B8/B9V	2.7	—	—
HIP 58901	B9V	2.5	—	—
HIP 59173	B6III	3.7	SB2, AO	C12, J21
HIP 59747	B2IV	7.8	SB2	C12
HIP 60009	B2.5V	6.8	SB2, AO	C12, J21
HIP 60379	B9V	2.5	—	—
HIP 60710	B3V	5.9	—	—
HIP 60823	B2V	7.8	INT	R13
HIP 60855	B8V	2.9	—	—
HIP 61257	B9V	2.5	—	—
HIP 61585	B2IV-V	7.8	SB2/INT	C12, R13
HIP 62058	B7.5V	3.1	—	—
HIP 62327	B3V	5.9	SB1	C12
HIP 62434	B0.5IV	13	SB1, AO	P04, J21
HIP 62786	B8V	2.9	—	—
HIP 63003	B2IV-V	7.8	—	—
HIP 63005	B5V	4.2	AO	J21
HIP 63210	B2IV	7.8	SB2	C12
HIP 63945	B5V	4.2	SB1, INT, AO	C12, R13, S02
HIP 64004	B1.5V	9	SB1	P04
HIP 65021	B9V	2.5	—	—
HIP 65112	B6V	3.7	EB	M06
HIP 66454	B8V	2.9	—	—
HIP 67464	B2IV	7.8	SB1, EB	P04
HIP 67669	B5III	4.2	SB1, INT	P04, S10
HIP 67703	B9V	2.5	—	—

Table 2.2: continued.

Target	SpT	Mass $M_\odot$	binarity	Ref.[a]
HIP 68245	B2IV	7.8	—	—
HIP 68282	B2IV-V	7.8	—	—
HIP 68862	B2V	7.8	—	—
HIP 69011	B9V	2.5	—	—
HIP 69618	B4V	5.1	—	—
HIP 70300	B7III	3.3	—	—
HIP 70626	B7IV	3.3	—	—
HIP 71352	B2V	7.8	SB2	C12
HIP 71353	B7V	3.3	—	—
HIP 71453	B8V	2.9	—	—
HIP 71536	B5V	4.2	INT	R13
HIP 71860	B1.5III	9	—	—
HIP 71865	B3V	5.9	INT	R13
HIP 73266	B9V	2.5	—	—
HIP 73624	B3V	5.9	AO	J21
HIP 74100	B7V	3.3	AO	S02
HIP 74449	B3IV/V	5.9	SB1	P04
HIP 74657	B9IV	2.5	—	—
HIP 74752	B9.5	2.4	—	—
HIP 74950	B7V	3.3	SB12, EB	B15
HIP 75141	B1.5IV	9	—	—
HIP 75304	B4V	5.1	INT	R13
HIP 75647	B4V	5.1	SB1	P04
HIP 76048	B7V	3.3	—	—
HIP 76126	B3V	5.9	—	—
HIP 76591	B9V	2.5	—	—
HIP 76600	B2.5V	6.8	SB2, INT	P04, R13
HIP 76633	B9V	2.5	—	—
HIP 77562	B9V	2.5	—	—
HIP 77968	B8V	2.9	—	—
HIP 78104	B2IV-V	7.8	SB1	P04
HIP 78168	B3V	5.9	SB2, EB	D19
HIP 78207	B8Ia/Iab	2.9	—	—
HIP 78324	B9V	2.5	—	—
HIP 78384	B2.5IV	6.8	—	—
HIP 78655	B6IV	3.7	—	—
HIP 78702	B9V	2.5	—	—
HIP 78918	B2.5V	6.8	—	—
HIP 78933	B1V	10	—	—
HIP 78968	B9V	2.5	—	—
HIP 79044	B9V	2.5	—	—
HIP 79404	B2V	7.8	SB1	P04
HIP 80142	B7V	3.3	—	—

Table 2.2: continued.

Target	SpT	Mass $M_\odot$	binarity	Ref.[a]
HIP 80208	B3V	5.9	—	—
HIP 80569	B2V	7.8	—	—
HIP 80911	B2III-IV	7.8	—	—
HIP 81208	B9V	2.5	—	—
HIP 81266	B0V	16	INT	R13
HIP 81316	B9V	2.5	—	—
HIP 81472	B2V	7.8	—	—
HIP 81474	B9.5IV	2.4	—	—
HIP 81891	B8V	2.9	—	—
HIP 81914	B6.5V	3.5	—	—
HIP 81972	B3V	5.9	—	—
HIP 82514	B1.5V	9	SB2, EB	B15
HIP 82545	B2IV	7.8[b]	—	—

[a] References. J21: Janson et al. (2021b); Q10: Quiroga et al. (2010).
C12: Chini et al. (2012); R13: Rizzuto et al. (2013); P04: Pourbaix et al. (2004).
M06: Malkov et al. (2006); S10: Schöller et al. (2010); S02: Shatsky & Tokovinin (2002).
B15: Budding et al. (2015); D19: David et al. (2019).
[b] The estimate was later raised to 9.1 $M_\odot$ (see Section 5.3).

2.2 The large-scale environment: Scorpius-Centaurus

Spanning an enormous area of approximately $80° \times 40°$ in the sky, the very young Sco-Cen ($t < 20$ Myr, Pecaut et al. 2012) association comprises a few regions still actively forming stars (Wilking et al. 2008). The exquisite concoction of closeness, youth and low extinction, allowing detection of members down to the brown dwarf regime, has made it the target of many studies in the last decades (e.g., de Zeeuw et al. 1999; Mamajek et al. 2002) involving binaries (e.g., Janson et al. 2013), primordial discs (e.g., Carpenter et al. 2006), high mass (Chen et al. 2012), Sun-like (e.g., Pecaut et al. 2012) and low-mass stars (e.g., Lodieu 2013), and even young planets (e.g., Janson et al. 2021b).

Sco-Cen is classically divided into three main subgroups (Blaauw 1946; de Zeeuw et al. 1999): going toward lower galactic longitude, Upper Scorpius (US), Upper Centaurus-Lupus (UCL) and Lower Centaurus-Crux (LCC). Both density and age have a spatial gradient, with US being more compact and younger than UCL and LCC (Pecaut & Mamajek 2016). We will explore in more detail the star formation history of the association in Chapter 4.

Thanks to the exquisite photometric and kinematic performances of Gaia, studies aimed at refining the census of Sco-Cen members have gained renewed vigor over the last few years. Damiani et al. (2019) constructed the largest sample of association members to date, comprising $\sim 11000 - 14000$ stars. We provide in Figure 2.2 a visual representation of the appearance of the association in the celestial sphere, with a special focus on the coordinates of BEAST targets.

As first outlined by Pecaut & Mamajek (2016), an intricate substructure in the association's age distribution exists, reflected in its kinematic structure; the existence of kinematic substructures is

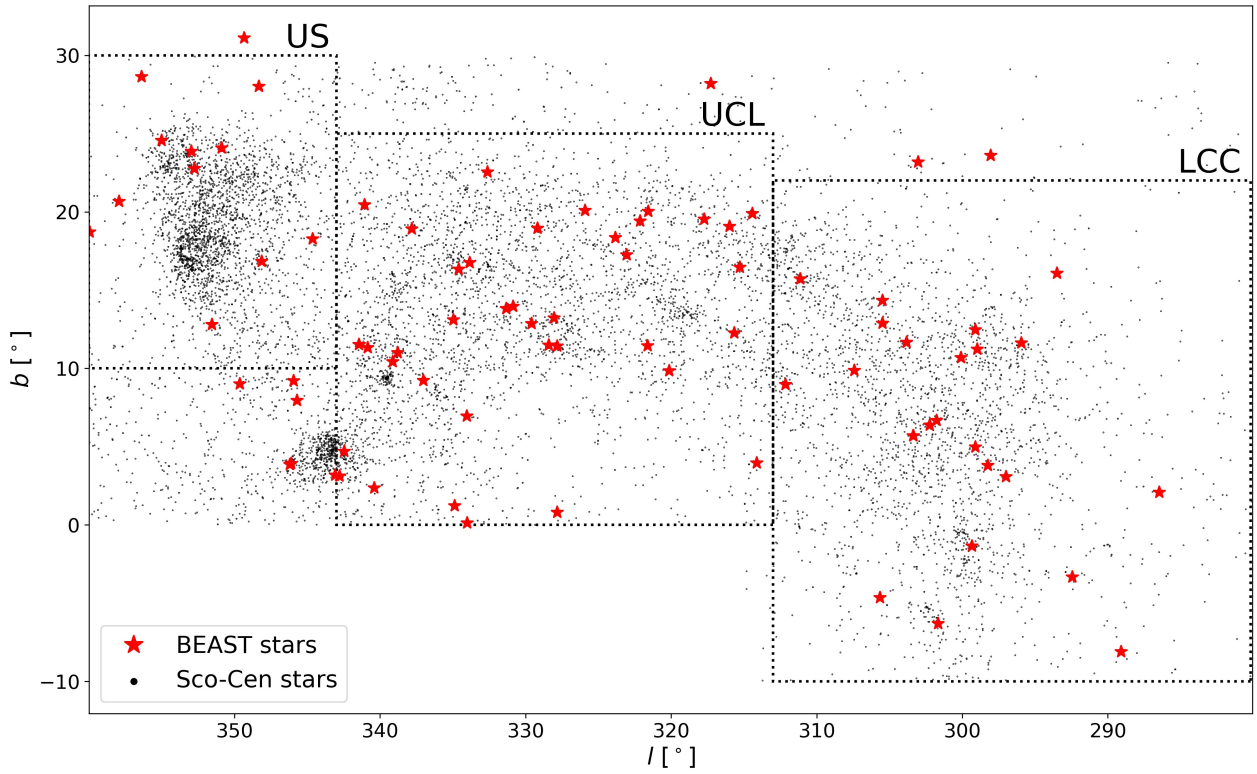

Figure 2.2: Galactic coordinates of Sco-Cen bona-fide sources (Damiani et al. 2019). BEAST targets are overplotted as red stars. Classical boundaries defining US, UCL and LCC are drawn through dotted lines and should be considered as purely indicative.

not the outcome of few large bursts of star formation, but rather of several minor subgroups, born independently of each other (Wright & Mamajek 2018).

We will see in Section 2.3 how this observation can be exploited to better characterize the targets of our survey.

2.3 Stellar ages: the need for indirect estimates

As we have seen in Chapter 1, the distribution of planetary masses is one of the main outputs of planet formation models, alongside with the orbital parameter distribution and the overall occurrence frequency. In order to convert the flux emitted by a substellar companions into a mass estimate – or to convert upper flux limits into upper mass limits for nondetections, a theoretical model describing the evolution of luminosity as a function of mass and age is necessary. However, the combination of observational uncertainties on measured magnitudes and theoretical uncertainties on the initial entropy and the cooling law for substellar objects hinders the simultaneous determination of ages and masses only based on photometry, resulting in a treacherous age-mass degeneracy (see, e.g., Burrows et al. 2001; Doyon et al. 2010; Marleau et al. 2019b). For this reason, obtaining precise ages for the targets of direct imaging studies is imperative to ensure a meaningful interpretation of the derived results.

Unlike other astrophysical parameters such as mass, radius, effective temperature, surface gravity and rotational velocity, age cannot be directly and solidly grounded to observable quantities and is instead heavily model-dependent. A few age indicators – each one focusing on specific phases of stellar evolution and/or mass ranges – have nonetheless been identified over the last three decades (see Barrado 2016): gyrochronology (Barnes 2007; Epstein & Pinsonneault 2014; Maxted et al. 2015) and chromospheric activity (Mamajek & Hillenbrand 2008; Zhang et al. 2021) for FGK stars, lithium depletion (Soderblom et al. 2014) for $20 \lesssim t \lesssim 450$ Myr M stars, and asteroseismology (e.g., Rodrigues et al. 2014; Martig et al. 2016; Mackereth et al. 2021). None of these indicators is adequate for B-type stars, for which the only direct age determination technique remains the classical *isochrone fitting*.

The position of a star in theoretical Hertzsprung-Russell diagrams (HRDs) or their observational counterpart, color-magnitude diagrams (CMDs) (Gaia Collaboration et al. 2018a), after being corrected for distance and interstellar extinction, can in principle be compared with theoretical grids derived from stellar evolution models to derive several astrophysical parameters, including mass, age, and metallicity. A strong degeneracy between age and metallicity exists (Howes et al. 2019); but even when metallicity is independently assessed, obtaining precise ages is an extremely challenging task for main-sequence stars (Soderblom 2010): the reason lies in the feeble variation of luminosity and effective temperature over main-sequence lifetime, keeping the isochrones very close to one another in the HRDs. This is the case for B-type members of Sco-Cen (Equation 1.5), for which additional factors such as the large uncertainty on parallax due to their brightness (Section 2.1.1), unresolved multiplicity (Section 2.1.2), and stellar rotation are expected to further exacerbate both propagated random uncertainties and inter-model spreads (which can reach a factor ~ 3 and ~ 1.5, respectively; see David & Hillenbrand 2015). Individual isochronal age estimates for BEAST targets should therefore be regarded as purely indicative (cf. Figure 6 by Pecaut & Mamajek 2016) unless multiplicity and rotational properties are well established.

An alternative approach consists in exploiting the membership of our targets to a large association (Section 2.2) to derive indirect age constraints from the statistical analysis of large groups of stars that should be approximately coeval. The ages of US, UCL and LCC have been estimated as 10 ± 7,

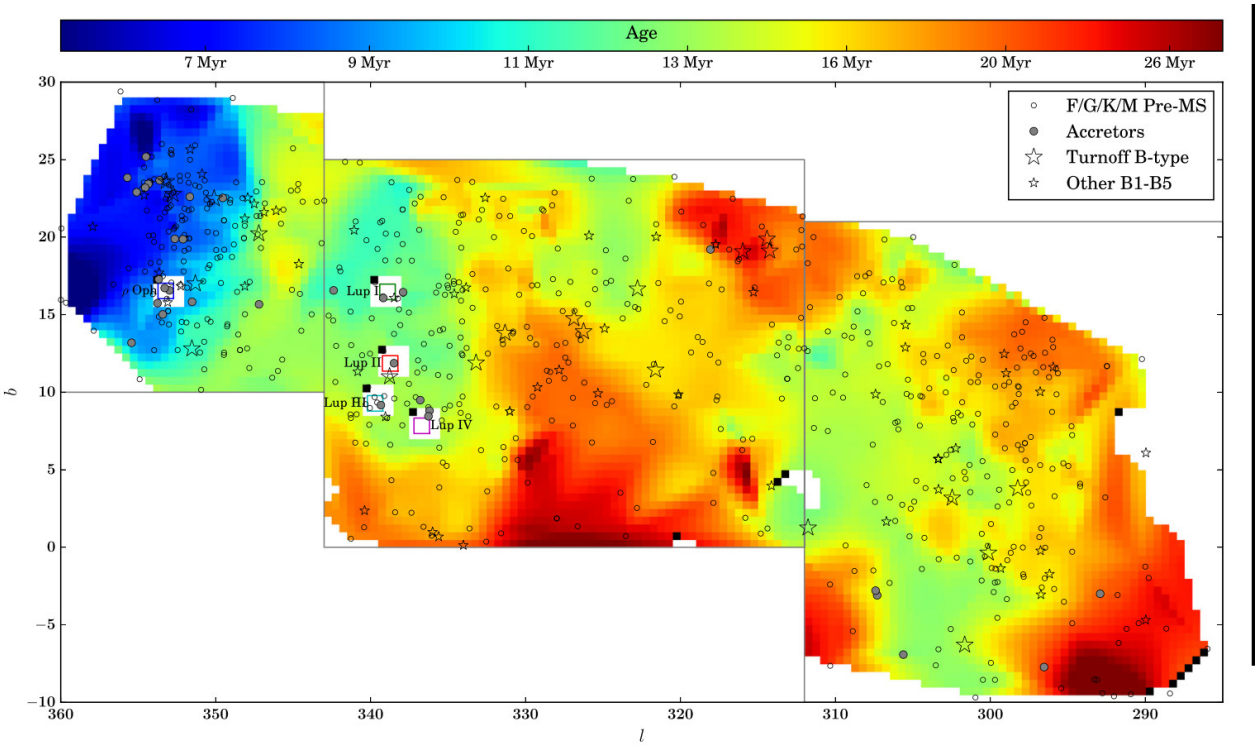

Figure 2.3: Derived mean age of Sco-Cen F5-G9 stars as a function of sky coordinates. A sample of members spectral types ranging from B to M are overplotted using different symbols. The youngest star forming regions (the ρ Ophiuchi and the Lupus clouds) have been masked. Source: Pecaut & Mamajek (2016).

16±7, and 15±6 Myr, respectively, based on isochronal analysis of their PMS F-type and G-type members (Pecaut & Mamajek 2016). The large dispersion associated to these estimates is related to the extended star formation history of the association, creating an intra-group age spread that can be as high as a factor two. In order to enhance the precision of these first-order estimates, we decided to focus on smaller angular scales within the association by means of a digitized version of the age map constructed in this same study (Figure 2.3); by interpolating at the corresponding coordinates of our targets, we are able to take into account exquisite small-scale variations occurring as a function of sky coordinates.

Being the Scorpius-Centaurus association the outcome of an intricate combination of small-scale star formation events (see Chapter 4), the usage of the age map by Pecaut & Mamajek (2016) is physically motivated. However, as nearby groups are expected to dissolve and intertwine over time, any accuracy improvement is limited not by spatial resolution, but rather by the neglect of kinematic information from the scheme. With this idea in mind, we devised a new approach that estimates individual ages based on isochronal dating of Sco-Cen members that are found close enough to the science targets in the 5D kinematic phase space[3]. We refer to these stars as comoving stars (CMS). We stress that most CMS are not physically bound to the target; rather, they can be collectively thought as the seeds of future young moving groups (Zuckerman & Song 2004; Torres et al. 2008).

[3]The parameters are the 3D positions and the proper motions; radial velocity data were not employed, as they are available for less than 10% of the stars of interest in Gaia DR2.

Motivated by the need to derive age estimates for CMS samples, I began developing MADYS, a tool that allows a fast and robust inference of age and mass estimates for arbitrarily long lists of stars and/or self-luminous substellar objects, based on the comparison between archival photometry and stellar/substellar evolution models. A depiction of the seminal ideas underlying MADYS, and its earliest implementation, is provided in Section 2.3.2; a detailed description of the first public release of the tool will be the subject of Chapter 3.

2.3.1 Identification of comoving groups

As a first step of our analysis, we transformed parallaxes and proper motions of all the entries of Gaia DR2 surrounding each target into velocities components v_α and v_δ and heliocentric distances d. The distance ξ between a candidate CMS with distance d_i and a target with distance d_0 is given by al-Kashi's theorem:

$$\xi = \sqrt{d_i^2 + d_0^2 - 2 d_i d_0 \cos \Delta\theta}, \tag{2.1}$$

where $\Delta\theta$ is the angular separation between the two objects on the sky. The 2D differential velocity Δv, given a candidate CMS with velocity v_i and a target with velocity v_0, is instead:

$$\Delta v = \sqrt{(v_{\alpha,i} - v_{\alpha,0})^2 + (v_{\delta,i} - v_{\delta,0})^2}. \tag{2.2}$$

In order to distinguish between CMS and non-CMS, we set a velocity threshold $\Delta v < \Delta v_{max} = 1.3$ km s^{-1}, similar to those found in other studies (e.g., Röser et al. 2018; Meingast et al. 2019). Given that 1 km s^{-1} $\approx$ 1 pc Myr^{-1} and $t \sim 15$ Myr, we additionally impose that $\xi < \xi_{max} = 20$ pc. We exclude stars that cannot be assumed as being below the velocity threshold with at least 2σ confidence: i.e., stars with $\left|\frac{v_\alpha - 1.3 \text{ km s}^{-1}}{\sigma_{v_\alpha}}\right| < 2$ or $\left|\frac{v_\delta - 1.3 \text{ km s}^{-1}}{\sigma_{v_\delta}}\right| < 2$. Lastly, to get highly reliable input for isochrone analysis, we reject stars with $\frac{5}{\varpi ln10} \cdot \sigma_\varpi > 0.07$, for which the distance uncertainty would propagate into errors on absolute magnitude greater than 0.07 mag.

We show in Figure 2.4 the on-sky positions of BEAST targets and their CMS; a clear distinction among the three subregions of Sco-Cen can be visually appreciated.

2.3.2 Isochronal analysis of comoving stars

After collecting photometric information from Gaia DR2 and 2MASS for each CMS, we defined four independent sets $\mathcal{F}$ of photometric pairs: $\{G, J\}$, $\{G, H\}$, $\{G, K\}$, and $\{Gbp, Grp\}$. Indeed, at least two parameters are needed to solve the degeneracy between mass and age, and the pairs are defined to exploit wavelength spans as large as possible. A correction for reddening was applied by integrating the STILISM 3D extinction map (Lallement et al. 2019); the conversion between E(B-V) and extinctions was based on coefficients from Wang & Chen (2019).

We compared then each photometric pair to the corresponding values from BT-Settl isochrones (Allard 2016) of solar metallicity in order to constrain age and mass of the respective star. Taken the k-th photometric band, we can relate the measured flux F_k to theoretical fluxes $F_{k,model}$. The model can be expressed in a compact form as a 3D matrix, whose elements $\{a_{ijk}\}$ are the fluxes relative to the i-th mass, the j-th age, and the k-th filter; a 2D distance matrix was built with elements δ_{ij}:

$$\delta_{ij} = \sqrt{\sum_{k \in \mathcal{F}} \left(\frac{F_k - F_{ijk,th}}{\Delta F_k} \right)^2}, \tag{2.3}$$

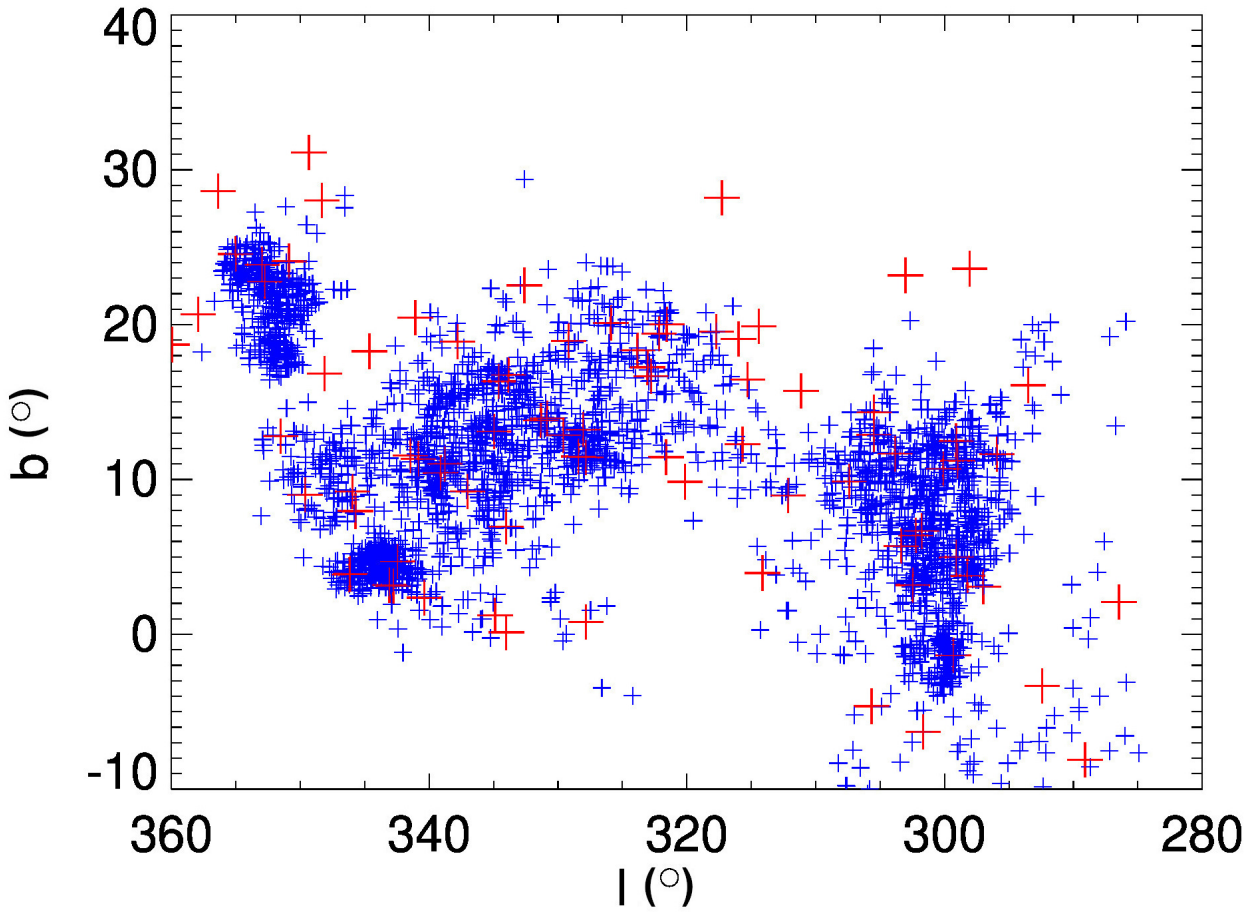

Figure 2.4: On-sky location of BEAST targets (red) and their CMS candidates (blue).

ΔF_k being the photometric error. The best approximation to the observed flux, $\delta_{\min} = \min \delta_{ij}$, gives mass and age estimates in the set $\mathcal{F}$. An estimate was rejected if $\delta_{min} > 3$ or if at least one flux error exceeded 10% (0.1 mag).

As the average number of CMS per target is 36 (see Table 2.3), the method should be able to provide very precise estimates. A few points, though, require careful consideration: firstly, we smoothed the sharp cut-off between CMS and non-CMS by calculating a weighted mean of the CMS ages with weights w_i:

$$w_i = \left[\left(\frac{\Delta v_{max}}{\xi_{max}} \xi \right)^2 + (\Delta v_\alpha)^2 + (\Delta v_\delta)^2 \right]^{-1/2}. \tag{2.4}$$

such that a closest CMS in the 5D parameter space contributes more to the final estimate; this stratagem effectively corresponds to a CMS probability function. The weighted mean, computed in logarithmic rather than linear space to better match the pace of stellar evolution, is computed as:

$$m = \sum_i ln(t_i)\tilde{w}_i, \tag{2.5}$$

where t_i represent individual ages and $\tilde{w}_i$ the corresponding normalized weights. The uncertainty on m, s, is given by:

$$s = \sqrt{\sum_i \tilde{w}_i (ln(t_i) - m)^2 \cdot \frac{n}{n-1} \sum_i \tilde{w_i}^2}, \tag{2.6}$$

with $\frac{n}{n-1}$ being the Bessel correction factor, adopted if $n > 1$. m and s are, by definition, logarithmic quantities; the corresponding linear values are $\mu = \exp(m)$ and $\sigma = \mu(\exp(s) - 1)$.

Up to this moment, the computations were performed independently in each filter set j; a unique estimate of the age of the target can be obtained as in Equation 2.5, using as weights:

$$w_j = \frac{1}{s_j^2} = \frac{1}{ln(\sigma_j/\mu_j) + 1}. \tag{2.7}$$

We have therefore derived indirect age estimates for our targets by means of the ages of their associated CMS. However, these estimates still have to be corrected for two biases that would otherwise skew our analysis: the *age-mass bias* and the *multiplicity bias*, which we will introduce in the next Section.

2.3.3 Correction of biases

A first matter requiring consideration is the observation that low-mass stars in young stellar regions appear to be systematically younger than their more massive counterparts when studied using isochrones (e.g. Pecaut & Mamajek 2016); the ages of young stars depend on spectral class, with low-mass star ages underestimated by 30-100% and high-mass star ages overestimated by 20-100% (Hillenbrand et al. 2008; Mayne & Naylor 2008; Naylor 2009; Bell et al. 2013). A significant insight is given by binary systems for which dynamical mass estimates are available: discrepancies between ages inferred for presumably coeval components have been confirmed by Rizzuto et al. (2016) and Asensio-Torres et al. (2019).

This age spread can *a priori* be attributed either to an extended star formation or to systematic effects inherent to models. An interesting solution has been put forward by Feiden (2016a): highlighting the difficulties in modeling convection for PMS stars, he noticed that the effect of magnetic fields on a protostar – stronger for less massive stars – is to slow down its radial contraction along the Hayashi line; the resulting luminosity at a fixed age is higher than predicted, leading to incorrectly infer younger ages if the effect is not taken into account. Theoretical works exploring the effect of magnetic fields and stellar spots exist (Feiden 2016a; Somers et al. 2020); however, the knowledge of these parameters is virtually inaccessible for our CMS sample, and these models have additionally been found to create problems with moving groups with well-defined age (Tucana-Horologium association, β Pictoris; see Bell et al. 2015). Therefore, we decided to correct for the bias in an empirical way.

Instead of restricting our CMS sample to FG stars as in Pecaut & Mamajek (2016) – the cut would impede the application of the method for a large fraction of our targets –, we computed a statistical correction factor β based on the targets with at least $n = 50$ CMS. For each target, β values were derived as the ratio between an age estimate t_c based only on >0.8 $M_{\rm sun}$ CMS and an age estimate t_0 based on the whole CMS sample. The mean $\hat{\beta} = 2.20 \pm 0.03$ was uniformly applied to all the age estimates in the sample.

A second source of bias, which we already discussed when dealing with B stars, is due to unresolved multiplicity: this feature makes a CMS look brighter and therefore shifts its position in the CMD, causing a bias in its age estimation. The effect is smaller in the CMS sample, since the multiplicity fraction decreases with primary mass (Duchêne & Kraus 2013). The average CMS

lies in the M-type spectral range, so we can estimate a multiplicity fraction of ∼30%; out of these multiples, ∼30% should have a magnitude difference with respect to the primary of <1 mag (Janson et al. 2012, 2014), causing a substantial perturbation to the position of the primary in the CMD that makes it appear younger. For each CMS group, we decided to reject the top 10% and bottom 10% of estimated ages (except if $n \leq 6$) and calculated a weighted mean of the remaining values according to the scheme introduced in the previous Section.

2.3.4 Final age estimates

We present the final age determinations for the BEAST sample in Table 2.3. Besides our CMS-based estimates, we show interpolated ages from the map by Pecaut & Mamajek (2016) and the ages of the corresponding subgroup of Sco-Cen.

The average CMS age across the sample is 16.5±0.7 Myr, fully consistent with average age obtained from age map of 16.2±0.6 Myr. Also, a Kolmogorov-Smirnov statistical test shows that the underlying distributions are equivalent at 95% confidence (Figure 2.5).

Table 2.3: Age estimations for the sample.

Target	CMS	CMS age[a] (Myr)	MAP age[b] (Myr)	SG age[c] (Myr)
HIP 50847	18	27.3±1.3	26.7	15±6
HIP 52742 [d]	1	82.5±21.8	—	15±6
HIP 54767 [d]	4	84.5±8.1	22.4	15±6
HIP 58452	21	20.0±0.6	—	15±6
HIP 58901	172	13.9±0.5	17.1	15±6
HIP 59173	52	13.7±0.6	20.6	15±6
HIP 59747	0	—	15.9	15±6
HIP 60009	14	19.8±0.9	16.2	15±6
HIP 60379	140	13.2±0.4	15.2	15±6
HIP 60710	12	20.6±1.5	20.4	15±6
HIP 60823	44	15.9±0.2	20.7	15±6
HIP 60855	0	—	—	15±6
HIP 61257	202	15.3±0.3	18.5	15±6
HIP 61585	0	—	14.6	15±6
HIP 62058	214	16.6±0.3	14.6	15±6
HIP 62327	57	12.7±0.6	14.8	15±6
HIP 62434	11	—	16.3	15±6
HIP 62786	0	—	—	16±7
HIP 63003	28	12.7±0.3	15.3	15±6
HIP 63005	93	12.0±0.4	15.3	15±6
HIP 63210	71	15.8±0.3	17.7	15±6
HIP 63945	0	—	16.4	15±6
HIP 64004	6	27.2±0.7	16.8	15±6
HIP 65021 [d]	17	49.6±3.5	14.4	15±6
HIP 65112	101	15.4±0.3	15.1	15±6
HIP 66454	0	—	19.5	16±7
HIP 67464	0	—	27.4	16±7

Table 2.3: continued.

Target	CMS	CMS age[a] (Myr)	MAP age[b] (Myr)	SG age[c] (Myr)
HIP 67669	0	—	—	16±7
HIP 67703	12	14.3±0.7	15.5	15±6
HIP 68245	0	—	29.6	16±7
HIP 68282	0	—	22.3	16±7
HIP 68862	0	—	29.4	16±7
HIP 69011	17	14.8±1.0	16.5	16±7
HIP 69618	10	13.8±1.3	16.4	16±7
HIP 70300	0	—	15.7	16±7
HIP 70626	111	16.0±0.6	15.1	16±7
HIP 71352	4	15.4±1.6	15.2	16±7
HIP 71353	0	—	15.0	16±7
HIP 71453	6	17.7±0.5	14.2	16±7
HIP 71536	0	—	17.9	16±7
HIP 71860	4	22.2±0.9	17.7	16±7
HIP 71865	0	—	15.1	16±7
HIP 73266	0	—	15.4	16±7
HIP 73624	7	19.7±0.5	16.2	16±7
HIP 74100	100	18.5±0.5	20.5	16±7
HIP 74449	0	—	21.7	16±7
HIP 74657	54	17.6±0.4	21.4	16±7
HIP 74752	46	14.8±0.4	20.0	16±7
HIP 74950	58	17.7±0.3	18.4	16±7
HIP 75141	0	—	18.6	16±7
HIP 75304	15	23.7±0.7	15.3	16±7
HIP 75647	31	22.6±0.8	14.8	16±7
HIP 76048	21	16.0±0.4	13.0	16±7
HIP 76126	0	—	—	10±7
HIP 76591	136	15.9±0.4	13.2	16±7
HIP 76600	0	—	12.6	16±7
HIP 76633	2	31.6±1.7	11.6	10±7
HIP 77562	8	16.9±0.7	30.7	16±7
HIP 77968	42	14.5±0.4	15.9	16±7
HIP 78104	0	—	15.7	10±7
HIP 78168	54	9.3±0.3	9.0	10±7
HIP 78207	0	—	8.3	10±7
HIP 78324	27	16.9±0.5	14.4	16±7
HIP 78384	0	—	14.1	16±7
HIP 78655	0	—	14.3	16±7
HIP 78702	97	9.7±0.3	9.0	10±7
HIP 78918	0	—	14.1	16±7
HIP 78933	0	—	9.2	10±7
HIP 78968	91	9.1±0.2	8.5	10±7
HIP 79044	228	17.0±0.4	14.1	16±7

Table 2.3: continued.

Target	CMS	CMS age[a] (Myr)	MAP age[b] (Myr)	SG age[c] (Myr)
HIP 79404	0	—	12.5	10±7
HIP 80142 [d]	10	28.5±1.0	18.2	16±7
HIP 80208	0	—	—	16±7
HIP 80569	0	—	6.8	10±7
HIP 80911	0	—	—	16±7
HIP 81208	61	12.7±0.3	—	16±7
HIP 81266	0	—	11.9	10±7
HIP 81316	36	13.6±1.0	19.0	16±7
HIP 81472	13	19.5±1.4	21.8	16±7
HIP 81474	0	—	—	16±7
HIP 81891	67	13.9±0.4	—	16±7
HIP 81914	192	15.6±0.5	—	16±7
HIP 81972	236	16.0±0.3	—	16±7
HIP 82514	0	—	—	16±7
HIP 82545	0	—	—	16±7

[a] Age based on comoving stars.

[b] Age based on the age map by Pecaut & Mamajek (2016).

[c] Age of the corresponding Sco-Cen subgroup.

[d] Star with low membership probability to Sco-Cen (see Section 2.1.1).

2.4 Observations and data analysis

2.4.1 Observing modes

As a large ESO program, BEAST observations have been acquired since mid-2018 during multiple periods over the following years; owing to the limited visibility of the Scorpius, Lupus, Centaurus and Crux constellations from Paranal, the annual observing window approximately lasts from February to October.

All the observations are taken in a mode known as IRDIFS-EXT (Zurlo et al. 2014): light is separated with a dichroic so that the wavelength range spanning the Y, J and H bands ($0.95-1.7$ μm) is recorded by the Integral Field Spectrograph (IFS, Claudi et al. 2008) at a resolution $R \sim 30$, while the (K1, K2) photometric doublet in the K band ($\lambda_{K1,peak} = 2.110$ μm, $\lambda_{K2,peak} = 2.251$ μm) pertains to the Infra-Red Dual-beam Imaging and Spectrograph (IRDIS, Dohlen et al. 2008). With a field of view (FoV) of $\sim 1.7'' \times 1.7''$, IFS is designed to focus on the innermost region around the target star, while the larger IRDIS FoV ($\sim 11'' \times 11''$) is able to probe, at the typical distance of Sco-Cen, the region where long-period companions ($T \gtrsim 100$ yr) should reside.

In order to filter out star light and reduce contamination affecting the true signal coming from a companion, we employ – as usual in direct imaging – advanced wavefront sensing techniques and a coronagraph (e.g., Males & Guyon 2018; Beuzit et al. 2019): in particular, we use SPHERE's apodized Lyot coronagraph in the N_ALC_YJH_S configuration (inner working angle: 92.5 mas) (Carbillet et al. 2011; Guerri et al. 2011). The observations are performed around a hour angle

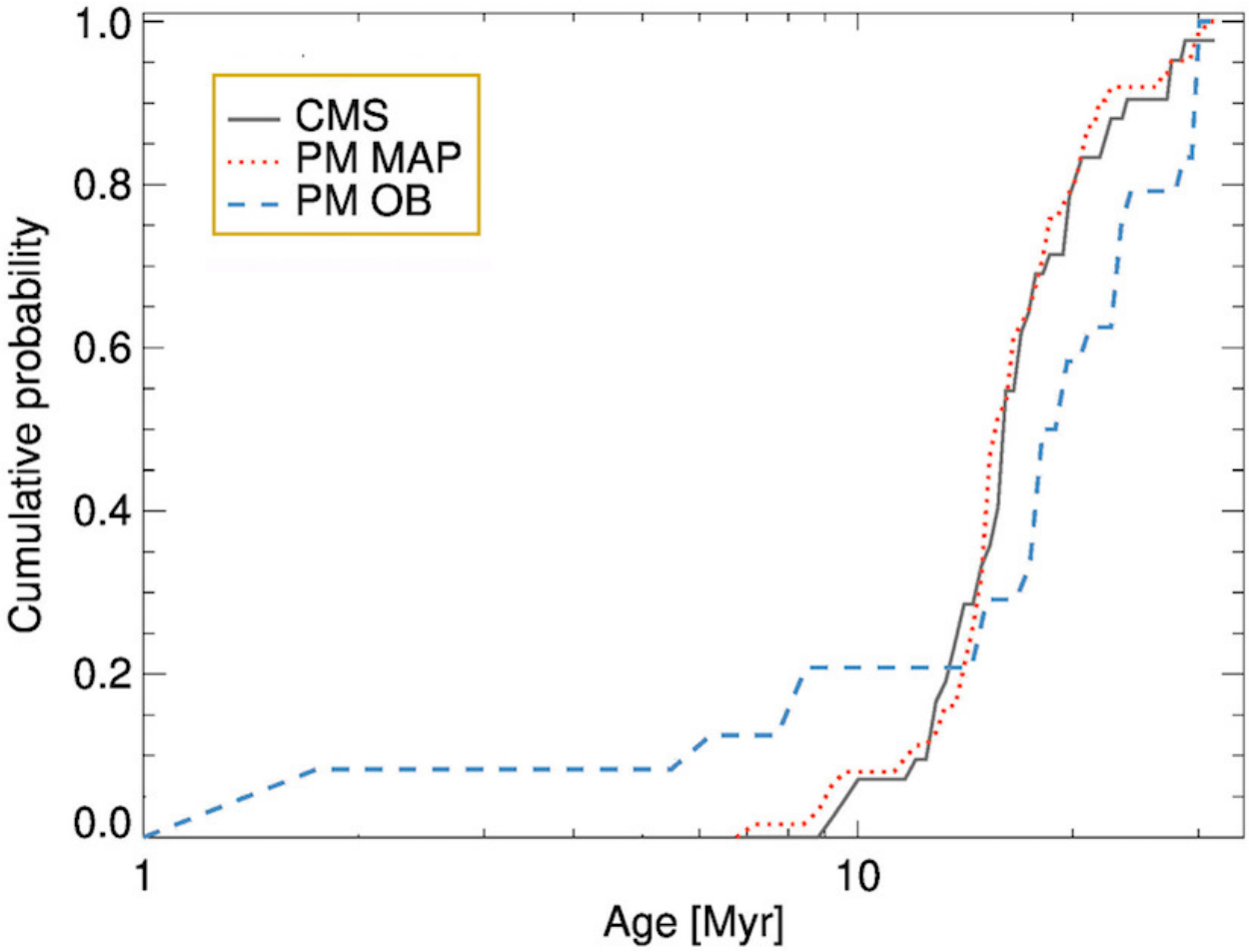

Figure 2.5: Comparison between cumulative distributions of CMS ages (black solid line), ages based on the map by Pecaut & Mamajek (2016) (red dotted line) and direct isochronal ages from the same paper (blue dashed line). The first two methods are consistent with one another; the third one, based on rotating models from Ekström et al. (2012), is typically less precise and thus not employed.

$h = 0$ to maximize field rotation; integration time (DIT) is computed as a trade-off between controlling overheads and read noise sensitivity (decreasing with shorter DIT) and ensuring adequate sensitivities at the smallest (~ 100 mas) separations (decreasing with longer DIT).

Calibration of scientific exposures involves the acquisition of several additional images, such as:

- a non-saturated image of the primary;
- a *waffle* image where the waffle mode of the deformable mirror is activated, so that ghost features appear: these features can be used for astrometric and photometric calibration;
- sky frames, needed to estimate the contribution of thermal background.

Every time a companion candidate is identified, one must ascertain whether it shares a common proper motion with the target or it is instead a background star. 708 such sources were identified during the first 67 observations of the program, that is to say, ~ 11 sources are seen on average around BEAST stars (Janson et al. 2021b). This is a result of the relatively low Galactic latitude

of Sco-Cen; indeed, the targets that are closest to the Galactic plane are usually surrounded by $50 - 120$ companion candidates (an example is provided in Figure 2.6).

For this purpose, at least a second observation is needed to assess the astrometric displacement of every companion candidate; given the typical proper motion of Sco-Cen members ($\sim 20 - 30$ mas yr^{-1}), the optimal temporal baseline between the two epochs should be $\gtrsim 1$ yr. A source will be confirmed as a physical companion if its motion is consistent with that expected for a bound object and significantly different from the cloud of background sources. For a companion candidate close enough to be imaged by IFS, each observation naturally provides a spectrum; therefore, additional follow-up turns out to be particularly important not only for the confirmation of companion candidates, but also for their spectroscopic characterization.

2.4.2 Data reduction and analysis

In the context of BEAST, basic data reduction comprises the following chain of operations (Maire et al. 2016):

- dark and flat field corrections;
- determination of the pixel scale with a precision of $0.01 - 0.02$ mas px^{-1}. Typical values are 12.25 mas px^{-1} for IRDIS and 7.46 mas px^{-1} for IFS;
- determination of the true north correction with a precision of $0.1°$. The typical value is $1.8°$;
- creation of a 4D datacube (x, y, t, λ), where t and λ sample the frame and the wavelength space, respectively;
- wavelength calibration.

Following the creation of calibrated datacubes, a second, more advanced level of reduction, mediated by the SpeCal package (Galicher et al. 2018), begins. For IRDIS, three different reductions are performed:

1. a simple non-ADI approach, which only employs de-rotation and temporal collapse of the frames;
2. a classical ADI reduction, that is conservative enough to maintain faint extended emission features such as debris disks;
3. a Template Locally Optimized Combination of Images (TLOCI; Lafrenière et al. 2007) approach, which is designed to search for point sources.

The procedure for IFS is the same, the only difference being the substitution of the non-ADI reduction with a Principal Component Analysis (PCA) approach known as Karhunen-Loève Image Projection (KLIP; Soummer et al. 2012; Pueyo 2016).

Point sources that are identified with S/N $> 5\sigma$ in the final reduced images are subsequently analyzed to compute their astrometry and their photometry.

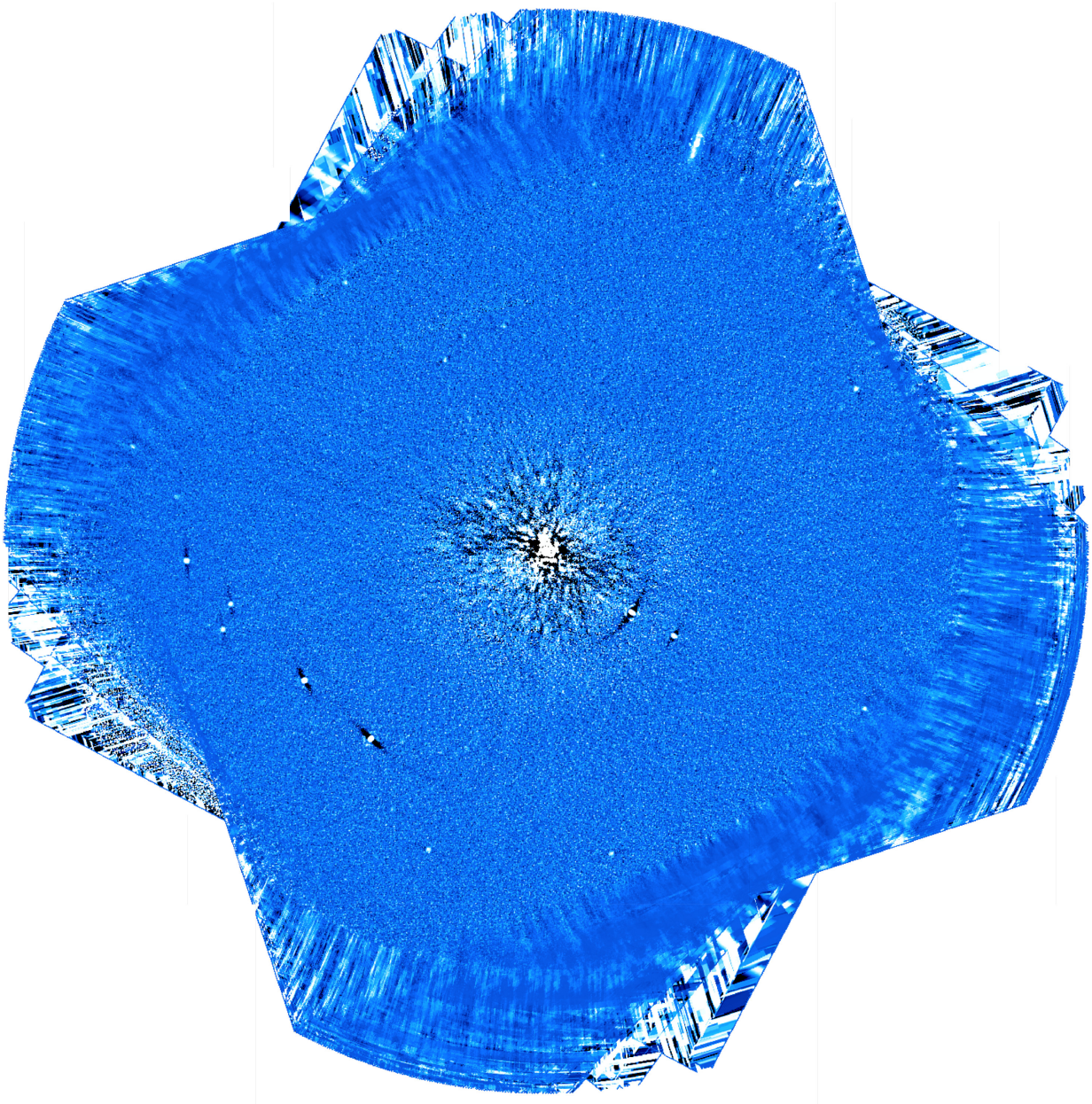

Figure 2.6: IRDIS image of the region around the star HIP82545 = μ^2 Scorpii. A large amount of background sources can be seen. This star will be the subject of Section 5.3.

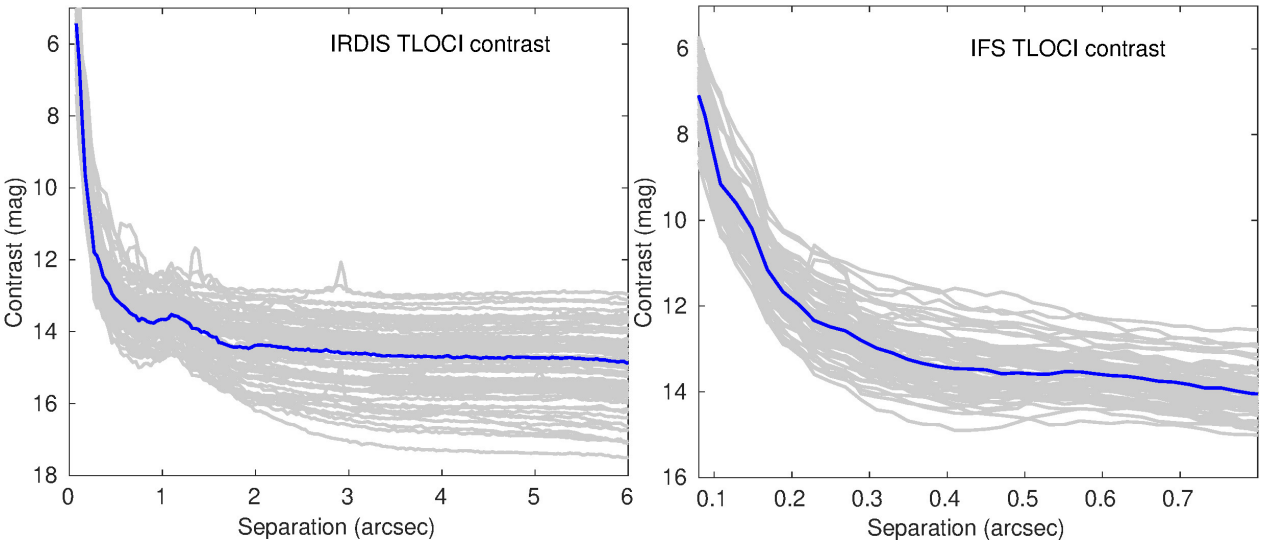

Figure 2.7: *Left panel*: contrast curves for IRDIS (TLOCI reduction, K1 band). *Right panel*: Contrast curves for IFS (TLOCI reduction, collapsed over all wavelengths). Gray lines indicate the contrast curves of individual targets, blue thick lines the median contrast curves for the whole sample.

2.4.3 Performance assessment

The performances of SPHERE were evaluated using 67 first-epoch observations of BEAST targets gathered between 2018 and 2020. Detection limits, expressed as contrast limits as a function of the projected separation from the target, are shown in Figure 2.7.

The combination of strong SPHERE performances, good observing conditions, and brightness of the targets (enabling excellent performances of wavefront sensing techniques) generally renders the achievable contrasts better than those obtained by SHINE (Desidera et al. 2021) and GPIES (Nielsen et al. 2019). Conversely, the depth of search – in term of minimum detectable companion mass – is lower due to the greater average mass of the targets (cf. Equation 1.14): starting from the contrast curves shown in Figure 2.7, stellar ages from Table 2.3, parallaxes and 2MASS magnitudes, we converted the contrast limits into mass limits using MADYS, the tool that will be the focus of Chapter 3. The derived detection maps are shown in Figure 2.8, and nicely convey the potential of BEAST in the context of planetary studies.

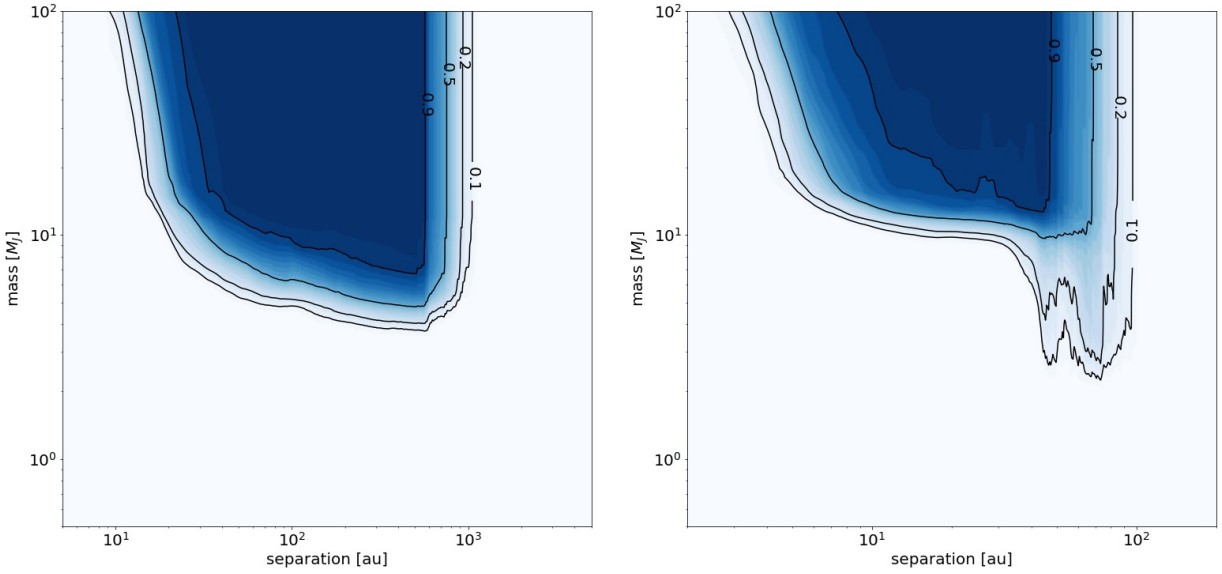

Figure 2.8: *Left panel*: detection map in the K1 band with IRDIS for the BEAST sample. *Right panel*: detection map with IFS for the BEAST sample. The contrasts, averaged over wavelength, were treated as if they were measured in SPHERE's J-band magnitude (which approximately lies at the center of IFS' wavelength range). The conversions from contrasts to magnitudes hinge upon the AMES-Dusty models (Allard et al. 2001).

Chapter 3

MADYS: the Manifold Age Determination for Young Stars

The derivation of age estimates for the stellar sample of BEAST, discussed in Chapter 2, was based on isochronal fitting of stars sharing a common proper motion with the targets. At the age of Sco-Cen, a large fraction of the stars is still in the pre-main sequence (PMS) phase, when the dependence of luminosity on age is steep enough to allow a simultaneous determination of age and mass; indeed, the spread between age predictions by different models – due to factors like initial helium abundance, metallicity, mixing length, convective core overshooting (Prada Moroni et al. 2016) – is generally acceptable ($\sim$ 20%) for F-G stars (Soderblom 2010). However, the accuracy rapidly degrades at later spectral types, so that the inter-model spread can be as high as a factor of 4-5 for late-K and M stars (Soderblom 2010) as a consequence of rotation, activity and magnetic fields (Feiden 2016b). Comparable problems affect, as we have seen in Chapter 1, high-mass stars.

In view of the large availability of theoretical models, a straightforward comparison of physical parameters obtained by different sets of isochrones would be particularly important to assess systematic uncertainties. To this aim, we developed the Manifold Age Determination for Young Stars (MADYS), a flexible Python tool for the age and mass determination of young stellar and substellar objects. Harmonizing the heterogeneity of publicly available isochrone grids, the tool allows one to choose amongst 17 models, many of which with customizable astrophysical parameters, for a total of $\sim$ 120 isochrone grids. This Chapter, based on a published paper (Squicciarini & Bonavita 2022), demonstrates the capabilities of MADYS, which will be subsequently employed to study the large-scale environment of Upper Scorpius (Chapter 4) and to characterize the μ^2 Scorpii system (Section 5.3). After introducing in Section 3.1 the key concepts behind MADYS, with a special focus on data retrieval and extinction estimates, we will present the algorithm for age and mass determination in Section 3.2; a few applications are then provided in Section 3.3, and a special focus on the contributions to published papers is placed in Section 3.4. In Section 3.5, we discuss the strengths and the limitations of the tool, and anticipate its future developments. In Section 3.6 we give a short summary of the tool and its scientific applications.

3.1 The tool

The Manifold Age Determination of Young Stars (MADYS), written in Python, is a tool that allows to derive the properties of arbitrarily large lists of young objects by comparison with several published evolution models. MADYS combines extensive cross-match capabilities, a careful assess-

ment of photometric data, the ability to estimate interstellar extinction in hundreds of photometric bands, and the homogenization of a large collection of stellar and substellar evolutionary models. The derivation of ages and masses can be performed under several configurations depending on the science case, allowing for the presence of multimodal posterior distributions.

The fully documented public release of MADYS is accessible via GitHub[1], while the underlying theoretical grids are stored in a Zenodo record[2]. Finally, several examples of code execution are provided in a dedicated Jupyter Notebook[3].

The tool can be used in two different modes, depending on the kind of input provided: either a list of object names (*mode 1*) or a table containing object names, photometry and, optionally, astrometry (*mode 2*). Generally speaking, the execution of the program triggers the following chain of operations: after retrieving – but only in mode 1, see Section 3.1.1 – photometric and astrometric data, reliable photometry is identified (Section 3.1.2); then, the estimation of interstellar extinction in all the bands of interest is performed (Section 3.1.3), resulting in a final database to be used for age and mass determination (Section 3.2.2).

The estimation of physical parameters is not done during initialization, but rather by calling a dedicated method that acts upon the database: in this way, it is possible to inspect data, to carefully decide the (sets of) theoretical model(s) suitable to the science case (Section 3.2.1), and to repeat multiple times the analysis of the same database.

3.1.1 Data retrieval

3.1.1.1 Mode 1

Building on the capabilities of `astroquery`[4] and TAP[5] to handle existing cross-matches between Gaia and other catalogs (Marrese et al. 2019), MADYS queries the Gaia Archive to return a single catalog containing astrometric, kinematic and photometric information from Gaia Data Release 2 (Gaia DR2; Gaia Collaboration et al. 2018b), Gaia DR3 (Gaia Collaboration et al. 2022) and 2MASS (Skrutskie et al. 2006). Optionally, AllWISE (Cutri et al. 2021), Pan-STARRS Data Release 1 (Chambers et al. 2016), and the Sloan Digital Sky Survey Data Release 3 (SDSS DR13; Albareti et al. 2017) can be added to the query as well[6].

Although it is recommended to use Gaia DR2 or Gaia DR3 IDs, it is also possible to use other naming conventions. In the latter case, input names are converted into their Gaia DR2 counterparts through a query of the SIMBAD database (Wenger et al. 2000).

The results of the query are provided as a table whose i-th row corresponds to the i-th star of the initial list of objects to allow an unambiguous pairing of input and output data. In other words, the query algorithm of MADYS is able to handle the cases in which more than one Gaia DR3 source is associated to the same Gaia DR2 source (or vice versa), selecting as best-mach the source with Gaia DR2 ID = Gaia DR3 ID or, if missing, the source in the VizieR catalog (Ochsenbein et al. 2000) having the closest G, G_{BP} and G_{RP} photometry in a suitable region accounting for the astrometric

[1] `https://github.com/vsquicciarini/madys`

[2] Currently accessible at: `https://zenodo.org/record/6958170`; as the link is expected to change at each future version of the tool, it is advised to refer to the stable link pointing at the GitHub repository.

[3] `https://github.com/vsquicciarini/madys/blob/main/examples/MADYS_examples.ipynb`

[4] https://astroquery.readthedocs.io/en/latest/

[5] https://github.com/mfouesneau/tap.

[6] A few additional catalogs (listed in https://gea.esac.esa.int/archive/documentation/GEDR3/Catalogue_consolidation/chap_crossmatch/sec_crossmatch_externalCat/) might be incorporated in future versions of the program, if considered useful by the community.

motion of the source over the two epochs [7]. This stratagem is able to find a cross-match for some high-proper motion stars which are not paired by the SIMBAD database. Likewise, a small ($\sim 0.5\%$) fraction of missing 2MASS matches is recovered by indirectly exploiting the AllWISE-2MASS cross-match, or – if explicitly required – by directly inspecting the SIMBAD database.

The typical speed of the query is about $\sim 100-150$ stars s^{-1}, meaning that a list of 1000 objects is fully recovered within few seconds. Large lists of objects ($\sim 10^4 - 10^5$) are handled efficiently by splitting the query into smaller chunks and later reassembling the results in the original order.

In any case, the resulting database always comprises data from Gaia DR2 and Gaia DR3. Parallaxes from Gaia DR3[8] and extinctions (Section 3.1.3) are combined with apparent photometry to get absolute magnitudes. Quality flags from selected surveys are retained with the aim of identifying reliable photometric data (Section 3.1.2).

3.1.1.2 Mode 2

In mode 2, a table containing full information needed for age and mass determination is provided. This mode is thought for objects that are not present in Gaia, such as self-luminous direct-imaged exoplanets and brown dwarfs.

Minimum requirements, in this case, consist of a column of object names and a column with magnitudes. If parallaxes are provided, input magnitudes are considered as apparent; otherwise, they are considered as absolute. By providing two columns with equatorial or galactic coordinates, it is possible for the program to evaluate interstellar extinction in the direction of the object(s) and to take it into account (see Section 3.1.3). Alternatively, values for the E(B-V) color excess can be manually provided.

More than 250 photometric filters are available in this mode, meaning that there is at least one theoretical model which they can be compared to. The full list of filters – including, for example, the full suite of the James Webb Space Telescope (JWST, Gardner et al. 2006) filters – can be found in the documentation.

3.1.2 Selection of appropriate photometry values

This Section describes the conditions for a photometric measurement to be retained in the final database. By default, MADYS' mode 1 collects photometric measurements from Gaia DR2/DR3 (G, G_{BP}, G_{RP}) and 2MASS (J, H, K_s). Gaia DR3 G magnitudes are corrected by adopting the prescriptions by Riello et al. (2021). As regards G_{BP} and G_{RP}, which are known to be intrinsically much more sensitive than G to contamination from nearby sources or from the background (Evans et al. 2018), the phot_bp_rp_excess_factor C is used as a proxy to evaluate the quality of photometric measurements. Following Riello et al. (2021), a color-independent corrected BP/RP excess factor C^* was defined for both Gaia DR2 and Gaia DR3:

$$C^* = C + k_0 + k_1\Delta G + k_2\Delta G^2 + k_3\Delta G^3 + k_4 G, \tag{3.1}$$

where $\Delta G = (G_{BP} - G_{RP})$.

The corrected BP/RP excess factor has an expected value of 0 for well-behaved sources at all magnitudes but, when considering subsamples of stars with similar brightness, it tends to widen out for fainter G; a varying standard deviation $\sigma(G)$ can be defined (Riello et al. 2021) as follows:

[7] In the latter case, the source X is considered a cross-match to source 0 only if $|G_0 - G_X| < 0.2$ mag and $|G_{BP,0} - G_{BP,X}| < 0.2$ mag and $|G_{RP,0} - G_{BP,X}| < 0.2$ mag.

[8] If the parallax for a source is present in DR2 but not in DR3, values from Gaia DR2 are used.

Table 3.1: Adopted values for Eq. 3.1-3.2.

DR2	$\Delta G < 0.5$	$0.5 \leq \Delta G < 3.5$	$\Delta G \geq 3.5$
k_0	-1.121221	-1.1244509	-0.9288966
k_1	+0.0505276	+0.0288725	-0.168552
k_2	-0.120531	-0.0682774	0
k_3	0	0.00795258	0
k_4	-0.00555279	-0.00555279	-0.00555279
c_0		0.004	
c_1		$8 \cdot 10^{-12}$	
m		7.55	
DR3	$\Delta G < 0.5$	$0.5 \leq \Delta G < 4$	$\Delta G \geq 4$
k_0	1.154360	1.162004	1.057572
k_1	0.033772	0.011464	0.140537
k_2	0.032277	0.049255	0
k_3	0	-0.005879	0
k_4	0	0	0
c_0		0.0059898	
c_1		$8.817481 \cdot 10^{-12}$	
m		7.618399	

$$\sigma_{C^*}(G) = c_0 + c_1 \cdot G^m. \tag{3.2}$$

Values for the constants for Eq. 3.1- 3.2 are taken from Riello et al. (2021) for DR3 and Squicciarini et al. (2021) for DR2, and are provided in Table 3.1.

We exclude G_{BP} and G_{RP} magnitudes with a corrected excess factor larger, in absolute value, than 3 $\sigma_{C^*}(G)$. As mentioned above, a value of C^* significantly different from zero might be due to blended Gaia transits or crowding effects; in addition to this, it can also be related to an over-correction of the background (if $C^*<0$) or to an anomalous SED (if $C^*>0$) characterized by strong emission lines in the wavelength window where the G_{RP} transmittivity is larger than the G transmittivity. This latter case can occur, for instance, for a source located in a HII region (see discussion in Riello et al. 2021).

From 2MASS and AllWISE, only sources with photometric flag ph_qual='A' are kept. If needed, a different value for the worst quality flag still considered reliable can be selected.

3.1.3 Interstellar extinction

The estimate of extinction (reddening) in a given band (color) is performed by integrating along the line of sight a suitable 3D extinction map. The integration algorithm draws a line from the position of the Sun toward that of the star of interest; the value of each pixel crossed by the line is weighted according to the portion of the total distance spent by the line in the pixel itself. This method ensures a rapid and precise evaluation of the integral, allowing 10000 stars to be handled in ~ 1 s under typical PC performances.
Two extinction maps can be selected:

- the STILISM 3D extinction map by Lallement et al. (2019): a Sun-centered (6000x6000x800) pc grid, with step equal to 5 pc;

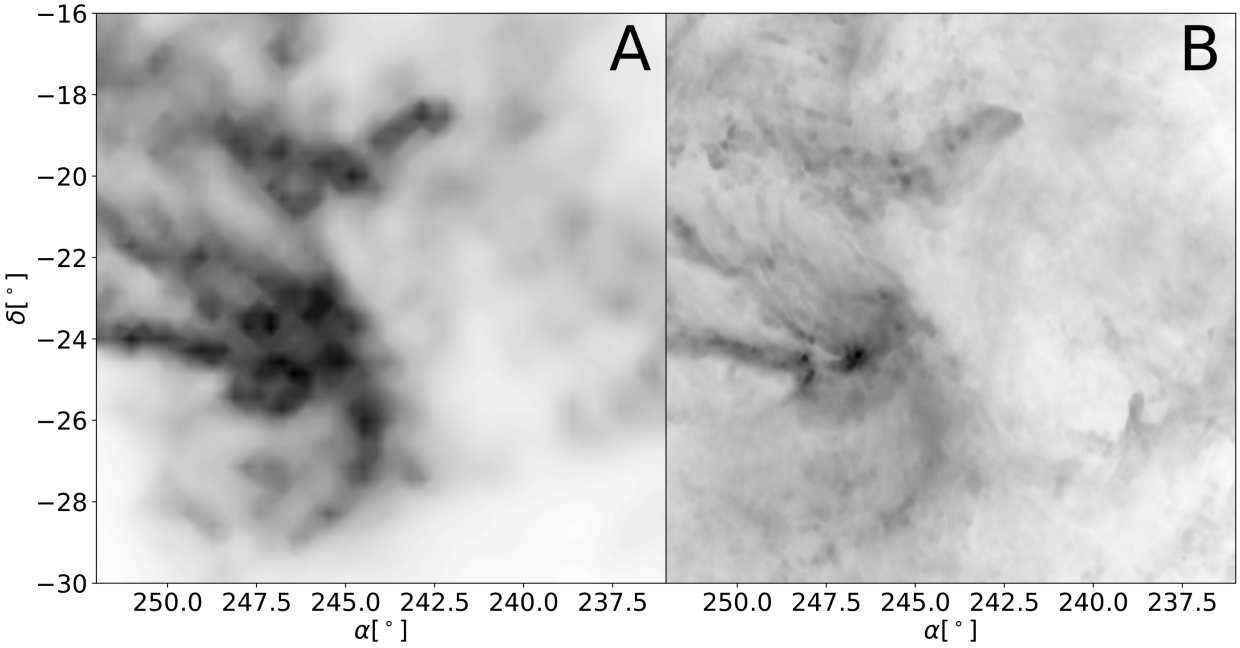

Figure 3.1: Integrated extinction toward Upper Scorpius. (A) G-band extinction map produced by MADYS by integrating the 3D map by Leike et al. (2020) up to a distance $d = 160$ pc. (B) Intensity Stokes map at 350 μm produced by the Planck satellite.

- the Galactic extinction catalog by Leike et al. (2020): a Sun-centered (740x740x540) pc grid with step equal to 1 pc.

Since the file with the selected map must be present in the local path where MADYS has been installed, the errors on the derived estimates – which would require the download of additional files – are currently not returned by the program.

Coordinate transformations from the equatorial or galactic frame to the right-handed galactocentric frame (i.e., a Cartesian galactic frame) is performed by means of the astropy package[9] (Astropy Collaboration et al. 2013).

As a test for the accuracy of the algorithm, we provide in Figure 3.1 a visual comparison between the integrated absorption in the Upper Scorpius region (already used in Squicciarini et al. 2021) obtained through the map by Leike et al. (2020) and the intensity Stokes map returned by the Plank satellite (Planck Collaboration et al. 2020) in the far infrared ($\nu = 857$ GHz $= 350$ μm). Given the large galactic latitude of the region ($l \in [10°, 30°]$), we expect the large majority of the integrated intensity in the Planck image to be produced by the association, with only a negligible background contribution. Indeed, the agreement between the two images is excellent.

The conversion between extinction and reddening is mediated by a total-to-selective absorption ratio $R = 3.16$ (Wang & Chen 2019). The extinction law is obtained by combining the extinction law by Wang & Chen (2019) in the range $[0.3, 2]$ μm and the diffuse average extinction by Gordon et al. (2021) in the range $[6.5, 40]$ μm; a linear combination of the two is used in the intermediate range $[2, 6.5]$ μm (Figure 3.2):

[9]Default parameters from the "pre-v4.0" are used: galcen_distance=8.3 kpc, galcen_v_sun=(11.1, 232.24, 7.25) km s^{-1}, z_sun=27.0 pc, roll=0.0 deg. See https://docs.astropy.org/en/stable/api/astropy.coordinates.Galactocentric.html for details.

Table 3.2: Adopted values for the coefficients in Eq. 3.3-3.7.

Name	Value	Name	Value
b_0	1	h_4	0.366
b_1	0.7499	β_4	-1.48
b_2	-0.1086	S_1	0.06893
b_3	-0.08909	S_2	0.02684
b_4	0.02905	λ_1	9.865
b_5	0.01069	γ_1	2.507
b_6	0.001707	a_1	-0.232
b_7	-0.001002	λ_2	19.973
h_2	0.3722	γ_2	16.989
β_2	-2.07	a_2	-0.273

$$\frac{A_\lambda}{A_V} = \begin{cases} \sum_{i=0}^{7} b_i\ \xi^i & \lambda \in [0.3, 1]\ \mu m \\ h_2 \lambda^{\beta_2} \equiv f_2(\lambda) & \lambda \in [1, 2]\ \mu m \\ [1 - q(\lambda)] f_2(\lambda) + q(\lambda) f_4(\lambda) & \lambda \in [2, 6.5]\ \mu m \\ h_4 \lambda^{\beta_4} + S_1 D_1(\lambda) + S_2 D_2(\lambda) \equiv f_4(\lambda) & \lambda \in [6.5, 40]\ \mu m \end{cases}, \tag{3.3}$$

where:

$$\xi = \frac{1}{\lambda} - 1.82\ \mu\mathrm{m}^{-1} \tag{3.4}$$

and

$$q(\lambda) = \frac{\lambda - 2\ \mu\mathrm{m}}{6.5\ \mu\mathrm{m} - 2\ \mu\mathrm{m}}, \tag{3.5}$$

while D_1 and D_2 are two modified Drude profiles, used to model the silicate absorption features at $\sim 10\ \mu$m and $\sim 20\ \mu$m:

$$D(\lambda) = \frac{(\gamma(\lambda)/\lambda_0)^2}{((\lambda/\lambda_0 - \lambda_0/\lambda)^2 + (\gamma(\lambda)/\lambda_0)^2)}. \tag{3.6}$$

Finally, $\gamma(\lambda)$ is in turn given by:

$$\gamma(\lambda) = \frac{2\gamma_0}{1 + \exp(a_0(\lambda - \lambda_0))} \tag{3.7}$$

(Gordon et al. 2021). We list in Table 3.2 all the coefficients from Eq. 3.3-3.7, where (γ_1, λ_1, a_1) and (γ_2, λ_2, a_2) indicate the coefficients for $D_1(\lambda)$ and $D_2(\lambda)$, respectively.

The adopted extinction law goes farther in the mid-infrared than widely used parametrizations, as those offered by the extinction package[10], delving into wavelength ranges amenable to forthcoming JWST observations. Individual extinction coefficients A_λ are directly taken from Table 3 of Wang & Chen (2019) whenever possible, or computed through Eq. 3.3 adopting as λ the mean wavelength indicated by the SVO Filter Profile Service (Rodrigo et al. 2012; Rodrigo & Solano 2020).

We would like to highlight that in the youngest ($t \lesssim 5$ Myr) star-forming regions, owing to the uneven and fragmentary nature of dust structures, the spatial variation of extinction usually occurs on smaller scales than when sampled by the available 3D maps. This limitation of the program can

[10] ttps://extinction.readthedocs.io/en/latest/

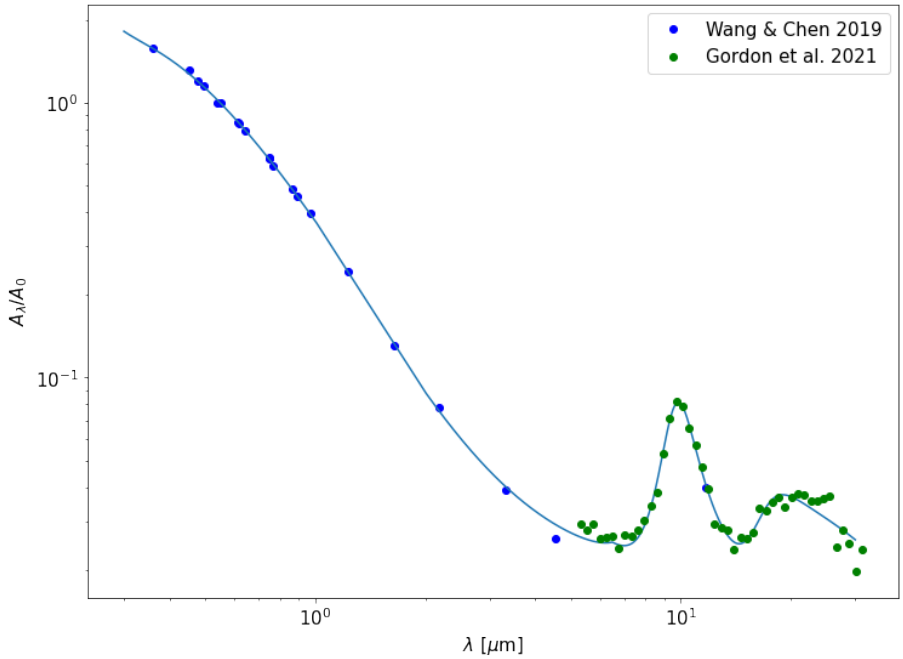

Figure 3.2: Adopted extinction law (solid line). Blue dots represent absorption coefficients in the visible and NIR (Wang & Chen 2019, Table 3), green dots in the MIR (Gordon et al. 2021, Table 8).

be currently handled by manually providing a vector of individual extinction values at initialization; a future version of MADYS will enable the simultaneous fit of extinction and (sub)stellar parameters based on available photometry.

3.2 Age and mass determination

3.2.1 Loading isochrone tables

As already mentioned, the determination of ages and masses in this first release of MADYS is performed via isochronal fitting, comparing the database obtained in Section 3.1.2 to the selected set of isochrones. We refer to these estimates as "photometric" or "isochronal" estimates interchangeably.

Overcoming the multifarious conventions of isochrone tables found in the literature, MADYS employs a version of the `evolution` routine[11] that was extended to support 17 different stellar and substellar evolutionary models. Some of these models offer the additional possibility to customize astrophysical parameters such as metallicity, rotational velocity, helium content, alpha enhancement and the spot fraction, for a total of $\sim$ 120 different isochrone tracks (Table 3.3.

Mass and age ranges for the grid can be externally imposed; otherwise, the program computes suitable mass limits that take into account both the dynamical range of the model and the range of values expected from a rough preliminary evaluation of the sample's absolute Gaia DR3 G-band and, if applicable, 2MASS K_s-band magnitudes based on the tables by Pecaut & Mamajek (2013).

After selecting a model, the program creates two vectors of masses and ages, whose points are equally spaced on a logarithmic scale, and builds the theoretical photometric grid. Linear

[11] https://github.com/avigan/Python-utils/tree/master/vigan/astro

Table 3.3: Isochrone models currently supported by MADYS with their bibliographic references. Adopted values for solar metallicity ($Z_\odot$) and the initial helium abundance (Y_0) are reported (u=unknown), together with mass (M) and age ranges (t). Customizable parameters (c.p.): metallicity (m), helium content (Y), alpha enhancement (α), rotational velocity (v), spot fraction (s).

Name	Y_0	$Z_\odot$	M	t	c. p.	reference
			$M_\odot$	Myr		
AMES-COND	0.247	0.018	[0.005,1.4]	$[1, 1.2 \cdot 10^4]$	—	Allard et al. (2001)
AMES-Dusty	0.247	0.018	[0.005,1.4]	$[1, 1.2 \cdot 10^4]$	—	Allard et al. (2001)
ATMO2020	0.275	0.0169	[0.001, 0.075]	$[10^0, 10^4]$	—	Phillips et al. (2020)
B97	0.27431	0.01886	$[10^{-3}$,0.04]	$[10^0, 10^4]$	—	Burrows et al. (1997)
BEX	0.27	0.0142	$[1.5 \cdot 10^{-5}$,0.002]	$[1, 4 \cdot 10^3]$	—	Linder et al. (2019); Marleau et al. (2019a)
BHAC15	0.271	0.0153	[0.01,1.4]	$[0.5, 10^4]$	—	Baraffe et al. (2015)
BT-Settl	0.271	0.0153	[0.01,1.4]	$[10^0, 10^4]$	—	Allard (2016)
Geneva	0.266	0.014	[0.8,120]	$[0.1, 10^2]$	—	Haemmerlé et al. (2019)
MIST	0.2703	0.0142	[0.1,150]	$[10^{-1}, 2 \cdot 10^4]$	m, α, v	Dotter (2016); Choi et al. (2016)
NextGen	0.247	0.018	[0.01,1.4]	$[10^0, 1.2 \cdot 10^4]$	—	Hauschildt et al. (1999)
PARSEC	0.2485	0.01524	[0.09,350]	$[10^{-1}, 10^4]$	m	Marigo et al. (2017)
PM13	—	—	[0.075,27]	—	—	Pecaut & Mamajek (2013)
SB12	0.27431	0.01886	$[10^{-3}$,$10^{-2}]$	[1,100]	—	Spiegel & Burrows (2012)
Sonora Bobcat	0.2735	0.0153	$[5 \cdot 10^{-4}, 10^{-1}]$	$[10^{-1}, 10^4]$	—	Marley et al. (2021)
SPOTS	0.2676	0.0165	[0.1,1.3]	$[10^0, 4 \cdot 10^3]$	s	Somers et al. (2020)
STAREVOL	0.269	0.0134	[0.2,1.5]	$[1, 1.26 \cdot 10^4]$	m, v	Amard et al. (2019)
YAPSI	0.2775	0.0142	[0.15,5]	$[0.5, 10^4]$	m, Y	Spada et al. (2017)

interpolation between consecutive points into the final grid is performed for every quantity, and no extrapolation is attempted outside the grids. The usage of a fixed grid, rather than real-time interpolation, was chosen for a twofold reason: to handle arbitrarily large group of stars while keeping computation times reasonable, and to allow a homogeneous treatment of statistical uncertainties. The spacing between consecutive steps can be adjusted, but is by default significantly smaller than any realistic uncertainty value.

Generally speaking, the choice of the isochrone set for a given sample should be carefully pondered depending on the expected mass and age ranges of the sample and on the photometric filters of interest. We notice that a few isochrone sets do not come equipped with Gaia and 2MASS filters: hence, they can only be used in mode 2. The program is not halted if it encounters a filter that is not available for the selected model, but – after printing a warning – it neglects all the photometry provided in that filter. For this reason, it is always recommended to look at the produced execution log.

3.2.2 Age and mass determination

For each object in the final database (Section 3.1.2), MADYS seeks the minimum of a suitable χ^2 function:

$$\chi^2 = \sum_k \left(\frac{M_k^{th} - M_k^{obs}}{\sigma_{M_k^{obs}}} \right)^2 \equiv \sum_k s_k^2 \tag{3.8}$$

which can be thought as a 2D distance matrix with same shape as the age-mass grid and elements:

$$\chi^2_{ij} = \sum_k \left(\frac{M_{ijk}^{th} - M_k^{obs}}{\sigma_{M_k^{obs}}} \right)^2, \tag{3.9}$$

where M_{ijk}^{th} is the theoretical magnitude in the k-th filter corresponding to the i-th mass and j-th age of the model grid, $M_{obs,k}$ is the observed magnitude in the same filter and $\sigma_{M_{obs,k}}$ its associated uncertainty. The sum is done only over the filters k passing the following prescriptions:

1. an error on the absolute magnitude smaller than 0.2 mag;
2. a best-match $M_{i_0 j_0 k}^{th}$ such that $|M_{i_0 j_0 k}^{th} - M^{obs}| < 0.2$ mag.

Individual age ranges can be provided for each target, and this is particularly useful when external constraints are available; the only caveat is that the kind of input should be the same for every target. In particular, if the age of each object star is explicitly imposed, or a triplet [optimal age, minimum age, maximum age] is provided (case 1), a single filter is sufficient for parameter estimation; conversely, if no age constraint is given, or just a doublet [minimum age, maximum age] is provided (case 2), the estimation is performed only if the following conditions are met:

3. at least three filters passed the prescriptions 1. and 2.;
4. after identifying the minimum χ^2, its third smallest associated $s_k^2 < 9$, or alternatively its third smallest $|M_k^{th} - M_k^{obs}| < 0.1$ mag.

In order to embed photometric uncertainty into the final parameter estimate, the procedure is repeated $q = 1000$ times while randomly varying, using a Monte Carlo approach, the apparent

photometry and the parallax according to their uncertainties (which are assumed to be distributed in a normal fashion).

In case 1, the age is not fitted, and the resulting mass distribution is assumed to be unimodal: in other words, the masses corresponding to the 16^{th},50^{th} and 84^{th} percentile of the sample composed by the q best-fit solutions are returned.

In case 2, the algorithm considers the possibility of a multimodal posterior distribution for both age and mass. At each iteration q, having a minimum $\chi^2 = \chi^2_q$, the set of (i, j) mass and age steps such that:

$$\chi^2_{i,j} < \chi^2_q + \Delta\chi^2 \tag{3.10}$$

are collected and added to a single array, $\bar{P}$. We decided to adopt $\Delta\chi^2 = 3.3$ as it defines the 68.3% confidence region around the best-fit joint parameter estimate for a two-parameter model (see, e.g., Verde 2010).

The final outcome of this procedure is an array of solutions, $\bar{P}$. The "hottest points" are the indices recurring more frequently; each occurrence of a point has an associated χ^2, and this should be properly reflected into the final weighted average. In general, the ensemble of points in $\bar{P}$ will not be connected, meaning that multiple families of solutions in the age-mass space can be possible.

An intuitive approach to identify these families consists in identifying connected regions in the age-mass grid. In order to reduce the strong dependence of the connection on random realizations of data perturbations, we decided to define as "attraction points" the points which appear at least in the 10% of the interactions in $\bar{P}$. Each isolated attraction point defines a family of solutions; a group of contiguous attraction points is treated as a single attraction point located in the group's center of mass, hence defining a single family of solutions as well. The remaining points are then assigned to the family of the closest attraction point.

Each family of solutions p corresponds, from a physical perspective, to a different physical solution; its associated age and mass estimates (t_p,m_p) are defined as the average of the i-th mass and the j-th age, weighted by a coefficient $1/\chi^2_{ij,q}$:

$$\log_{10} m_p = \frac{\sum_{(i,j)\in p} \log_{10} m_i \cdot (\chi^2_{ij,q})^{-1}}{\sum_{(i,j)\in p} (\chi^2_{ij,q})^{-1}}, \tag{3.11}$$

$$\log_{10} a_p = \frac{\sum_{(i,j)\in p} \log_{10} a_j \cdot (\chi^2_{ij,q})^{-1}}{\sum_{(i,j)\in p} (\chi^2_{ij,q})^{-1}}, \tag{3.12}$$

where, of course, points (i, j) repeating in different iterations are summed each time with a weight corresponding to the $\chi^2_{ij,q}$ of the q-th iteration.

The variances associated to $\log_{10} m_p$ and $\log_{10} a_p$ are given by:

$$\sigma^2_{m_p} = \frac{\sum_{(i,j)\in p} (\log_{10} m_i - \log_{10} m_p)^2 \cdot (\chi^2_{ij,q})^{-1}}{\sum_{(i,j)\in p} (\chi^2_{ij,q})^{-1}}, \tag{3.13}$$

$$\sigma^2_{a_p} = \frac{\sum_{(i,j)\in p} (\log_{10} a_i - \log_{10} a_p)^2 \cdot (\chi^2_{ij,q})^{-1}}{\sum_{(i,j)\in p} (\chi^2_{ij,q})^{-1}}. \tag{3.14}$$

Couples of solutions (p_1,p_2) that are consistent with representing the same solution, that is to say with:

$$\Delta d = \frac{(\log_{10} m_{p_1} - \log_{10} m_{p_2})^2}{\sigma^2_{m_{p_1}} + \sigma^2_{m_{p_2}}} + \frac{(\log_{10} a_{p_1} - \log_{10} a_{p_2})^2}{\sigma^2_{a_{p_1}} + \sigma^2_{a_{p_2}}} < 8, \tag{3.15}$$

are merged together. The outcome of the process is a set of solutions $\{p\}$, each one bearing a fraction of the total region of the solutions $\bar{P}$ equal to:

$$w_p = \frac{\sum_{(i,j)\in p}(\chi^2_{ij,q})^{-1}}{\sum_{(i,j)\in \bar{P}}(\chi^2_{ij,q})^{-1}}. \tag{3.16}$$

The solution with the maximum w_p is returned as the best-fit solution, but the other solutions can be inspected as well. Both the χ^2 map for nominal photometric values and the weight map W, defined as the 2D matrix with elements:

$$w_{ij} = \frac{1}{\sum_{(i,j)\in \bar{P}}(\chi^2_{ij,q})^{-1}} \tag{3.17}$$

referring instead to the whole fitting process, can be returned and plotted through a dedicated method.

3.3 Applications

3.3.1 Age substructures

The advent of Gaia has brought our view of the Galaxy to its grandest level of sharpness, paving the way for precise large-scale measurements of stellar luminosity and effective temperature, which in turn allow one to discern exquisite features inside CMDs (Gaia Collaboration et al. 2018a). In addition to this, the exquisite precision of Gaia's proper motion measurements has been enormously beneficial to the study of stellar moving groups, associations and clusters, leading to the compilation of large catalogs of confirmed members for known regions (e.g., Cantat-Gaudin et al. 2018; Gagné et al. 2018; Luhman & Esplin 2020) and even to the discovery of new ones (e.g., Cantat-Gaudin et al. 2019b). A complete census of star-forming regions is, in turn, the first step toward resolving kinematic substructures within them and connecting these structures with star formation history (e.g., Kuhn et al. 2019; Cantat-Gaudin et al. 2019a; Pang et al. 2022).

The ability of MADYS to handle thousands of stars at once makes it particularly suited to the systematic study of young ($t \gtrsim 5$ Myr) regions with a clear kinematic fingerprint. Indeed, the requirement of a significant portion of the stellar sample in the PMS phase and the caveat for the derived extinctions (Section 3.1.3) naturally define an optimal age range for MADYS between 5-10 Myr and a few hundred million years.

As a possible application of the code, we compute here the age of confirmed members of the Scorpius-Centaurus association. The association, that is the nearest star-forming region to the Sun, is classically divided into three subgroups: Upper Scorpius (US), Upper Centaurus-Lupus (UCL) and Lower Centaurus-Crux (LCC) (de Zeeuw et al. 1999).

We start from the list of bona fide Scorpius-Centaurus members compiled by Damiani et al. (2019) using Gaia DR2 data. In order to define the subregions, we employ classical coordinate boundaries as in de Zeeuw et al. (1999) and subsequent works: for US, $l \in [343°, 360°]$, $b \in [10°, 30°]$; for UCL, $l \in [313°, 343°]$, $b \in [0°, 25°]$; for LCC, $l \in [280°, 313°]$, $b \in [-10°, 23°]$.

Starting from Gaia DR2 IDs, MADYS recovers the photometry and computes extinction values as described in Section 3.1.3. The age and mass determination, initialized with only a modest constraint on age ($t \in [1, 300]$ Myr), is done here with the BHAC15 models (Baraffe et al. 2015).

A visual inspection of the $(G_{BP} - G_{RP}, G)$ CMD shows that some stars appear to be too old to be members of the association, and indeed they have fitted ages $\gtrsim 100$ Myr. Therefore, we exclude

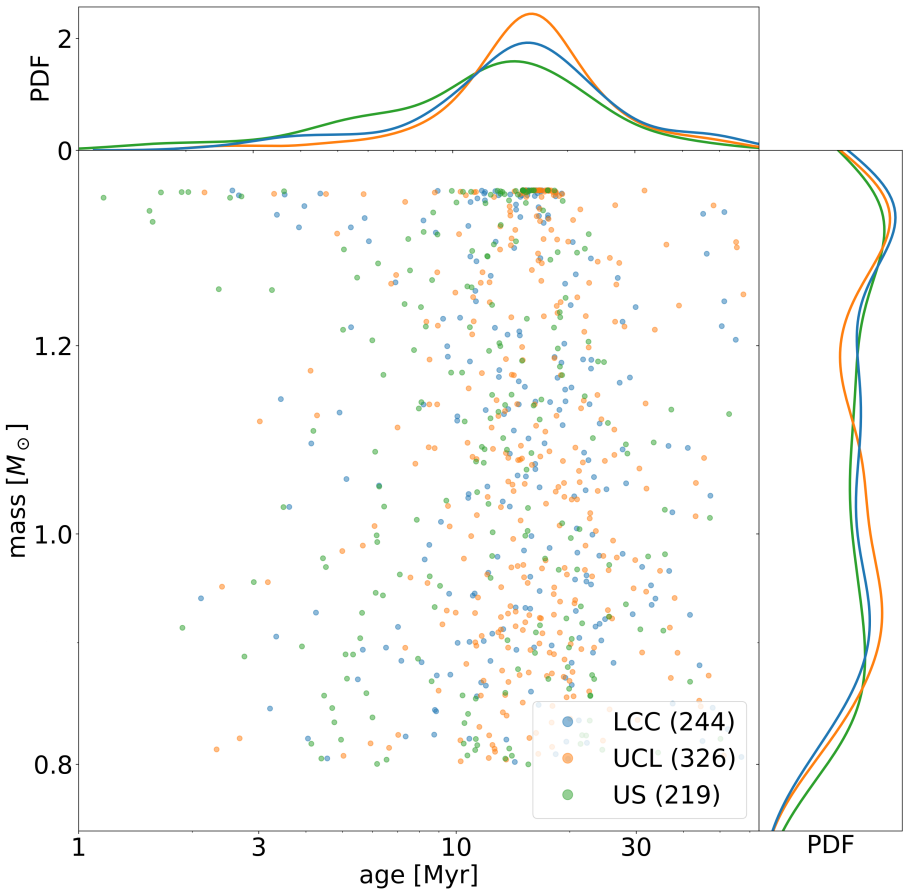

Figure 3.3: Derived age and mass distribution of the Sco-Cen sample, restricted to stars with $M > 0.8M_\odot$. The insets represent a kernel-density estimate of the underlying distributions. The clump of sources at the upper mass end is an artifact due to the sharp mass cut of BHAC15 isochrones at $1.4M_\odot$.

the stars with best-fit ages greater than 60 Myr; for the few stars with multiple possible solutions, meaning that there is an overlap between a PMS solution and an evolved MS solution, we pick the youngest one.

The derived ages and masses for the three subgroups, computed as the 16^{th},50^{th} and 84^{th} percentile of the age distribution of their members, are:

$$US : 6.6^{+5.6}_{-3.0} \text{ Myr},$$
$$UCL : 9.1^{+4.8}_{-3.7} \text{ Myr},$$
$$LCC : 8.7^{+5.6}_{-3.2} \text{ Myr}.$$

We recover some facts which are already known from the literature (see, e.g. Pecaut & Mamajek 2016): firstly, the observation that US is younger than UCL and LCC; secondly, the existence of a positive correlation between age and mass; in other words, M stars appear younger than their F and G counterparts (see Chapter 4). Although an age spread between the two cannot be completely ruled out, most of the observed spread is likely due to a slowed-down contraction of low-mass stars caused by magnetic fields (Feiden 2016a). Indeed, if we restrict to stars with a best-fit $M > 0.8M_\odot$

(Figure 3.3), the results become: US : $13.1^{+8.3}_{-7.1}$ Myr, UCL : $16.0^{+6.9}_{-5.0}$ Myr, LCC : $15.3^{+7.9}_{-6.4}$ Myr. The results are similar, both in the median value and in the associated scatter, to the estimates by Pecaut & Mamajek (2016).

With these caveats in mind, the possibility of computing individual age estimates for PMS stars with MADYS opens up important opportunities for the study of young star-forming regions, whose exquisite substructures are being more and more connected with their star formation history (e.g., Kerr et al. 2021; Krolikowski et al. 2021). An application of this very idea will constitute the subject of Chapter 4.

3.3.2 Stellar physical parameters

Although by construction MADYS is able to return age estimates for main-sequence stars, we stress that in this case they should be regarded as purely indicative. Nevertheless, the argument can be reversed: if external age constraints are available, MADYS can return precise determination of stellar parameters such as mass, effective temperature, radius and surface gravity for large samples of stars.

As an example of this possibility, we recovered from the literature a collection of stars with interferometrically measured angular diameters. Our sample combines the six main-sequence stars studied by Huber et al. (2012) and the full samples by Boyajian et al. (2012a,b), spanning a spectral range that stretches from A- to M-type. We combined angular measurements with the latest parallaxes from Gaia DR3 to have radius estimates with median precision $\sim 1\%$.

Our parameter estimates are based on PARSEC isochrones; we applied only a modest age constraint ($t \in [500, 7000]$ Myr); with respect to metallicity, we refer to [Fe/H] estimates from the original studies. Under the assumption [Fe/H] $\approx$[M/H], we used for each star the isochrone grid with the closest metallicity rather than interpolating [12].

The results are shown in Figure 3.4. The mean and standard deviation of the fractional difference between interferometric radii and those returned by MADYS are $+1\%$ and 6%, respectively.

3.3.3 Mass of directly imaged substellar companions

The systematic inter-model spread described for low-mass stars continues to exacerbate below the hydrogen-burning limit ($\sim 0.08 M_\odot$) which separates stars from brown dwarfs (Spiegel & Burrows 2012). Thanks to the development of high-contrast imaging facilities, young luminous brown dwarfs and giant exoplanets are being increasingly found both in isolation (Miret-Roig et al. 2022) and as companions to members of moving groups and associations (e.g., Vigan et al. 2021). In this case, a simultaneous isochronal estimate of age and mass is no more feasible, and independent constraints are needed to lift the degeneracy between age and mass. Given the importance of the derived properties of these young substellar objects, to study the low-mass end of the stellar initial mass function (IMF) on the one hand (e.g., Kirkpatrick et al. 2019), and exoplanet demographics on the other hand (e.g., Nielsen et al. 2019), it becomes a crucial task to compare the different predictions done by different models. In fortunate cases, mass estimates can be compared to model-independent dynamical masses, possibly disentangling among formation mechanisms (e.g., Marleau & Cumming 2014; Brandt et al. 2021a).

MADYS includes several models describing the luminosity evolution of young self-luminous gas giants and brown dwarfs. Mode 2 is precisely intended for objects that are not found in Gaia, such as objects discovered in direct imaging studies, either in isolation or as companions to stellar objects. In the latter case, MADYS can be used in two steps of the chain: to obtain the age of the stellar

[12] The available metallicities for this example were: [Fe/H] $= [-1.0, -0.75, -0.5, -0.25, 0.0, 0.13, 0.25, 0.5, 0.75, 1.00]$.

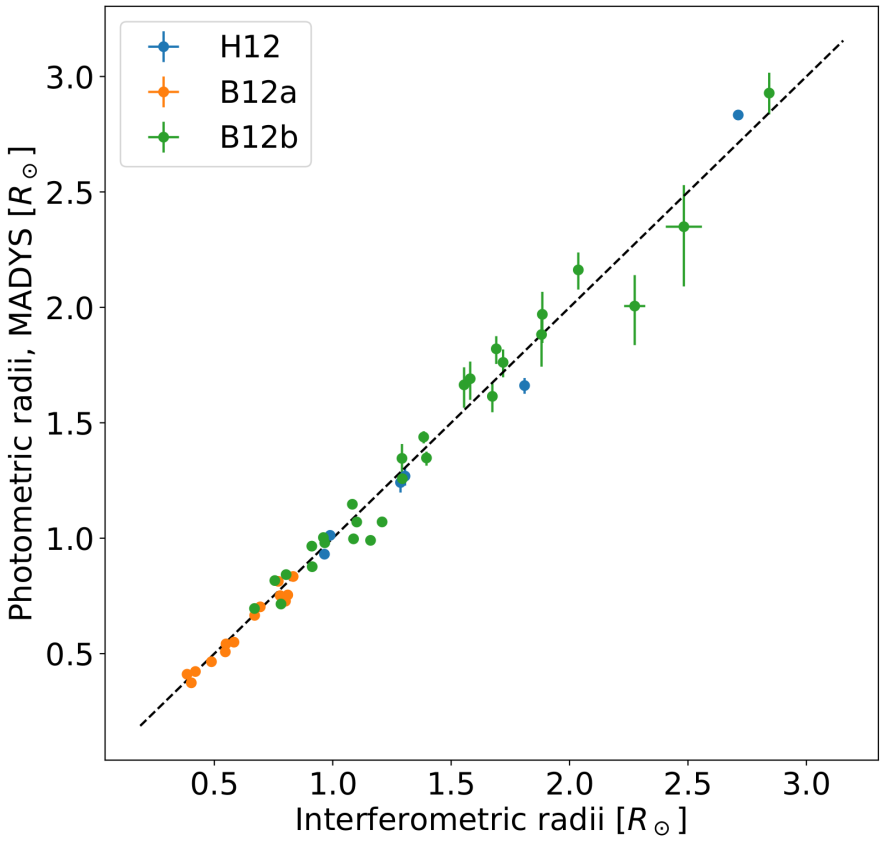

Figure 3.4: Comparison between photometric radius estimates obtained by MADYS and interferometric radii from the literature: Huber et al. (2012) (H12), Boyajian et al. (2012a) (B12a), Boyajian et al. (2012b) (B12b).

target – either directly or by exploiting its kinematic neighbors – and to use such information to derive a mass estimate for the companion. A combination of indirect kinematic constraints and literature data will be applied in Section 5.3 to derive age and mass estimates for both a stellar target of BEAST and its companions.

We present in this Section an application of MADYS to the HR 8799 system (Marois et al. 2008), one of the cornerstones of direct imaging studies. With four giant planets detected around a $1.47^{+0.11}_{-0.08} M_{\odot}$ primary (Wang et al. 2018), the system is a unique laboratory to test the accuracy of substellar evolutionary models.

Several age estimates have been derived for the system in the recent literature: $10 - 23$ Myr from Sepulveda & Bowler (2022), 33^{+7}_{-13} Myr from Baines et al. (2012) or 42^{+6}_{-4} Myr from Bell et al. (2015); we notice that the last estimate, based on the lithium-depletion boundary for the Colomba association which the star appears to be a member of, is independently indicated by MADYS when inspecting the kinematic neighborhood of the star. Indeed, we identified three stars[13] with projected separation < 3 pc and tangential velocity difference < 3 km s^{-1}: all of them have a best-fit mass $\in [0.7, 1] M_{\odot}$ and age ~ 40 Myr.

Nevertheless, we conservatively start from two possible age intervals, $t \in [10, 23]$ Myr and $t \in [30, 60]$ Myr, to compare our estimates with already published results. As a consequence of the uncertainty on age, we expect the model-dependent uncertainty on the derived photometric mass estimates to be broadened.

Table 3.4 reports literature estimates for the masses of the four planets, obtained with photometric or dynamical methods, together with new estimates obtained by MADYS. We collected contrasts measurements from Zurlo et al. (2016) in SPHERE bands J ($\lambda_{\rm peak} = 1.245$ μm), H_2 ($\lambda_{\rm peak} = 1.593$ μm), H_3 ($\lambda_{\rm peak} = 1.667$ μm), K_1 ($\lambda_{\rm peak} = 2.110$ μm) and K_2 ($\lambda_{\rm peak} = 2.251$ μm), and combined them to 2MASS magnitudes and Gaia DR3 parallax for HR 8799 to obtain absolute magnitudes.

Mass estimates were obtained through four models: namely, AMES-Dusty, AMES-Cond, ATMO2020 (in particular, the chemical equilibrium grid) and Sonora Bobcat [14].

The results are also summarized in Figure 3.5. While the results of photometric estimates can significantly differ from one another even in the same age window, tighter dynamical constraints[15] coming from thorough astrometric follow-up in the next few years will help distinguishing among them, shedding light into the still poorly constrained cooling timescale of young self-luminous Super Jupiters.

3.4 Published results based on MADYS

Besides the applications described in Chapters 2, 4 and 5.3, MADYS has been already used in several publications (Bonavita et al. 2022a,b, ;Raj et al. submitted).

Bonavita et al. (2022b) present multiple stellar systems incidentally discovered during the planet-hunting SHINE survey. Despite removal of known stellar companions within $s < 5.5''$ from their

[13] Gaia EDR3 2838213864935858816, Gaia EDR3 2835796794780262912 and Gaia EDR3 2830197806693622272.

[14] For ATMO2020 and Sonora Bobcat, which currently lack SPHERE filters, we employed theoretical magnitudes in the closest photometric system available: the Mauna Kea Observatories photometric system (MKO, Tokunaga et al. 2002), and 2MASS, respectively. In particular, $J_{\rm SPHERE} \sim J_{\rm MKO} \sim J_{\rm 2MASS}$, $K_{\rm SPHERE} \sim K_{\rm MKO} \sim K_{s,\rm 2MASS}$, $0.5 \cdot (H_{2,\rm SPHERE} + H_{3,\rm SPHERE}) \sim H_{\rm MKO} \sim H_{\rm 2MASS}$.

[15] The small errorbar of the dynamical mass estimates by Goździewski & Migaszewski (2020) is a consequence of the assumption that the planets are in an exact 8:4:2:1 mean-motion resonance, and should therefore be taken with caution.

Table 3.4: Mass estimates for the planets in the HR 8799 system. We compare the best-fit results from MADYS with photometric (p) and dynamical (d) masses taken from the literature. Two age ranges ($t \in 10-23$ Myr, $t \in 30-60$ Myr) and four models (D: Ames-Dusty; A: ATMO2020; C: Ames-COND; S: Sonora Bobcat) are used for the independent estimates.

source	age Myr	b M_J	c M_J	d M_J	e M_J	method
Marois et al. (2008)	$30-60$	$5-7$	$7-10$	$7-10$	$7-10$	p
Wilner et al. (2018)	—	$5.8^{+7.9}_{-3.1}$	—	—	—	d
Wang et al. (2018)	42 ± 5	5.8 ± 0.5	$7.2^{+0.6}_{-0.7}$	$7.2^{+0.6}_{-0.7}$	$7.2^{+0.6}_{-0.7}$	p
Goździewski & Migaszewski (2020)		5.7 ± 0.4	7.8 ± 0.5	9.1 ± 0.2	7.4 ± 0.6	d
Brandt et al. (2021b)	42^{+24}_{-16}	—	—	—	$9.6^{+1.8}_{-1.9}$	d
Sepulveda & Bowler (2022)	$10-23$	$2.7-4.9$	$4.1-7.0$	$4.1-7.0$	$4.1-7.0$	p
Zurlo et al. (2022)	—	$5.54-6.20$	$6.84-8.10$	$9.07-10.05$	$7.11-10.66$	d
MADYS	$10-23$	$6.9^{+0.9}_{-1.2}$	$7.8^{+1.0}_{-1.3}$	$7.5^{+1.0}_{-1.3}$	$7.9^{+1.0}_{-1.3}$	D
	$30-60$	$10.7^{+0.4}_{-1.1}$	$11.3^{+0.3}_{-0.6}$	$11.1^{+0.4}_{-0.8}$	$11.4^{+0.3}_{-0.6}$	D
	$10-23$	$3.8^{+0.5}_{-0.7}$	$6.9^{+0.9}_{-1.2}$	$7.5^{+1.0}_{-1.4}$	$7.2^{+1.0}_{-1.3}$	A
	$30-60$	$6.5^{+0.9}_{-1.0}$	$10.9^{+0.8}_{-1.2}$	$11.4^{+0.5}_{-1.0}$	$11.2^{+0.6}_{-1.1}$	A
	$10-23$	$4.0^{+0.6}_{-0.8}$	$5.8^{+0.9}_{-1.1}$	$6.0^{+1.0}_{-1.1}$	$6.1^{+1.0}_{-1.1}$	C
	$30-60$	$7.0^{+0.9}_{-1.0}$	$9.9^{+0.8}_{-1.3}$	$10.1^{+0.6}_{-1.4}$	$10.4^{+0.5}_{-1.4}$	C
	$10-23$	$4.5^{+0.7}_{-0.8}$	$7.2^{+1.0}_{-1.1}$	$7.7^{+1.0}_{-1.1}$	$7.5^{+1.0}_{-1.1}$	S
	$30-60$	$7.5^{+0.8}_{-1.1}$	$11.0^{+0.6}_{-1.0}$	$11.3^{+0.4}_{-0.8}$	$11.2^{+0.5}_{-0.9}$	S

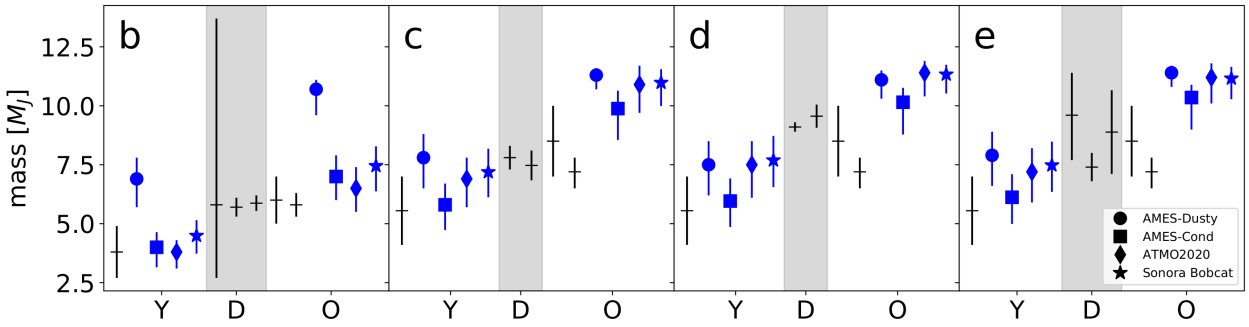

Figure 3.5: Literature (black) and new (blue) mass estimates for the HR 8799 planets. Each panel refers to the eponymous planet. For the sake of clarity, dynamical estimates (D) have been placed in the gray region, which visually separates the estimates based on a younger (10-23 Myr) age (Y) from those estimates based on an older (30-60 Myr) age (O). Different symbols for MADYS estimates refer to different models.

primaries, 78 out of 463 systems turned out to possess at least one unknown stellar companion; 56 systems are newly discovered – the remaining having either escaped the vetting process or found by other studies to be multiple after the beginning of SHINE; 21 systems are triple or with higher multiplicity. After compensating for the bias against binaries and restricting the analysis to a mass ratio regime which is virtually complete ($0.05 < q < 0.5$) and a separation range 5 au $< s <$ 40 au, we found a slightly higher binary frequency (14.2±2.9% vs 11%) than in previous studies (Duquennoy & Mayor 1991; Raghavan et al. 2010), and a two-peaked mass ratio distribution showing an excess of equal-mass binaries.

Orbital parameters could be derived for 25 systems by combining SPHERE observations with literature data. Interestingly enough, for the 12 targets having rotational periods measured by the Transiting Exoplanet Survey Satellite (TESS; Ricker et al. 2015), the comparison between the observed $V \sin i$ and the predicted values assuming the alignment between stellar and orbital axes is generally good: this tentative result hints toward an in-disk formation of the companions, as predicted by gravitational instability (Section 1.5.2).

As it might be expected, the derivation of stellar masses constituted a crucial step of the work: starting from age constraints related to the membership to moving groups and/or to indirect age indicators, MADYS was consistently applied to the whole stellar sample (primaries and companions), combining absolute photometry from 2MASS with SPHERE contrasts. We employed BT-Settl models for stars with $M < 1.4 M_{\odot}$, and the empirical tables by Pecaut & Mamajek (2013, PM13 in Table 3.3) for more massive stars. For the systems with a full orbital characterization, the comparison between model-free dynamical masses and photometric masses obtained by MADYS was excellent, the estimates being almost always consistent within errors (Figure 3.6).

A targeted search for companions was the purpose of the COPAINS Pilot Survey (Bonavita et al. 2022a), a SPHERE survey addressing targets with a significant proper motion difference ($\Delta\mu$) between different astrometric catalogs, indication of the possible presence of unseen companions. Indeed, the study resulted in an extraordinarily high yield of ten companions (including four brown dwarfs) out of a sample comprising only 25 stars. Again, the comparison between photometric and dynamical masses – computed assuming circular face-on orbits – shows a very good agreement (Figure 3.7).

3.5 Discussion

Since the algorithm behind age determination in MADYS is based on isochronal fitting, the tool automatically inherits the same drawbacks of this technique, which have been the subject of extensive discussion in the literature (see, e.g., Soderblom 2010; Barrado 2016).

In particular, MADYS alone cannot be used to understand if a star is young ($t \lesssim 100$ Myr) or not: a degeneracy exists between young PMS stars and evolved stars that have left the MS, and this is naturally reflected into different families of solutions that arise if the age is left completely unconstrained. A young solution is to be preferred if independent youth indicators (e.g., activity indicators such as X-ray, UV, H_{α} emission) are available.

A conceptually different youth indicator is the membership to a young star-forming region. Indeed, the integration of kinematic information into MADYS will be the subject of a second version of the tool. For the moment being, MADYS can exploit existing lists of confirmed members of these regions to unveil correlations between the star formation history and kinematic substructures (see Chapter 4).

A strong asset of MADYS is the ability to collect and handle photometric data for thousands of

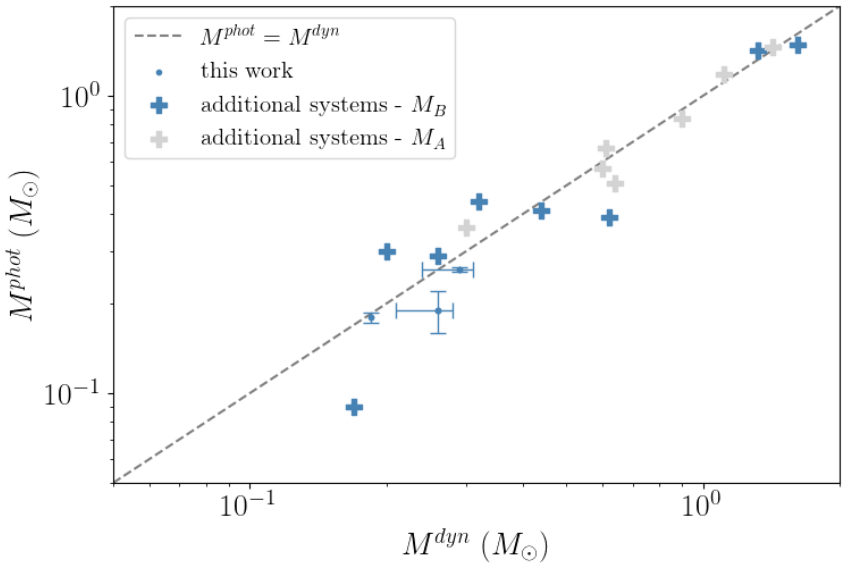

Figure 3.6: Comparison between dynamical masses (M^{dyn}) and photometric masses (M^{phot}) for the companions for which a dynamical mass estimate was possible (blue dots), and for primaries and secondaries for which an orbital solution was obtained by Tokovinin & Briceño (2018). Source: Bonavita et al. (2022b).

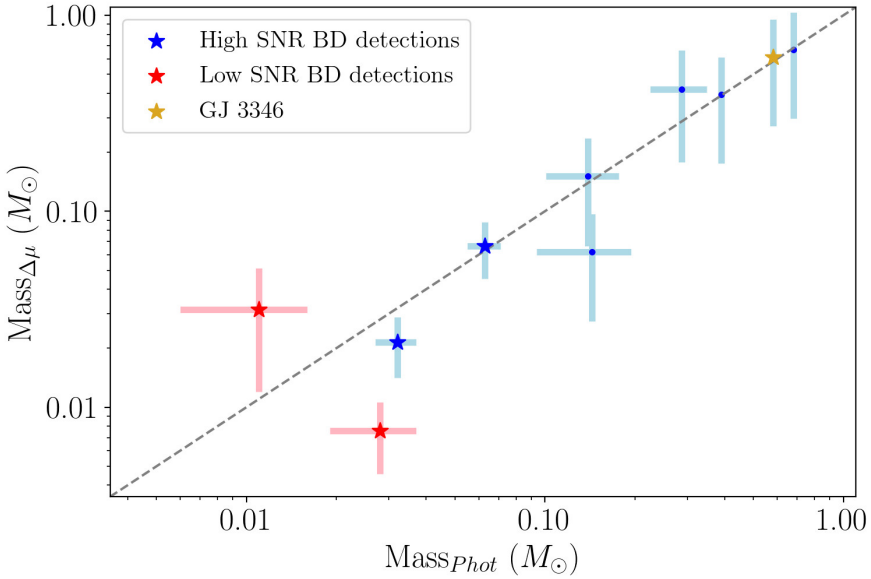

Figure 3.7: Comparison between dynamical masses ($Mass_{\Delta\mu}$) and photometric masses ($Mass_{Phot}$) for the companions detected in the COPAINS survey. MADYS estimates are based on the Ames-COND models. Source: Bonavita et al. (2022a).

stars. The age determination is rapid, taking about one second per star under typical conditions. In this sense, our tool constitutes a step forward in the automation of the process with respect to existing tools such as `PARAM` (Rodrigues et al. 2017), `ARIADNE` (Vines & Jenkins 2022), `stardate` (Angus et al. 2019) or `isochrones` (Morton 2015); on the other hand, unlike them, it does not currently allow one to exploit additional information coming, for instance, from asteroseismology or spectroscopy during the fitting process.

A second strength of MADYS is the possibility to employ a large collection of stellar and substellar models, allowing the possibility to evaluate the impact of different input physics into the final results. This is particularly important not only for the PMS phase of stars, but also in the context of direct imaging studies of cooling substellar objects, where there is still no established standard on how photometric mass determinations are to be obtained.

3.6 Conclusions

With an eye on the study of star-forming regions and the other on directly imaged substellar objects, we developed the Manifold Age Determination of Young Stars (MADYS): a Python tool aimed at obtaining photometric age and mass estimates for arbitrarily large groups of young stellar or substellar objects. The main strengths of the tool are:

- the ability to query and crossmatch different catalogs to yield highly reliable catalogs of potentially large lists of objects;
- the possibility to take interstellar extinction into account;
- the ability to derive photometric ages and mass estimates by comparing dozens of filters with a large suite of substellar or stellar evolutionary models;
- the possibility to unambiguously compare the predictions of different models, and to see the effect of changing astrophysical parameters;
- the large plotting options for efficient data visualization.

These features give MADYS a large number of possible scientific applications, such as:

- the study of young star-forming regions, connecting kinematic data with age determinations;
- direct-imaging studies, including forthcoming JWST observations. Even in the case of a non-detection, the tool can be useful to turn contrast limit into mass limits, paving the way to a systematic assessment of the demographics of direct-imaged exoplanets and brown dwarfs.

Besides the inclusion of new models and filters, future developments of MADYS will include the possibility to do the following: simultaneously deriving extinction and (sub)stellar parameters under the current optimization scheme; implementing an indirect method for age determination based on empirical kinematic properties; and, finally, providing a systematic comparison of isochronal and kinematic results with those obtained through other age determination techniques.

Chapter 4

The star formation history of Upper Scorpius

In Chapter 3 we have introduced MADYS and its large variety of possible scientific applications. In the context of BEAST, the tool was applied to derive indirect age estimates for the stellar targets, as described in Chapter 2.

The underlying assumption behind our approach is that a similarity in motion within a group of stars reflects a common origin. This is particularly true for associations, whose low densities ensure that the initial velocity structure can be conserved over the several Myr before being irremediably altered by the galactic tidal field (Wright & Mamajek 2018). We decided therefore to investigate whether kinematic substructures could still be discerned nowadays in Sco-Cen, and if we could use our present knowledge of the association to constrain its history. In this Chapter I will describe the results of this effort, summarized in a dedicated scientific paper (Squicciarini et al. 2021), that justifies and reinforces the approach employed throughout this dissertation; Section 5.3 will show how important the membership of the planet-host μ^2 Scorpii to a small kinematic group within Sco-Cen is to ensure a precise and accurate characterization of the system.

After defining the selection criteria for our sample of US stars, together with the astrometric, kinematic and photometric data (Section 4.2), we apply MADYS to the region to recover and characterize the dual kinematic substructure found within the association (Section 4.3). Section 4.4 is dedicated to the age determination of clustered and diffuse populations, conducted in a threefold way. In Section 4.5, we discuss our results within the framework of previous studies of the region, with particular emphasis on its star formation history. Finally, in Section 4.6 we provide a brief summary of the results of this Chapter. Appendix 4.A and 4.B explore in greater detail two quantities introduced to correctly handle data coming from Gaia: namely, a quality cut defined to exclude unreliable G_{BP} and G_{RP} photometric measurements and a set of corrections to remove the fraction of individual proper motions due to the reflection of the relative motion of US with respect to the Sun.

4.1 Scientific context

It has long been known (Ambartsumian 1954) that, following the collapse and fragmentation of gigantic structures called *molecular clouds*, a plethora of stars (N = 10 to 10^5) begins to form; initially concealed by the same dusty envelope which they are born from, they rapidly (2-7 Myr; Kim et al. 2021) divest themselves of it by means of harsh stellar winds and ionising radiation, mostly

originating from massive stars; HII regions, the impressive product of the irremediable alteration of the original cloud, are ruthlessly sculpted by the injection of energy and momentum from exploding supernovae (Barnes et al. 2020); after just a few Myr, the region is virtually devoid of its original gas reservoir (Kroupa et al. 2001). The abrupt change within stellar natal environment is proven by observations showing that, while at $t < 5$ Myr stars are often still embedded in their parent cloud, after 10 Myr only $\sim 10\%$ of stars are found in bound clusters (Lada & Lada 2003). What we witness as an *association* for just – in cosmic terms – the blink of an eye (10-100 Myr, Moraux 2016), is therefore a young system, still dwelt by bright ephemeral OB stars and regions of active stellar formation (Kroupa et al. 2001).

The kinematic signature of members of clusters and associations, first recognized in the Hyades cluster and in Ursa Major already in the 19th century (Proctor 1869), is slowly eroded as the galactic differential rotation and tides spread the stars, turning them into moving groups or streams (Larson 2002). Given that the observed densities of associations are too low to give rise to significant close encounters and scatterings, their initial velocity structure can largely be conserved over the timescale of several Myr (Wright & Mamajek 2018), as the above-mentioned perturbation induced by the galactic tidal field is expected to begin dominating on timescales of $\sim 10^7$ yr (Wright & Mamajek 2018). If this is the case, we might think to use our present knowledge of an association to delve into its past. The first attempt in this direction was done by Blaauw (1946, 1964), who devised a simple linear expansion model, where all the sibling stars move away at a constant pace from their natal position. By tracing back their motion, it is in principle possible to obtain an estimate of the association age in a way that is independent of stellar evolution models. However, a quantitative assessment of the expansion model has long been considered elusive due to difficulties, on the one hand, in distinguishing real members from interlopers and, on the other hand, to obtain precise measurements of stellar distances and motions. This is why the idea has largely been shelved for decades (Brown et al. 1997), even though the notion of OB associations as the inflated outcome of compact clusters kept being popular (Lada & Lada 2003).

Ultra-precise astrometry from Gaia has been revolutionising our knowledge of the Galaxy. Especially when combined with radial velocities from external catalogues, Gaia is able to delve deeper than ever into the core of association architectures, unearthing exquisite fragments of their history. Some examples include the Gamma Velorum cluster, showing two distinct kinematic components (Jeffries et al. 2014), Taurus (Kraus et al. 2017), Cygnus OB2 and its complex substructures (Wright et al. 2016), and even smaller structures like the TWA moving group (Ducourant et al. 2014). OB associations, in particular, are spectacularly confirming the expectation that their kinematic substructure is reminiscent of its initial structure (e.g., Larson 1981; Wright et al. 2016). The same complexity emerges when studying the geometry and the internal motion of molecular clouds (Falgarone et al. 1991; Hacar et al. 2013): starting from structure analysis of prestellar cores (Ladjelate et al. 2020) and from the variegated shapes taken by filaments and filamentary networks in the early phase of stellar formation (Hacar et al. 2018; Hoemann et al. 2021) that give rise to distinct stellar populations (e.g., Arzoumanian et al. 2019), it is natural to think that the complex, fractal structure is inherited by young stars (Elmegreen & Elmegreen 2001; Gutermuth et al. 2008).

Focusing our attention to Sco-Cen, it has long been known that its star formation history is closely related to its spatial structure. As already mentioned in Section 2.2, Sco-Cen is classically divided into three main subgroups (Blaauw 1946; de Zeeuw et al. 1999): going toward lower galactic longitude, Upper Scorpius (US), Upper Centaurus-Lupus (UCL) and Lower Centaurus-Crux (LCC). Both density and age have a spatial gradient, with US being more compact and younger than UCL and LCC (Pecaut & Mamajek 2016). This intriguing observation led Preibisch & Zinnecker (1999) to put forward the idea of a triggered star formation, where the process, started in LCC,

gradually expanded eastward by means of supernova shocks, causing star formation in US after some Myr. The same US is thought to have triggered a minor burst of star formation in the ρ Ophiuchi complex, which is still ongoing (Wilking et al. 2008). However, the picture is complicate, and the three subgroups appear composed of many smaller entities, each bearing a peculiar mark while being conditioned by feedback from the surrounding environment (Wright & Mamajek 2018). This tension between nature and nurture has given renovated impulse to the idea of investigating the substructure of the three subgroups to gain knowledge into their star formation histories.

The presence of at least a certain degree of substructure is evident even to visual inspection in the youngest part of Sco-Cen, US. This rather compact ($98\times24\times18$ pc^3, Galli et al. 2018) region of Sco-Cen, home to the bright Antares (Ohnaka et al. 2013), received a great attention on its own due to the interplay of kinematic and age peculiarities. Notably, a consistent age determination for US has long been elusive. While the first photometric studies argued for an age of ~ 5 Myr with no significant spatial and temporal spread (Preibisch & Zinnecker 1999; Preibisch et al. 2002), recent work has been increasingly prone to an older age ($t \sim 11$ Myr) with a significant spread ($\Delta t \sim 7$ Myr, Pecaut et al. 2012); the debate on the dependence of the latter on position (Pecaut & Mamajek 2016), spectral class (Rizzuto et al. 2016), systematic artefacts due to stellar models (Feiden 2016a) or an extended star formation history (Fang et al. 2017) has been vivid in recent years.

In this context, insight from kinematic studies are pivotal to shed light on the problem. While the first studies, limited to few bright members, could not but aim at assessing a single common expansion age (Blaauw 1978) – a solid lower limit of ~ 10 Myr, in this regard, was put by Pecaut et al. (2012) –, nowadays we do have the means to investigate the whole kinematic substructure of US.

4.2 Data

4.2.1 Sample selection

Motivated by the idea of exploiting the full potential of the latest Gaia release (EDR3, Gaia Collaboration et al. 2021), we decided to construct a novel sample of US sources, independent from the DR2-based samples already present in the literature (e.g., Luhman & Esplin 2020). A preliminary deep query was done in a region virtually encompassing the whole Upper Scorpius, employing just minimal cuts on astrometry (α, δ, ϖ) and kinematics ($\mu^*_\alpha = \mu_\alpha \cdot \cos(\delta)$, μ_δ) to exclude stars either from the field or belonging to the nearby Upper Centaurus-Lupus (UCL) subgroup (Table 4.1.). No attempt has been done to remove, as many previous studies, sources belonging to the nearby Rho Ophiuchi region (from this moment on, ρ Ophiuchi) since we intend to explore in detail its relation with the bulk of US. We will simply refer to our sample as *US*.

Membership to US has been defined operationally, by inspecting the 5D phase space $(\alpha, \delta, \varpi, v_\alpha, v_\delta)$, with

$$v_\alpha \text{ [km s}^{-1}] = A \cdot \mu^*_\alpha / \varpi \tag{4.1}$$

$$v_\delta \text{ [km s}^{-1}] = A \cdot \mu_\delta / \varpi \tag{4.2}$$

with $A = 4.74$ km yr s^{-1} being the conversion factor between AU yr^{-1} and km yr s^{-1}. The line of sight velocities v_α and v_δ are more suitable than proper motion components in a region of non-negligible radial depth ($\Delta r \sim 50$ pc) and with parallax uncertainties no more as limiting as it was in the pre-Gaia era.

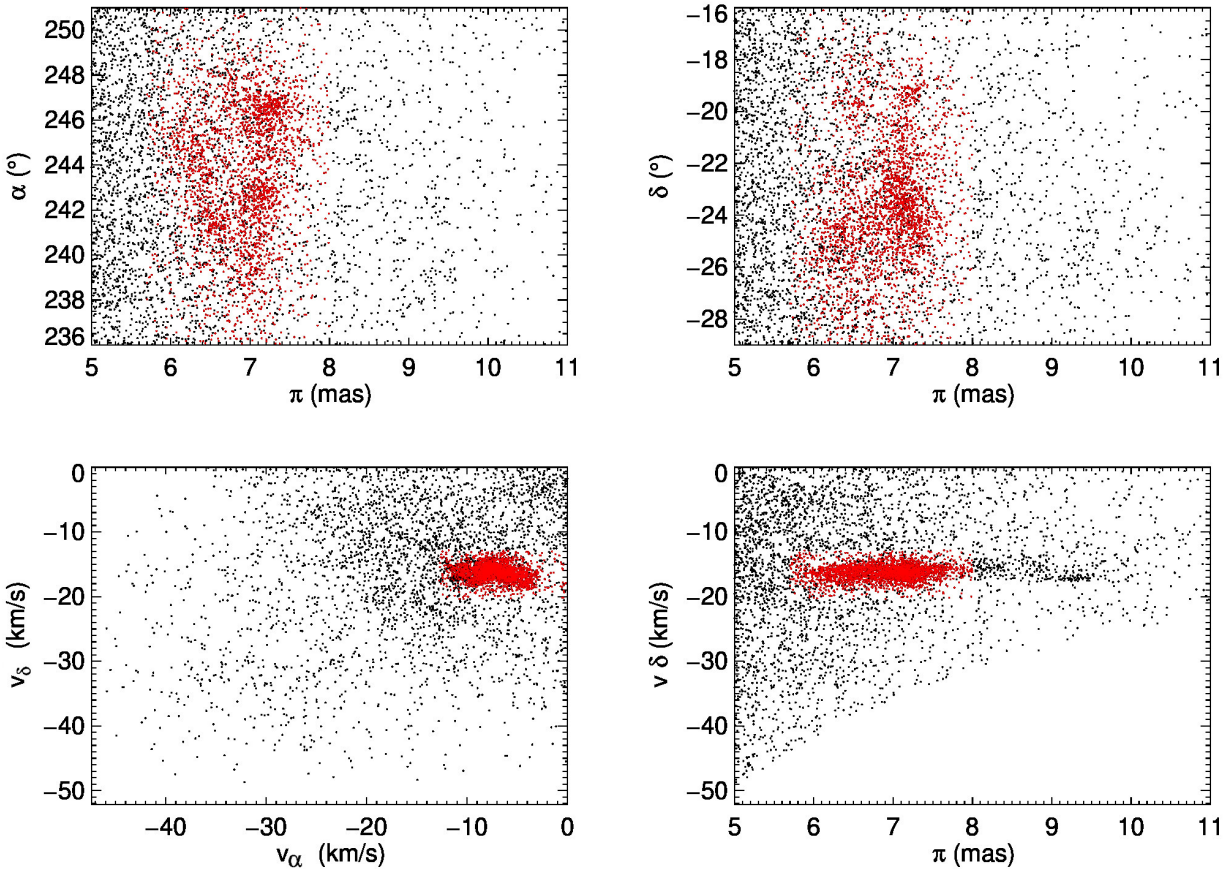

Figure 4.1: Detection of US (red) within the 5D phase space. Only field stars (black) with $236° < \alpha < 251°$, $-29° < \delta < -16°$, $G < 20$ mag and $\sigma_\varpi/\varpi < 0.1$ are shown for the sake of clarity.

A clear concentration of sources emerges, distinguishing US from the field (Figure 4.1). A comparison with an independent sample, the DR2-based catalogue of Sco-Cen members by Damiani et al. (2019)[1], yielded excellent agreement: out of their 2330 stars, 2129 ($\sim 91\%$) were recovered; the fraction would have risen to 2298/2330 ($\sim 98\%$), if we employed their same cut on minimum distance ($\varpi < 10$ mas). However, we opted for a more conservative $\varpi < 8$ mas not to detrimentally affect field contamination.

We consider those stars – the only additional caveats being $G < 20$ and $\sigma_\varpi/\varpi < 0.1$ – as our final sample (which we will call *2D sample*). The complete set of defining criteria are summarized in Table 4.1, while the sky distribution of the sample, comprising 2745 stars, is shown in Figure 4.2.

4.2.2 Radial velocities

An unbiased analysis of an extended region on the sky cannot be achieved, due to projection effects, without a full knowledge of the 6D phase space of its members: radial velocities (RV) are crucial not only to identify interlopers but also, more importantly, to correctly analyze stellar motions (see

[1] Actually, with the subsample defined by the same cuts on α and δ as our sample in order to exclude UCL members. Only their *bona fide* members were considered.

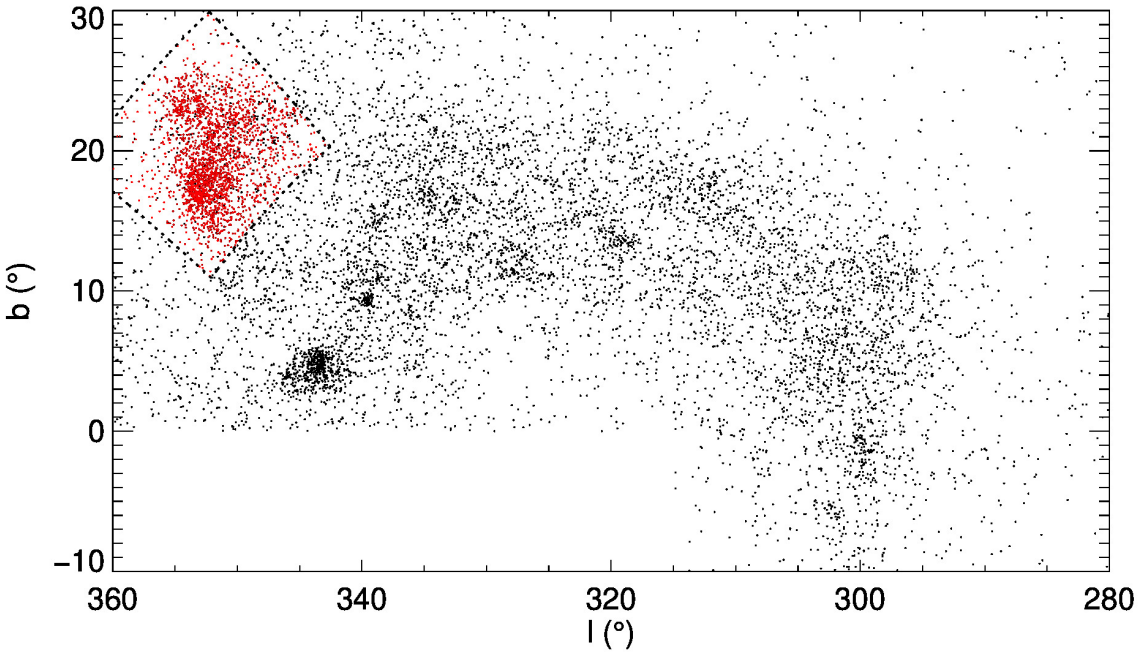

Figure 4.2: Sco-Cen bona fide members from Damiani et al. (2019), shown in black. Upper Scorpius can easily be distinguished in the upper left. The sample used throughout this Chapter and defined by the cuts of Table 4.1 is displayed in red. The criteria on right ascension and declination define the region bordered by the dashed lines.

Table 4.1: Criteria for the selection of the 2D sample. Coordinates and proper motions are referred – as usual for Gaia EDR3 – to the ICRS at epoch J2016.0.

Initial query	
Query position (α_0, δ_0)	$(245°, -25°)$
Query radius (°)	20
Parallax (mas)	$5 < \varpi < 11$
Proper motion along α (mas yr^{-1})	$-50 < \mu^*_\alpha < 0$
Proper motion along δ (mas yr^{-1})	$-53 < \mu^*_\delta < 0$
No. of sources	408465
Final criteria	
Right ascension (°)	$236 < \alpha < 251$
Declination (°)	$-29 < \delta < -16$
Parallax (mas)	$5.7 < \varpi < 8$
Parallax error	$\sigma_\varpi/\varpi < 0.1$
Velocity along α (km s^{-1})	$v_\alpha > -12.8$
Velocity along δ (km s^{-1})	$-20.4 < v_\delta < -12.8$
Apparent G magnitude (mag)	$G < 20$
No. of sources	2745

Appendix 4.B for details).

A complete analysis in the 6D phase space has been performed on the subsample possessing reliable RV measurements. In addition to Gaia EDR3, we collected data from APOGEE DR16 (Ahumada et al. 2020) and GALAH DR3 (Buder et al. 2021); whenever multiple measurements were present, the datum with the smallest error bar was chosen. After selecting sources with a relative error on RV < 0.1 or an absolute error < 1 km s^{-1}, we defined the Cartesian frame (x, y, z):

$$\begin{cases} x = r\ \cos(\delta - \delta_P)\ \sin(\alpha - \alpha_P) \\ y = r\ \cos(\delta - \delta_P)\ \cos(\alpha - \alpha_P) \\ z = r\ \sin(\delta - \delta_P) \end{cases} \tag{4.3}$$

where the pole $(\alpha_P, \delta_P) = (243.09°, -23.03°)$ points, for convenience, toward the mean equatorial coordinates of the sample. Finally, we restricted only to sources with propagated errors on v_x, v_y and v_z simultaneously satisfying the three conditions[2]:

- $|\sigma_{v_x}/v_x| < 0.1 \quad \text{OR} \quad \sigma_{v_x} < 0.1$ pc Myr^{-1},
- $|\sigma_{v_y}/v_y| < 0.1 \quad \text{OR} \quad \sigma_{v_y} < 0.1$ pc Myr^{-1},
- $|\sigma_{v_z}/v_z| < 0.1 \quad \text{OR} \quad \sigma_{v_z} < 0.1$ pc Myr^{-1}.

The final RV sample (*3D sample*) comprises 771 stars, $\sim 28\%$ of the 2D sample (Table 4.2).

Although we decided not to appoint the 3D sample as our main focus, because it only imperfectly reproduces the real distribution of sources[3], we will employ it in a twofold way: on the one hand, it will provide us with a way to quantify the effect of the association's mean motion with respect to

[2] 1 km s^{-1} = 1.02 pc Myr^{-1}.

[3] The distribution of sources possessing RV does not appear as a random pick of the Gaia sample, but rather – as expected – as the union of distinct surveyed regions.

Table 4.2: Median uncertainties on astrometry and kinematics for the 2D and 3D samples.

2D sample		3D sample	
No. of sources	2745	No. of sources	771
Median σ_{ϖ} (mas)	0.06	Median σ_x (pc)	0.03
Median $\sigma_{\mu^*_\alpha}$ (mas yr^{-1})	0.07	Median σ_y (pc)	0.82
Median σ_{μ_δ} (mas yr^{-1})	0.05	Median σ_z (pc)	0.03
Median σ_{v_α} (km s^{-1})	0.08	Median σ_{v_x} (pc Myr^{-1})	0.05
Median σ_{v_δ} (km s^{-1})	0.14	Median σ_{v_y} (pc Myr^{-1})	0.04
		Median σ_{v_z} (pc Myr^{-1})	0.10

the Sun (which we will call, from this moment on, *bulk motion*); on the other hand, it will offer a constant comparison with the 2D sample to check the validity of our results: by comparing, whenever possible, features observed in 2D with their 3D counterparts, we are able to rule out the possibility of a random alignment of sources lying at different distances, i.e. a perspective effect.

As regards the former aspect, a simple geometrical argument proves that, taken a group of stars, the knowledge of their proper motions alone is not sufficient to disentangle between a real expansion and a nonzero mean radial motion with respect to the line of sight through its centre, i.e. a *virtual expansion* (see discussion in de Zeeuw et al. 1999). Transverse motions, too, are split up into velocity components depending on (α, δ, ϖ). Thus, any nonzero bulk motion will manifest itself as a bias in the kinematic reconstruction.

Once having estimated that the centre of the 3D sample approximately lies at $(\alpha_c, \delta_c, r_c) = (244.55°, -23.79°, 143.3$ pc), we computed the mean velocity components in a Cartesian frame centred on it. Expressed in the standard right-handed Cartesian Galactic frame, our 3D sample has median velocity components $(U, V, W) = (-4.788 \pm 0.019, -16.378 \pm 0.015, -6.849 \pm 0.016)$ km s^{-1}, with a precision gain of almost one order of magnitude relative to previous estimates (Luhman & Mamajek 2012; Galli et al. 2018). Finally, we determined the projections of this bulk motion on the proper motions of each star of the 2D sample, and subtracted them (see Appendix 4.B for details). We verified that, due to the angular extent of US, this bias does not significantly affect the shape of the substructures nor the timing of their maximum spatial concentration.

Even correcting for bulk motion, a similar (although smaller) projection effect keeps affecting individual stellar velocities, due to the rotation of the $(v_\alpha, v_\delta, v_r)$ plane with (α, δ). Again, the angular extent of the association is not too big to hinder the approach altogether[4].

4.2.3 Photometry

Whereas astrometric and kinematic data were gathered from Gaia EDR3, the photometry comes from Gaia DR2 (Gaia Collaboration et al. 2018b): the reason is that the set of isochrones that we used relies on Gaia DR2, and the filter response is not exactly the same between the two releases[5]. As G_{BP} and G_{RP} photometry can be severely contaminated by the background at faint magnitudes (Busso et al. 2021), a quality cut was needed to discriminate whether G_{BP} and G_{RP} magnitudes

[4]. Choosing a fixed Cartesian $(\hat{x}, \hat{y}, \hat{z})$ frame around a star defined by $(\alpha_0, \delta_0, \varpi_0, v_{\alpha,0}, v_{\delta,0}, v_{r,0})$ such that $\hat{x} \parallel v_{\alpha,0}$, $\hat{y} \parallel v_{r,0}$ and $\hat{z} \parallel v_{\delta,0}$, the mixing between velocity components for a second star having $(\alpha_1 = \alpha_0 + 10°, \delta_1 = \delta_0 + 10°, \varpi_1, v_{\alpha,1}, v_{\delta,1}, v_{r,1})$ is such that $v_x = 0.985v_{\alpha,1} - 0.030v_{\delta,1} + 0.171v_{r,1}$, $v_y = -0.174v_{\alpha,1} - 0.171v_{\delta,1} + 0.970v_{r,1}$, $v_z = 0.985v_{\delta,1} + 0.174v_{r,1}$.

[5]We verified that, for our initial sample of 408465 sources, G_{BP} magnitudes are on average 0.3 mag dimmer in EDR3.

could be considered reliable or not. Following the line of reasoning by Riello et al. (2021), a color-independent *BP-RP excess factor* C^* was defined, starting from the available bp_rp_excess_factor C:

$$C^* - C = \begin{cases} a_0 + a_1\Delta G + a_2\Delta G^2 + a_4 G & \Delta G < 0.5 \\ a_0 + a_1\Delta G + a_2\Delta G^2 + a_3\Delta G^3 + a_4 G & 0.5 \leq \Delta G < 3.5 \\ a_0 + a_1\Delta G + a_4 G & \Delta G \geq 3.5 \end{cases} \tag{4.4}$$

where $\Delta G = (G_{BP} - G_{RP})$; the distribution of C^* peaks at about 0 for well-behaved sources at all magnitudes but, when considering subsamples of stars with similar brightness, it tends to widen out for fainter G; a varying standard deviation $\sigma_{C^*}(G)$ can be defined as:

$$\sigma_{C^*}(G) = k_1 + k_2 \times G^{k_3} \tag{4.5}$$

Setting a rejection threshold at 3σ, we labelled 889/2745 sources (32%) as having unreliable (G_{BP}, G_{RP}) magnitudes; the effect is larger, as expected, at fainter ($G \gtrsim 15$) magnitudes. Details on the derivation of C^* and σ_{C^*}, as well as the numerical values of the constants of Eq. 4.4- 4.5 can be found in Appendix 4.A.

Infrared measurements from 2MASS (Skrutskie et al. 2006) were gathered and cross-matched with Gaia magnitudes, by inspecting the radial distance r between nearby Gaia and 2MASS sources. About 96% of the source pairs have $r < 0.7''$, so this value was chosen to establish whether a pair actually referred to the *same* source. Only measurements labelled by the best quality flag ("A") were used.

In order to study the fraction of disk-bearing stars, additional photometric data were collected from WISE (Wright et al. 2010) and ALLWISE (Cutri et al. 2021). If simultaneously present, ALLWISE magnitudes were preferred over WISE data. As with 2MASS data, only measurements with the best quality flag ("0") were employed; measurements with $W1 < 8.1$ mag, $W2 < 6.7$ mag, $W3 < 3.8$ mag and $W4 < -0.4$ mag were not considered, due to saturation problems at bright magnitudes (Cutri et al. 2012). The effect of flux contamination from nearby sources, increasingly affecting surveys with longer wavelengths, will be assessed in Section 4.4.3.

4.2.4 Extinction

Despite the proximity of the region, interstellar extinction is not to be overlooked: the youngest region here studied, the ρ Ophiuchi cloud, can reach $A_V \sim 40 - 50$ mag in its core (Wilking & Lada 1983), preventing detection of its embedded protostars (Grasser et al. 2021) in optical surveys, while the corners of the association hardly reach $A_V \approx 0.2$ mag. In order to take such intrinsic spatial variability into account, the absolute photometry of each star was corrected via the interstellar extinction map by Leike et al. (2020). The resolution of the map is 1 pc, which at $d \sim 140$ pc typically translates into an angular resolution $\Delta\theta = 0.4°$, comparable to the extent of the largest molecular clouds within ρ Ophiuchi (Rigliaco et al. 2016). The provided G-band extinction was converted, case by case, to the appropriate band using a total-to-selective absorption ratio $R = 3.16$ and extinction coefficients A_λ taken from Wang & Chen (2019). A sketch of the integrated G-band extinction at a constant distance of $d = 160$ pc is shown in Figure 4.3.

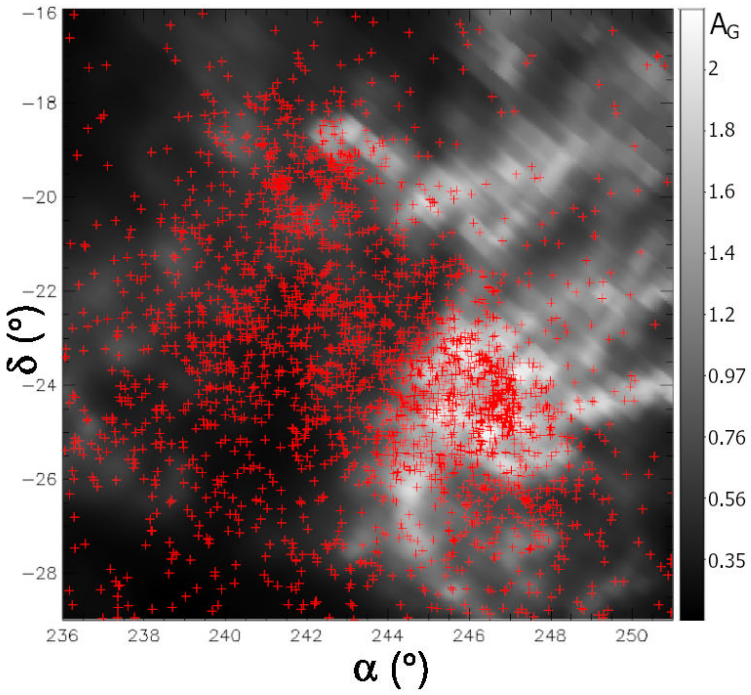

Figure 4.3: Line of sight G-band extinction (mag) in the direction of US. The 2D sample is overplotted in red. The values, derived from the map by Leike et al. (2020), are computed for simplicity at a fixed $d = 160$ pc, encompassing $\sim 90\%$ of the sample.

4.3 Analysis

4.3.1 Kinematic subgroups

As hinted in the previous sections, our method works by tracing back the celestial coordinates of the 2D sample on the basis of their present μ_α and μ_δ, under the assumption that dynamical interactions among members are negligible. The inspection of the time evolution of the sample[6] in the (α, δ) plane suggests that a wealth of information is still encapsulated beneath the present structure of US: the sight of different parts of the association, clustering at different times in the past, was what encouraged us to tentatively distinguish subgroups based on a purely kinematic way (Figure 4.4).

Our 2D sample was inspected via a semi-automated approach based on iterative k-means clustering (Everitt et al. 2011). The analysis takes place in n 4D planes $(\alpha(t), \delta(t), v_\alpha, v_\delta)$:

$$\alpha(t) = \alpha_0 + \frac{\mu_\alpha^*}{\xi \cos(\delta)} \tag{4.6}$$

$$\delta(t) = \delta_0 + \frac{\mu_\delta}{\xi} \tag{4.7}$$

where (α_0, δ_0) are the present coordinates, $\xi = 3.6 \frac{\text{deg Myr}^{-1}}{\text{mas yr}^{-1}}$ is a factor needed to express angular velocities in units of [deg Myr^{-1}] and n represents the number of time steps of an evenly spaced temporal grid ($t \in [-15, 15]$ Myr, $\Delta t = 0.2$ Myr). Every time a coherent group was visually

[6] Available in the supplementary material as a .mp4 movie.

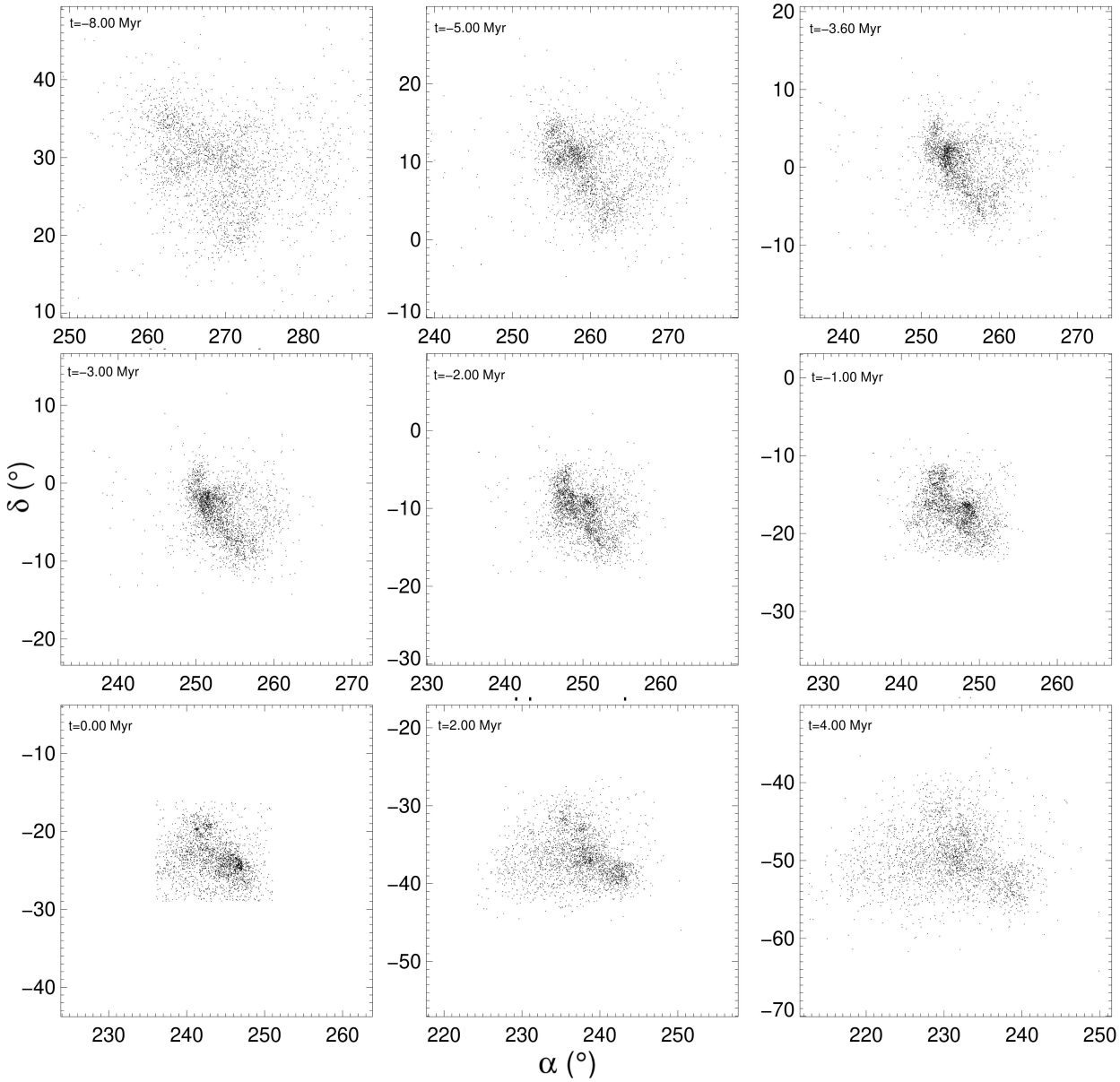

Figure 4.4: A few frames of the time evolution of Upper Scorpius. Some clear overdensities of sources emerge at different times.

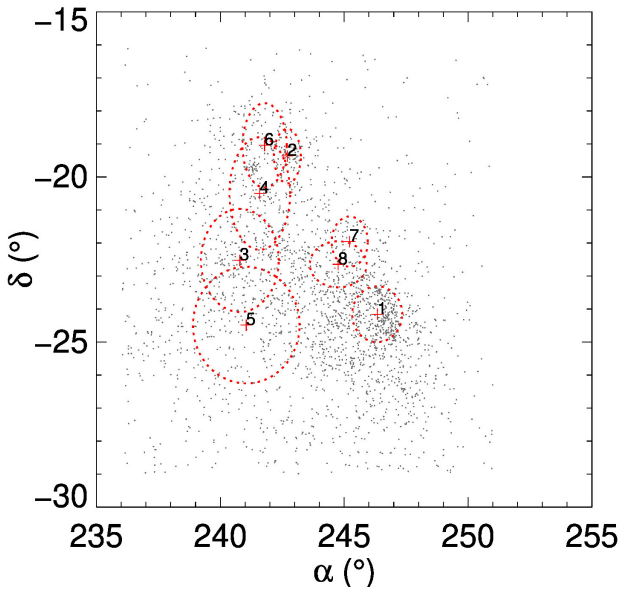

Figure 4.5: Mean positions of the groups at present time, with 1σ ellipses shown as dashed red curves.

identified at a certain t, it was subtracted from the sample. The procedure, which we will refer to as *2D analysis*, was iterated, until no additional groups could be found with confidence.

A total of 8 subgroups was identified, each with a peculiar mark in the phase space (Figure 4.5-4.6); their main properties are summarized in Table 4.3, and include an estimate of the moment of maximum coherence t_K, which we will define in Section 4.4.1.

To get an estimate of the false alarm probability for these overdensities, i.e. to rule out that similar features could be produced by chance, we set up, for each subgroup, the following test: we built reshuffled 2D samples by randomly assigning to each star a quintuplet $(\alpha, \delta, \varpi, \mu_\alpha, \mu_\delta)$, every parameter being drawn independently from its natal distribution; then, we traced back the positions at the appropriate t_K, and excluded the most distant star – with respect to the 5D normal distribution – in an iterative way, until as many stars as in the original subgroup were left. Then, we estimated the false alarm probability (2DP) as the ratio between the number of simulations ending up – at any time – with a more clustered group than the observed one and the total number of performed simulations:

$$2\text{DP} \approx f = \frac{N_{good}}{N_{good} + N_{bad}} \tag{4.8}$$

We considered as a *success* a simulation yielding a median angular distance from its centre and a 1σ velocity ellipse $\sigma_{v_\alpha} \cdot \sigma_{v_\delta}$ smaller than the observed ones. Similarly, a 3D false alarm probability (3DP) was computed by assigning to each star a sextuplet (x, y, z, v_x, v_y, v_z) and considering as *success* a simulation yielding a smaller median distance from the centre than the real one and a 1σ velocity ellipse[7] $\sigma_{v_x} \cdot \sigma_{v_y} \cdot \sigma_{v_z}$ smaller than the observed ones.

As already mentioned in 4.2.2, the results is not influenced significantly by removal of projection effects due to US' bulk motion: the distinction among subgroups was carried out on the original

[7]Computed, in the 3D case, from the samples restricted to the [16,84] percentiles to minimize the impact of possible outliers.

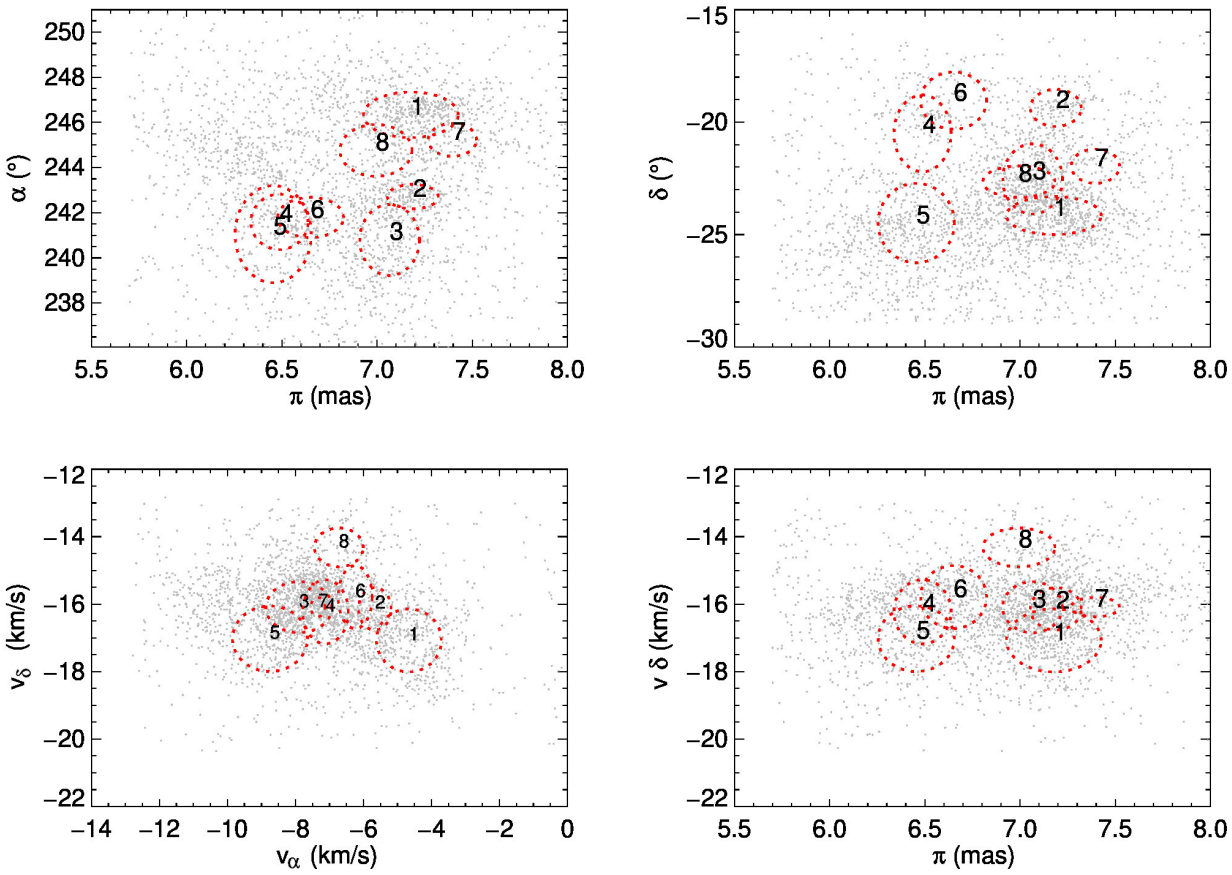

Figure 4.6: Distribution of the groups in the 5D phase space, with 1σ ellipses shown as dashed red curves.

2D sample, using the corrected velocities as a tool to estimate their t_K. Also, errors on v_α and v_δ, increasing linearly with time, cannot be the source of the pattern observed, as 95% of the sources has error $< 0.5°$ at $t = -5$ Myr.

We find strong evidence for the physical nature of groups 1, 2, 3, 4, 5 and the tiny group 7. While Group 1 corresponds to the ρ Ophiuchi region, as confirmed by a cross-match with the catalogue by Cánovas et al. (2019)[8], Group 2 and Group 3 visually resemble Group E and Group H of a recent work by Kerr et al. (2021). The latter, an elongated structure spanning $\sim 1° \times 3°$ with a North-South orientation, is remarkable in many aspects: at a mean distance of 141 ± 4 pc, its shorter side, somewhat broadened by proper motion uncertainties (the 1σ angular error at $t = -3.5$ Myr is $\sim 0.15°$), spans just ~ 2 pc.

The randomness of groups 6 and 8 – for which the 3D sample is quite small – cannot be ruled out. For the moment being, we will keep on retaining the division in subgroups, which will be further discussed in Section 4.5.

4.3.2 Clustered and diffuse populations

An even more interesting result is obtained if we put together the stars belonging to the subgroups, and compare the resulting population with the remaining stars. We might call them the *clustered population* (1442 stars) and the *diffuse population* (1303 stars), respectively. The difference between the two populations is profound: while the former appears to clump, both in 2D and in 3D, at different times in the past, the latter does not.

Since the clustered population has been created by assembling subgroups detected individually during the 2D analysis, the result is somewhat surprising. The 3D sample strengthens the idea of a kinematic duality within the association, that we tried to quantify by taking the median distance from the mean 3D position for the whole sample and for the two subpopulations:

$$d_M(t) = \text{median}\left(\sqrt{[x(t) - \bar{x(t)}]^2 + [y(t) - \bar{y(t)}]^2 + [z(t) - \bar{z(t)}]^2}\right) \tag{4.9}$$

Looking at Figure 4.7, it is clear that $\tilde{d}_M := \min(d_M(t))$ is smaller for the clustered population ($\tilde{d}_M = 7.4 \pm 0.1$ pc) than for the diffuse population ($\tilde{d}_M = 12.4 \pm 0.2$ pc), and reaches its minimum value earlier for the former ($t = -3.2$ Myr) than for the latter ($t = 0$ Myr). Errors are computed via a Monte Carlo simulation for uncertainty propagation, i.e. by repeating the procedure while randomly varying, in a normal fashion, input velocities according to their uncertainties.

While the moment minimising $d_M(t)$ cannot be assumed as an age estimate but rather as a lower limit (see Section 4.5), its minimum value is indeed a measure of the degree of concentration of the population at that time. To shed light on the significance of its difference between the clustered and diffuse population, we ran the same set of 3D simulations described in Section 4.3.1, using $t_K = 3.2$ Myr. Out of 100000 simulations, none behaved better than the original sample; the best-fitting Gaussian distribution of their $\tilde{d}_M(t)$, defined by $(\mu, \sigma) = (9.68 \text{ pc}, 0.16 \text{ pc})$, places a confidence level on the observed clustering at $\sim 14\sigma$.

[8]Out of 517 stars that are both in their sample and in our 2D sample, 342 (66%) have been assigned to Group 1. Most of the remaining stars have not been assigned to any group.

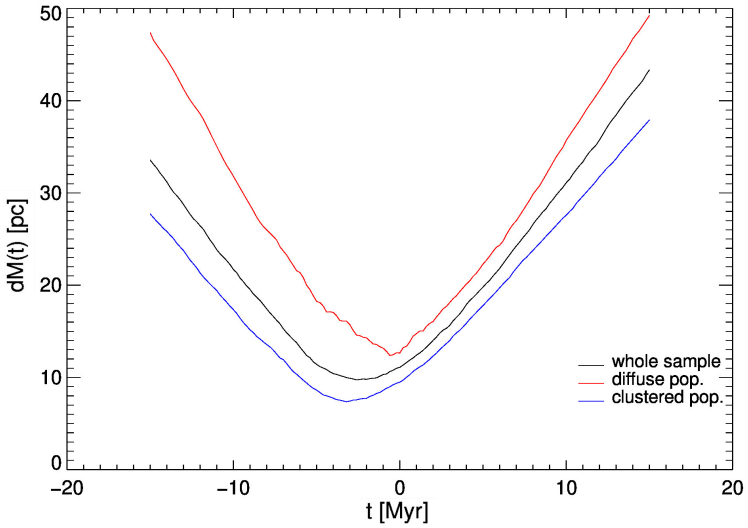

Figure 4.7: The trend of $d_M(t)$, defined by Eq. 4.9, for the clustered and the diffuse population. The clustered population reaches a minimum $d_M \approx 7.4$ pc at $t = -3.2$ Myr, while the diffuse population does not appear not to have been more clustered in the past.

Table 4.3: Number of stars (n) and mean positions in the phase space of the groups (i). Errors should be read as sample standard deviations, equivalent to the semimajor axes of the ellipses in Figure 4.6.

i	2D n	3D n	2DP	3DP	α deg	δ deg	ϖ mas	v_α km s^{-1}	v_δ km s^{-1}
1	467	121	$< 0.1\%$	$< 0.1\%$	246.3 ± 1.0	-24.2 ± 0.8	7.2 ± 0.2	-4.7 ± 1.0	-17.1 ± 0.9
2	114	64	$< 0.1\%$	$< 0.1\%$	242.7 ± 0.5	-19.4 ± 0.8	7.2 ± 0.1	-5.7 ± 0.5	-16.1 ± 0.6
3	396	196	$< 0.1\%$	$< 0.1\%$	240.8 ± 1.6	-22.5 ± 1.6	7.1 ± 0.2	-7.9 ± 1.0	-16.1 ± 0.8
4	156	67	$< 0.1\%$	$< 0.1\%$	241.6 ± 1.2	-20.5 ± 1.7	6.5 ± 0.2	-7.1 ± 0.7	-16.2 ± 1.0
5	166	44	12.2%	0.2 %	241.0 ± 2.2	-24.5 ± 1.8	6.5 ± 0.2	-8.7 ± 1.1	-17.0 ± 1.0
6	58	13	13.5%	18.4%	241.8 ± 0.9	-19.0 ± 1.3	6.7 ± 0.2	-6.2 ± 0.5	-15.8 ± 0.9
7	45	23	1.0%	$< 0.1\%$	245.2 ± 0.7	-22.0 ± 0.8	7.4 ± 0.1	-7.3 ± 0.2	-16.1 ± 0.3
8	40	11	40.0%	< 0.1 %	244.8 ± 1.1	-22.6 ± 0.7	7.0 ± 0.2	-6.7 ± 0.7	-14.3 ± 0.6

4.4 Age determination

The presence of a kinematic duality within Upper Scorpius poses new questions: is there any difference in the age distribution of the clustered and diffuse population? Is the distribution of t_K reflected into an age spread between the groups? To provide tentative answers, we tried to compute the age of both the groups and the diffuse population in a threefold way: via usual isochrone fitting, through the fraction of disk-bearing stars and in a purely kinematic way.

The results of our analysis are summarized in Table 4.4.

4.4.1 Kinematic age

We have seen in Figure 4.7 that at least part of the association was more clustered in the past, as visually evident in Figure 4.4. We might think to exploit this observation to constrain the age of the groups, since their very detection encapsulates, by definition, an age estimate: the moment of maximum spatial coherence might reflect that of the common birth of the members.

For each group, a quantitative estimate can be obtained by defining a coherence function $K(t)$ as the length of the minimum spanning tree connecting the points at time t. To minimize the impact of possible outliers, we excluded the 10% longer branches for 2D estimates, and the 32% for 3D estimates.

The minimum of $K(t)$ provides us with an age estimate, that we will call *kinematic* age t_K. For 2D estimates we employed both corrected and uncorrected proper motion components, with minimal influence on the results: from this moment on, we will always think as t_K as referring to the latter case. The trend of $K(t)$ for all the groups is shown in Figure 4.8, while the appearance of individual groups at $t = t_K$ is shown in Figure 4.9. The error on t_K, again, was computed via $N = 1000$ Monte Carlo simulations per group.

4.4.2 Isochronal ages

We derive a second age estimate for the groups using MADYS, our age determination tool introduced in Chapter 3.

We decided to employ BT-Settl CIFIST2011_2015 isochrones (Baraffe et al. 2015) due to their large dynamical range ($m \in [0.01, 1.4]$ $M_\odot$, $a \in [1, 1000]$ Myr), spanning from young PMS objects in the brown dwarf regime to F-type stars. A constant solar metallicity, typical of most nearby star-forming regions, was assumed (D'Orazi et al. 2011).

The best-fitting solution for individual stars was found by leveraging as more as possible the available Gaia and 2MASS photometry: we averaged three estimates per stars, coming from the *channels* $\mathcal{F} = \{G, J\}$, $\mathcal{F} = \{G, H\}$ and $\mathcal{F} = \{G_{BP}, G_{RP}\}$; in this way, it was possible to simultaneously employ the precision of Gaia G magnitude, the long color baseline of $G - J$ and $G - H$, protecting against measurements errors, and a third channel that is simultaneously independent of G and 2MASS data.

Whenever a filter in one channel did not fulfil the conditions described in Section 4.2.3, the corresponding channel was not used; also, a channel was ignored every time its total photometric error was larger than 0.15 mag; stars lying at more than 3σ outside the region delimited by the isochrones were considered unfitted.

The results for the subgroups are shown in the second row of Table 4.4: going from Group 1 to Group 7, the median age grows by ~ 4 Myr. What really stands out is the comparison between the clustered and the diffuse population (Figure 4.10): while the former has a median age of ~ 4.5 Myr

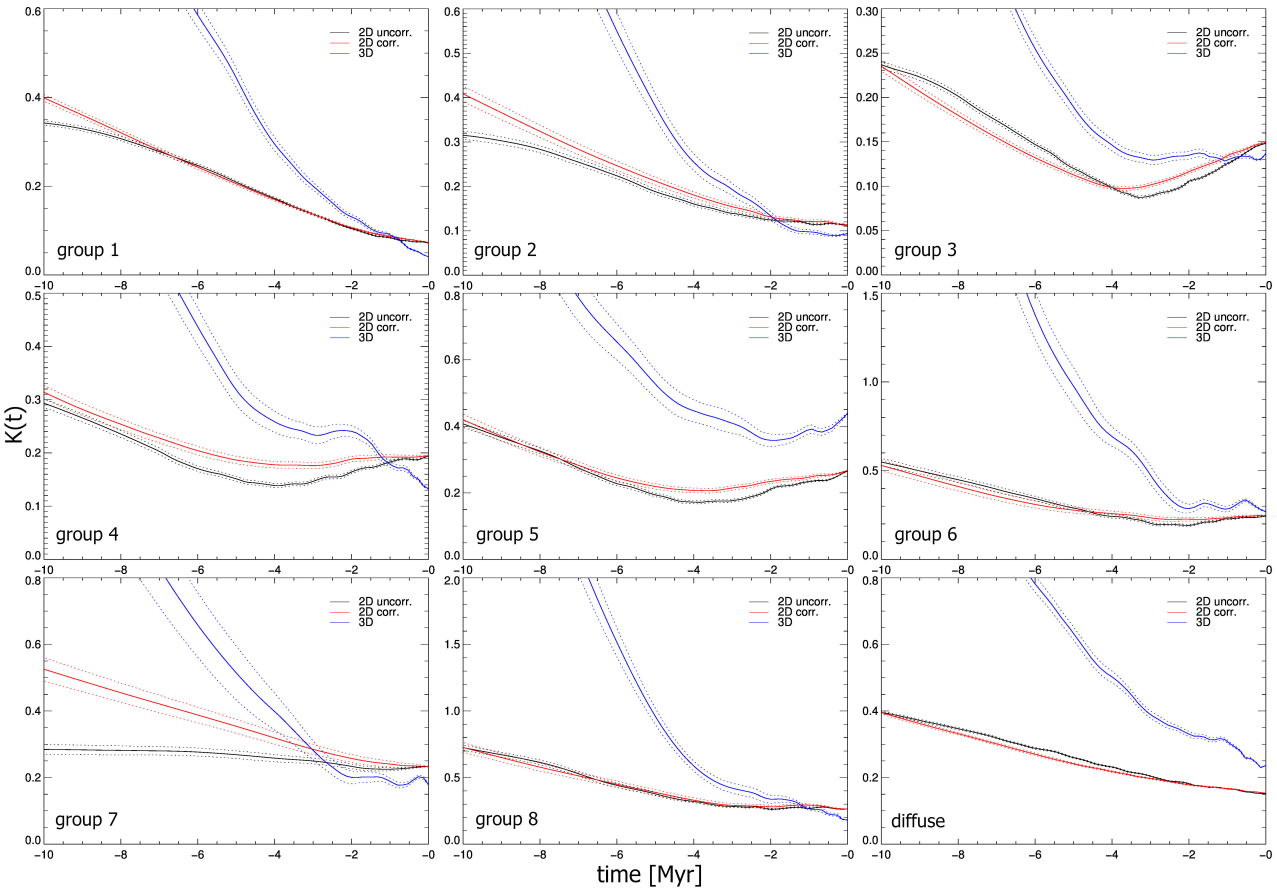

Figure 4.8: Coherence function $K(t)$ for the groups, computed in the 2D case – with uncorrected proper motions (black) and corrected proper motions (red) – and in the 3D case (blue), and shown in arbitrary units. 1σ errors are shown as dashed lines. The minimum of $K(t)$ pinpoints a kinematic age. The diffuse population, as expected, does not cluster in the past.

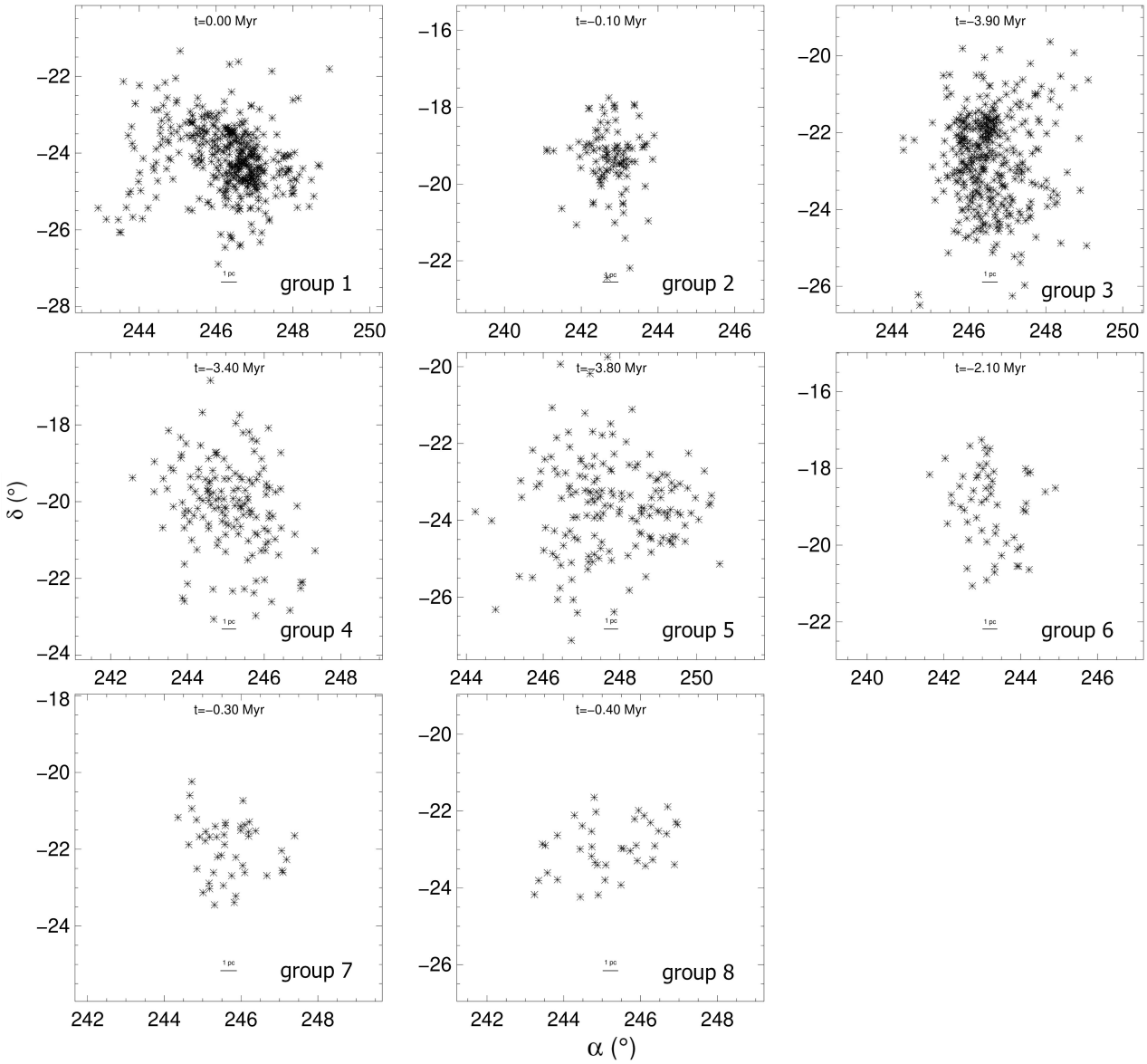

Figure 4.9: All groups, at their maximum coherence, span just a few degrees in sky coordinates, corresponding to projected separations of a few pc.

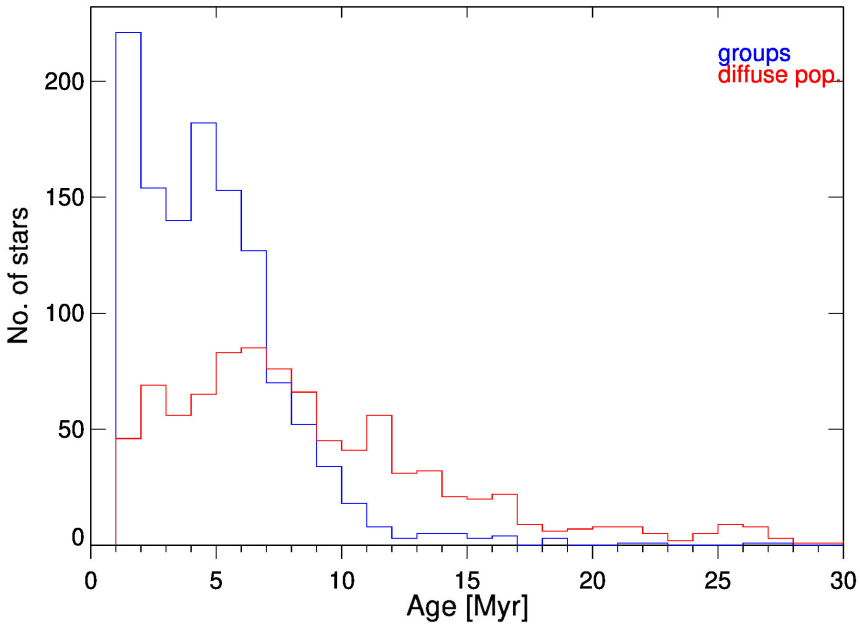

Figure 4.10: Age distribution for the clustered (blue) and diffuse (red) population.

and two well-defined peaks at $\sim$ 1 Myr and $\sim$ 5 Myr, the latter has a median age of $\sim$ 8.2 Myr, with a much flatter distribution.

4.4.3 Fraction of discs

Even though US has largely depleted its initial gas and dust reservoir (Mathews et al. 2012), hints of accretion might still be found for some stars (Dahm & Carpenter 2009). Indeed, the disappearance of primordial discs, signalled by the opening of holes and gaps increasingly straining their initial SED (Espaillat et al. 2012), has been shown to occur with an exponential fashion (Haisch et al. 2001): the fraction of disk-bearing stars within young populations ($t \lesssim 10$ Myr) can therefore be used as an independent age estimator.

The long wavelengths of WISE *W1, W2, W3, W4* filters are particularly suitable for detecting young discs, with longer wavelengths probing larger distances from the star due to their intrinsic thermal structure (Lada & Wilking 1984). While IR excesses in *W2* and *W3* are suggestive of inner discs, *W4* is associated to a colder outer disk (Kuruwita et al. 2018). The effect that we wish to look for is enormous: the luminosity of these discs in *W3* and *W4* can outshine that of the star itself (Luhman & Mamajek 2012). Previous works like Luhman & Mamajek (2012); Pecaut & Mamajek (2016) have greatly used *W4* magnitudes – often in combination with *W3* – for this scope, due to its capability of probing outer disk zones.

To construct a reliable *W3* (*W4*) sample, we selected only data with the best photometric quality flag ('0'), photometric error < 0.2 and apparent magnitudes $W3 > 3.8$ ($W4 > -0.4$)[9]. An insidious problem is that of *flux contamination*: since the angular resolution θ_i increases for redder bands[10], the

[9]The last criterion, due to saturation problems leading to a flux overestimation (Cutri et al. 2012), was virtually unnecessary, given the distance of US.

[10]2" for *J*, *H* and *K*, 6.1" for *W1*, 6.4" for *W2*, 6.5" for *W3*, 12.0" for *W4*.

measured flux becomes more at risk of including a non-negligible contribution of nearby, unresolved sources. To quantify this effect, all the sources within an angular distance θ_i were looked for in Gaia EDR3[11]. Then, the G, G_{BP}, G_{RP} fluxes were converted into $W3$ and $W4$ fluxes. A semi-empirical relation between input and output fluxes was used, combining the 8 Gyr BT-Settl isochrone for $0.01 < M/M_\odot < 1.4$ and the empirical tables by Pecaut & Mamajek (2013) for $1.4 < M/M_\odot \lesssim 20$.

The fluxes from field sources were derived averaging four estimates: from G and parallax, if $\sigma_\varpi/\varpi < 0.5$, from G and G_{BP} if $\sigma_G + \sigma_{G_{BP}} < 0.4$, from G and G_{RP} if $\sigma_G + \sigma_{G_{RP}} < 0.4$, from G_{BP} and G_{RP} if $\sigma_{G_{RP}} + \sigma_{G_{BP}} < 0.4$. Correction for extinction was applied whenever possible. If no estimate was available for even a single neighbor of a certain star, we employed G fluxes, for consistency, for all the neighborhood too.

The so-called contamination fraction f_c was defined as $f_c = F_{cont}/F_{tot}$, where F_{tot} is the flux from the M-band of interest and F_{cont} the flux from all the field sources within θ_i. Its effect consists in a magnitude decrease $\delta M = 2.5 \cdot \log_{10}(1 - f_c)$. We subtracted it to measured magnitude: this correction goes *against* disk detection, as it makes magnitudes fainter. To be protected against the uncertainties in field star distances, ages, and on the correction itself, we decided to employ in this analysis only stars with $f_c < 0.2$. This limits the corrections to $-\delta M \approx 0.25$ mag, far less than the expected effect for full discs (several mag).

The combination of quality and contamination cuts, though, greatly reduces the availability of $W4$ data, which additionally show a tendency for being *always* redder than expected, perhaps indicating debris discs (Cody & Hillenbrand 2018) that are known to be common in the association (Carpenter et al. 2009). For these reason, we decided at the end to employ only $W3$ magnitudes.

Abundant groups like 1 and 3 show a neat bimodality in their $(G - W3, G)$ CMD, with a second sequence of stars running parallel to discless stars, but with an offset of ~ 2 magnitudes. Hence, we chose to use the same criterion as Pecaut & Mamajek (2016), i.e. we compute the excess $E(K-W3)$ relative to the expected color, and identify full discs as those with $E(K - W3) > 1.5$ mag. The choice of K is based on the fact that its λ ($\approx 2.2\mu$m) is simultaneously too short to carry along a significant non-photospheric contribution and long enough to be protected against uncertainties in the extinction. We compute the expected $(K - W3)$ as that of the isochrone corresponding to the group isochronal age, computed in Section 4.4.2. We perform the same computation[12] with $(G - W3)$, both as a consistency check and as a way to recover those few stars excluded by quality cuts in 2MASS photometry.

The fraction of primordial discs f_D spans from $\sim 30\%$ to $\sim 10\%$, going from Group 1 to the diffuse population. Under the assumption of an exponential decay of f_D (see, e.g., Mamajek 2009), we derived the *disk age*:

$$t = -\tau \ln f_D \tag{4.10}$$

where $\tau = 2.5$ Myr (Mamajek 2009).

The fraction of discs we found within US is $f_d = 0.19 \pm 0.01$, comparable to that found by Esplin et al. (2018) and Luhman & Esplin (2020).

The clustered population appears younger than the diffuse population, whose disk fraction has been computed using as expected colors those produced by individual ages and masses. Again, setting a fiducial line in this way produces a bias *against* disk detection and hence against an age spread [13].

[11] Gaia EDR3 is essentially complete at $\theta > 1.5''$, and can be relied upon until $\theta = 0.7''$ for equal-mass sources (Fabricius et al. 2021).

[12] Adopting the same threshold of 1.5 mag, as $G-$band emission is purely photospheric.

[13] If the excess is computed starting from individual positions rather than from a fiducial line, it will be harder for

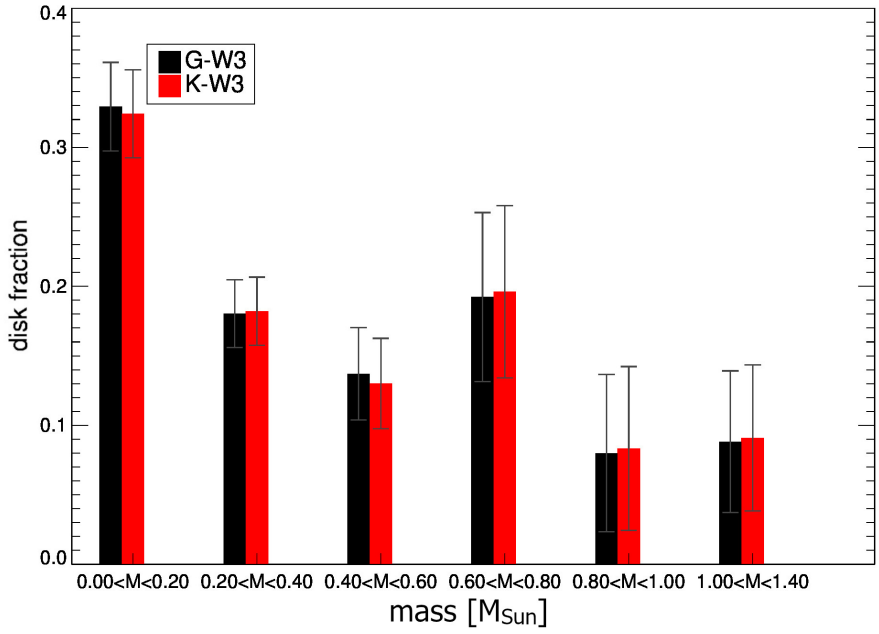

Figure 4.11: Disc fractions for different bins of stellar mass. Black bars give the fraction of stars where disks were detected from the G-W3 color; red bars those with disks detected from the K-W3 color. Going towards bins of increasing stellar mass, a clear decrease in the disk fraction is seen.

A comparison of our sample of disk-bearing stars with that by Luhman & Esplin (2020) shows that, among 161 full discs having a cross-match, 145 (148) are there identified as full-discs, the remaining 16 (13) being labelled as debris/evolved transitional discs, for the criterion employing $G-W3$ ($K-W3$). It is significant that the number of false negatives, i.e. sources not labelled here as full discs but that are identified there as such, is comparable: 84/1261 (81/1261). We can reasonably assert that our disk fraction estimates are not biased in one direction or another.

The assumption of a single τ hides the different timescales of disk decay with stellar mass: it has been shown that the lifetime of a disk steadily decreases with stellar mass (Ribas et al. 2015). The dependence of the disk fraction on stellar mass is shown in Figure 4.11: the fractions for the first bin and the last two are in complete agreement with the dedicated IR survey performed by Luhman & Mamajek (2012) and with Pecaut & Mamajek (2016).

We show in Figure 4.12, 4.13, 4.14 the comparison between the three estimates for the eight groups. While disk and isochronal age show a remarkable correlation (0.84), kinematic ages appears always underestimated, hinting at the presence of factors not taken into account so far. We will discuss the findings of the age analysis in Section 4.5.

4.5 Discussion

4.5.1 Kinematic analysis

As many recent studies have shown (e.g., Roccatagliata et al. 2020), the formation of associations cannot be reduced to the simple scenario of a monolithic burst. The idea of a coherent, uniform

the youngest stars to have an excess beyond 3σ; the opposite applies for stars older than the fiducial line, but they are usually not expected to show an IR excess at all. The overall effect goes against disk detection.

Table 4.4: Age estimates obtained through photometry (t_P), discs (t_D) and kinematics (t_K). The number of stars in each group (n), the sample standard deviation of isochronal ages (s) and the fraction of discs (f_D) are shown too.

Group	n	t_P [Myr]	s	f_D (%)	t_D [Myr]	t_K [Myr]
1	467	2.6 ± 0.1	1.5	31 ± 3	3.0 ± 0.3	0.0 ± 0.1
2	114	4.4 ± 0.1	1.0	27 ± 6	$3.2^{+0.6}_{-0.5}$	0.1 ± 0.2
3	396	4.8 ± 0.1	1.1	25 ± 3	3.5 ± 0.3	3.7 ± 0.3
4	156	5.2 ± 0.1	1.4	17 ± 4	$4.5^{+0.7}_{-0.5}$	3.4 ± 0.6
5	166	6.1 ± 0.2	1.6	14 ± 4	$4.8^{+0.8}_{-0.6}$	3.8 ± 0.4
6	58	4.4 ± 0.2	1.2	26 ± 8	$3.4^{+0.9}_{-0.7}$	2.1 ± 0.6
7	45	6.2 ± 0.2	1.2	9 ± 4	$6.0^{+1.7}_{-1.0}$	0.3 ± 0.4
8	40	5.4 ± 0.3	1.7	12 ± 6	$5.3^{+1.7}_{-1.0}$	0.4 ± 0.8
clust.	1442	4.5 ± 0.1	1.5	24 ± 2	3.6 ± 0.2	—
diff.	1303	8.2 ± 0.1	3.7	10 ± 1	5.7 ± 0.3	—

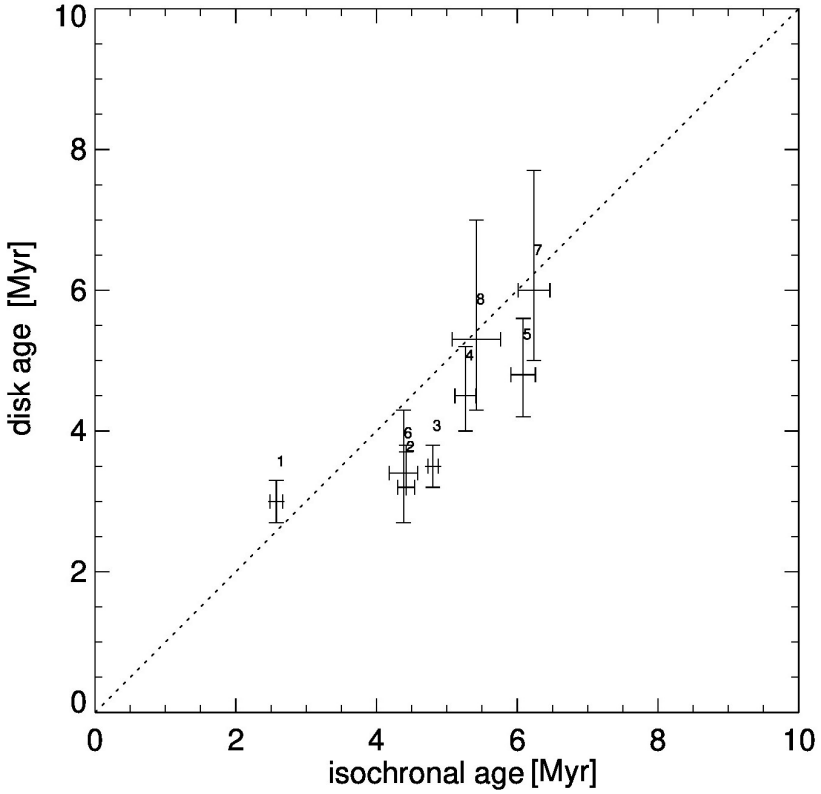

Figure 4.12: Isochronal vs disk ages for USCO groups. These estimates show a remarkably high correlation (0.84).

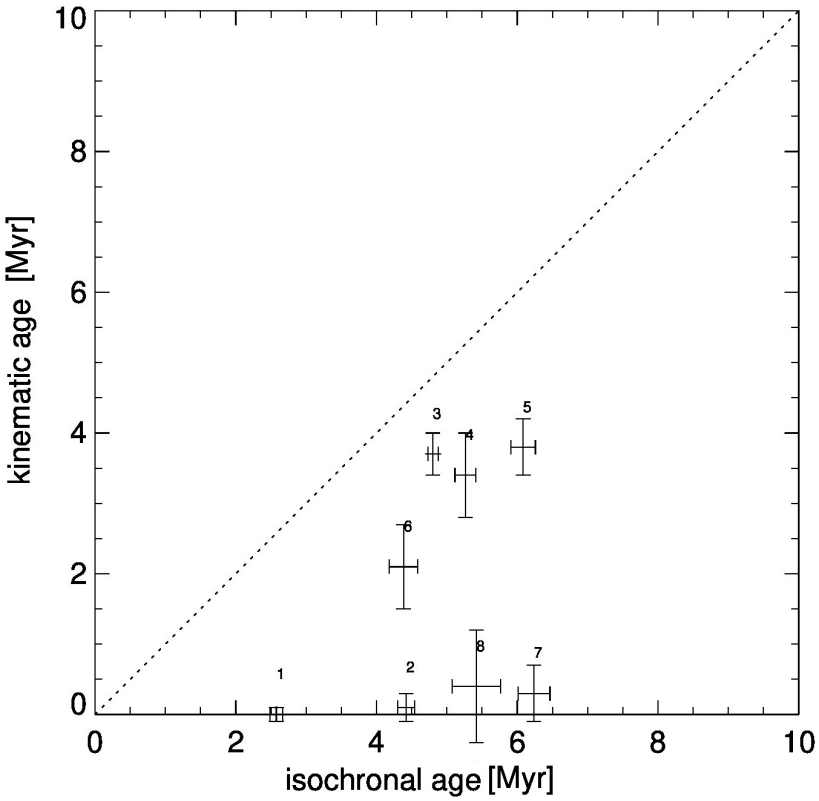

Figure 4.13: Isochronal vs kinematic ages for US groups. Kinematic ages always appear to be underestimated.

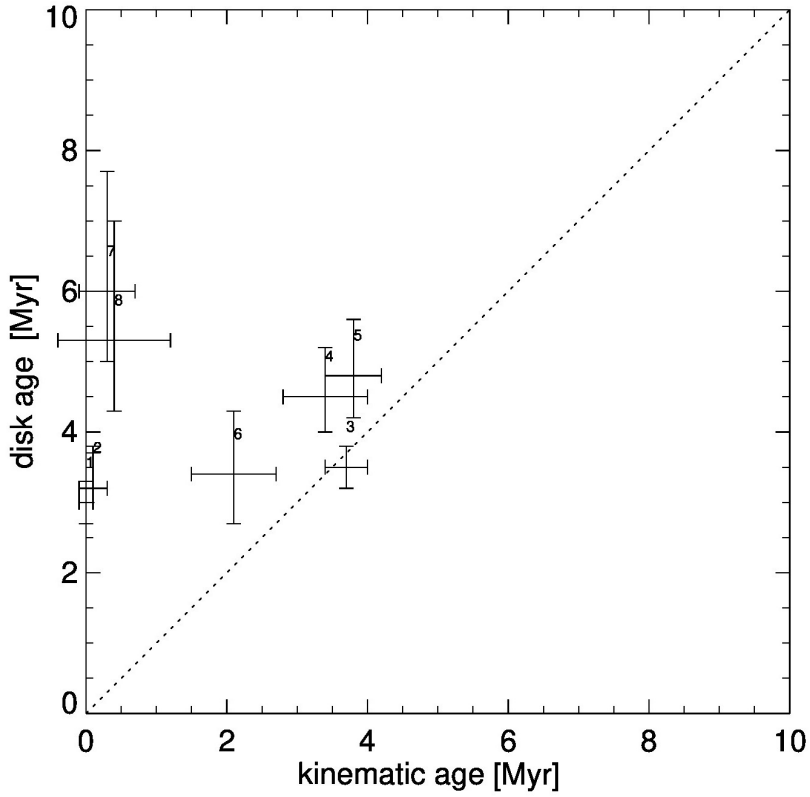

Figure 4.14: Kinematic vs disk ages for US groups. The same considerations as in Figure 4.13 apply.

expansion has given way to that of a complex star formation history, prolonged over million of years and with a large spatial variability. While this might seem an argument against kinematic reconstruction (e.g., Pecaut & Mamajek 2016), the substructures themselves dissolve over time (Damiani et al. 2019), so they might in principle be targeted by the same approach.

The presence of a high degree of substructure within Upper Scorpius has been recently quantified by González et al. (2021), confirming a long-held suspicion (e.g., Wright & Mamajek 2018). However, Damiani et al. (2019) concluded that this complex structure seen at present time cannot be unfolded and brought out into a global pattern of motion: regions of higher and lower density do not bear distinct kinematic imprints, and close proximity on the sky is not equivalent to proximity in velocity, as if the different populations are mixed up. This is similar to what is observed in young clusters (e.g., Jeffries et al. 2014; Tobin et al. 2015; Sacco et al. 2015; Damiani et al. 2017). The general trend that denser regions appear younger than the sparser ones hints at the presence of multiple populations or, at least, of an extended star formation history.

The initial substructure of a group of stars can be irremediably altered not only by the violent relaxation following the removal of the initial gas reservoir (Lynden-Bell 1967), but also by subsequent dynamical interactions (Scally & Clarke 2002), leading to its complete disappearance, if the dynamical timescale of the region is shorter than its age[14]. If, like in associations, dynamical interactions may be neglected, a memory of the initial velocity pattern can be preserved for a longer time (Goodwin & Whitworth 2004), since the main factor leading to the erosion of the original velocity structure now becomes the galactic tidal field, acting on timescales of $\sim 10^7$ yr (Wright & Mamajek 2018).

Galli et al. (2018), employing Gaia DR1 data of 1322 stars, found that the shape of US is approximately ellipsoidal; they conclude that the association is not dynamically relaxed, meaning that its shape is an imprint of its star formation history. Based on these considerations, we decided to employ a kinematic approach to see how much the initial structure of the association is still perceptible beneath its present velocity structure.

The method employed was the classical linear trace-back, in which individual star motions are traced back in time. The approach differed from the classical studies of US both in depth, number of stars and purposes: contrary to earlier studies, with typical sample sizes of a few hundreds, our sample comprises about 3000 stars and did not aim at finding a single kinematic age for the whole US – something already excluded by Pecaut et al. (2012) –, but rather at investigating its degree of substructure.

As can be imagined, the feasibility of a trace-back analysis is ultimately limited by the precision of the available velocities (Goldman et al. 2018). The need for precise radial velocities ($\sigma_v << 1$ km/s, Donaldson et al. 2017) was here satisfied by combining RV data from APOGEE and GALAH to those provided by Gaia: we have built a catalogue of 771 US sources (our "3D sample") with median velocity uncertainty $\sigma_v = 0.12$ km s^{-1}. Being the 3D sample size only $\sim 30\%$ of the 2D sample, the former was employed to verify and complement the results of the main analysis, carried in 2D.

Our cluster analysis found eight groups, which are seen to clump at different times at the past. The real nature of Groups 1, 2, 3, 4, 5 and 7 is extremely likely, comparing it with random clustering of sources in 2D or in 3D, while Groups 6 and 8 would need additional RV measurements to confirm their physical nature. None the less, it is worth mentioning that the disk fraction of Group 6 is higher than that of the field with a confidence level of $\sim 2\sigma$.

[14]The picture is even more complex, as the dynamical timescale itself can change over time as a result of its density variations, with the counter-intuitive result that the presence of high degree of structure today rules out the existence of highly compact states in the past (Parker 2014).

The results for Group 1, that should be interpreted as ρ Ophiuchi's bark, the region that is not too extinct to be undetectable in Gaia's optical bands, are consistent with the study by Erickson et al. (2011), that derived a disk fraction of $27 \pm 5\%$ and an isochronal age of about 3.1 Myr. When cross-matching our US sample with the ρ Ophiuchi sample by Cánovas et al. (2019), we find that 5 % of its sources belong to our Group 7 and another 5 % to our Group 8. The subdivision of sources between Group 0 and Group 8 closely resembles that of Grasser et al. (2021), with compatible (α, δ, v_a, v_d, ϖ) between our Group 1 and their "Pop 1" and our Group 8 and their "Pop 2". The concentration of sources in the northern region of US ($352° < l < 355°$, $22° < b < 25°$), coming with a complex velocity structure, was already noted by previous studies (Damiani et al. 2019; González et al. 2021); here we suggest the division of those stars in three different groups (2, 4 and 6) as a possible solution to this conundrum.

A particular fruitful comparison can be done with the recent work by Kerr et al. (2021), which employs a density-based hierarchical clustering algorithm to identify substructures within young nearby associations. Contrary to their approach, based on a thorough inspection of the present phase space structure, our simpler, semi-automated method tried to incorporate in the classification scheme the time variable too. This is what led us to identify, for instance, the rather spread and populous Group 3, which was very concentrated in the past. A comparison of their Table 6 with our Table 4.3 likely leads to associate their Group E, F, G, H and I with our Groups 2, 7, 6, 3, 1, respectively.

The most interesting result came when putting together the groups, and comparing them with the stars that could not be put in a group. The clustered population appears to have been more compact in the past (with a peak at $t \sim 3.5$ Myr ago, dominated by Group 3), with a confidence level on this result of 14σ. This is not true for the diffuse population, which instead shows its tightest configuration at present time. These results came as a surprise, as the age for US members should be 5-11 Myr, and led us to investigate whether the retrieved substructures were correlated to age gradients within the region: to this aim, we employed both isochrones for PMS and discs.

4.5.2 The age conundrum

The first robust result of the age analysis is that the clustered population appears younger than the diffuse population, in a similar way as Damiani et al. (2019) noticed with their distinction based on the present projected source density. The natural explanation for this fact is that star formation in US appears to have happened in small groups that disperse after a few Myr, dissolving in the field of the older population, but retaining for some time memory of their original velocity structure.

The clustered population itself shows an internal age gradient, as expected from previous works on the region (Pecaut & Mamajek 2016). The youngest group is Group 1 (ρ Ophiuchi), with a $t \sim 3$ Myr consistent with the literature (Erickson et al. 2011); Group 2, 3 and 6 are approximately coeval, while the small comoving Group 7 appears the remnant of an older formation event.

An independent age estimate was obtained through the disk fraction f_D, defined as the fraction of stars within the sample still bearing marks of a primordial disk. We decided to follow the criterion for distinction of disk classes used by other studies (Luhman & Mamajek 2012; Pecaut & Mamajek 2016), but the enormous restriction of W4 data, due to a combination of quality cuts and contamination from the field, made us lean towards the use of the sole criterion on W3. We employed as color benchmark both K-W3 and G-W3, finding consistent results, and validated our proxy with a cross-match with Luhman & Esplin (2020). The price to pay was the impossibility to reliably identify looser disk evolutionary stages (evolved, transitional), which none the less are not used when inferring the age of a population.

We find an average full disk fraction of about 0.19 ± 0.01, consistent with previous work (Carpenter et al. 2006; Luhman & Mamajek 2012; Luhman & Esplin 2020; Cody & Hillenbrand 2018), and a well-defined trend with stellar mass consistent with Luhman & Mamajek (2012). The disk fraction is again significantly higher for the clustered (0.24 ± 0.02) than for the diffuse population (0.10 ± 0.01). Since disk statistics has been shown not to be influenced by binarity, as circumbinary discs in US decay with the same pace as circumstellar discs (Kuruwita et al. 2018), the robust correlation of f_D (0.84) with isochronal estimates reinforce the idea of a real age spread between the groups.

It should be underlined that, whilst recognising full disk can be considered safe and little model-dependent, the e-folding time of disk decay is usually derived from comparison with isochronal ages, generating a circular argument when confronting t_K and t_P. Estimates of τ include 2.3 Myr (Fedele et al. 2010), 2.5 Myr (Mamajek 2009), 3 Myr (Ribas et al. 2014) and even 5 Myr (Richert et al. 2018) for models including magnetic-driven radius inflation; additionally, τ has been shown to depend on environmental conditions like the mass and the rotation rate of the parent molecular cloud core, and on the stellar mass itself (e.g., Lada et al. 2006; Mamajek 2009; Ribas et al. 2015). Therefore, our disk ages must be considered relative, rather than absolute.

The issue with isochronal ages is similar and, if anything, even more severe, as the history of age determinations in US bears witness. The first systematic studies of the region argued for a uniform age of $\sim$ 5 Myr (Preibisch & Zinnecker 1999; Preibisch et al. 2002), but then Hillenbrand et al. (2008) showed that the ages of young stars depend on the spectral class, with low-mass star ages underestimated by 30-100% and high-mass star ages overestimated by 20-100%; a twofold variation of the inferred ages for intermediate and low-mass stars emerged for other clusters too (Mayne & Naylor 2008; Naylor 2009; Bell et al. 2013). Significant insights on the problem are given by binary systems for which dynamical mass estimates are available: discrepancies between ages inferred for presumably coeval components have been confirmed by Rizzuto et al. (2016) and Asensio-Torres et al. (2019). A total reassessment of the problem of age determination in US was carried out by Pecaut et al. (2012), who used F-type stars as a benchmark to establish a revised age of 11 ± 2 Myr. The picture was confirmed in a subsequent study (Pecaut & Mamajek 2016), alongside with a strong dependence of age estimates on spectral class, with younger ages for both K- (5 ± 2 Myr) and B-type stars (7 ± 2 Myr) than for F- (10 ± 1 Myr) and G-type (13 ± 1 Myr) stars. Interestingly enough, the derived age spread for the association was as large as 7 Myr.

While the debate on the age of US is still ongoing (e.g., David et al. 2019), a parallel discussion involves the above-mentioned age spread, either attributed to an extended star formation or to systematic effects inherent to models. An interesting solution has been put forward by Feiden (2016a): highlighting the difficulties in modelling convection for PMS stars, he noticed that the effect of magnetic fields on a protostar – stronger for less massive stars – is to slow down its radial contraction along the Hayashi line; the resulting luminosity at a fixed age is higher than predicted, leading to incorrectly infer younger ages if the effect is not taken into account. By means of Dartmouth magnetic models (Feiden & Chaboyer 2012) equipped with the maximum allowed surface magnetic field strength, he found that a consistent 10 Myr isochrone could fit the observed Hertzsprung-Russell diagram (HRD) of US across all spectral types. The explanation by Feiden (2016a), though, can create problems with moving groups with well-defined age (Tucana-Horologium association, β Pictoris; see Bell et al. 2015).

A completely different approach is that of Fang et al. (2017), who emphasize the importance of incorporating the star formation history (SFH) into the study of associations. Dividing stars by spectral type is risky because, at fixed mass, a younger star is of a later type than an older one. While low-mass stars ($M < 0.4 M_\odot$) enter the MS via the Hayashi line, intermediate stars develop a radiative core that makes them move along the horizontal Henyen track; given that the ascension

toward earlier spectral types acts on a timescale of 1-10 Myr, a population forming through a burst of comparable duration will generate spurious age differences if divided according to spectral class.

We will discuss how our results can be reconciled with this framework in Section 4.5.4, shifting for the moment the focus to the discussion of some biases impacting on both kinematic and photometric considerations.

4.5.3 Assessment of biases

A particularly tricky bias, affecting both the kinematics and isochronal ages, is that resulting from unresolved binaries. Assessing the fraction of binaries f_b in stellar populations has been the aim of several studies in the last years. A general trend is the increase of f_b with the primary mass: $f_b = 27 \pm 1\%$ for $M = 0.075 - 0.6 M_\odot$ (Winters et al. 2019), $f_b = 41 \pm 3\%$ for $M = 0.78 - 1.02 M_\odot$ (Raghavan et al. 2010), $f_b = 54 \pm 4\%$ for $M = 1.02 - 1.25 M_\odot$ (Raghavan et al. 2010); however, environmental effects can play an important role, as shown by US itself that, contrary to the field, shows a fairly constant $f_b = 35\%$ for early M and G-K stars (Tokovinin & Briceño 2020) and a value as high as $\sim 70\%$ for B-A-F stars (Kouwenhoven et al. 2005, 2007b).

We envisage the effect of unresolved binary stars on our sample to be twofold. As regards the kinematics, we expect that the wobbling of the photocentre is reflected in a perturbation of the system's true proper motion with the result that, when performing kinematic trace-back, binaries will be preferentially directed towards the diffuse population rather than to the clustered population. As regards the photometry, the presence of a cooler secondary star can shift the whole system towards lower temperatures and higher luminosities in the HRD. The combination of the two effects makes unresolved binaries appear younger than they are. It has recently been shown (Sullivan & Kraus 2021) that this factor is able to create a large apparent spread in a coeval population, especially when accompanied by high parallax uncertainties. None the less, the correlation that we found between the isochronal age and the disk age is reassuring, as the latter is expected to be independent of multiplicity (Kuruwita et al. 2018).

To quantify the impact of these considerations on our results, we started from the sample of 614 US stars constructed by Tokovinin & Briceño (2020) to assess the multiplicity in the region. Their sample, covering the mass range $[0.7, 1.5] M_\odot$], is invaluable for two reasons: on the one hand, it was accurately vetted not to be biased against or towards binaries; on the other hand, it was extensively studied to look for companions by means of speckle interferometry, pushing the detection sensitivity well below Gaia's[15].

A tentative diagnostic of possible binarity is the renormalized unit weight error (RUWE), a parameter associated to each source of Gaia EDR3 and quantifying how much the assumption of *isolated point source* is suited to the astrometric solution; values of RUWE$>$1.4 are usually used as a threshold to flag a potential non-single star nature (Fabricius et al. 2021). After removing 70 companions of their list that are resolved by Gaia (having angular separations $\theta \gtrsim 1''$), we are left with a sample of 180 companions. We have two samples of primary stars, that we may dub "single" (S) and "binary" (B). We retrieved the RUWE parameter for all these stars and verified that the fraction of stars with RUWE$>$1.4 (f_R) is significantly higher for sample B (76%) than for sample S (19%). On the ground of the expected multiplicity of US, we would expect for our 2D sample a $f_R \sim 30 - 35\%$. Instead, we find that $f_R = 16 \pm 1\%$, equal for the clustered ($15 \pm 1\%$) and the diffuse ($17 \pm 1\%$) populations. Exceeding the natural bias against strict binaries proper to

[15]The detection limits of their survey, outside $\theta \approx 0.1''$ (corresponding to a projected physical distance $d \approx 15 AU$), are such that the survey is complete at a contrast $\Delta I = 2$ mag.

Gaia-based samples (Tokovinin & Briceño 2020), our selection criteria appear to have preferentially excluded binaries from the 2D sample.

To verify it explicitly, we applied the same selection criteria of Table 4.1. Whereas we recover 87% of stars from sample S, we only recover 67% from sample B. Although the median parallax uncertainty is larger (0.089 vs 0.023 mas), the effect is mostly due to velocity cuts. This basically means that proper motions of unresolved binaries can be so large to slide them out of the selection window 25% of the time.

The high-RUWE stars of our clustered (diffuse) sample are significantly younger than their parent population, having a median $t = 2.6$ Myr ($t = 4.4$ Myr). To verify if this result is consistent with a population of unresolved binaries, we set up a simulation of 10000 binary systems, with initial mass function (IMF) and mass ratio distribution (CMRD) as in Reggiani & Meyer (2011). After randomly generating primary masses according to the IMF and secondary masses according to the CMRD and the IMF, we assigned each star a set of magnitudes (J, H, G, G_{BP}, G_{RP}), coming from the same set of models used in the isochronal analysis, and a fixed age. For an age of $t = 5$ Myr (comparable to the BT-Settl result for the clustered population), the derived median age shifts to $t = 3.0$ Myr; for $t = 8$ Myr (similar to the diffuse population), it shifts to $t = 4.8$ Myr. The similar relative magnitude of the age deviation, coupled with the comparable fraction of high-RUWE stars, does not constitute an argument against the age spread between the two kinematic populations of Upper Scorpius, but naturally explains the young tail seen in the diffuse one (Figure 4.10).

A second issue worth considering is the already mentioned difficulty in assessing ages of low-mass stars. If we divide our sample in bins of fitted mass, we recover 119 stars with $M > 1 M_{\odot}$[16]): 80 stars in the diffuse, 39 in the clustered population, with median ages 13.7 Myr and 8.1 Myr, respectively (Figure 4.15). The unequal division of mass might point to different properties of the two populations; Galli et al. (2018) presented evidence for a somewhat different spatial distribution of the brightest and the faintest stars in US, hint of a different relaxation state that would imply an earlier formation of massive stars. We don't have the means to answer this question, but even a general increase of our fitted ages would not be detrimental to our main arguments.

As concerns field contamination, expected to some extent due to the rough definition of the 2D sample, it tends to create an age overestimate. Starting from the 3D sample, we applied an iterative exclusion of the stars that are more than 3 sigma out of the velocity distribution, up to convergence: 82/924 stars ($\sim 9\%$) are excluded in this way. The median of their ages is twice as large (11 Myr) as that of the full sample. A similar fraction of interlopers is found by applying the same algorithm to the age distribution of the 2D sample: out of 2183 stars with an age estimate, those excluded are 210 ($\sim 10\%$), mostly (91%) belonging to the diffuse group.

4.5.4 The SFH of Upper Scorpius

Turning back the attention to our main point, we might notice that the fraction of stars found in the clustered population is $\sim 50\%$. This fraction, likely underestimated because of field contamination, is much higher than the 14.5% found by Damiani et al. (2019) across the whole Sco-Cen, suggesting an evolutionary scenario of kinematic structures, consistent with the younger age of US compared to UCL and LCC. In the former, even though the present space distribution is quite well-mixed, the velocity distribution is not, and still allows a distinction of subgroups; but velocity patterns are beginning to fade away, too, as confirmed by the diffuse population, that has lost, or is losing, its initial kinematic imprint.

[16]The smallness of the sample is due not only to the IMF but also to selection effects: bright stars at the typical distance of US tend to have poorer astrometric solutions than low-mass stars.

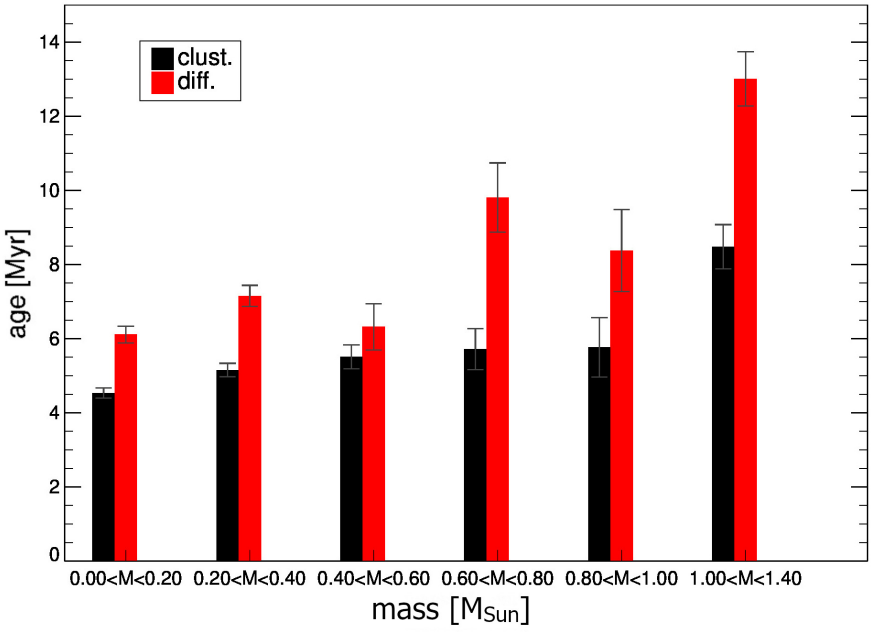

Figure 4.15: Average isochronal ages for different bins of stellar mass. Black bars give the average age for members of the clustered population; red bars for those of the diffuse population.

The classical picture of star formation in Scorpius-Centaurus, first put forward by Preibisch & Zinnecker (1999), envisions the first outburst of star formation (not before 30 Myr, see Damiani et al. 2019) in LCC, that triggered shortly after activity in the adjacent UCL, and finally events like the explosion of supernovae led to star formation in US. But this should be considered no more than a zeroth order approximation of a more complex sequence of events. Indeed, a thorough study by Pecaut & Mamajek (2016) proved the existence of an intricate substructure in its age distribution within the subgroups themselves, reflected in the kinematic structure of the association: Wright & Mamajek (2018) concluded that there's no evidence to say that the three subgroups of Sco-Cen are the result of a global expansion of three small, independent clusters; rather, they argue for the existence of substructures, that they could not resolve due to the small sample size; such subgroups should not be the outcome of single, individual bursts of star formation, but rather of several minor subgroups, born independently of each other.

All the elements of our analysis converge towards a single solution: namely, that star formation in US must have lasted more than 10 Myr. After starting producing stars almost simultaneously with LCC ($\sim$ 15 Myr ago), as confirmed by the presence of stars coeval to the latter (Damiani et al. 2019), the formation continued: the existence of B-type stars with clear indication of youth like τ Sco (Rizzuto et al. 2015) or HD 142184 (Tetzlaff et al. 2011) argues for some star formation occurred between the first outburst and the age of ρ Ophiuchi. Whether this star formation was continuous or rather experienced a late burst is a different question: in this regard, the existence of a kinematic bimodality similar, albeit less pronounced, to that of Taurus (Kraus et al. 2017), is significant, as it is intriguingly consistent with the late-burst scenario put forward by Fang et al. (2017).

The intricacy of star formation in US lies in the fact that it happens in small formation episodes (a few 10s-100s stars each), as already pointed out by (Pecaut & Mamajek 2016), and that the older events have at present time lost their kinematic imprint. This is seen also in the compact

populations in Lupus within LCC, where the stars are younger than the diffuse population not only of the surrounding LCC, but also of US (Damiani et al. 2019). The most compact population of Upper Scorpius, ρ Ophiuchi, has a population of protostars still embedded in the molecular clouds – hence invisible to Gaia – only 0.3-1 Myr old (Luhman & Rieke 1999; Wilking et al. 2008), with external, less extinct regions spanning between 2 and 5 Myr, as we have shown. The interesting fact is that the group is under strong influence from the rest of US (Ladjelate et al. 2020), with positive feedback on the star formation rate in the L1688 cloud (Nutter et al. 2006), whose stars have not dispersed yet (Ducourant et al. 2017); moreover, a possible echo of its formation related to a shock wave by a supernova might still be seen as a radial velocity gradient of ~ 1.0 km s^{-1} pc^{-1} (Rigliaco et al. 2016). An even more significant observation is that the bubble around the eponymous star ρ Ophiuchi is inflating with a velocity ~ 1.3 km s^{-1}, so that the time needed to inflate the bubble ($d \approx 1.36$ pc) is ~ 1.2 Myr (Pillitteri et al. 2016). The isochronal ages of the members of this bubble is about $\sim 5 - 10$ Myr, much higher than the kinematic age of the bubble. Pillitteri et al. (2016) speculate that the assumption of a constant expansion is not valid in the first phases, when the dense material surrounding the young stars actively acts to delay the expansion.

This conclusion is directly reflected into what we have found in our work: kinematic ages of the subgroups of US are always smaller than isochronal ages, even neglecting issues inherent to age determination of low-mass stars that would further raise the discrepancy. The idea that stars in US formed well before their group started dispersing can be related to a initial bound state of the gas-rich structures, disrupted after the dispersal of gas by stellar feedback (Krumholz 2014). Therefore, the timescale of gas removal – quantified as 2-7 Myr for some nearby galaxies (Kim et al. 2021) – could be intriguingly estimated as the difference between isochronal and kinematic ages.

4.6 Conclusions

We have shown that the star-forming region Upper Scorpius can be divided into two populations, carrying a distinct kinematic imprint. The existence of a clustered population cannot be attributable to a random concentration of sources, as shown with both a 2D and a 3D kinematic analysis. While the diffuse population does not appear to have been more concentrated in the past, the clustered population shows a clear tendency towards a more compact past configuration. We have further divided the clustered population in 8 groups, the most evident clustering at ~ 4 Myr ago.

This duality within US is clearly reflected in the age determinations obtained through isochrone fitting: the diffuse population is characterized by a flatter age distribution than the clustered population, whose relative youth is consistent with a late burst of star formation. The fraction of stars bearing mark of primordial discs is significantly higher for the latter ($f_D = 0.24 \pm 0.02$) than for the former ($f_D = 0.10 \pm 0.01$).

Even if the absolute ages t_P and t_D provided here should be taken with caution due to known uncertainties in theoretical models, the relative ages are significant, and argue for a strong difference between the populations and, on a lesser extent, among the groups themselves. The star formation history in Upper Scorpius appears to have been heavily substructured, with several small events comprising at most a few hundreds of stars, and spread over ~ 10 Myr. The kinematic structure of the association is still visible inside the youngest part of the association, but has already been erased in the oldest. The systematic differences between kinematic and isochronal ages are likely due to the timescale of gas dispersal, intriguingly building a bridge from the early phases of star formation in molecular clouds to the final stages of star dispersal into the galactic field.

4.A Gaia DR2 corrected bp_rp_excess_factor

A known problem of Gaia's G_{BP} and G_RP photometry is the insensitivity to variation in local background levels, affecting the derived photometry especially for faint magnitudes (Riello et al. 2018). For this reason, Evans et al. (2018) put forward the idea of a quality metric, named *BP-RP excess factor*, which is the ratio of the sum of the two fluxes and the G–band flux:

$$C = \frac{F_{BP} + F_{RP}}{F_G} \tag{4.11}$$

and derives its effectiveness from the behavior of instrumental passbands and response; $C \approx 1$ for well-behaved sources. Riello et al. (2021) show that the actual distribution of C is more complex and color-dependent, with larger expected values at redder colors, and introduce a *corrected BP-RP flux excess factor* C^* defined as:

$$C^* = C - f(G_{BP} - G_{RP}) \tag{4.12}$$

where $f(G_{BP} - G_{RP})$ is an appropriate piecewise polynomial function. C^* is defined in such a way that its expected value is zero for well-behaved sources, and its value can be used as a way to discriminate between sources with *good* and *bad* (G_{BP}, G_{RP}) photometry. As the standard deviation of C^* increases at fainter magnitudes, with standard deviation given by:

$$\sigma_{C^*}(G) = c_0 C + c_1 G^m \tag{4.13}$$

they suggest to remove the sources such that $|C^*| > N\sigma(G)$.

As a thorough analysis of this kind is not known to the authors for Gaia DR2 photometry, it was chosen to follow the same line of reasoning of Riello et al. (2021), but applied to the photometry of Gaia DR2. To start with, we recovered the set of standard stars by Stetson (2000) that was used by Riello et al. (2021), comprising $\sim$ 200000 stars. After reproducing their results for Gaia EDR3 photometry, we repeated the analysis for Gaia DR2. Reasoning in the same way as in their discussion, a piecewise polynomial was fitted to the data (Figure 4.16). However, an additional dependence on magnitude was observed in the corrected excess, showing up as a small counterclockwise rotation in the (G, C^*) plane, well fitted by a straight line.

The final equation defining the *corrected BP-RP excess factor* is given by:

$$C^* = C + a_0 + a_1 \Delta G + a_2 \Delta G^2 + a_3 \Delta G^3 + a_4 G \tag{4.14}$$

where $\Delta G = (G_{BP} - G_{RP})$; numerical values for the constants are provided in Table 4.5. The distribution of C^* peaks at about 0 for well-behaved sources at all magnitudes but, when considering subsamples of stars with similar brightness, it tends to widen out for fainter G (Figure 4.17); a varying standard deviation $\sigma_{C^*}(G)$ can be defined as:

$$\sigma_{C^*}(G) = 0.004 + 8 \times 10^{-12} \times G^{7.55} \tag{4.15}$$

We decided to use a cut at 3σ, as it effectively excludes stars that look visibly far from their expected positions in the $(G_{BP} - G_{RP}, G)$ diagram. The trend of C^* with G for our 2D sample is shown in Figure 4.18: 889/2745 sources (32%) were flagged for unreliable (G_{BP}, G_{RP}) photometry. Given that most of these stars behave well in the (G, J), (G, H) colors, this filter yields a significant improvement of the quality of isochronal age estimates.

Table 4.5: Best-fitting parameters for Eq. 4.14

	$\Delta G < 0.5$	$0.5 \leq \Delta G < 3.5$	$\Delta G \geq 3.5$
a_0	-1.121221	-1.1244509	-0.9288966
a_1	+0.0505276	+0.0288725	-0.168552
a_2	-0.120531	-0.0682774	0
a_3	0	0.00795258	0
a_4	-0.00555279	-0.00555279	-0.00555279

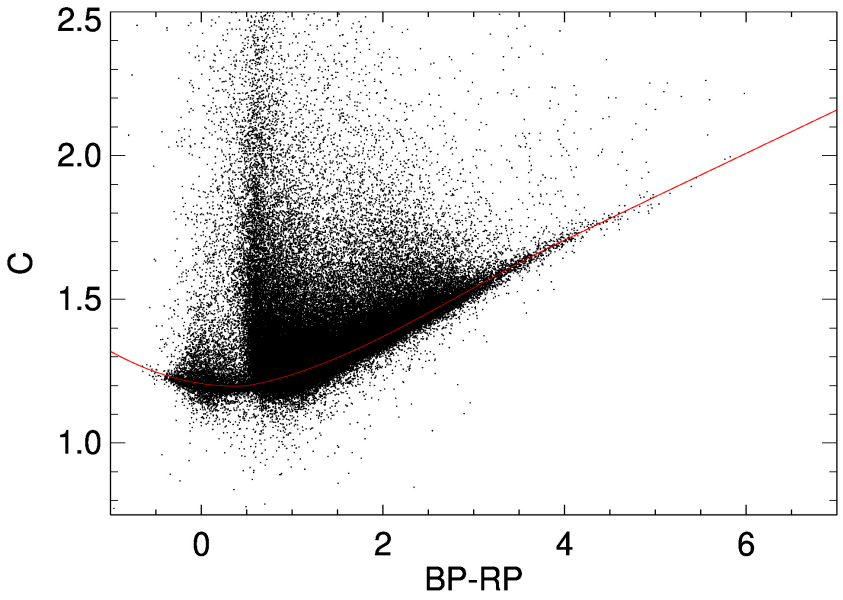

Figure 4.16: Dependence of the bp_rp_excess_factor on $G_{BP}-G_{RP}$ color, using the set of standard stars by Stetson (2000). The best-fitting polynomial is overplotted in red.

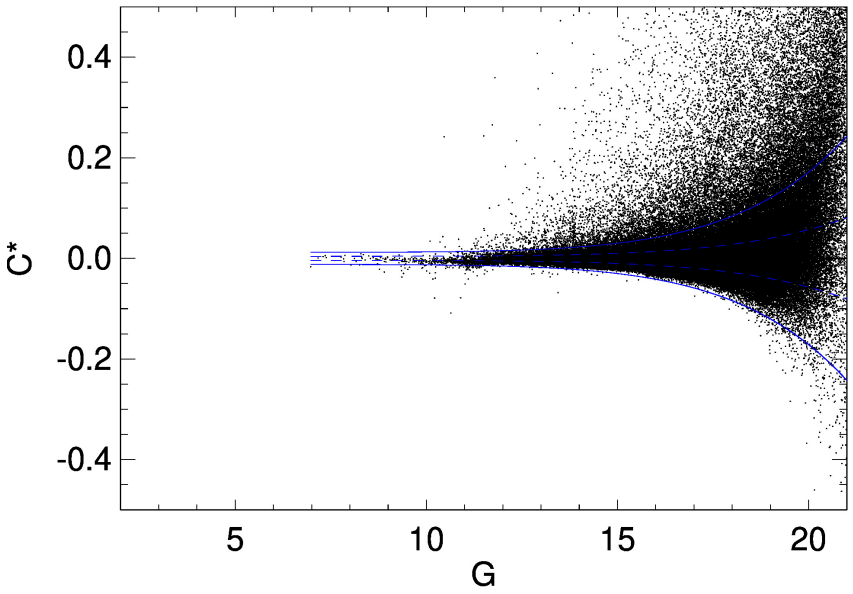

Figure 4.17: Trend of C^* with G for the set of standard stars. As expected, the distribution widens out at fainter magnitudes. In blue, the 3σ threshold that we applied to exclude sources with unreliable (G_{BP}, G_{RP}) photometry.

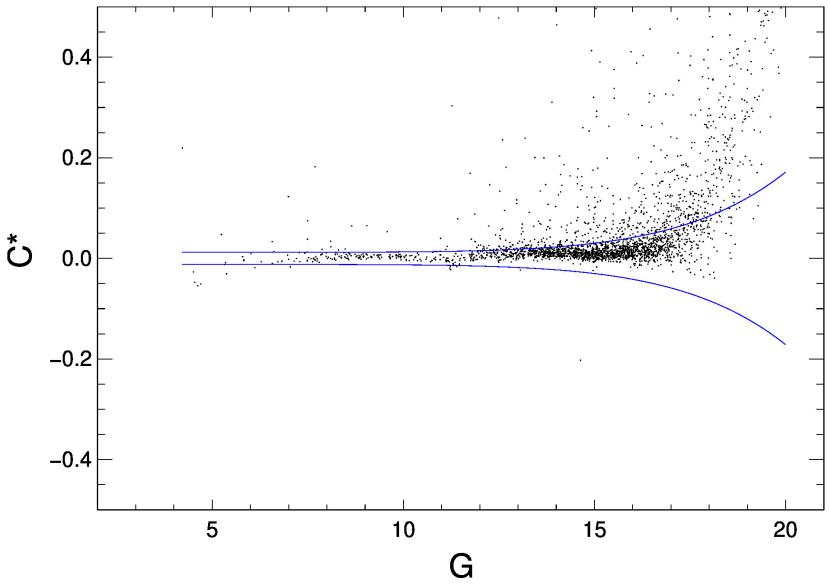

Figure 4.18: Same as Figure 4.17, but using our 2D sample.

4.B Corrected proper motions

Any nonzero motion of an association with respect to the Sun will manifest itself as a bias in the kinematic reconstruction.

Let us suppose, for instance, that a group of stars is rigidly approaching the Sun with velocity $v_{r,c}$. If we conveniently define a Cartesian frame $(\hat{x}, \hat{y}, \hat{z})$ with one axis, let's say $\hat{y}$, connecting the centre of the group to the Sun, we might say that all the stars have velocity $(0, v_{r,c}, 0)$. However, when we describe the position of individual stars on the sky plane, $v_{r,c}$ will be split in $(v_\alpha, v_\delta, v_r)$ depending on the relative (α, δ) with respect to the centre of the association. It is easy to verify that this results in a contribution to proper motions, that are seen to 'escape' from the centre. This is referred to as *virtual expansion*, and reflects the simple idea that the approaching association will span, as time passes, a greater extension on the sky. In a similar way, any tangential motion of the group along x and z will contribute differently to $(v_\alpha, v_\delta, v_r)$ according to (α, δ), producing a spurious velocity difference among group members.

This argument explains why, if interested in the analysis of peculiar motions within an association, one must estimate and subtract from observed proper motions the contribution coming from the bulk motion.

In order to take this factor into account, we began by looking for the centre of Upper Scorpius; starting from our 3D sample, we estimated the centre at approximately $(\alpha_c, \delta_c, r_c) = (244.55°, -23.79°, 143.3$ pc).

Then, we performed a coordinate transformation analogue to that of Eq. 4.3:

$$\begin{cases} x = r\cos(\delta - \delta_c)\sin(\alpha - \alpha_c) \\ y = r\cos(\delta - \delta_c)\cos(\alpha - \alpha_c) \\ z = r\sin(\delta - \delta_c) \end{cases} \tag{4.16}$$

The relation among velocities is found by deriving:

$$\begin{pmatrix} v_x \\ v_y \\ v_z \end{pmatrix} = \begin{pmatrix} r\cos\Delta\alpha\cos\Delta\delta & -r\sin\Delta\delta\sin\Delta\alpha & \cos\Delta\delta\sin\Delta\alpha \\ -r\sin\Delta\alpha\cos\Delta\delta & -r\sin\Delta\delta\cos\Delta\alpha & \cos\Delta\delta\cos\Delta\alpha \\ 0 & r\cos\Delta\delta & \sin\Delta\delta \end{pmatrix} \begin{pmatrix} \mu_\alpha \\ \mu_\delta \\ v_r \end{pmatrix} \tag{4.17}$$

where we define $\Delta\alpha := \alpha - \alpha_c$ and $\Delta\delta := \delta - \delta_c$. We might write, in a compact form, $v_{cart} = Av_{eq}$. Let us consider the simplest case in which the peculiar motions are null, and the associations moves rigidly in the sky with constant (V_x, V_y, V_z). The reflection of the bulk motion in equatorial coordinates is given by $v_{eq} = A^{-1}v_{cart}$, i.e.:

$$\begin{pmatrix} \mu_\alpha \\ \mu_\delta \\ v_r \end{pmatrix} = \begin{pmatrix} \frac{\cos\Delta\alpha}{r\cos\Delta\delta} & \frac{\sin\Delta\alpha}{-r\cos\Delta\delta} & 0 \\ \frac{\sin\Delta\alpha\sin\Delta\delta}{-r} & \frac{\cos\Delta\alpha\sin\Delta\delta}{-r} & \frac{\cos\Delta\delta}{r} \\ \sin\Delta\alpha\cos\Delta\delta & \cos\Delta\alpha\cos\Delta\delta & \sin\Delta\delta \end{pmatrix} \begin{pmatrix} v_x \\ v_y \\ v_z \end{pmatrix} \tag{4.18}$$

In order to get consistent $\mu^*_\alpha = \mu_\alpha \cdot \cos\delta$, μ_δ [mas yr^{-1}] and v_r [km s^{-1}], a conversion factor $p = 1000/4.74$ must be used in the equations for proper motion components.

We estimate bulk Cartesian velocities as the median velocity components of the 3D sample: $(V_X, V_Y, V_Z) = (-7.20\pm0.01, -4.58\pm0.02, -16.29\pm0.01)$ km s^{-1}, where the errors are computed with $N = 10000$ realizations of the same Monte Carlo approach employed throughout this Chapter. The velocity dispersion, computed using the 16th and 84th percentiles of the distribution, corresponds to $(\sigma_{V_X}, \sigma_{V_Y}, \sigma_{V_Y}) = ([-1.98, +2.62], [-1.64, +1.61], [-1.25, +0.50])$ km s^{-1}, for a total 3D dispersion ~ 3 km s^{-1}.

To directly compare our results to those obtained by previous studies, we converted our velocities into the standard galactic right-handed frame UVW, where the origin lies in the Sun, X heads towards the Galactic centre, Y follows the Galactic rotation and Z is directed towards the Galactic North Pole. We find $(U, V, W) = (-4.788 \pm 0.019, -16.378 \pm 0.015, -6.849 \pm 0.016)$ km s^{-1}, comparable with both Galli et al. (2018) and Luhman & Mamajek (2012).

Subtracting the first two equations of Eq. 4.3 from proper motions from Gaia EDR3, we have shifted to a reference frame jointed to US, so that only peculiar motions are left. Projection effects of peculiar motions are not eliminated (see footnote 4), but it's the best we can achieve without possessing radial velocities for all the stars.

Chapter 5

Early results of the BEAST survey

After exploring the link between the current kinematic structure of Upper Scorpius and its star formation history, we turn back our attention to BEAST. At the moment of writing (August 2022), the collection of first-epoch observations has already interested 78 out of 85 targets (92%). 39 second epochs have been acquired, and a smaller number of third (8) and fourth (1) epochs were gathered for particular targets. Considering the number of observations collected over the last two years (24 in 2021, 21 in 2022), we expect the survey to be completed by the end of 2024.

This Chapter will briefly present the first two systems in BEAST showing evidence for the presence of substellar companions, and later devote extensive space to the third such system, the one around μ^2 Scorpii. We defer to the final Chapter 6 an extensive discussion of these early stimulating results of the survey in the context of planet formation models.

HIP79098 (Section 5.1) is a spectroscopic binary that, after being excluded from the target list due to an existing SPHERE observation (cf. footnote 2), was found to possess a companion candidate already detected in the literature. Previous studies discarded it as a background contaminant due to its peculiar colors; conversely, a full astrometric reassessment of archival data allowed Janson et al. (2019) to confirm with confidence level $\approx 3\sigma$ a physical association with the central binary.

In Section 5.2, we will present the first discovery unequivocally based on BEAST observations: a $10.9 \pm 1.6 M_{\rm J}$ companion to the binary b Centauri system (Janson et al. 2021a). Remarkably setting the record for the most massive planet-hosting system to date, this object provides the first piece of evidence for the possibility of planet formation around stars with $M > 3 M_{\odot}$.

The discovery of b Centauri (AB)b acquired even higher significance when coupled with a second detection around the single star μ^2 Scorpii (Squicciarini et al. 2022). With an estimated mass of $M_* = 9.1 \pm 0.3 M_{\odot}$, this star is so massive that it could explode as a supernova in the next 10–20 Myr. Most of this Chapter will be dedicated to the analysis of this unique system, containing a confirmed $14.4 \pm 0.8 M_{\rm J}$ and possibly even a second $\sim 20 M_{\rm J}$ object that would be the most irradiated substellar companion ever discovered through direct imaging.

5.1 HIP 79098

The study of HIP 79098 has been presented in Janson et al. (2019), before the starting date of my Ph.D.. A brief report of the paper is provided here, as it will be useful for the discussion of the survey results presented in Chapter 6.

Table 5.1: Main astrometric, kinematic and photometric properties of HIP 79098 collected from the literature. References: (1): Gaia Collaboration et al. (2018b); (2): Kervella et al. (2019); (3): Worley et al. (2012); (4) Kharchenko & Roeser (2009); (5): Cutri et al. (2003); (6) Abt & Morrell (1995).

Name	Value	Reference
α (°, J2015.5)	242.182120214(33)	(1)
δ (°, J2015.5)	-23.685524394(16)	(1)
μ^*_α (mas yr^{-1})	-10.366 ± 0.013	(2)
μ_δ (mas yr^{-1})	-25.450 ± 0.009	(2)
ϖ (mas)	6.83 ± 0.12	(2)
RV (km s^{-1})	highly variable	(3)
V (mag)	5.881 ± 0.004	(4)
G (mag)	5.8264 ± 0.0006	(1)
J (mag)	4.15 ± 0.28	(5)
H (mag)	4.159 ± 0.25	(5)
K (mag)	4.292 ± 0.31	(5)
spectral type	B9IV	(6)

5.1.1 The star

Based on Gaia DR2, it is possible to establish with 98% probability the membership of HIP 79098 to the Upper Scorpius association (Gagné et al. 2018). The main astrometric, kinematic, and photometric properties of the star are reported in Table 5.1.

Owing to its large RV variability (from -42 km s^{-1} to $+73$ km s^{-1}, Worley et al. 2012), the star has been long recognized as a spectroscopic binary (Levato et al. 1987). If the spectral type of the system reflects that of the primary component, a primary mass $M_* \approx 2.5 M_\odot$ can be derived using the same method as in Section 2.1.2; the mass of the secondary is virtually unconstrained by current observations. The system can be assumed to be 10 ± 3 Myr old on the ground of its membership to US.

Literature studies estimate the color excess in the direction of HIP 79098 to be $E(B-V) \approx 0.12 \pm 0.02$ mag (Norris 1971; Castelli 1991; Pecaut & Mamajek 2013; Huber et al. 2016), corresponding to $A_V = 0.38 \pm 0.06$ mag according to the conversion by Fiorucci & Munari (2003).

5.1.2 Observations and data reduction

A companion candidate was identified in several archival observations:

- a 2000 set from ADONIS (Beuzit et al. 1997) in J and K_s bands, published in Shatsky & Tokovinin (2002); independent observations were acquired in the same period by Kouwenhoven et al. (2005);
- a 2004 set from NACO (Rousset et al. 2003) in J, H, and K_s bands, published in Kouwenhoven et al. (2007a);
- an unpublished 2015 set from SPHERE in K_1 and K_2 bands (Figure 5.1).

SPHERE data were reduced with the SpeCal pipeline using a radial profile subtraction; photometry and astrometry were then extracted from the reduced data by means of template fitting (Galicher et al. 2018).

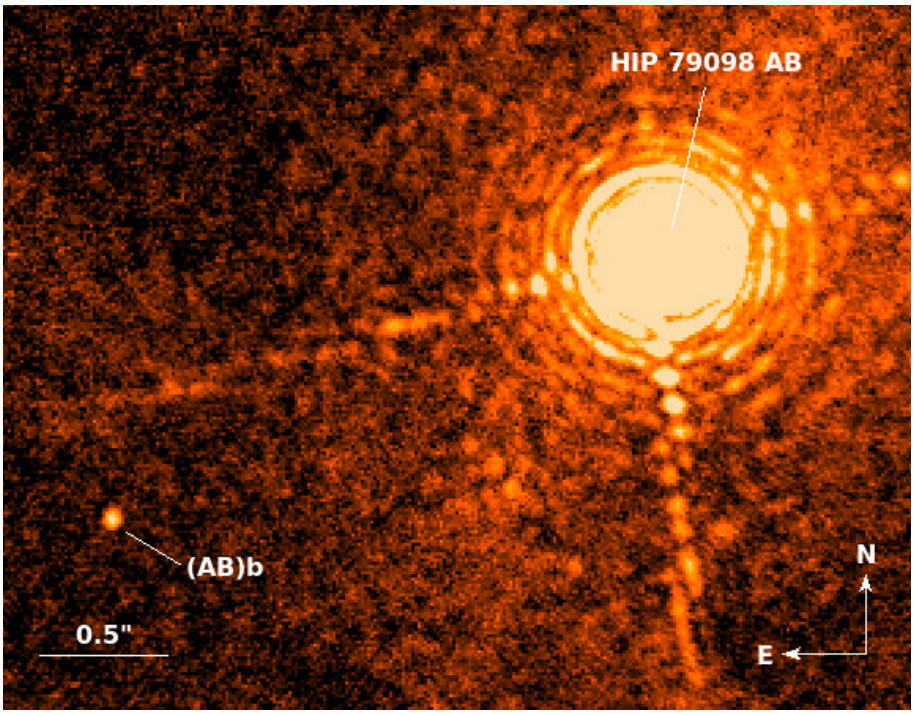

Figure 5.1: SPHERE observation (K_1 band) of HIP 79098 and its companion candidate HIP 79098 (AB)b. No PSF subtraction is applied. Source: Janson et al. (2019).

5.1.3 Companion confirmation

Table 5.2 lists the relative astrometry of the companion candidate with respect to the central binary for the three above-mentioned archival observations. A comparison with the motion expected for a static background object is shown in Figure 5.2. While the source clearly appears to be comoving, a physical association with the target cannot be firmly established without estimating the probability that a background contaminant randomly happens to possess a similar proper motion to the observed one (see, e.g., Nielsen et al. 2017).

In order to test this alternative hypothesis, a synthetic stellar population was generated using the Besançon Galaxy Model interface[1] (Czekaj et al. 2014): selecting stars with distance $d < 50$ kpc, coordinates such that they appear in a 1 deg^2 field centered on HIP 79098, and a K-band magnitude within 2σ from the observed one, a sample of 1675 stars was recovered. The mean proper motion and the associated standard deviation of this sample are (-3.96 mas yr^{-1}, 6.89 mas yr^{-1}) along right ascension, and (-4.52 mas yr^{-1}, 6.95 mas yr^{-1}) along declination; the observed shifts lie $\sim 3.5\sigma$ away, setting a false alarm probability of $\sim 2.6\%$[2]. The conclusion is strongly reinforced by the observation that the probability for a star in the sample to end up within 2.4 arcsec from HIP 79098 only amounts to 0.2%. Similar numbers ($\approx 0.3\%$) are obtained when taking into account 2MASS sources in a $150' \times 150'$ FoV that are at least as bright as the companion candidate in the K band. On the grounds of astrometrical monitoring over a 15-yr baseline, it is therefore possible to unambiguously establish HIP 79098 (AB)b as a substellar circumbinary companion to the central

[1] Available at https://model.obs-besancon.fr/modele_home.php.

[2] The FAP is computed as the fraction of stars exceeding a 3.5σ deviation from the mean in any direction. The value is higher than analytically expected due to non-gaussianity of the actual proper motion distribution.

pair.

Table 5.2: Astrometry of HIP 79098 (AB)b at different epochs.

Date	MJD (d)	Instrument	s (arcsec)	PA (deg)
2000-05-26	51690	ADONIS	2.357±0.033	116.6±0.8
2004-06-09	53165	NACO	2.370±0.011	116.46±0.30
2015-07-20	57223	SPHERE	2.359±0.001	116.13±0.06

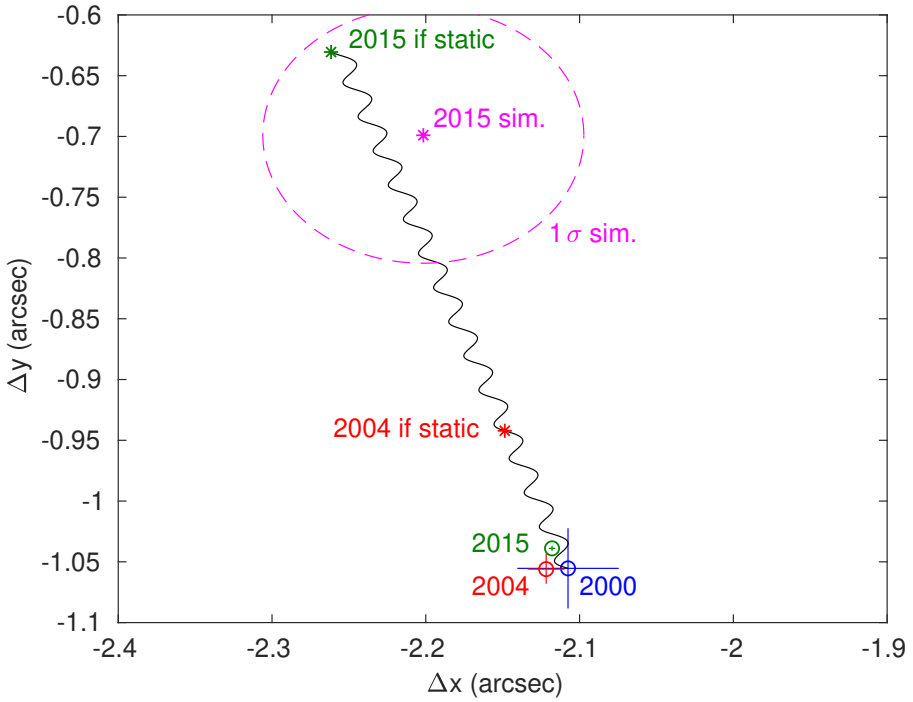

Figure 5.2: Comparison between measured astrometric shifts of HIP 79098 (AB)b (labeled as "2000", "2004", "2015") and the track expected for a static background source, using as reference the 2000 epoch. The mean and 1σ error ellipse of the synthetic background sample are plotted as a magenta asterisk and dashed line, respectively. Source: Janson et al. (2019).

5.1.4 Companion characterization

Given the adopted age for the system, a comparison of the measured photometry with BT-Settl tracks (Table 3.3) yields $M_p \sim [16, 18, 20, 25, 23]$ M_J for J-, H-, K_s-, K_1-, and K_2- photometry, respectively; these estimates correspond to $T_{\rm eff} \in [2300, 2600]$ K and a spectral type in the M9-L0 range according to the near-IR standard spectral templates for young brown dwarfs and low-mass stars (Luhman et al. 2017).

The observed wavelength dependence of the derived mass is consistent with the observation that the object is redder than model predictions: indeed, this was exactly the primary motivation behind the former classification of the source as a reddened background contaminant (Shatsky & Tokovinin 2002; Kouwenhoven et al. 2005, 2007a). More recent studies, including the brown dwarf companion

Table 5.3: Absolute magnitudes, mass, $T_{\rm eff}$ and projected separation for HIP 79098 (AB)b.

J	H	K_s	K_1	K_2	Mass	q	$T_{\rm eff}$	Proj. sep
mag	mag	mag	mag	mag	$M_{\rm J}$		K	au
10.00 ± 0.21	9.07 ± 0.21	8.32 ± 0.21	8.24 ± 0.09	8.02 ± 0.10	16-25	0.003-0.01	2300-2600	345 ± 6

to HIP 64892 discovered in SHINE (Cheetham et al. 2018), have highlighted how the colors of young brown dwarfs can systematically deviate from theoretical expectations (see, e.g., Liu et al. 2013; Gizis et al. 2015; Bonnefoy et al. 2016; Faherty et al. 2016).

With a mass $M_p \in [16, 25] M_{\rm J}$, and taking into account the ignorance about the secondary mass, the companion has a mass ratio $q = 0.3-1\%$ with respect to the binary. We will discuss in Chapter 6 whether, from a formation standpoint, the key quantity for stars of varying masses is the mass or the mass ratio; for the moment, we stress that the mass of HIP 79098 (AB)b lies beneath – that is, on the planet-like side of – the brown dwarf desert identified for solar-type stars (Ma & Ge 2014), and that its mass ratio would be typical of Super Jupiters for $M \sim 1 M_\odot$ primaries.

A summary of the properties of the companion is provided in Table 5.3.

5.2 HIP 71865 = b Centauri

The work on b Centauri was presented in a paper on the high-impact journal Nature (Janson et al. 2021a). The impact of our findings is due to the fact that this was the first planet discovered around a massive early-B binary, breaking by a factor 2-4 the previous limit of $\sim 2.7 M_\odot$. My main contribution to the work involved the discussion of the age of the star and its location within the Sco-Cen association.

5.2.1 The star

HIP 71865 = b Centauri (b Cen) is a member of the Upper Centaurus-Lupus region of Sco-Cen (Table 2.1). Based on the age map introduced in Section 2.3, we were able to assign to this star an age $t = 15$ Myr; as regards the uncertainty associated to the estimate, we observed that the standard deviation in a circular region with radius 5° centered on b Cen is only 1 Myr: we assign our star a conservative uncertainty of ±2 Myr.

As for HIP 79098, the source is actually an unresolved binary system, first recognized thanks to radial velocity variations (Gutierrez-Moreno & Moreno 1968). The primary component has a spectral type B2.5V (Houk 1982), corresponding to $T_{\rm eff} = 18310 \pm 320$ K (Janson et al. 2021a). A possible interferometric detection of the second component by the Sydney University Stellar Interferometer (SUSI; Davis et al. 1999) is reported by Rizzuto et al. (2013) at a projected separation $s = 9.2$ mas $\equiv 1.0$ au; however, the combination of a single-epoch, single-baseline observation and low S/N urges extreme caution in the interpretation of this data point; in particular, the measured contrast (1.06 mag in the R band) should be treated as a lower limit.

At the present time, dynamical data are insufficient to derive the orbital properties of the system, that would yield valuable model-independent masses. An isochronal analysis of the system was therefore performed using PARSEC isochrones (Table 3.3), assuming two extremes scenarios which likely delimit the true system masses:

1. the flux of b Cen B is negligible with respect to that of b Cen A;

Table 5.4: Main astrometric, kinematic and photometric properties of HIP 79098 collected from the literature. References: (1): Gaia Collaboration et al. (2018b); (2): Kervella et al. (2019); (3): Gutierrez-Moreno & Moreno (1968); (4): Wolff et al. (2007); (5) Kharchenko & Roeser (2009); (6): Cutri et al. (2003); (7) Houk (1982).

Name	Value	Reference
α (°, J2015.5)	220.48979918(16)	(1)
δ (°, J2015.5)	-37.79363232(12)	(1)
μ^*_α (mas yr^{-1})	-29.798 ± 0.026	(2)
μ_δ (mas yr^{-1})	-30.959 ± 0.020	(2)
ϖ (mas)	10.24 ± 0.64	(2)
RV (km s^{-1})	variable	(3)
$V \sin i$ (km s^{-1})	129	(4)
V (mag)	3.990 ± 0.002	(5)
G (mag)	3.924 ± 0.006	(1)
J (mag)	4.637 ± 0.244	(6)
H (mag)	4.628 ± 0.076	(6)
K (mag)	4.487 ± 0.026	(6)
spectral type	B2.5V	(7)

2. the R-band contrast between the two components is exactly equal to that measured by SUSI.

In the former case, a similar value to the one determined spectroscopically (Table 2.2) is obtained ($M_A = 6M_\odot$); in the latter case, the derived masses are $M_A = 5.6M_\odot$ and $M_B = 4.4M_\odot$. In the light of the uncertainties on the properties of the secondary, we adopt a weak constraint on the total mass: $M_* \in [6, 10]M_\odot$.

Based on literature studies, we estimate the color excess in the direction of b Cen to be $E(B - V) \approx 0.015 \pm 0.005$ mag (Niemczura 2003; Fitzpatrick & Massa 2005), corresponding to $A_V = 0.047 \pm 0.016$ mag. We summarize the main astrometric, kinematic, and photometric properties of the system in Table 5.4.

5.2.2 Observations and data reduction

The first observation of b Cen was collected on 20 March 2019. Three companion candidates were detected in the IRDIS FoV (Figure 5.3); a second observation was therefore acquired on 10 April 2021. Due to the lack of CCs in the IFS FoV, this observation was taken with IRDIS in a stand-alone mode, employing the J_2 ($\lambda_{\rm peak} = 1.190$ μm) and J_3 ($\lambda_{\rm peak} = 1.273$ μm) bands to expand as much as possible the photometric coverage of the sources.

Image calibration and data reduction were performed following the standard scheme (Section 2.4.2). In particular, negative injection of fake planets was used to extract photometry and astrometry in the TLOCI reduction. Astrometric and photometric properties of the three CCs are reported in Table 5.5.

An additional archival observation of the brightest CC was found in Shatsky & Tokovinin (2002): due to its faintness with respect to the star, the source was there assumed to be a background contaminant. We will prove in the next Section 5.2.3 that the source is actually a physical companion to b Cen; in this regard, this serendipitous epoch turned out to be extremely useful for the purpose of orbital analysis, extending the temporal baseline to ~ 21 yr.

Table 5.5: Astrometric and photometric properties of the companion candidates detected around b Cen. Here the apparent magnitudes $(F_1, F_2) = (K_1, K_2)$ for the 2018 epoch, (J_2, J_3) for the 2021 epoch, and n.d. = not detected.

ID	MJD	s	PA	F_1	F_2
		mas	$^\circ$	mag	mag
1	51690	5301 ± 53	243.1 ± 0.1	—	—
	58563.33	5351.76 ± 3.66	241.872 ± 0.034	16.37 ± 0.06	16.13 ± 0.06
	59315.27	5362.04 ± 6.69	241.722 ± 0.068	17.98 ± 0.25	17.64 ± 0.25
2	58563.33	3625.80 ± 14.99	262.217 ± 0.152	20.90 ± 0.18	n.d.
	59315.27	3552.06 ± 8.68	263.064 ± 0.134	23.02 ± 0.48	23.14 ± 0.52
3	58563.33	4954.49 ± 3.74	279.346 ± 0.035	18.50 ± 0.06	18.40 ± 0.08
	59315.27	4919.19 ± 6.08	280.124 ± 0.067	19.90 ± 0.25	19.62 ± 0.25

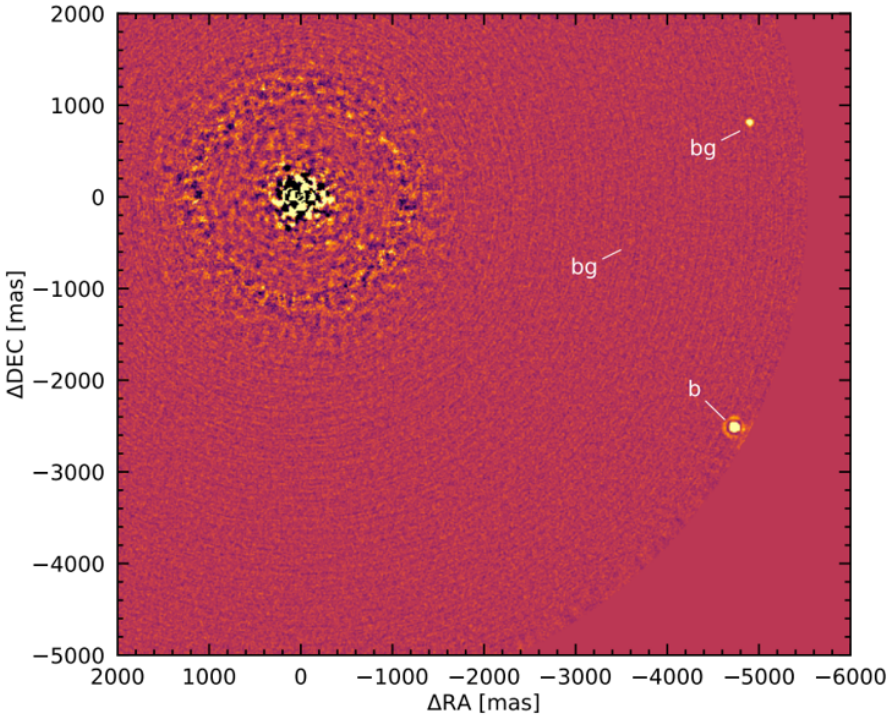

Figure 5.3: SPHERE observation (J_2 band) of b Centauri; the central binary, lying at the origin of the reference frame, is artificially obscured by the coronagraph. The substellar companion is labeled by "b", while the two background sources are indicated through "bg". Source: Janson et al. (2021a).

Table 5.6: Best-fit bolometric luminosity, mass, projected separation, semimajor axis, eccentricity and inclination for b Cen b.

$\log L_p/L_\odot$	Mass M_J	q	Proj. sep au	e	i $^\circ$
-3.98 ± 0.19	10.9 ± 1.6	0.0010-0.0017	556 ± 17	<0.4	128-157

5.2.3 Companion confirmation

Using the astrometric measurements taken in 2019 and 2021, the motion of the sources with ID = 2 and ID = 3 is consistent with the one expected for background sources. Conversely, the source with ID = 1 in Table 5.5 shows strong evidence for common proper motion with the target, being $\approx 14.2\sigma$ away from the position expected in the second epoch for a static background source. A more realistic assessment of the matter, taking into account the proper motion distribution of background sources, was performed in a similar way as we have seen for HIP 79098 (Section 5.1.3): the hypothesis that the observed astrometric shifts of the CC are due to an extreme high-proper motion background source can be rejected at a confidence level 7.3σ. We were therefore able to conclude that the source is a physical companion to the b Cen binary system: from this moment on, we will refer to the companion as *b Cen (AB)b* or *b Cen b*.

Orbital parameters for the companion were derived by fitting an orbit to the three astrometric epochs (2000, 2019, 2021) through the orbitize! Python package[3] (Blunt et al. 2020). The results are shown in Figure 5.4.

5.2.4 Companion characterization

After combining photometric contrasts in the four measured bands with 2MASS magnitudes for the primary (Table 5.4), an estimate of the bolometric luminosity L_p was obtained by comparison with AMES-Cond and AMES-Dusty models (Table 3.3). The resulting $\log L_p/L_\odot = -3.98 \pm 0.19$ was then compared to a range of possible initial entropies of the planet as done in Marleau et al. (2019a), yielding an average mass estimate $M_p = 10.9 \pm 1.6 M_\mathrm{J}$. Based on the current definition of exoplanet (Section 1.3), b Cen turned out to be the most massive stellar system hosting an exoplanet, surpassing by 2-4 times the former record-holding star, HD 106906 AB (Nguyen et al. 2021); very intriguingly, its mass ratio to the central binary is similar to that of Jupiter to the Sun.

The final parameters of the system are summarized in Table 5.6.

5.3 HIP 82545 = μ^2 Scorpii

These findings are described in a paper published on *Astronomy and Astrophysics* which I led (Squicciarini et al. 2022). In addition to the overall responsibility of the paper, most of the writing and of the scientific discussion, my specific contributions to this paper concerned the identification and the analysis of the kinematic subgroup where μ^2 Sco abides, the determination of its main astrophysical parameters – notably distance and age –, the astrometric analysis of all companion candidates, the confirmation of the physical association of two sources with the target after a careful assessment of false alarm probabilities, the complete characterization of both the confirmed and the probable companion and, finally, the comparison between a star-like and a planet-like formation scenario for the BEAST companions discovered so far (see Chapter 6). The paper was also selected

[3]Available at https://github.com/sblunt/orbitize .

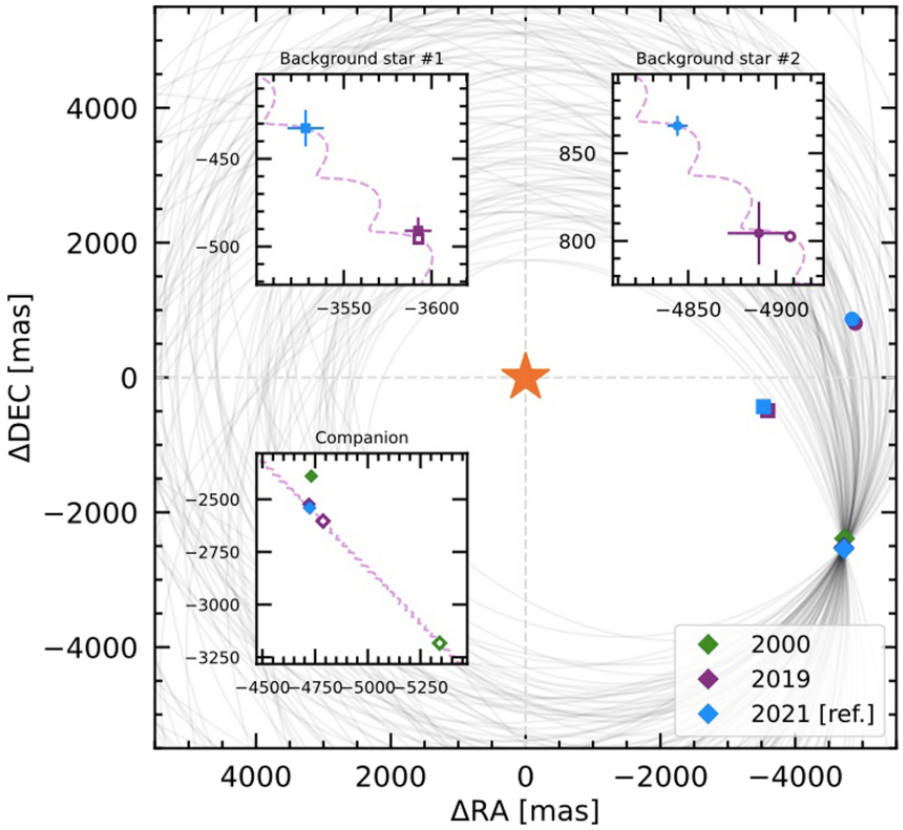

Figure 5.4: Astrometric motion of the three CCs spotted around b Cen (indicated through the orange star). Squares and circles indicate the locations of the background stars with ID = 2 and 3, respectively; diamonds refer to b Cen (AB)b. The colors code the three epochs (2000=green, 2019=purple, 2021=blue), while filled and open symbols indicate the measured and predicted motion for a static background source, respectively. In the main figure, gray tracks represent a sample of possible orbits for b Cen (AB)b. Source: Janson et al. (2021a).

Table 5.7: Main astrometric, kinematic and photometric properties of μ^2 Sco collected from the literature. References: (1): Gaia Collaboration et al. (2021); (2): Kervella et al. (2019); (3): Gontcharov (2006); (4): Brown & Verschueren (1997); (5) Mermilliod (2006); (6): Cutri et al. (2003); (7) Hiltner et al. (1969).

Name	Value	Reference
α (°, J2016.0)	253.083869820(64)	(1)
δ (°, J2016.0)	-38.017636551(38)	(1)
μ^*_α (mas yr^{-1})	-11.772 ± 0.022	(2)
μ_δ (mas yr^{-1})	-23.105 ± 0.021	(2)
RV (km s^{-1})	1.3 ± 0.8	(3)
$v \sin i$ (km s^{-1})	52 ± 5	(4)
V (mag)	3.565 ± 0.005	(5)
G (mag)	3.543 ± 0.003	(1)
J (mag)	4.15 ± 0.28	(6)
H (mag)	4.159 ± 0.25	(6)
K (mag)	4.292 ± 0.31	(6)
spectral type	B2IV	(7)

as a research highlight by Nature (Nature 609, 13 (2022)) because it presented the first evidence for a planet-like system around a star that will eventually explode as a supernova.

5.3.1 The star

μ^2 Sco (also known as HR 6252, HD 151985, HIP 82545, Pipirima[4]) is a naked-eye star belonging to Upper Centaurus Lupus (Table 2.1). Its main astrometric, kinematic, and photometric properties are reported in Table 5.7.

Recalling that several stellar parameters (notably distance, age and mass) are of utmost importance for the characterization of directly imaged exoplanets, our primary goal was to reduce the large uncertainty on distance that had historically limited a self-consistent physical analysis of μ^2 Sco. After exploiting for the first time kinematic information to indirectly constrain its distance, we combined this new information with data from the literature to perform a Monte Carlo analysis that determines posterior distributions for stellar mass, age, radius and effective temperature. A discussion on the adopted priors is provided in Section 5.3.1.1-5.3.1.6, and the derivation of the final parameters is done in Section 5.3.1.7.

5.3.1.1 Distance and membership to the Eastern Lower Scorpius group

μ^2 Sco appears to lie within a small clump of stars (a region centered on galactic coordinates $(l, b) = (343.1°, 4.7°)$ with a radius of about 2° that, while classically assigned to UCL (de Zeeuw et al. 1999), has recently started being recognized in its own right as an independent entity (Röser et al. 2018). This group, which we will refer to as Lower Scorpius (LS), is still poorly known: hence, we performed a more specific characterization.

[4]Pipirima is the Tahitian name for the pair μ^2 and μ^1 Sco, referring to mythological twin siblings. The IAU Working Group on Star Names (WGSN) adopted Pipirima as the proper name for μ^2 Sco in 2017 (https://www.iau.org/public/themes/naming_stars/).

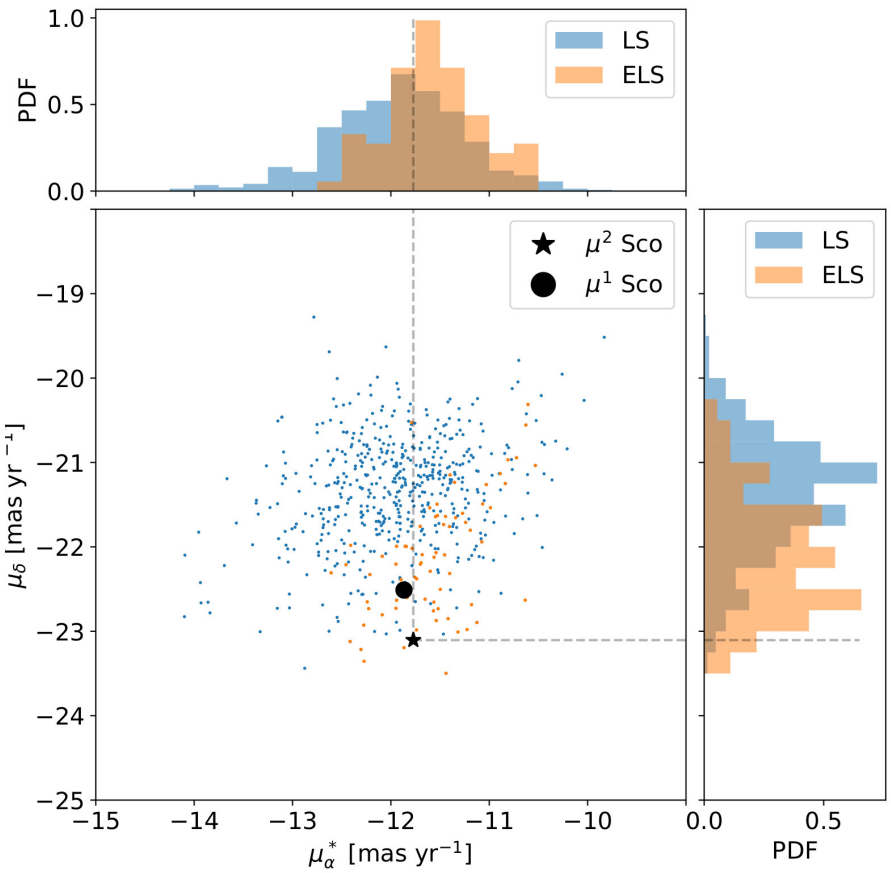

Figure 5.5: Proper motion components of LS (blue) and ELS (orange) members. Both μ^1 Sco and μ^2 Sco are consistent with membership to ELS.

Starting from the Gaia DR2-based catalog of bona fide Sco-Cen sources by Damiani et al. (2019), we create a census of LS stars (575 members) through the criteria shown in Table 5.8. We also crop from the same catalog an UCL sample, to be used for comparison purposes, using the classical boundaries by de Zeeuw et al. (1999) and excluding the sources already assigned to LS.

Inspection of the Gaia EDR3 catalog reveals an inconsistency of the star's proper motions with those of LS and a parallax that, although consistent with LS, suffers from a large uncertainty. The values of Gaia EDR3, however, are also inconsistent with those from Gaia DR2 and Hipparcos (Table 5.14). The inaccuracy of the astrometric solution in Gaia for such a bright star (which saturates the detector) is expected without invoking the presence of an unresolved stellar companion (Appendix 5.3.A). Adopting the robust long-term proper motion by Kervella et al. (2019), computed as the difference between the astrometry of Hipparcos (J1991.25) and Gaia DR2 (J2015.5), the star is fully consistent with membership to LS (Figure 5.5).

We notice that our target (together with its sibling μ^1 Sco) actually lies in a peripheral area of LS, $\sim 2^\circ$ eastward of its core: using the more sensitive Gaia EDR3 to expand the census of LS to fainter stars, we constructed a catalog of members of this small clump that includes 73 stars, that we call Eastern Lower Scorpius (ELS; see Table 5.8, Figure 5.6). ELS appears somewhat closer to the Sun than the whole LS: we adopt its parallax distribution (modeled as a normal, $\varpi = 5.9 \pm 0.2$

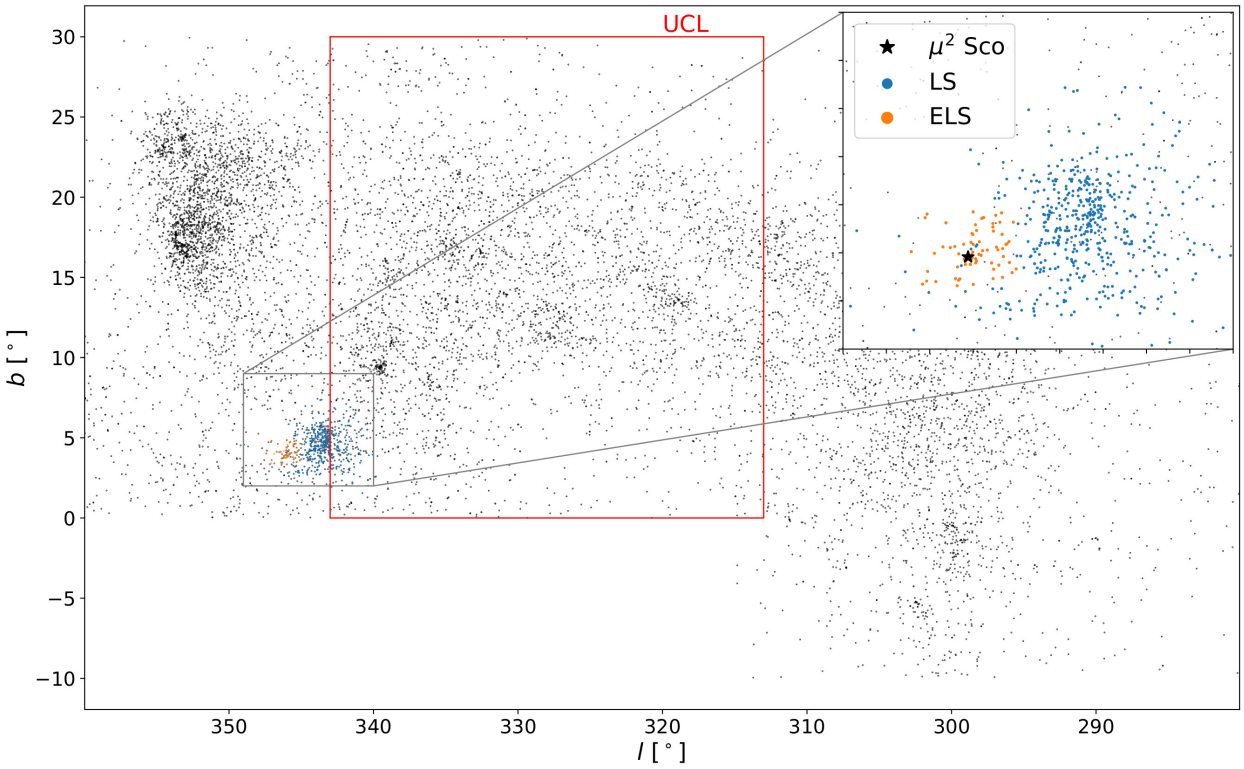

Figure 5.6: Sky coordinates of bona fide Sco-Cen members from Damiani et al. (2019), shown as black dots. Classical boundaries for UCL are indicated by the red box. A zoom of LS (blue) and ELS (orange) region is drawn in the upper-right corner; μ^2 Sco is indicated by the black star.

mas) as our parallax prior (Figure 5.7).

5.3.1.2 Mass and radius

The mass estimate in the first BEAST paper (Table 2.2) was based on an underestimated distance from Gaia DR2: we therefore expect a higher mass than previously assumed. We conservatively start from a uniform prior distribution, $M \in [5, 12] M_{\odot}$. Likewise, we do not favor a particular initial value for the radius: $R \in [3.5, 10.0]$ $R_{\odot}$. For a B2V star on the main sequence we expect $R \sim 4$ $R_{\odot}$ (Pecaut & Mamajek 2013), but the classification of the star as a B2IV (Hiltner et al. 1969) argues for a larger radius.

5.3.1.3 Age

Using our tool MADYS (Chapter 3), we collected photometry from Gaia DR2/EDR3 and 2MASS for both LS and ELS and compared it to PMS isochrones to simultaneously derive individual mass and age estimates for their members. To avoid known systematic uncertainties on absolute ages with this method, we decided to employ the whole UCL ($\sim$ 4000 stars) as a control sample, comparing the derived age distributions with each other.

The age distribution of ELS stars, derived by comparison with the BHAC15 isochrones (Table 3.3 of solar metallicity, is consistent with that of the whole UCL according to a Kolmogorov-Smirnov

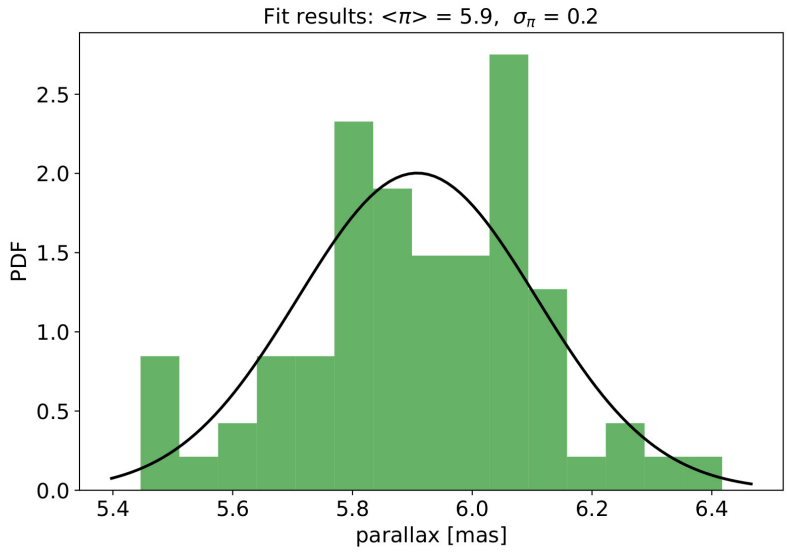

Figure 5.7: Parallax distribution of ELS stars. We adopt $\varpi = 5.9 \pm 0.2$ mas as parallax prior for μ^2 Sco.

Table 5.8: Defining criteria for the UCL, LS and ELS samples used throughout this paper. The criteria should be interpreted as an addition to the cuts already applied in the definition of the initial catalog. Equatorial coordinates and proper motions refer to the ICRS at epoch J2016.0.

Criterion	UCL	LS	ELS
initial catalog	Damiani et al. (2019), bona fide sources	Damiani et al. (2019), bona fide sources	Gaia EDR3
galactic longitude (°)	$313 < l < 343$	$339 < l < 350$	$345 < l < 347.5$
galactic latitude (°)	—	$1.5 < b < 7.7$	$3.3 < b < 5.0$
right ascension (°)	—	—	$251 < \alpha < 255$
declination (°)	—	—	$-40 < \alpha < -36$
parallax (mas)	—	$5.3 < \varpi < 6.2$	$5.3 < \varpi < 6.5$
proper motion along α (mas yr^{-1})	—	—	$-18.7 < \mu^*_\alpha < -10.2$
proper motion along δ (mas yr^{-1})	—	—	$-25.0 < \mu_\delta < -16.1$
velocity along α (km s^{-1})	—	$-11.2 < v_\alpha < -8.5$	$-10 < v_\alpha < -7$
velocity along δ (km s^{-1})	—	$-19.3 < v_\delta < -16.5$	$-21 < v_\alpha < -16$
no. of sources	3842	575	73

test ($\alpha = 0.05$)[5].

In the absence of tighter constraints, we adopt the age of UCL ($t = 16 \pm 7$ Myr: Pecaut & Mamajek 2016) as our age prior.

We highlight that an independent age estimate could come in the next years from asteroseismology: based on its light curve from TESS (Ricker et al. 2015), the star, clearly evolved off the zero-age main sequence, shows evidence for β Cephei type variability and in particular for that of a slowly pulsating B-star (SPB) β Cep hybrid. A quantitative analysis of the observed wealth of pulsational modes – especially if complemented by new observations in different photometric bands – might constitute the subject of a future work aimed at estimating the core hydrogen fraction, closely related to stellar age.

5.3.1.4 Reddening

To estimate the reddening $E(B-V)$ in the direction of μ^2 Sco in a robust way, we considered six different determinations:

- starting from UBV photometry from Mermilliod (2006) and $uvby\beta$ photometry from Hauck & Mermilliod (1997), we employ the Q-method of Johnson & Morgan (1953) to deredden OB stars with the modern calibration of Pecaut & Mamajek (2013): $E(B-V) = 0.022$ mag;
- dereddening the $uvby\beta$ photometry through the calibration of Castelli (1991): $E(B-V) = 0.019$ mag;
- dereddening the $uvby\beta$ photometry with the older, independent calibration of Shobbrook (1983): $E(B-V) = 0.020$ mag;
- from Lyman α observations, Savage & Panek (1974) estimate the interstellar column density of HI toward μ^2 Sco to be $N(H) = 2.5 \cdot 10^{20}$ cm^{-2}. Adopting the recent relation between interstellar reddening and hydrogen column densities by Lenz et al. (2017), valid in the low column-density regime as in our case: $E(B-V) = 0.031$ mag;
- starting from the absorption EW(D1) of interstellar neutral sodium (NaI) D1 line toward μ^2 Sco by Hobbs (1978), and using the reddening vs EW(D1) correlation by Poznanski et al. (2012): $E(B-V) = 0.019$ mag;
- integrating the STILISM 3D reddening map (Lallement et al. 2018) along the line of sight up to a distance $d = 165$ pc: $E(B-V) = 0.025 \pm 0.024$ mag.

By averaging these estimates, we obtain $E(B-V) = 0.022 \pm 0.006$ mag. Adopting a total-to-selective extinction ratio $R_V = A_V/E(B-V) = 3.05$, appropriate for early B-type stars (McCall 2004), we estimate $A(V) = 0.068 \pm 0.015$ mag and $A(K) = 0.0062 \pm 0.0014$. Being negligible with respect to photometric errors, extinction values will be from this moment on treated as constants.

[5]The higher (~ 5 and ~ 4 times, respectively) density of LS and ELS with respect to the coeval UCL is likely due to significant self-gravity, slowing down the expansion caused by random turbulent motion within the natal molecular cloud. Indeed, the dispersion of proper motions of ELS (0.71 mas yr^{-1} $\approx$ 0.55 km s^{-1} is lower than the escape velocity of ~ 0.72 km s^{-1} obtained by summing the masses of all observed members ($\sim 50\ M_\odot$) and considering its projected size ($\rho \sim 17' \sim 0.85$ pc). The lifetime of a small cluster such as ELS against tidal disruption is about 35 Myr (Lamers et al. 2005), about twice its estimated age.

Table 5.9: New effective temperature estimates for μ^2 Sco. Details on the derivation of each estimate are provided in the text.

#	$T_{\rm eff}$ (K)
1	20913
2	21083
3	21655
4	21989
5	22063
6	22700 ± 270
7	25978
adopted	21900 ± 1000

5.3.1.5 Effective temperature

Concerning the stellar effective temperature, μ^2 Sco – persistently classified as a B2IV star (Hiltner et al. 1969) – has a nearly identical combination of colors and reddening ($B-V=-0.214$, $U-B=-0.844$, $E(B-V)=0.022$) to the Morgan-Keenan B2IV standard star δ Cet ($B-V=-0.219$, $U-B=-0.850$, $E(B-V)=0.018$) which has a median $T_{\rm eff}$ in the recent literature of $T_{\rm eff} \simeq 21600$ K (Cardiel et al. 2021). Hence we do not expect the effective temperature of μ^2 Sco to differ too much from that of δ Cet.

In Table 5.9 we list several new $T_{\rm eff}$ estimates for μ^2 Sco based on photometric data from the literature. The estimates are derived in the following way:

1. photometry from Hauck & Mermilliod (1997), dereddened through Castelli (1991) using Balona (1994) $T_{\rm eff}$ calibration;
2. photometry from Hauck & Mermilliod (1997), $T_{\rm eff}/H_\beta$ relation by Balona (1984);
3. employing the $(U-B)_o$ vs $T_{\rm eff}$ trend based on B2IV standard stars Pecaut & Mamajek (2013);
4. photometry from Hauck & Mermilliod (1997), dereddened through Castelli (1991) using Napiwotzki et al. (1993) $T_{\rm eff}$ calibration;
5. photometry from Hauck & Mermilliod (1997), using [c1] index adopting Nieva (2013) $T_{\rm eff}$ scale;
6. comparing IUE spectrophotometry[6] in the wavelength range [110-195] nm with the grid of model atmospheres by Castelli & Kurucz (2003);
7. photometry from Hauck & Mermilliod (1997), using [u-b] index adopting de Geus et al. (1989) $T_{\rm eff}$ scale.

We adopted the averaged value ($T_{\rm eff} = 21900 \pm 1000$ K) as our $T_{\rm eff}$ prior.

5.3.1.6 Surface gravity

The stellar surface gravity was not used as a free parameter, but rather as one of the observational constraints for the optimization tests. Based on literature estimates (Table 5.10), we adopted a value of $\log g \in [3.6, 4.0]$.

[6]Taken from https://archive.stsci.edu/iue/.

Table 5.10: Literature surface gravity estimates for μ^2 Sco. References for each estimate are provided in the first column. References: (1): de Geus et al. (1989); (2): Wolff (1990); (3): Grigsby et al. (1992); (4): Nieva (2013).

Source	$\log g$
(1)	3.9 ± 0.2
(2)	3.9
(3)	3.6 ± 0.2
(4)	3.916
adopted	3.8 ± 0.2

5.3.1.7 Derivation of stellar parameters

Our optimization tests for the parameters of μ^2 Sco start from the prior distributions of $(M, R, T_{\rm eff}, \varpi)$ described in Section 5.3.1. We create a synthetic sample of 10^7 stars, each one described by a quadruplet $(M, R, T_{\rm eff}, \varpi)$, where every parameter is randomly drawn from its prior distribution. The empirical table of intrinsic colors and temperatures of 5-30 Myr old stars by Pecaut & Mamajek (2013) allows a straightforward conversion of bolometric luminosities into V magnitudes by means of calibrated bolometric corrections. Starting from the stellar luminosity expected for main sequence stars:

$$\frac{L}{L_\odot} = \left(\frac{R}{R_\odot}\right)^2 \cdot \left(\frac{T}{T_\odot}\right)^4, \tag{5.1}$$

we apply the interpolated bolometric correction as a function of $T_{\rm eff}$, the fixed extinction and the derived distance modulus to get synthetic apparent V magnitudes. A filter was then applied to select only the quadruplets that simultaneously satisfy the three conditions:

- $V \in [3.52, 3.60]$, where the broadened error bar allows for some uncertainty in the bolometric correction itself;
- $\log g \in [3.6, 4.0]$;
- a mass M such that $|M - M_L|/M < 0.15$, where M_L is the mass derived through a $L(M)$ relation valid for main sequence stars with $M > 2\ M_\odot$.

The $L(M)$ relation (in solar units) is derived, for consistency, by fitting L as a function of M using the same tables:

$$\log L = 0.47 + 3.36 \log M. \tag{5.2}$$

Although the mean fractional error of the fitted points is about 4%, we opted for a less stringent 15% tolerance to account for possible deviations from the standard behavior of the underlying sample. We underline that this test does not allow to constrain the age of the star, since the tables are built by averaging over stars of different ages.

The posterior distributions of $(M, R, T_{\rm eff}, \varpi)$ are shown in Figure 5.8. While the mean values of effective temperature and distance do not change significantly, a strong preference for a large value of radius appears ($R = 5.8 \pm 0.3\ R_\odot$), while the mass distribution shifts to very high values ($M = 10.0^{+1.0}_{-0.9}\ M_\odot$).

Considering that older stars on the main sequence are brighter, that is, age and mass are anti-correlated for MS stars of the same magnitudes, we expect our mass estimate to be corrected toward higher or lower values depending on the adopted age. In order to introduce the age into the

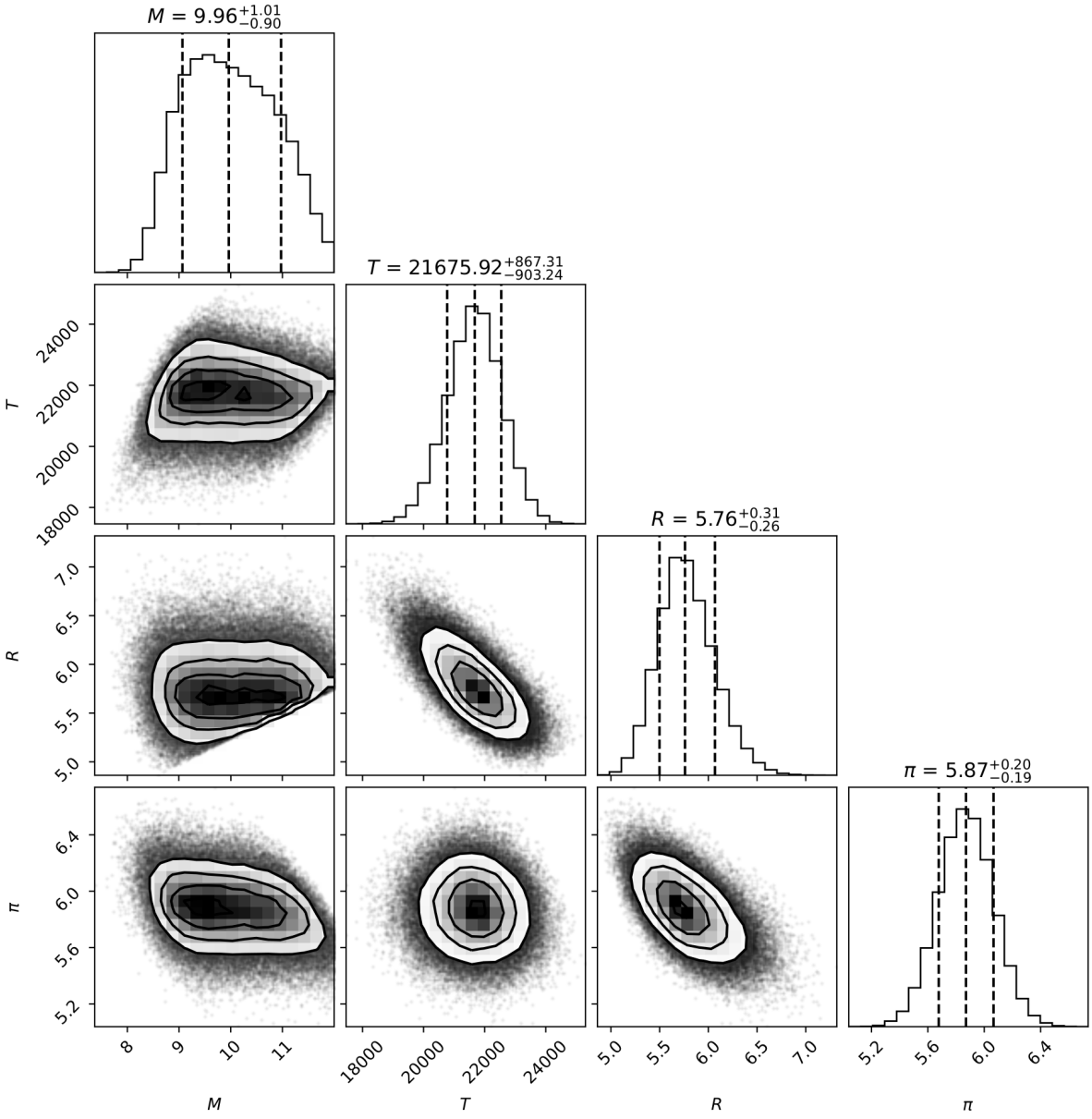

Figure 5.8: Results of the first optimization test of stellar parameters. Corner plot showing the posterior distribution of the quadruplets $(M, R, T_{\rm eff}, \varpi)$ consistent with the observational filter for the optimization test based on Pecaut & Mamajek (2013).

Table 5.11: Stellar parameters of μ^2 Sco derived in this Chapter.

Name	Value
parallax (mas)	5.9 ± 0.2
$T_{\rm eff}$ (K)	21700 ± 900
$E(B-V)$ (mag)	0.022 ± 0.006
$A(V)$ (mag)	0.068 ± 0.015
age (Myr)	20 ± 4
mass ($M_\odot$)	9.1 ± 0.3
radius ($R_\odot$)	5.6 ± 0.2

discussion, we ran a similar but independent test that only relies on PARSEC isochrones (Marigo et al. 2017) of varying age and metallicity; drawing 10^7 masses and parallaxes as above, we selected the combinations that simultaneously satisfied:

- apparent Gaia magnitudes (G, G_{BP}, G_{RP}) within 0.1 mag from their observed values; absorption coefficients were taken from Wang & Chen (2019);
- a derived $\log(g) \in [3.6, 4.0]$ as before;
- $T_{\rm eff} \in [20900, 22900]$ K.

The test could never be passed using the nominal age ($t = 16$ Myr) and metallicity ([[Fe/H] = 0.00), but increasing at least one of the two constraints ($t \in [16, 25]$ Myr or [Fe/H] $\in [0.10, 0.20]$) a family of solutions appeared (Figure 5.9-5.10); the posterior mass distribution is consistent with the result of the first test ($M = 8.8 \pm 0.3\ M_\odot$ for the run at constant metallicity, $M = 9.2 \pm 0.2\ M_\odot$ for the run at constant age; we may combine the two to get $M = 9.0 \pm 0.3\ M_\odot$). We average the two mass determinations from the independent methods to a derive a final $M = 9.1 \pm 0.3\ M_\odot$. In the same way, we derive $R = 5.6 \pm 0.2\ R_\odot$; the median values of the posteriors of the first test will be used as best-fit estimates for $T_{\rm eff}$ and ϖ. Finally, while we are not able to solve the age-metallicity degeneracy, we encapsulate the general tendency for a larger age in a revised age estimate $t = 20 \pm 4$ Myr.

We list in Table 5.11 the final parameters obtained in this Section.

With a spectral type of B2IV, corresponding to a best-fit effective temperature of 21700 ± 900 K, μ^2 Sco is one of the brightest stars in the BEAST sample (Janson et al. 2021b). Indeed, its fitted mass of $M = 9.1 \pm 0.3\ M_\odot$ qualifies the star, from a stellar evolution standpoint, as a "massive star" ($M > 8 M_\odot$): a star that could explode as a supernova in the next 10–20 million years (Nomoto & Leung 2017), in particular as an electron-capture supernova (Nomoto 1984). As a 20 ± 4 Myr star, μ^2 Sco is currently evolving off the main sequence, consistently with its spectral classification.

We note that in the specific case of μ^2 Sco, the use of model isochrones -properly constrained to reduce degeneracies- should be considered reliable, given that the star does not show any evidence for unresolved companions (see Appendix 5.3.A), strong magnetic field or rapid rotation (see Appendix 5.3.B). A more precise derivation of its properties might be enabled, in the near future, by a dedicated asteroseismologic follow-up.

5.3.2 Observations

The first observation of μ^2 Sco was obtained on April 24th, 2018, the second one on June 4th, 2021 (Table 5.12). Both observations were carried out in the standard IRDIFS-EXT mode (Section 2.4.1).

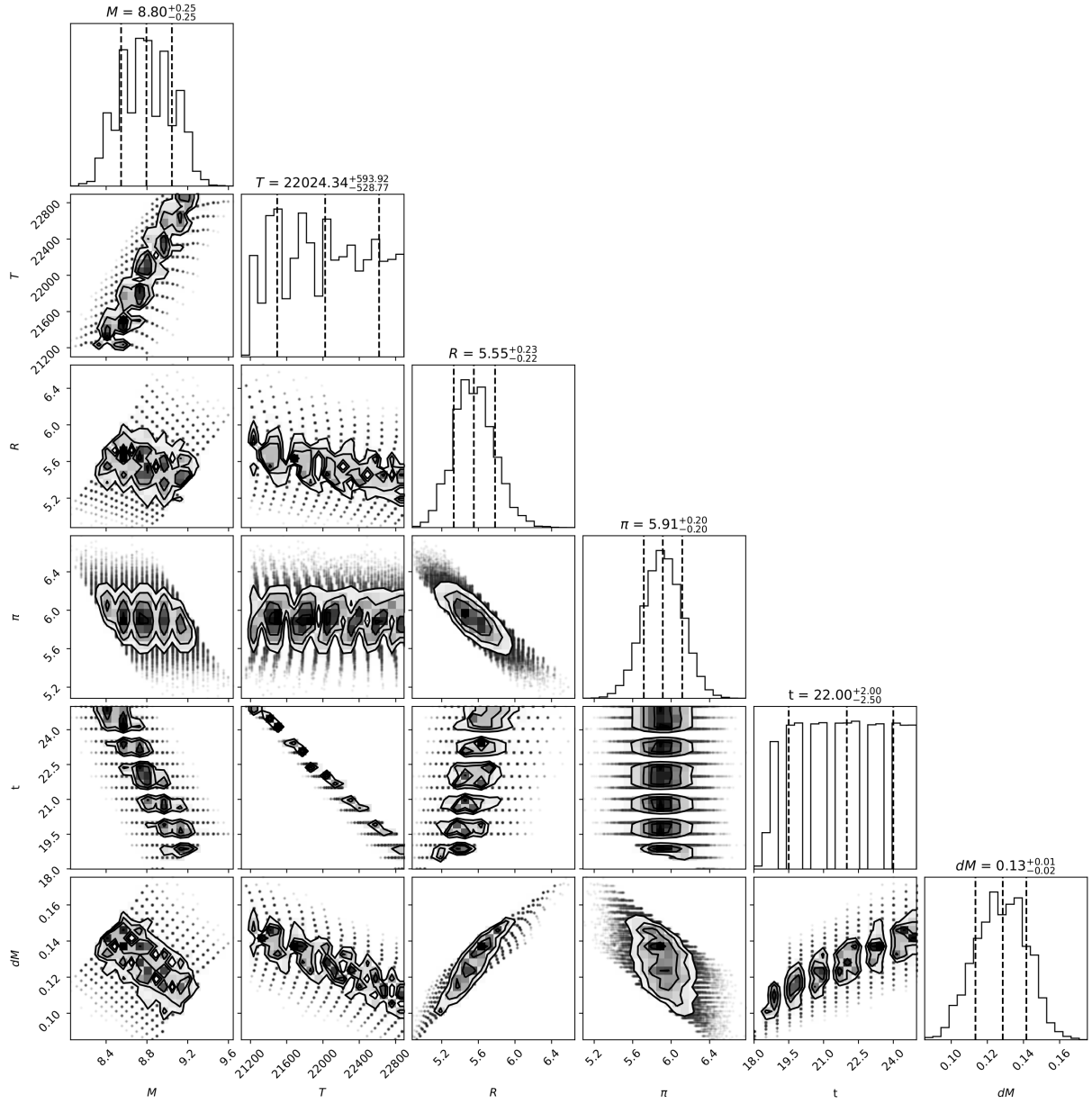

Figure 5.9: Results of the second optimization test of stellar parameters (constant metallicity). Corner plot showing the posterior distribution of the doublets (M, ϖ) consistent with the observational filter for the optimization test based on PARSEC isochrones at fixed [Fe/H] = 0.00. The corresponding $T_{\rm eff}$, R and age distribution are shown too.

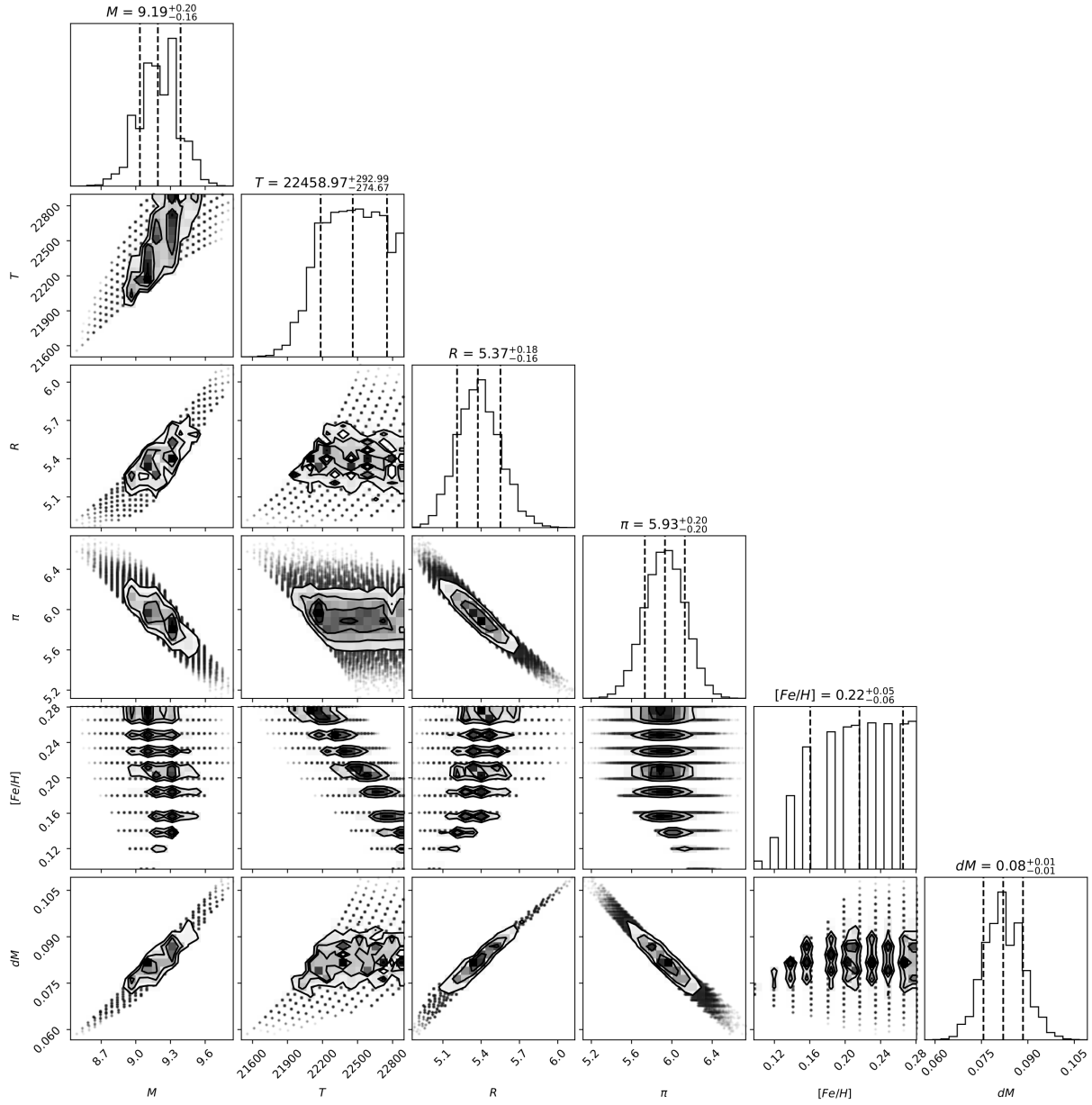

Figure 5.10: Results of the second optimization test of stellar parameters (constant age). Corner plot showing the posterior distribution of the doublets (M, ϖ) consistent with the observational filter for the optimization test based on PARSEC isochrones at fixed $t = 16$ Myr. The corresponding $T_{\rm eff}$, R and [Fe/H] distribution are shown too.

Table 5.12: Details of the observations of μ^2 Sco. DIT is the integration time, N_{exp} the number of frames after selection (out of 192 frames), Rot is the total FoV rotation. The seeing and the Strehl ratio are averages over the duration of the exposures.

UT Date	Instr.	Filter	DIT	N_{exp}	Rot	Seeing	Strehl	Airmass	True north corr.	Platescale
			s		°	"	H band		°	mas pixel^{-1}
2018-04-24	IFS	YJH	16	174	53.0	0.35	0.91	1.03	-1.761 ± 0.06	7.46 ± 0.02
2018-04-24	IRDIS	K12	16	104	43.8	0.35	0.91	1.03	-1.761 ± 0.06	12.256 ± 0.016
2021-06-04	IFS	YJH	16	186	53.2	0.33	0.90	1.03	-1.780 ± 0.07	7.46 ± 0.02
2021-06-04	IRDIS	K12	16	161	51.3	0.33	0.90	1.03	-1.780 ± 0.07	12.261 ± 0.005

The APLC2 coronagraph (Carbillet et al. 2011) was used, masking the star out to a radius of 92.5 mas. As for all observations in the BEAST survey, calibration observations were taken together with science exposures: they included a flux calibration, allowing normalization to the peak of the star image, obtained by offsetting the star position off the coronagraphic mask with a suitable neutral density filter to avoid saturation of the image; a center calibration, obtained by imprinting a sinusoidal pattern to the deformable mirror, providing satellite images of the star; and empty sky exposures centered a few arcsec from the star position. Details of the observations are provided in Table 5.12.

5.3.3 Data reduction

As usual in BEAST, the raw data were reduced at the SPHERE Data Center by means of the SpeCal pipeline. For IRDIS data, besided the standard TLOCI reduction, we performed an additional PACO simultaneous Angular and Spectral Differential Imaging (ASDI) analysis (Flasseur et al. 2020) to better analyze a specific companion candidate (Section 5.3.4.2). For IFS we used three data analysis methods: ASDI and monochromatic Principal Component Analysis (PCA) (Mesa et al. 2015), PACO ASDI (Flasseur et al. 2020) and TRAP (Samland et al. 2021). The calibration of true north and pixel scale employs observations of far compact stellar cluster as in Maire et al. (2016), while the recovery of astrometry and photometry of the companion candidates relied on the injection of negative planets on their position and minimization of residuals.

The final IRDIS and IFS images are shown in Figure 5.11 and Figure 5.12, respectively.

5.3.4 Companion candidates

5.3.4.1 Identification of companion candidates

As expected from the low galactic latitude ($b = 3.86°$) of the target, the final images are abundant in detected sources: two companion candidates are seen inside the IFS FoV Figure 5.12, while in the wider IRDIS FoV there are 46 objects (Figure(5.11) detected either in the first or in the second epoch, with the majority – 34 – being observed in both epochs. Excluding CC1 – seen in both epochs by IFS – we are left with 11 dim CCs only seen by IRDIS in the second epoch.

The quality of the final IRDIS image is somewhat better for the second epoch, which is on average ~ 0.25 mag deeper than the first one: this explains why some of the faintest CCs in the IRDIS FoV are only detected in the second epoch. The derived properties of all the CCs within the IFS and IRDIS FoV, labeled through a unique numeric ID, can be found in Table 5.15.

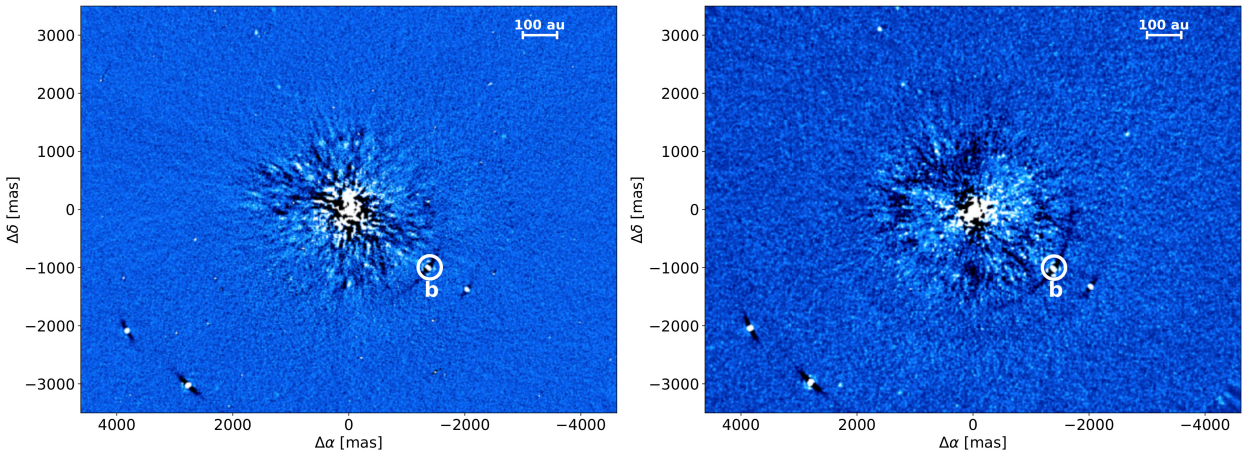

Figure 5.11: IRDIS images of μ^2 Sco obtained with TLOCI (*left panel*: first epoch; *right panel*: second epoch). The star, artificially obscured by the coronagraphic mask, is at the center of the image. Several background sources can be easily seen as bright point sources. μ^2 Sco b is the source inside the white circle.

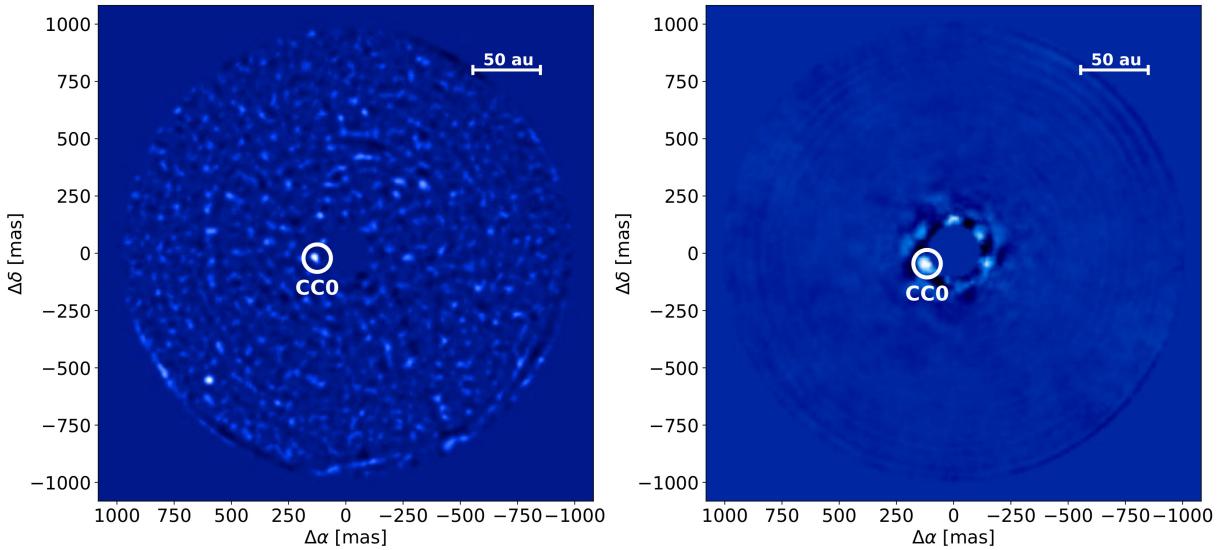

Figure 5.12: IFS images of μ^2 Sco obtained with ASDI-PCA with 25 modes (*left panel*: first epoch; *right panel*: second epoch). The star is at the center of the image but not visible due to the presence of the coronagraphic mask – which artificially masks the innermost ~ 90 mas of the image – and the aggressive data analysis method used. The probable companion CC0 is the source inside the white circle. A background source is visible on the lower left of the first-epoch image.

5.3.4.2 The closest companion candidate: CC0

Unlike the other CCs, the proximity of CC0 to the edge of the coronagraphic mask and its faintness invokes special caution to rule out the possibility of a systematic artifact. In order to assess the reliability of the detection of CC0, the analysis of IFS data was performed – as already mentioned above – by means of three different methods:

- ASDI-PCA consists in the subtraction of the first n principal components from the 4D data cube, obtained by combining the 39 individual monochromatic images – corresponding to the different DITs on the detector – after radially scaling them with wavelength; to avoid the data cube to be too large, we averaged each consecutive DIT; after dropping a few poor images, the final data cube includes $90 \times 39 = 3510$ images. We considered $n = 25$ modes, a value suited for small separations, and averaged the resulting data cube according to the expected contrast spectrum for a late M star. We then constructed a signal-to-noise ratio (S/N) map where the noise is evaluated along rings at constant separation and corrected it for the low number statistics penalty factor given by Mawet et al. (2014). In this way, we detect CC0 in the first epoch as a source with peak S/N $\sim$ 8.0, separation = 128 ± 2 mas and PA = $99.5 \pm 1.1°$. Although not significant (S/N=2.5), a source at a similar location (separation = 123 ± 7 mas, PA = $114 \pm 4°$) is tentatively spotted in the second epoch too.

- PACO-ASDI is based on local learning of patch covariances, in order to capture the spectral and temporal fluctuations of background structures; the statistical modeling is exploited to provide a detection algorithm and a spectrum estimation method. The modeling of spectral correlations is useful in reducing detection artifacts. Using this algorithm, we detected the same source found with ASDI-PCA in both epochs but with higher S/N: S/N=10.6, separation $\sim$ 126 ± 2, PA = $99.9 \pm 0.8°$ for the first epoch, S/N=5.0, separation = 125 ± 3, PA = $111.0 \pm 1.6°$ for the second epoch. These S/N estimation include the contribution of spectral correlations (Flasseur et al. 2020) and are performed locally (at a scale of a few pixels). This method tends to be more efficient in detecting very faint signals but it also tends to produce detection maps with slightly higher residual correlations. We also checked the detection maps obtained with the less local (at a scale of a few dozen pixels) algorithm, given S/N slightly above 5 for 2018 data with and without priors. The distribution of both detection criterion is (approximately) Gaussian in the absence of sources. While the first epoch detection employed a flat spectrum (i.e., no prior) and a late-M spectral template, the second epoch detection was obtained only when using the latter prior;

- TRAP is a data-driven approach to modeling the temporal behavior of stellar light contamination, rather than the spatial distribution of the speckle halo (Samland et al. 2021). Due to the field-of-view rotation of the image sequence, each pixel affected by planet signal sees a distinctive light curve which can be modeled and thereby distinguished from other systematic temporal trends of the data. This is achieved by a causal regression model, trained on other pixel light curves at a similar separation from the host star and fit simultaneously with the planet model for each pixel. This approach works well at small separations: no training data is lost due to insufficient field rotation, as the model is not trained locally. Default parameters, as described in the original paper, were used. The resulting contrast maps for each channel were then fitted with a L-type, T-type and flat contrast spectral template, assuming a BT-NextGen stellar model (Allard et al. 2011) of the companion. In addition we used the extracted PACO-ASDI spectrum of CC0 as a template to derive contrast limits for the object.

Given the measured contrast by PACO-ASDI, a S/N between 2.5 and 3.5 would be expected at the position, but no signal above S/N=0.5 was detected.

Assuming Gaussian noise distributions and considering the number of independent points sampled in an IFS image ($\sim 2 \times 10^4$), the S/N obtained with PCA-ASDI and PACO-ASDI corresponds to values of the False Alarm Probability (FAP) equal to $\sim 10^{-11}$, that are extremely low even accounting for the fact that we have observed at least once 75 stars so far in the BEAST survey. However, these values underestimate the real FAP because the distributions are actually not exactly Gaussian[7] (likely because of the edge effects introduced by the coronagraphic mask) and the FAP is therefore higher and not well determined.

The physical nature of CC0 is reinforced by the observation that, at both epochs, CC0 is the peak of the IFS S/N map, and that the second-epoch PA is found within $\sim 11°$ from the first-epoch PA, the separation being the same ($d_{CC0} \approx 127$ mas) within errors. The probability p_{RPA} of this fact happening by chance was estimated in an empirical way. We expect the astrometric shift between the two epochs Δr not to be larger than the fraction Δr_{max} of the face-on circular orbit with $r = d_{CC0}$ covered over the timespan $\Delta t \approx 3.1$ yr separating the two epochs:

$$\Delta r \lesssim \Delta r_{max} = \frac{2\pi d_{CC0}}{T_{orb}} \cdot \Delta t \approx 78 \text{ mas}, \tag{5.3}$$

where $T_{orb} = 1 \text{ yr} \cdot (s \text{ [au]})^{3/2} \cdot (M_*[M_\odot])^{-1/2}) = 1 \text{ yr} \cdot \sqrt{21^3/9.1} \approx 32$ yr is the period of the circular orbit with $s = 1 \text{ au} \cdot d_{CC0}/\text{parallax} \approx 21$ au around μ^2 Sco ($M_* = 9.1 M_\odot$). As a comparison, the observed shift of CC0 is $\Delta r_{obs} = 26 \pm 4$ mas.

Due to the presence of the coronagraph at ~ 100 mas, we conveniently define as "interesting area" the annular sector, centered on CC0's first-epoch PA, with separation 100 mas $< d <$ 200 mas and semiangular width $\Delta\text{PA} = \frac{\Delta r_{max}}{2\pi d_{CC0}} \cdot 360° \approx 35°$.

We then examined all BEAST images and verified that – after deleting those with clear companion candidates – in 19 out of 99 IFS images the S/N peak lies within 200 mas from the central star. The probability p_{RPA} of a nonphysical peak of the S/N map (e.g., a speckle) to be found within the interesting area defined above is given by $p_{RPA} \sim 19/99 \cdot 35°/360° \sim 4\%$.

Finally, the separation of CC0 is constant with wavelength at both epochs (Figure 5.13), further supporting the detection, since separation of speckles from the center of the image is expected to be proportional to wavelength. Intriguingly, a bright spot exactly at the location of CC0 is also detected with TLOCI in IRDIS K_1 and K_2 data at first epoch – although at a very low S/N$\sim$2 – However, given the very low S/N of these IRDIS detections, we consider them as upper limits in the following discussion.

On the other hand, CC0 was not detected using TRAP. The limiting magnitude obtained with this reduction is brighter than the PCA-ASDI and PACO-ASDI detections (because the wavelength dependence of speckle position is not exploited by TRAP), but should result in a marginal detection; it is at present unclear if the nondetection is due to lacking sensitivity as no Spectral Differential Imaging is used, or because the ASDI techniques underestimate errors and false alarm probabilities. New observations with high-contrast imaging and near-IR interferometry are needed to shed light

[7] A Shapiro-Wilk test for Gaussianity (`https://www.statskingdom.com/shapiro-wilk-test-calculator.html`) was run for the inner 50×50 pixels (about 0.37×0.37 arcsec) region of all these S/N map, eliminating the area within 0.5 λ/D of the coronagraphic edge and that around CC0 and using pixels having even indices in both coordinates, to avoid the concern related to covariance of adjacent pixels. Depending on the case, this test found or not some small deviations from Gaussianity. However, the kurtosis is almost always higher than expected for a Gaussian distribution, suggesting that outliers are more common than expected with a Gaussian distribution.

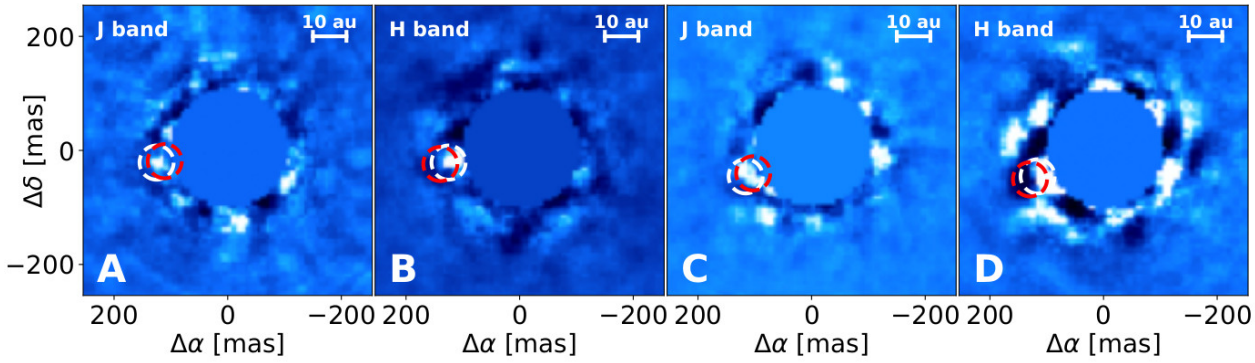

Figure 5.13: Position of CC0 at different wavelengths. (A) J-band image, first epoch; (B) H-band image, first epoch; (C) J-band image, second epoch; (B) H-band image, second epoch. The Y-band image is not shown due to the extreme faintness of the source. White circles indicate the best-fit positions from Table 5.15; circle radii have been enlarged to ~ 10 times the uncertainties on best-fit positions to enhance visibility. Unlike a speckle (red circle), the separation of CC0 does not increase with wavelength.

into the problem; for the time being we suggest that caution must be taken about the actual detection of CC0, that we consider as a probable detection but not a definite one.

5.3.5 Analysis of companion candidates

5.3.5.1 Photometric analysis

Before analyzing the astrometric shifts of the CCs seen at both epochs, we tried to assess whether 9 dim CCs that are only seen in the second epoch could be confidently labeled as background contaminants based on their colors (Figure 5.14). However, owing to the large color uncertainty, their position in the $(K_1 - K_2,\ K_1)$ color-magnitude diagram (CMD) does not provide us with a definitive answer. The same applies for CC29 and CC30, only seen in K_1 in one epoch. Given that the geometric probability of a random alignment between a background source and a target star with separation d is $\propto d^2$, we are only able to argue that the presence of several secure background sources that have a smaller separation to μ^2 Sco than each of these 11 sources[8], is strongly suggestive of a background nature for the 11 sources as well. We excluded all these CCs from the following analysis, in absence of any evidence for a physical association to our target.

5.3.5.2 Astrometric analysis

With regard to the IRDIS CCs seen in both epochs, we are able to confidently label 33 out of 34 objects as background interlopers through astrometric analysis (see Figure 5.15).

On the other hand, CC0 and CC2 show a completely different motion compared to the remaining sources. The mean astrometric shifts of this cloud of sources with respect to the position expected for a static source are -5.5 ± 1.2 mas (rms: 6.7 mas) along right ascension, -15.2 ± 1.8 mas (rms: 10.2 mas) along declination. The astrometric shift of CC0 is -44.4 ± 3.5 mas along RA, -96.1 ± 4.0 mas along declination; that of CC2 is -40.7 ± 2.1 mas along RA, -77.9 ± 2.1 mas along declination.

[8] 5 sources for CC7 and CC8, 6 for CC10 and CC11, 14 for CC20, 18 for CC25, 21 for CC29 and CC30, 24 for CC34 and CC35, 30 for CC42.

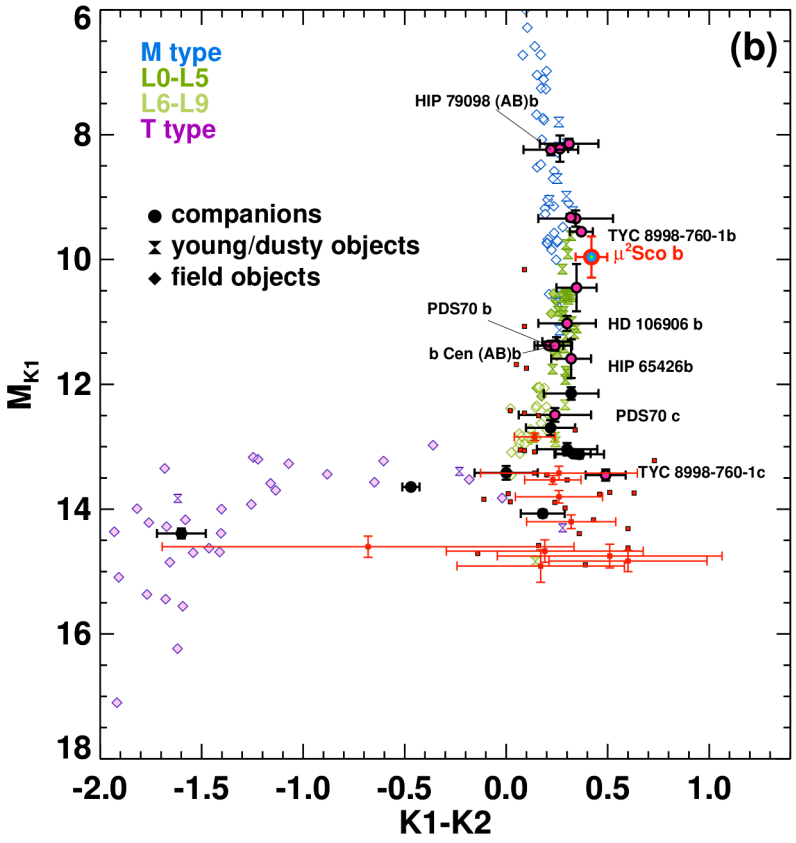

Figure 5.14: $(K_1 - K_2,\ K)$ color magnitude diagram of known substellar companions and field objects. IRDIS CCs only seen in one epoch are shown as red dots. The position of CC0 (=μ^2 Sco b) is consistent with that expected for a young object.

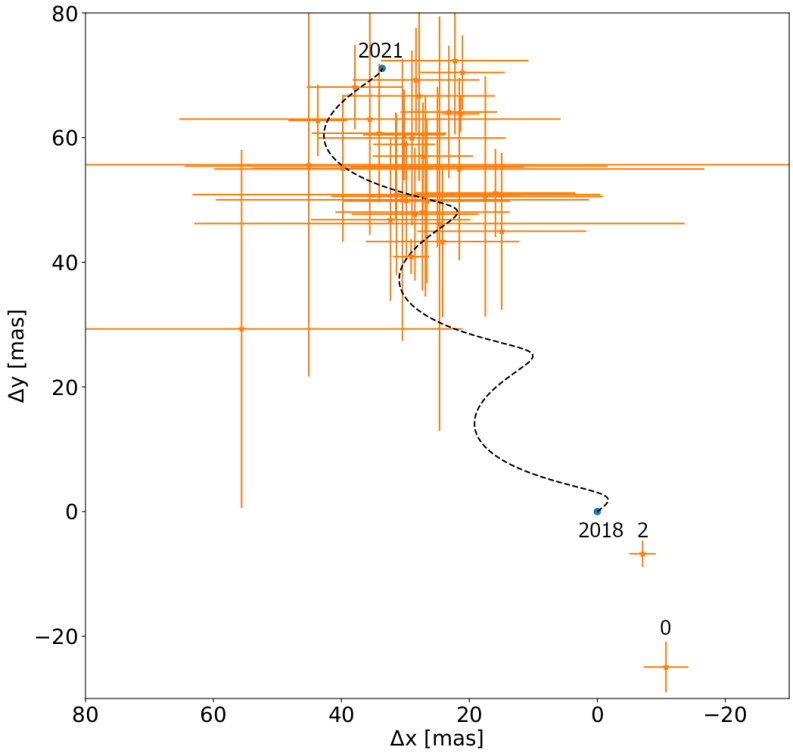

Figure 5.15: Astrometric motion of CCs present in both epochs. As the plot shows the difference in separation between the two epochs, a comoving source should be close to the origin (labeled by "2018"). A background source with null proper motion will move according to the dashed curve as a reflection of the target's motion, ending in the blue circle labeled as '2021' at the second epoch. The motion of CC0 (labeled by "0") and CC2 (labeled by "2") is distinct from the cloud of background contaminants.

Hence, the observed shifts of CC0 and CC2 are $\sim 8\sigma$ and $\sim 9\sigma$ away from the cloud of background sources (we call it "CC cloud"). The conclusion is robust to systematic astrometric offsets between the two epochs, equally affecting all the CCs. CC0 and CC2 are then plausible candidates as physical companion. We examine their cases in more detail in Section 5.3.6.

5.3.5.3 Motion of background sources

As shown by Figure 5.15, the CC cloud is shifted on average by ~ -16 mas with respect to the position expected on the basis of the motion of μ^2 Sco. After carefully checking the centering of our images to exclude a large systematic effect, we are left with three possible causes (or a combination of them):

1. the adopted proper motion is not correct, the error being approximately 3 mas/yr in both right ascension and declination;
2. the photocenter of μ^2 Sco is offset with respect to the barycenter of the system by a different quantity at the two epochs. This might or might not be related to point 1;
3. the field stars have on average a proper motion that is not null. This might be a reflection of the galactic rotation curve (it is important to note that the line of sight toward μ^2 Sco passes at about 15 degrees from the galactic center and the background interlopers are expected to be stars of the inner part of the galactic disk at a few kpc from the Sun).

Scenario 1 seems unlikely: the proper motion considered for μ^2 Sco is very similar to that of its neighbor μ^1 Sco ($\mu_\alpha = -11.867 \pm 0.043$ mas yr^{-1} in RA and $\mu_\delta = -22.511 \pm 0.035$ mas yr^{-1} in Dec) and to the average value for ELS ($\mu_\alpha = -11.57 \pm 0.48$ mas yr^{-1} and $\mu_\delta = -22.12 \pm 0.70$ mas yr^{-1}); the differences are too small to explain the observed residuals.

If the correct scenario were 2, it would apply to both field stars and physical companions; indeed, the motion of CC0 and CC2 appears similar to the offset of the field stars with respect to the prediction for null motion. This would require a substantial motion of μ^2 Sco caused by an (unseen) companion with an orbital period less than 24 yr; a massive short-period companion would likely cause large variations in the radial velocities, which instead are rather constant within a few hundreds of m/s over ~ 10 years (see Appendix 5.3.A).

To investigate scenario 3, we looked for Gaia EDR3 data of field stars near μ^2 Sco. Given that none of the IRDIS background stars is bright enough to be present in Gaia, we searched for field stars within 5 arcmin from our target (we label it "Gaia bg sample"). The main properties of the Gaia bg sample, composed of 6286 stars, are:

$$\begin{aligned} < G > &= 20.09 \text{ mag}, \\ < \varpi > &= 0.30 \text{ mas}, \\ < \mu^*_\alpha > &= -2.681 \pm 0.042 \text{ mas yr}^{-1} \ (rms: 3.367 \text{ mas yr}^{-1}), \\ < \mu_\delta > &= -3.848 \pm 0.043 \text{ mas yr}^{-1} \ (rms: 3.431 \text{ mas yr}^{-1}). \end{aligned}$$

The mean proper motion of the CC cloud, that is simply the ratio between the mean astrometric shift and the time baseline, is instead -1.77 ± 0.37 mas yr^{-1} (rms: 2.17 mas yr^{-1}) along RA and -4.87 ± 0.56 mas yr^{-1} (rms: 3.29 mas yr^{-1}) along dec. We anticipate that a small systematic offset, of about -0.6 ± 0.4 mas along RA and $+1.7 \pm 0.4$ mas along dec, is likely to affect the proper motions of our CCs (see Section 5.3.6.1). With this caveat in mind, we see that the proper motion of the Gaia bg sample is indeed similar to that of the CC cloud; the latter is likely the

M-type part of the same population probed, at brighter magnitudes, by the former, as indicated by the following qualitative argument. From the median parallax of the Gaia bg sample we infer a distance of ∼3 kpc, and absolute magnitudes $M_G \sim 7.5$, that correspond to late K stars; since we are neglecting reddening, these objects may be even intrinsically brighter. This G magnitude translates to $M_K \sim 4.8$ according to the tables by Pecaut & Mamajek (2013). The corresponding apparent magnitude $K \sim 17.4$ gives a contrast with respect to μ^2 Sco of $\mathrm{d}K = 13.1$ mag; these stars are roughly two magnitudes brighter than the CC cloud (median contrast: $\mathrm{d}K \sim 15$ mag). If we assume that IRDIS CCs are on average at the same distance of the Gaia bg sample, their absolute K magnitudes are $M_K \sim 6.7$; according to the tables by Pecaut & Mamajek (2013) this corresponds to M3V stars that have an absolute $M_G \sim 10.0$, and to an apparent magnitude $G \sim 22.6$. IRDIS CCs are too faint to be detected by Gaia (that has a limiting magnitude of $G \sim 21$), and conversely we expect about a couple of Gaia stars (with a density of 1 star every 45 square arcsec) within the IRDIS FoV; the relative frequency agrees with expectation for a reasonable mass distribution (e.g., Salpeter-like) if they belong to the same parent population.

5.3.6 Confirmation of physical companion(s) to μ^2 Sco

In this subsection, we examine the possibility that CC2 is not a bound companion of μ^2 Sco considering two possible alternatives:

- that CC2 is a high proper motion background star;
- that CC2 is a brown dwarf (BD) member of Scorpius-Centaurus that appears projected close to μ^2 Sco.

We note that while the following considerations refer to CC2, they equally apply to CC0 which has a higher proper motion and a smaller separation than CC2, hence intrinsically lower false alarm probabilities (FAP).

5.3.6.1 CC2 is not a background star

Having shown that the cloud of sources seen in the IRDIS images is made of background interlopers, it is necessary to estimate the probability that an object drawn from the same population could have been considered an "interesting" companion candidate to μ^2 Sco because of a "remarkable" astrometric shift relative to μ^2 Sco. Two factors must be taken into account: the probability of finding an object within certain boundaries of μ^*_α and μ_δ; the fact that we have fully[9] observed 25 stars[10] in the survey.

Starting from the Gaia bg sample, we identify as interesting the stars with $\mu^*_\alpha < -9.8$ mas yr^{-1} and $\mu_\delta < -21.1$ mas yr^{-1} [11]. After excluding a few objects that, despite passing the test, have parallax > 5 mas (which would correspond to $4 \lesssim dK \lesssim 10$ mag) and are thus so bright that they would have been disguised as stellar – and not substellar – companions, we obtain that 5 out of 6286 stars satisfy this criterion. This implies a fraction of interesting background objects of $f_G = 1.67 \cdot 10^{-5}$. The FAP of finding one star with these features in our observations of μ^2 Sco (that is, within the IRDIS field of view), given that we observe 36 CCs in both epochs, is then $6 \cdot 10^{-4}$.

[9] That is, at least twice. As already mentioned, two observations are needed to compute relative proper motions.

[10] This value referred to the epoch of our analysis of μ^2 Sco (Nov. 2021 − Jan. 2022); the second epoch for 14 further objects was obtained in 2022 and their analysis is currently in progress.

[11] This is a conservative approach that considers interesting all the objects having a larger relative proper motion – with respect to the CC cloud – than μ^2 Sco itself; see below.

A similar argument can be made by creating a synthetic sample of background stars by means of the Besançon Galaxy Model interface[12] (Czekaj et al. 2014). We selected a sample of stars with distance $d \in [0, 50]$ kpc, apparent K magnitude similar to that observed for CC0 ($K \in [15, 17]$ mag), radius $\rho = 5$ arcmin around the position of μ^2 Sco. Out of 6595 stars, just 4 (corresponding to $f_B = 1.34 \cdot 10^{-5}$) pass the proper motion test described above; this yields a FAP -given 36 CCs- of $4.8 \cdot 10^{-4}$.

Thus, the Besançon-based test and the Gaia-based test give very similar results. We point out that, by defining an unbound region of the proper motion space of 'fast-moving stars', we are actually overestimating the FAP: a source with an unusually large absolute value of the proper motion would not have been consistent with being bound to the star, and would have been discarded.

The probability of having seen at least one background source with these features throughout the entire survey can be estimated in this way. The median proper motion of BEAST targets is -in absolute value- larger than that of μ^2 Sco, but we assume for simplicity a strict equality; if we further assume that the fractions f_B and f_G computed above do not depend on the sky coordinates, we can extend the above reasoning to the whole survey. Given that we have fully observed 25 targets, and that on average we see ~ 11 sources per observation (Janson et al. 2021b), we obtain a FAP of having seen at least one background object disguised as a possible companion within the entire survey of $4.6 \cdot 10^{-3}$ (Gaia-based test) and $3.7 \cdot 10^{-3}$ (Besançon-based test). We conclude that CC2 (and even more likely CC0) is not a background object at a high level of confidence.

5.3.6.2 CC2 is not a free-floating brown dwarf

Whilst confirming that the sources are comoving, the astrometric analysis does not strictly allow exclusion of an alternative scenario: namely, that the sources are free-floating UCL substellar objects that happen by chance to be close to the line of sight of μ^2 Sco. In order to quantify this false alarm probability, three points need to be considered: the probability of finding an "interesting" ($M = 1 - 75\ M_{\rm J}$) object; the probability of finding it within the IRDIS field of view; the fact that we have fully observed 25 stars in the survey.

Assessing the number of free-floating UCL members necessarily requires some assumptions on the initial mass function (IMF) of the association[13].

Recently, Miret-Roig et al. (2022) have uncovered a rich population of free-floating planets and brown dwarfs in Upper Scorpius, extending the IMF of the association down to 0.005 $M_\odot$. As US is a subregion of Sco-Cen, we expect that this IMF can be safely adopted for UCL too. By normalizing their IMF we obtain a probability density function (PDF); we are thus able to compute the fraction of objects in the mass range $[5M_{\rm J}, 75M_{\rm J}]$. We do not consider objects below $5M_{\rm J}$ not only because they are not covered by their data, but also, more importantly, because this is approximately the lower mass to which we are sensitive in BEAST. Integration of the PDF yields 0.205, meaning that one out of five objects in Sco-Cen is expected to belong to this mass range. This PDF should be multiplied by the projected density of objects in the region around μ^2 Sco. To estimate this quantity, we take again the list of bona fide members compiled by Damiani et al. (2019). The faintest members of UCL have apparent G =18.5-19.5, and the corresponding masses reach down to 0.013 $M_\odot$ (see "Stellar system analysis"). Since Gaia is complete within this magnitude range (its limiting magnitude is $G \sim 21$), we assume a sharp transition between 100% completeness above 15 $M_{\rm J}$ to 0% completeness below 15 $M_{\rm J}$. We rescale the number of sources we see in UCL (3842), ELS

[12] Available at https://model.obs-besancon.fr/modele_home.php.

[13] Given that any Gaia-based census of association members is not complete at such low masses.

(575) and LS (73) by dividing by the integral of the PDF above 0.015 $M_{\odot}$, obtaining a complete census of approximately ~ 4021 sources for UCL, ~ 602 for LS, ~ 76 for ELS.

Multiplying these numbers by the integral of the PDF from $5M_{\rm J}$ to $75M_{\rm J}$, we obtain the expected number of interesting objects $\tilde{N}$:

$$\begin{aligned} \tilde{N}_{LS} &\sim 123, \\ \tilde{N}_{ELS} &\sim 16, \\ \tilde{N}_{UCL} &\sim 823. \end{aligned}$$

In order to turn the expected number of objects into a projected density (i.e. the number of expected BD interlopers per arcsec^2), the areas of LS, ELS and UCL must be evaluated. For UCL, coordinate boundaries $(l, b) = [313°, 343°] \times [2°, 28°]$ as in Pecaut & Mamajek (2016) were used. For LS and ELS we computed the mean <l>, <b> and the related standard deviations σ_l and σ_b, and defined the areas as $[< l > -2\sigma_l, < l > +2\sigma_l] \times [< b > -2\sigma_b, < b > +2\sigma_b]$. We get:

$$\begin{aligned} A_{LS} &= 23.2 \text{ deg}^2 = 3.0 \cdot 10^8 \text{ arcsec}^2, \\ A_{ELS} &= 3.8 \text{ deg}^2 = 4.9 \cdot 10^7 \text{ arcsec}^2, \\ A_{UCL} &= 747.0 \text{ deg}^2 = 9.7 \cdot 10^9 \text{ arcsec}^2, \end{aligned}$$

so that the projected densities are:

$$\begin{aligned} \Sigma_{LS} &= \tilde{N}_{LS}/A_{LS} = 4 \cdot 10^{-7} \text{ arcsec}^2, \\ \Sigma_{ELS} &= \tilde{N}_{ELS}/A_{ELS} = 3.2 \cdot 10^{-7} \text{ arcsec}^2, \\ \Sigma_{UCL} &= \tilde{N}_{UCL}/A_{UCL} = 8.5 \cdot 10^{-8} \text{ arcsec}^2. \end{aligned}$$

The mean density of sources in the environment of BEAST stars is usually not as high as in LS. The value that is more representative of the median behavior of the sample is probably that of UCL; we retain the value for LS as a (very high) upper limit to this source of contamination. It is possible now to estimate the number of BD interlopers expected in the IRDIS FoV (a square of 11" × 11"):

$$\begin{aligned} N_{BD,UCL} &= \Sigma_{UCL} \cdot (11")^2 = 1.0 \cdot 10^{-5}, \\ N_{BD,LS} &= \Sigma_{LS} \cdot (11")^2 = 5.0 \cdot 10^{-5}, \end{aligned}$$

and finally the false alarm probability of having seen at least one of these objects across the 25 targets that we have observed at least twice using a binomial distribution is:

$$\begin{aligned} p_{BD,UCL} &= 2.6 \cdot 10^{-4}, \\ p_{BD,LS} &= 1.0 \cdot 10^{-3}. \end{aligned}$$

The probability of a chance alignment by free-floating objects is negligible for CC2 (and even more for CC0).

Finally, the position of both CC0 and CC2 is constant with wavelength, as expected for physical sources. We are therefore able to confirm in a robust way the source CC2 as being a substellar companion to μ^2 Sco (μ^2 Sco b). As regards CC0, based on the reliability arguments presented in the Section 5.3.4.2, we consider it to be a probable detection that would make it a second physical companion to μ^2 Sco.

5.3.7 Companion characterization

The star μ^2 Sco appears to be surrounded by one, and possibly two, physical companions. We recall that, while the existence of CC2 is firmly established (S/N=80–120), the detection of CC0, owing to its extreme proximity to the target, is more sensitive to the reduction method employed, stretching from a robust detection (S/N=10.6 in the first epoch, S/N=5.7 in the second epoch) in one case to a nondetection where a marginal detection (S/N=2.5–3.5) was expected in another case.

Given the not unambiguous outcome of the different reductions and the subtleties in the derivation of confidence levels and false alarm probabilities, we highlight the need for follow-up observations to definitely confirm or rule out its existence. With this caveat in mind, we continue to refer to both the robust μ^2 Sco b and the probable CC0, deriving the properties of the latter from the results of our successful detections.

5.3.7.1 Spectra and photometry

The PACO-ASDI algorithm (Flasseur et al. 2018) provides a spectrum for the probable companion CC0 for both epochs. As expected, the spectrum relative to the second epoch is characterized by a significantly lower S/N than the first-epoch one[14]. From this moment on we always refer to the first-epoch spectrum, the only one which allows a tentative characterization of CC0.

After combining the spectrum from the first epoch with upper limits in the K_1 and K_2 band provided by the same algorithm applied to the IRDIS first-epoch dataset (see Figure 5.16), we fit the spectrum with those provided by the AMES-Dusty models – suitable for substellar objects and low-mass stars – assuming our age and distance estimates for μ^2 Sco. The best-fit model has a mass of $M_c = 19.5 \pm 0.9\ M_\mathrm{J}$, a temperature of T_eff=2262 $\pm$ 28 K and $\log L/L_\odot = -3.08 \pm 0.03$. The comparison is generally fairly good (reduced $\chi^2 = 2.55$); most of the contribution to χ^2 is due to the region around the J-band, where the observed spectrum is much lower than expected. As no strong molecular band is expected in the region around 1.25 μm according to any realistic atmospheric model (compare, e.g., Marley et al. 2021), we attribute this discrepancy to residual speckle noise. A similar fit with BHAC15 models yields $M_c = 17.4 \pm 0.9 M_\mathrm{J}$, $T_\mathrm{eff} = 2274 \pm 28$ K and $\log L/L_\odot = -3.04 \pm 0.03$. We account for theoretical uncertainties by averaging the two estimates to obtain a final mass of $M_c = 18.5 \pm 1.5 M_\mathrm{J}$.

We highlight that, despite the high level of irradiation at its expected orbital distance (21 ± 1 au), radiation from the probable companion would be almost completely due to its self-luminosity rather than reflected light from the star. In fact, for an albedo similar to the Earth, the equilibrium temperature of CC0 is about 900 K; comparing it with our best-fit effective temperature of about 2270 K, we estimate that stellar irradiation contributes only about 2% to the total luminosity of the object, a value well within observational uncertainties.

As regards μ^2 Sco b, for which we could not extract a spectrum as it lies outside the IFS FoV, the available photometric information is limited to the measured contrasts in the K_1 and K_2 band; combining them with the K magnitude of the primary, we derive absolute (K_1, K_2) magnitudes. No significant photometric variation is observed between the two epochs. The position of the companion in the ($K_1 - K_2$, K) color-magnitude diagram confirms its compatibility with a substellar object lying at the very beginning of the sequence of L dwarfs (L0-L2 type; see Figure 5.14). A comparison of the photometry with theoretical magnitudes from the same two models used for CC0 provides us with two mass estimates, which again we average to get a final mass $M_b = 14.4 \pm 0.8\ M_\mathrm{J}$.

[14] As a consistency check, we stress that in the H-band region, where the signal is highest, the two spectra are consistent with one another.

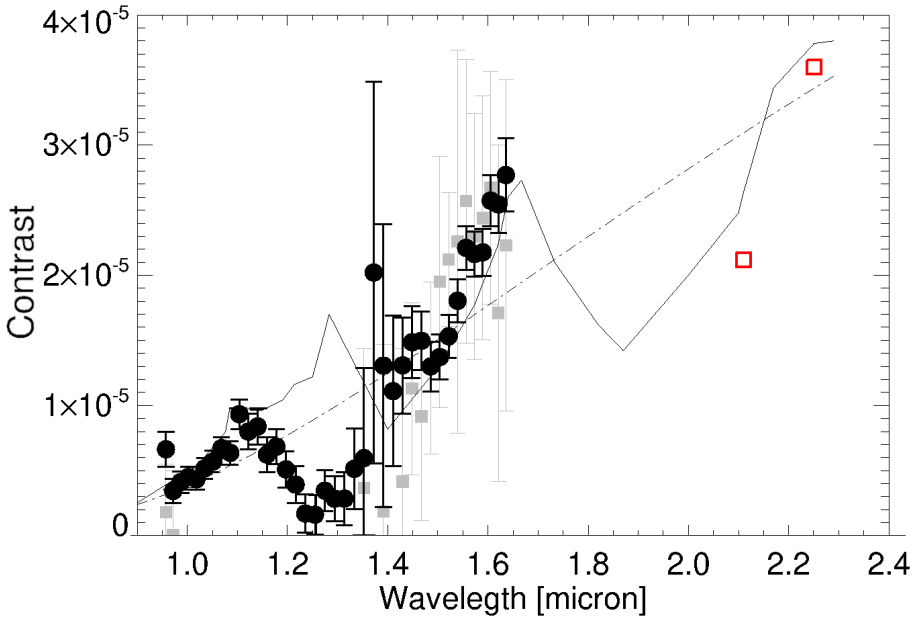

Figure 5.16: Contrast spectrum for CC0 obtained with PACO-ASDI from 2018 IFS data (black dots) and from PACO-ASDI for IRDIS data acquired at the same epoch (5σ upper limits; red squares). The second-epoch ASDI-PCA spectrum (gray squares) is shown for reference. The solid line is the contrast spectrum expected for a 20 Myr old, $19.5 M_J$ brown dwarf using AMES-Dusty models. The dot-dashed line is a black body curve with the same temperature and radius as this model.

5.3.7.2 Astrometry and orbits

CC0 and μ^2 Sco b have angular separations of 0.128 ± 0.002 arcsec and 1.709 ± 0.005 arcsec from the star that translate, at a distance $d = 169 \pm 6$ pc, into projected separations of 21 ± 1 au and 290 ± 10 au, respectively. These positions are not exactly constant over the two epochs, showing a significant displacement of ~ 20 mas and ~ 10 mas, respectively: a possible hint of orbital motion around the star. Before analyzing this aspect quantitatively, we quantified the accuracy of the relative astrometry provided by SPHERE observations exploiting the large amount of background CCs present in the images.

Starting from the Gaia bg sample defined in Section 5.3.5.3 (6286 sources), we select the 2741 sources with parallax 0.1 mas$< \varpi <$5 mas (i.e., 0.2 kpc $< d <$ 10 kpc). The mean proper motion of this "restricted Gaia bg sample" is -2.51 ± 0.07 mas yr^{-1} (rms=3.53 mas yr^{-1}) along right ascension, and -3.82 ± 0.07 mas yr^{-1} (rms=3.76 mas yr^{-1}) along declination.

To test whether the two samples are drawn from the same parent distribution, we performed two independent Kolmogorov-Smirnov (KS) tests (one for μ^*_α, one for μ_δ) at level $\alpha = 0.05$. While the null hypothesis could not be rejected for μ^*_α ($p = 0.13 > \alpha$), a significant difference exists with respect to μ_δ ($p = 0.008 < \alpha$). In particular, the CC cloud appears to have a somewhat higher μ^*_α and lower μ_δ than the restricted Gaia bg sample. To quantify this, we identified the range of μ^*_α and μ_δ shifts to be solidly applied to the whole all CC cloud so that the KS test is passed at level $\alpha = 0.05$.

The range of shifts needed for μ^*_α is $\Delta\mu^*_\alpha \in [-1.44, +0.22]$ mas yr^{-1}, while for μ_δ it is $\Delta\mu_\delta \in [0.55, 2.81]$ mas yr^{-1}. The mean values within these ranges are -0.61 mas yr^{-1} and 1.68 mas yr^{-1},

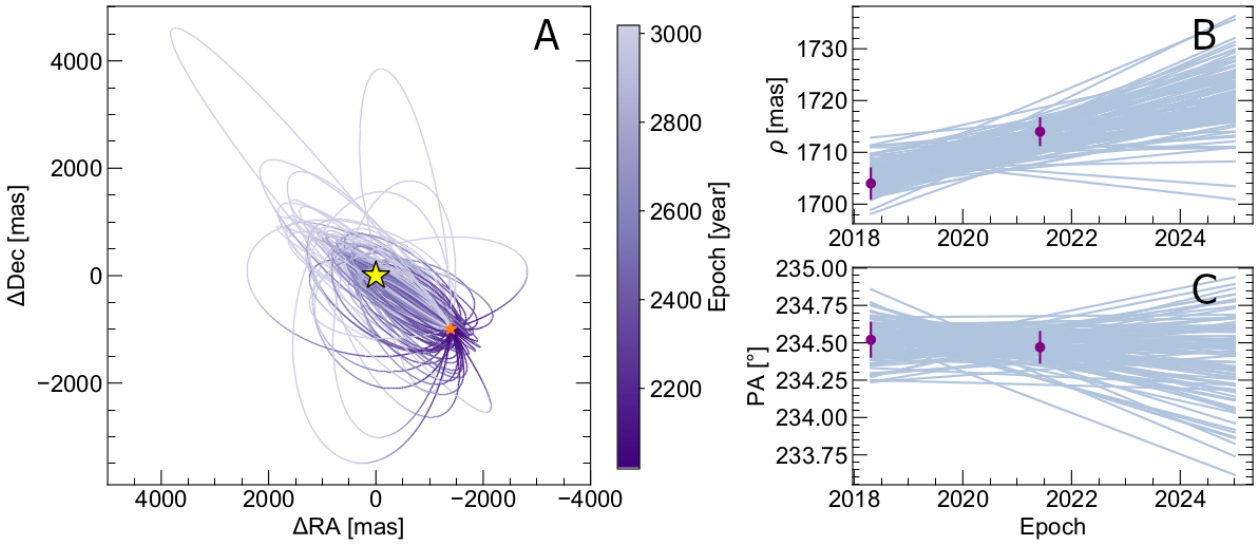

Figure 5.17: Subset of possible orbits for the robust companion candidate μ^2 Sco b. (A) Sky-projected orbital fit (orange star icon) based on the 2018 and 2021 epochs which overlap at this scale, showing 100 randomly drawn orbits from the orbitize! MCMC chains. The position of μ^2 Sco is indicated by the yellow star. (B) Evolution over time of the planet-star separation (ρ); measured points and the corresponding error bars are shown in purple. (C) Evolution over time of the position angle (PA); again, measured points and the corresponding error bars are shown in purple.

respectively. Multiplying by the temporal baseline, and equally splitting the correction between the two epochs, we get $\Delta\alpha = -1.34$ mas, $\Delta\delta = 3.73$ mas, which can be attributed to a not perfect centering of the star in one or both epochs (note that this is much smaller than what cited at Section 5.3.6.1 and well within typical uncertainties of star centering in SPHERE astrometry: see Maire et al. 2016).

Instead of using these values to fix the astrometry of μ^2 Sco b and CC0, we conservatively opted for treating $\Delta\alpha$ and $\Delta\delta$ as an additional source of random uncertainty on their relative astrometry, and propagate it to derive final uncertainties σ_d and $\sigma_{\rm PA}$ on separation and PA, respectively, that are somewhat broadened with respect to those in Table 5.15: for CC0, $(\sigma_d, \sigma_{\rm PA}) = (2.5\ {\rm mas}, 2.0°)$ and $(3.3\ {\rm mas}, 2.2°)$ for the first and second epoch, respectively; for CC2 = μ^2 Sco b, $(\sigma_d, \sigma_{\rm PA}) = (3.1\ {\rm mas}, 0.12°)$ and $(2.8\ {\rm mas}, 0.11°)$ for the first and second epoch, respectively.

Starting from the measured separations and PA and their broadened uncertainties, orbital parameters were estimated separately for the probable companion CC0 and for the robust one μ^2 Sco b using the orbitize! package, run with the recommended parameters for reliable convergence, for a total of $2 \cdot 10^6$ orbits. The priors used for the MCMC were stellar mass and parallax, taken from Table 5.11, as well as the star-planet separations and position angles, taken from Table 5.15. A subsample of suitable orbits, as well as the posterior distributions of semimajor axis, eccentricity, and inclination, are shown in Figure 5.17-5.20.

A preference for large inclinations and/or large eccentricities emerges. To understand whether the best-fit orbital configuration of the system can be dynamically stable, we refer to the Hill criterion. Let M_* be the mass of the primary star, (m_1, a_1, e_1) and (m_2, a_2, e_2) the mass, semimajor axis and eccentricity of the inner and outer companion, respectively. Under the hypothesis that $m_1 \ll M_*$ and $m_2 \ll M_*$, a system is Hill stable, meaning that the two companions will avoid close approaches

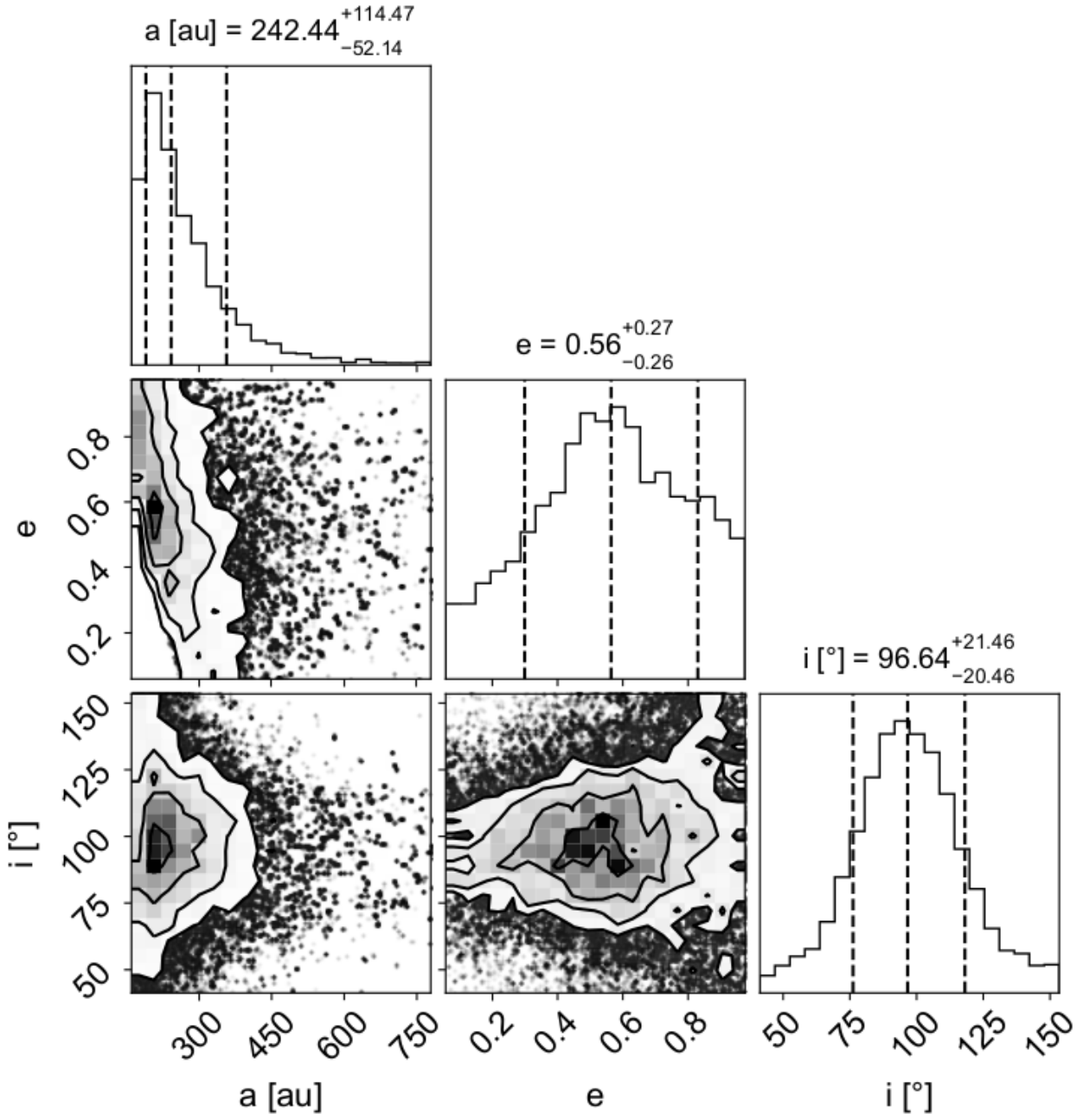

Figure 5.18: Posterior distributions of orbital parameters for the robust companion μ^2 Sco b. Corner plot showing the posterior distributions from orbitize! for semi-major axis (a), eccentricity (e) and inclination (i). The 16th (left dashed line), 50th (middle dashed line) and 84th (right dashed line) percentiles of each parameter distribution are indicated, and the 50th percentile (median) value is listed with 1σ uncertainties derived from the lower and upper percentiles. One percent of all chains, representing long-tail values, have been excluded from the corner plots for clarity, but are still considered for the percentile calculations. No priors or constraints have been given for any of the parameters.

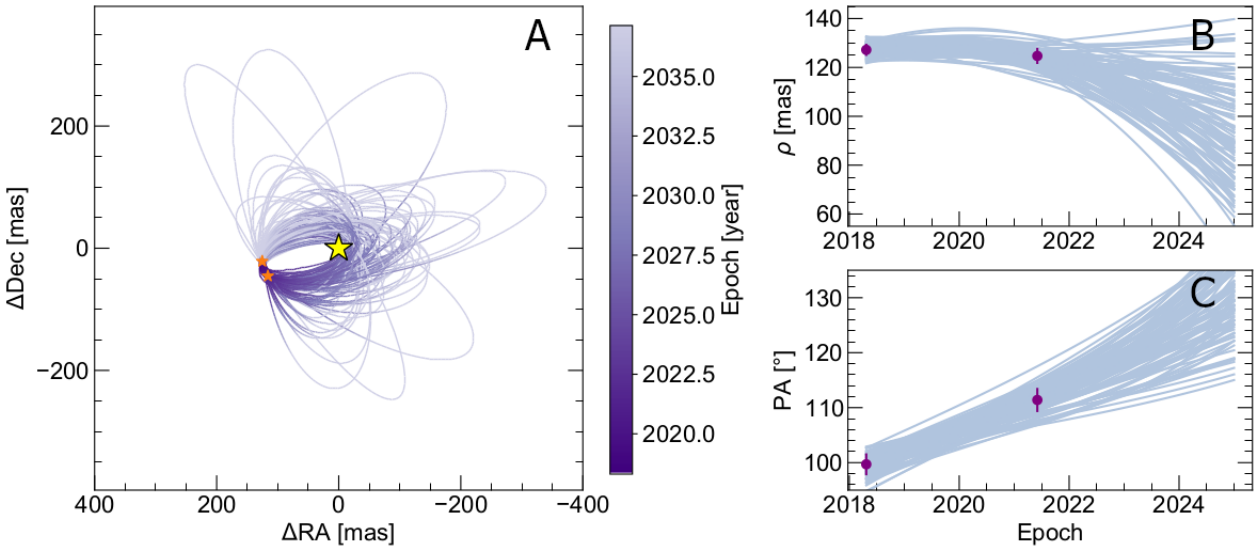

Figure 5.19: Subset of possible orbits for the probable CC0. (A) Sky-projected orbital fit (orange star icons) based on the 2018 and 2021 epochs, showing 100 randomly drawn orbits from the orbitize! MCMC chains. The position of μ^2 Sco is indicated by the yellow star. (B) Evolution over time of the planet-star separation (ρ); measured points and the corresponding error bars are shown in purple. (C) Evolution over time of the position angle (PA); again, measured points and the corresponding error bars are shown in purple.

at all times, if:

$$\alpha^{-3}\left(\mu_1+\frac{\mu_2}{\delta^2}\right)\left(\mu_1\gamma_1+\mu_2\gamma_2\delta\right)^2 \geq 1+3^{4/3}\frac{\mu_1\mu_2}{\alpha^{4/3}} \tag{5.4}$$

Gladman (1993). Here $\mu_1 = m_1/M_*$, $\mu_2 = m_2/M_*$, $\alpha = \mu_1+\mu_2$, $\Delta = a_2 - a_1$, $\delta = \sqrt{1+\Delta/a_1}$, $\gamma_1 = \sqrt{1-e_1^2}$, $\gamma_2 = \sqrt{1-e_2^2}$.

Using nominal values for orbital parameters and masses, the orbits of b and CC0 are Hill stable; more accurately, taking the uncertainty on the orbital parameters into account, the system is Hill stable about 70% of the time. Likewise, the high nominal eccentricity values make it difficult to have additional stable orbits over a wide range of semimajor axes (from $\sim$ 5 au up to $\sim$ 800 au), though this cannot be excluded at present due to the large uncertainties still existing on the orbital parameters.

The final parameters of μ^2 Sco b and the candidate CC0 derived throughout this Section are reported in Table 5.13. The magnitudes of CC0 have been computed by collapsing IFS spectral channels 12-21 (1.159-1.333 μm) and 30-38 (1.504-1.636 μm) from the first epoch to build the two bands $J_{IFS} = 1.246$ μm (band width=0.174 μm) and $H_{IFS} = 1.570$ μm (band width=0.132 μm), and by adding to these contrasts the 2MASS J and H magnitudes of the primary.

5.3.A Possible binarity of μ^2 Sco

The astrometric solution of μ^2 Sco in the literature appears highly problematic (Table 5.14). As shown by Kervella et al. (2019), a significant deviation of proper motion components from the long-term motion reconstructed by cross-matching Hipparcos and Gaia can be suggestive of the

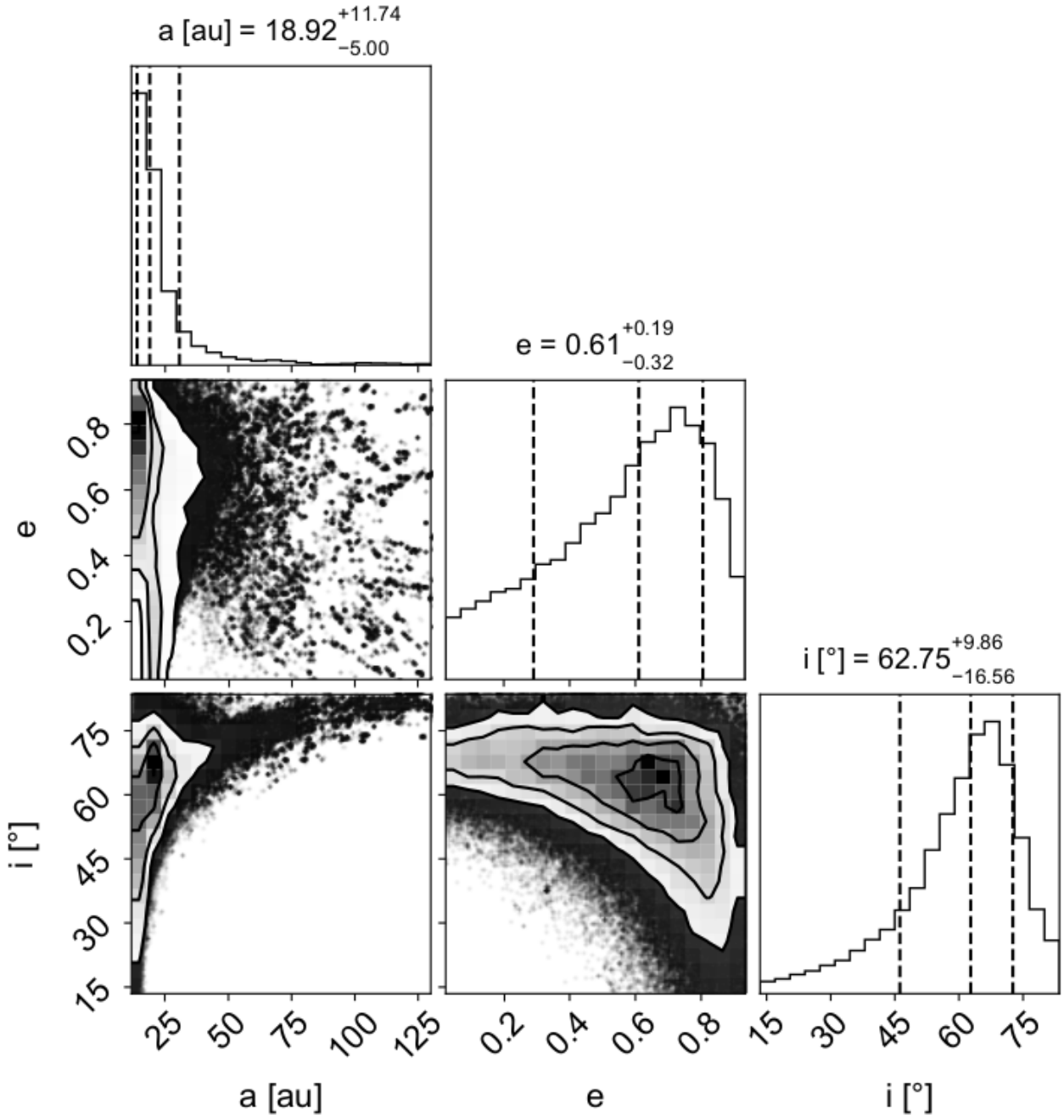

Figure 5.20: Posterior distributions of orbital parameters for the probable CC0. Corner plot showing the posterior distributions from orbitize! for semi-major axis (a), eccentricity (e) and inclination (i) derived in the same way as in Figure 5.18.

Table 5.13: Absolute magnitudes, mass, projected separation, semimajor axis, eccentricity and inclination for the robust μ^2 Sco b and the probable CC0. Here (F_1, F_2) = (K_1, K_2) for μ^2 Sco b, (J, H_2) for CC0.

	F_1	F_2	Mass	q	Proj. sep	a	e	i
	mag	mag	M_J		au	au		°
μ^2 Sco b	9.86 ± 0.33	9.48 ± 0.32	14.4 ± 0.8	0.0015(1)	290 ± 10	$242.4^{+114.5}_{-52.1}$	$0.56^{+0.27}_{-0.26}$	$96.6^{+21.5}_{-20.5}$
CC0	11.51 ± 1.10	9.69 ± 0.38	18.5 ± 1.5	0.0019(2)	21 ± 1	$18.9^{+11.7}_{-5.0}$	$0.61^{+0.19}_{-0.32}$	$62.8^{+9.9}_{-16.6}$

gravitational effects from an unseen stellar companion. Given the importance of the system architecture for a correct characterization and interpretation of our results, we tried to put constraints on possible unresolved stellar companions.

Table 5.14: Astrometric solutions for μ^2 Sco in the recent literature. The values adopted throughout this paper combine proper motions by Kervella et al. (2019) and the kinematic parallax based on membership to ELS. References: (1): Hipparcos (1997 reduction); (2): Hipparcos (2007 reduction); (3) Gaia DR2; (4) Gaia EDR3; (5) Kervella et al. (2019).

Source	ϖ	μ^*_α	μ_δ
	mas	mas yr^{-1}	mas yr^{-1}
(1)	6.31 ± 0.86	-12.92 ± 0.66	-23.80 ± 0.61
(2)	6.88 ± 0.12	-11.09 ± 0.13	-23.32 ± 0.11
(3)	7.92 ± 0.55	-9.98 ± 0.96	-19.87 ± 0.78
(4)	5.66 ± 0.28	-12.11 ± 0.30	-22.57 ± 0.27
(5)	—	-11.77 ± 0.02	-23.11 ± 0.02
adopted	5.9 ± 0.2	-11.77 ± 0.02	-23.11 ± 0.02

Although Kervella et al. (2019) reports a significant (S/N=4.1) proper motion anomaly (PMA) at Hipparcos era, the PMA was not significant at Gaia DR2 era. Thus, we checked the consistency of the astrometric solution from Hipparcos, finding that the 2007 reduction yields a PMA along right ascension with an opposite sign and similar magnitude (about 0.7 mas yr^{-1}) compared to the 1997 reduction based on the same raw data (Perryman et al. 1997). Therefore, the tabulated PMA of Hipparcos cannot be trusted for this star. We use the nonsignificant Gaia DR2 PMA as a separation-dependent upper limit on the stellar companion mass.

μ^2 Sco is neither a visual binary (Gaia Collaboration et al. 2021) nor an interferometric binary (Rizzuto et al. 2013); additionally, it does not appear as an X-ray source in ROSAT (Berghoefer et al. 1996). The upper limit on the X-ray luminosity, given in units of $L_X = \log f_x$ [erg s^{-1}], is $L_X = 29.82$. Since the estimate assumes a distance $d \sim 206$ pc, recalibration with the distance adopted in this Chapter yields $L_X = 29.65$. Such an emission is below the predicted plateau of a K5 star (Poppenhaeger & Wolk 2014), posing an upper limit, independent of separation, of $M_2 < 0.7$ M$_\odot$.

We then analyzed HARPS (Mayor et al. 2003) and FEROS (Kaufer et al. 1999) radial velocity data, spanning about 10 years retrieved from the ESO Science Archive[15]: after extraction of RV from 37 He I and atomic lines, we verified that the rms of the observations (0.21 km s^{-1}) is smaller than individual uncertainties (~ 0.3 km s^{-1}). Spectra taken at short temporal separation can push

[15]Data available at http://archive.eso.org/scienceportal/home, Programs 69.D-0677, 091.C-0713, 187.D-0917.

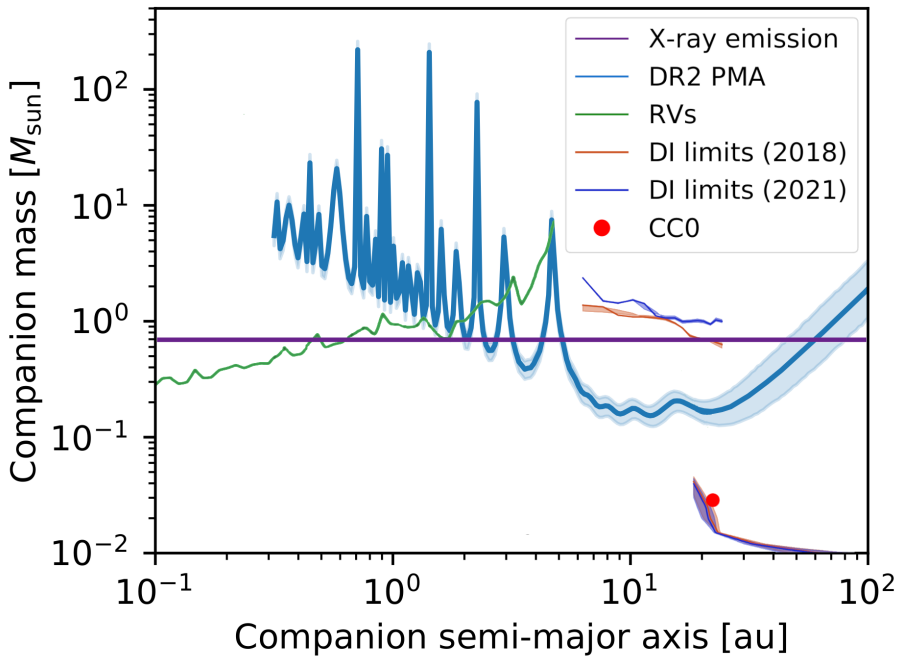

Figure 5.21: Limits on the mass of a possible unresolved stellar companion coming from several techniques. A $M > 0.3 - 0.5\ M_{\odot}$ companion is excluded at sub-au separations by RVs (95% confidence interval), a $M > 0.7\ M_{\odot}$ is excluded at 1-5 au by the lack of X-ray detection. Astrometry (PMA) and coronagraphic observations place even stronger limits at $d > 5$ au. At ~ 290 au, μ^2 Sco b lies outside the x range.

the sensitivity further: the four HARPS observations provide a small scatter of 74 m/s, and the two FEROS observations acquired on JD=56523.66 only differ by 90 m/s. The overall shallow trend of ~ 50 m s^{-1} yr^{-1} can be used to derive an additional upper mass limit: we used the Exo-DMC code (Bonavita 2020) under default assumptions to derive a 95% confidence interval for this mass limit.

Looking at Figure 5.21, we can reasonably exclude the presence of a close stellar companion with $q > 0.08$; additionally, we do not have any evidence to support the existence of a smaller stellar companion. We notice that the parallax error in the latest Gaia release is in line with that expected in Gaia EDR3 for a source with $G = 3.5$ (Lindegren et al. 2021): the high errors associated with Gaia's astrometric solution are likely a mere consequence of the extreme brightness of the star.

5.3.B Stellar magnetic fields and rotation

As the presence of a strong magnetic field can hinder a reliable comparison with model isochrones (see Section 2), we analyzed three high-resolution spectra of μ^2 Sco obtained as part of the Magnetism in Massive Stars (MiMeS) project (Wade et al. 2016): two taken by the spectropolarimeter ESPaDOnS (Donati et al. 2006) in 2014 and 2015, and one taken by spectropolarimeter HARPSpol (Piskunov et al. 2011) in 2011. To begin with, comparison of the intensity spectrum (Stokes I) with a non-LTE TLUSTY synthetic model (Hubeny & Lanz 2011) yields values for the stellar parameters that are fully consistent with those derived through our optimization tests. We analyzed both Stokes I and Stokes V (circular polarization) spectra applying the Least-Squares Deconvolution technique (LSD) to perform a sort of weighted mean in all the spectral lines (Donati et al. 1997). This method

provides mean photospheric Stokes I and V profiles with a S/N much better than in the individual lines, and allows therefore to put stringent constraints on the surface magnetic field.

The weights used in LSD are the predicted central depth of the intensity lines, the wavelength and the Landé factor. The mask, that is the list of predicted lines, has been obtained by using the VALD atomic line database[16], removing only some usually very strong lines (Balmer and He I) affected by non-LTE effects.

The resulting LSD profiles are shown in Figure 5.22. The bottom profile shows the mean Stokes I profile, typical of a photospheric profile of a massive star, with broad wings indicating a significant macroturbulent velocity. The profile is clearly disturbed by the β Cephei pulsations. The top profile is Stokes V, and the middle one is the null profile N, computed in a way that allows us to check that no spurious polarization is present in our data. All the curves are normalized to the mean continuum intensity, I_c.

The Stokes V profile is totally flat, indicating that there is no Zeeman detection in the data. All the measurements of the line-of-sight component of the magnetic field averaged over the surface of the star, called the longitudinal magnetic field Bl, are consistent with 0 G with an uncertainty of $\sim 15G$. Using a Monte Carlo simulation (Alecian et al. 2016), we estimate that if a dipole field at the pole with $B \geq 170$ G exists, we would have had a 90% chance to have detected it. As the typical magnetic fields of massive stars are between a few hundreds of Gauss to few kG, μ^2 Sco is not likely to host a strong fossil field.

With respect to rotational velocity, the low observed $v \sin i = 52$ km s^{-1} implies a geometric probability of having $v > 100$ km s^{-1} of about 13%. By comparison, the median $v \sin i$ for B stars belonging to ~ 20 Myr regions has been estimated as ~ 125 km s^{-1} (Wolff et al. 2007). μ^2 Sco appears therefore to be a slow rotator.

[16] Available at http://vald.astro.uu.se/.

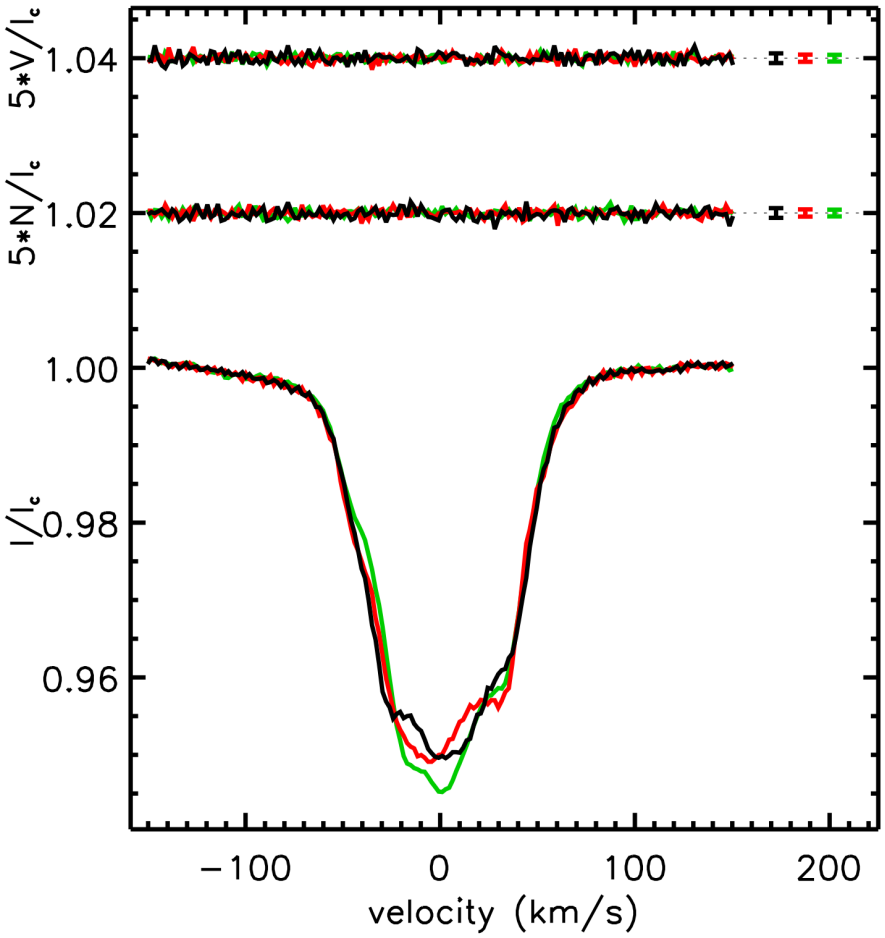

Figure 5.22: Resulting LSD profiles for the three μ^2 Sco spectra (black: ESPaDOnS 2014; red: ESPaDOnS 2015; green: HARPSpol 2011)

. Top profile: Stokes V. Middle profile: null profile. Bottom profile: mean Stokes I profile. For each observation, the typical errorbars of individual spectral points are shown on the right. A vertical offset was applied to the top and the middle curve for better visibility.

5.3.C Companion candidates

Table 5.15: Astrometric and photometric properties of the CCs. The contrasts (F_1, F_2) = (K_1, K_2) for IRDIS, and (J, H_2) for IFS.

		First epoch				Second epoch			
ID	Instr.	d (mas)	PA (°)	F_1 (mag)	F_2 (mag)	d (mas)	PA (°)	F_1 (mag)	F_2 (mag)
Comoving companions									
0	IFS	127 ± 2	99.7 ± 1.1	13.50 ± 1.05	11.68 ± 0.29	124.7 ± 2.8	111.4 ± 1.5	—	—
2	IRDIS	1704 ± 2	234.52 ± 0.05	11.72 ± 0.07	11.34 ± 0.06	1714 ± 1	234.47 ± 0.05	11.73 ± 0.06	11.35 ± 0.05
Background sources									
1	IFS	722 ± 6	132.7 ± 0.4	—	—	703 ± 3	127.2 ± 0.2	—	15.64 ± 0.20
	IRDIS	—	—	—	—	715 ± 6	127.08 ± 0.55	15.25 ± 0.11	14.99 ± 0.37
3	IRDIS	2214 ± 11	24.58 ± 0.26	16.13 ± 0.16	15.67 ± 0.24	2282 ± 6	24.73 ± 0.16	16.00 ± 0.13	15.57 ± 0.27
4	IRDIS	2478 ± 3	236.55 ± 0.06	13.55 ± 0.07	13.43 ± 0.07	2424 ± 1	237.53 ± 0.06	13.51 ± 0.06	13.46 ± 0.06
5	IRDIS	2481 ± 6	29.84 ± 0.15	15.50 ± 0.13	15.14 ± 0.18	2527 ± 5	29.63 ± 0.13	15.81 ± 0.10	15.52 ± 0.18
6	IRDIS	2633 ± 9	259.42 ± 0.15	16.07 ± 0.18	—	2594 ± 9	260.38 ± 0.17	16.23 ± 0.14	—
9	IRDIS	2999 ± 6	295.39 ± 0.11	15.29 ± 0.12	15.43 ± 0.35	3007 ± 3	296.40 ± 0.09	15.25 ± 0.08	15.11 ± 0.14
12	IRDIS	3491 ± 6	27.84 ± 0.09	15.07 ± 0.09	14.88 ± 0.30	3566 ± 3	27.72 ± 0.07	14.91 ± 0.07	14.77 ± 0.09
13	IRDIS	3649 ± 8	257.86 ± 0.54	—	16.41 ± 0.38	3588 ± 2	258.13 ± 0.17	16.72 ± 0.17	16.33 ± 0.40
14	IRDIS	3703 ± 6	10.66 ± 0.08	15.40 ± 0.09	15.45 ± 0.29	3775 ± 4	10.77 ± 0.07	15.36 ± 0.08	15.06 ± 0.12
15	IRDIS	3731 ± 6	20.78 ± 0.09	15.59 ± 0.15	15.36 ± 0.21	3780 ± 4	20.89 ± 0.08	15.58 ± 0.08	15.57 ± 0.18
16	IRDIS	3748 ± 1	50.70 ± 0.60	—	16.30 ± 0.45	3798 ± 8	50.35 ± 0.16	16.41 ± 0.16	16.25 ± 0.29
17	IRDIS	3847 ± 7	142.84 ± 0.14	15.76 ± 0.12	15.62 ± 0.28	3812 ± 5	141.99 ± 0.12	15.67 ± 0.08	15.78 ± 0.40
18	IRDIS	4142 ± 4	136.94 ± 0.05	12.02 ± 0.07	11.95 ± 0.06	4127 ± 1	135.90 ± 0.05	11.99 ± 0.06	11.90 ± 0.05
19	IRDIS	4424 ± 6	118.12 ± 0.07	—	12.86 ± 0.07	4422 ± 2	117.24 ± 0.05	12.90 ± 0.06	12.81 ± 0.05
21	IRDIS	4842 ± 7	149.25 ± 0.11	15.65 ± 0.12	15.65 ± 0.70	4812 ± 4	148.66 ± 0.11	15.71 ± 0.09	15.69 ± 0.22
22	IRDIS	4974 ± 11	132.12 ± 0.16	16.51 ± 0.28	—	4965 ± 8	131.32 ± 0.14	16.54 ± 0.15	16.68 ± 0.70
23	IRDIS	4997 ± 6	192.24 ± 0.13	14.91 ± 0.08	14.64 ± 0.18	4944 ± 3	192.05 ± 0.13	14.88 ± 0.07	14.81 ± 0.09
24	IRDIS	5043 ± 11	178.95 ± 5.93	16.58 ± 0.22	15.97 ± 0.87	4986 ± 9	178.42 ± 3.47	16.60 ± 0.13	—
26	IRDIS	5166 ± 5	99.50 ± 0.05	14.29 ± 0.07	14.20 ± 0.08	5192 ± 2	98.69 ± 0.05	14.25 ± 0.06	14.23 ± 0.07
27	IRDIS	5185 ± 11	117.99 ± 0.13	16.34 ± 0.25	16.18 ± 0.35	5189 ± 9	117.21 ± 0.11	16.45 ± 0.15	15.85 ± 0.42
28	IRDIS	5226 ± 18	284.20 ± 0.20	17.27 ± 0.30	16.66 ± 0.40	5222 ± 11	284.78 ± 0.13	16.76 ± 0.18	—
31	IRDIS	5294 ± 11	295.91 ± 0.10	16.16 ± 0.13	—	5298 ± 6	296.68 ± 0.08	16.22 ± 0.11	15.86 ± 0.32
32	IRDIS	5366 ± 6	103.59 ± 0.05	14.34 ± 0.07	14.22 ± 0.08	5382 ± 3	102.89 ± 0.05	14.29 ± 0.06	14.20 ± 0.07
33	IRDIS	5418 ± 7	36.73 ± 0.07	14.96 ± 0.10	14.86 ± 0.13	5491 ± 4	36.64 ± 0.07	14.89 ± 0.08	14.80 ± 0.11
36	IRDIS	5651 ± 9	297.64 ± 0.09	—	14.31 ± 0.12	5644 ± 2	298.22 ± 0.05	14.33 ± 0.06	14.17 ± 0.08
37	IRDIS	5683 ± 10	274.35 ± 0.08	16.22 ± 0.16	15.90 ± 0.33	5661 ± 7	274.87 ± 0.08	16.14 ± 0.13	15.54 ± 0.19
38	IRDIS	5744 ± 6	243.75 ± 0.05	14.49 ± 0.07	14.33 ± 0.10	5695 ± 3	244.13 ± 0.06	15.05 ± 0.07	14.32 ± 0.14

(continues)

		First epoch				Second epoch			
ID	Instr.	d (mas)	PA (°)	F_1 (mag)	F_2 (mag)	d (mas)	PA (°)	F_1 (mag)	F_2 (mag)
Background companions									
39	IRDIS	5809 ± 6	91.49 ± 0.05	13.60 ± 0.07	13.53 ± 0.07	5839 ± 2	90.94 ± 0.05	13.57 ± 0.06	13.47 ± 0.05
40	IRDIS	5882 ± 11	285.40 ± 0.10	16.08 ± 0.20	—	5865 ± 5	285.96 ± 0.07	15.72 ± 0.10	15.48 ± 0.25
41	IRDIS	5986 ± 8	352.50 ± 0.33	15.42 ± 0.13	15.27 ± 0.17	6032 ± 5	352.85 ± 0.31	15.59 ± 0.10	15.13 ± 0.13
43	IRDIS	6226 ± 9	312.07 ± 0.09	15.72 ± 0.17	15.56 ± 0.21	6238 ± 5	312.58 ± 0.08	15.56 ± 0.10	15.05 ± 0.29
44	IRDIS	6391 ± 7	316.04 ± 0.07	14.52 ± 0.12	14.50 ± 0.15	6414 ± 4	316.61 ± 0.07	14.56 ± 0.09	14.22 ± 0.13
45	IRDIS	6456 ± 8	351.89 ± 0.30	15.47 ± 0.14	15.13 ± 0.16	6508 ± 6	352.15 ± 0.27	15.28 ± 0.10	15.08 ± 0.16
46	IRDIS	6526 ± 11	279.64 ± 0.10	15.46 ± 0.22	—	6511 ± 6	280.16 ± 0.08	15.57 ± 0.13	14.94 ± 0.27
Uncertain status									
7	IRDIS	—	—	—	—	2687 ± 9	321.04 ± 0.31	16.66 ± 0.17	16.06 ± 0.35
8	IRDIS	—	—	—	—	2727 ± 5	199.96 ± 0.64	16.74 ± 0.26	16.58 ± 0.32
10	IRDIS	—	—	—	—	3087 ± 9	332.14 ± 0.35	16.58 ± 0.19	16.07 ± 0.52
11	IRDIS	—	—	—	—	3388 ± 6	157.53 ± 0.26	16.03 ± 0.11	15.71 ± 0.19
20	IRDIS	—	—	—	—	4621 ± 10	45.06 ± 0.19	16.43 ± 0.17	17.11 ± 1.00
25	IRDIS	—	—	—	—	5135 ± 3	158.03 ± 0.08	14.67 ± 0.06	14.53 ± 0.08
29	IRDIS	—	—	—	—	5232 ± 8	227.93 ± 0.14	16.45 ± 0.14	—
30	IRDIS	—	—	—	—	5249 ± 10	345.87 ± 0.36	16.54 ± 0.17	—
34	IRDIS	—	—	—	—	5474 ± 3	209.68 ± 0.08	15.36 ± 0.07	15.13 ± 0.12
35	IRDIS	—	—	—	—	5588 ± 9	101.86 ± 0.10	16.50 ± 0.18	16.31 ± 0.45
42	IRDIS	—	—	—	—	6064 ± 5	80.94 ± 0.07	15.63 ± 0.10	15.37 ± 0.19

Chapter 6

Discussion and conclusions

As we have been stressing throughout this dissertation, the BEAST program was explicitly designed to ascertain whether the observed dearth of planets around $M \gtrsim 2.5 M_{\odot}$ stars is physically motivated by the rapid dispersal of protoplanetary disks or is rather a mere selection effect of the most common planet-hunting techniques. In order to accomplish its scientific goal, the survey is probing the $\sim 10 - 1000$ au region around young ($5 - 20$ Myr) B-type members of the Scorpius-Centaurus, the youngest OB association to the Sun.

While the survey is still ongoing, its early results are already intriguing and, in many respects, unexpected. This Chapter will discuss the implications of our discoveries on the view of giant planet formation around high-mass stars, pointing the way forward for future work in the field.

6.1 Possibility of giant planet formation around B stars

While HIP 79098 is as massive ($\sim$ 2.5 $M_{\odot}$) as the most massive planet-hosting stars identified through radial velocity searches, the discovery of substellar companions to b Centauri and μ^2 Scorpii has no counterparts in the literature and pushes up the frontiers of exoplanetary studies by a factor 3 in stellar mass. The novelty of this result urges for extreme caution in the interpretation of our results.

In principle, the observation of two objects such as b Centauri b and μ^2 Scorpii b might be reconciled with the notion that planet-forming processes are inhibited around high-mass stars if they formed elsewhere in the association – either as independent objects or as companions to less massive stars – and were later captured by their current hosts. Free-floating substellar objects, reaching down at least to ~ 5 $M_{\rm J}$, are indeed common in associations, and a copious population of such objects has been recently uncovered in Upper Scorpius (Miret-Roig et al. 2022).

Motivated by the discoveries of BEAST, Parker & Daffern-Powell (2022) have theoretically explored this possibility. In a series of $N_c = 20$ simulations, they randomly filled a cube of side $\ell = 2$ pc with 1000 stars; the stars are spatially distributed according to a box-fractal distribution to mimic the initial spatial and kinematic structure found in new-born associations (see Daffern-Powell et al. 2022). Due to a random sampling of the stellar initial mass function, the number of B stars in the cubes varies between 44 and 65. Half of the stars with $M_* < 2.4 M_{\odot}$ are assigned a 1 $M_{\rm J}$ planet in a circular orbit at $a = 30$ au. The dynamical evolution of each cube was followed via N-body integration for 10 million years.

A total of 18 planets is captured in the simulations, giving a frequency of captured planets $f_p \sim 18/(55 \cdot 20) \approx 0.016$ per star. Since, at the moment of writing, 39+1 systems have been

completely analyzed (Chapter 5), the probability p_{capt} of finding at least three captured planets under this scenario can be estimated via a binomial distribution:

$$p_{capt} = 1 - \sum_{k=0}^{2} \binom{40}{k} f_p^k (1 - f_p)^{40-k} \approx 0.028. \tag{6.1}$$

A crucial feature of the simulations, the median stellar density of the fractal regions is of order $\sim 10^4$ pc^{-3}, comparable to the average stellar density found in a globular cluster (Symposium et al. 2010). We argue that such a compact configuration is not adequate to describe Scorpius-Centaurus, that has never been in a tightly-packed configuration in the past (Galli et al. 2018). Also, the assumed frequency of Jupiter-sized planets in wide orbits is unrealistically high if compared to observational evidence (Bowler 2016; Nielsen et al. 2019; Vigan et al. 2021). Therefore, we can expect the value of p_{capt} to be significantly lower. An empirical estimate might be roughly derived by using the present configuration of the relatively compact Lower Scorpius (Section 5.3.1.1) as a proxy for a the initial state of a typical star-forming subgroup within Sco-Cen. The timescale for a close encounter can be estimated as:

$$\tau_{enc} \approx 3.3 \times 10^7 \text{ yr} \left(\frac{100 \text{ pc}^{-3}}{n} \right) \left(\frac{v_\infty}{1\text{km s}^{-1}} \right) \left(\frac{10^3 \text{ au}}{r_{min}} \right) \left(\frac{M_\odot}{m_t} \right), \tag{6.2}$$

where n is the stellar number density, v_∞ the stellar mean relative speed at infinity, r_{min} the encounter distance, and m_t the total mass participating in the close encounter (Malmberg et al. 2007). The latter factor ($M_\odot/m_l$) is inserted to account for gravitational focusing – i.e., the deflection of stars towards each other caused by their mutual attraction –, a process which greatly increases the effective stellar cross section.

Adopting $n \approx 1$ pc^{-3}, $v = 0.7$ km s^{-1} (Section 5.3.6.2), a typical $m_l = 5M_\odot$, and considering close encounters within 1000 au, the equation yields:

$$\tau_{enc} \approx 460 \text{ Myr}. \tag{6.3}$$

Based on the SHINE survey, Vigan et al. (2021) determined the fraction of $1-75M_\text{J}$ companions with a semimajor axis $\in [5, 300]$ au to be $5.8^{+4.7}_{2.8}$% and $12.6^{+12.9}_{7.1}$% around FGK and M hosts, respectively. We assume a constant fraction $f_c = 10\%$. As regards free-floating objects ($5M_\text{J} \lesssim M \lesssim 75M_\text{J}$), we recover from Section 5.3.6.2 that their fraction with respect to the total Sco-Cen population is $f_{ff} \sim 20\%$. If *every* close encounter with a bound or free-floating objects results in a capture event, f_p can be computed as:

$$f_p \approx \frac{20 \text{ Myr}}{460 \text{ Myr}} \cdot (f_c \cdot (1 - f_{ff}) + f_{ff}), \tag{6.4}$$

so that, over the whole survey,

$$p_{capt} = 1 - \sum_{k=0}^{2} \binom{40}{k} f_p^k (1 - f_p)^{40-k} \approx 0.013. \tag{6.5}$$

We stress that the probability sharply decreases to 0.2% if only half of the encounters are successful. We conclude that the capture scenario is quite unlikely from a statistical standpoint, and evidence argues instead for in-situ formation. This consideration leads us toward a whole range of questions about how these objects came into being.

6.2 A disk-borne origin

The mean irradiations that μ^2 Scorpii b and b Centauri b receive from their hosts are comparable to those of Jupiter and Saturn, tentatively hinting – even in absence of a significant outward migration – at a formation within the protoplanetary disk (Figure 6.1). Similarly to irradiation, the outer extension of the initial circumstellar disk is characterized by a positive scaling with stellar mass: disks that extend more than 1000 au have been found around 7-10 $M_{\odot}$ stars (Cesaroni et al. 2005; Schreyer et al. 2006).

On the other hand, these companions might constitute the low-mass tail of a wide companion population – mostly belonging to the stellar regime – that formed independently from the primary. Several routes have been put forward to explain binary formation (Duchêne & Kraus 2013): notably, core fragmentation, where multiple overdensities in the natal core independently collapse (Offner et al. 2010, 2016), and disk fragmentation (Kratter et al. 2010), that is another name for the gravitational instability mechanism introduced in Section 1.5.2. While an order-of-estimate cutoff between the prevalence of the former and the latter might be set at ~ 500 au, the actual transition is smooth and the two mechanism are not necessarily mutually exclusive (e.g., Offner et al. 2016). Interestingly for our purposes, observational evidence of disk fragmentation has already been found around 10 $M_{\odot}$ stars (Cadman et al. 2020; Suri et al. 2021).

If the parent distribution of the two companions is generated by a mechanism unrelated to the protostellar disk, we should expect that its mass distribution is similar[1] to the IMF; in the opposite case, the analysis of its mass and orbital distribution will constitute a powerful diagnostics to shed light into its origin.

Our investigation starts by constructing a unified sample of all the companions, either stellar or substellar, discovered during the BEAST and SHINE surveys. Besides the similar sensitivity granted by SPHERE, we selected only these two surveys because of an in-depth knowledge of their stellar sample and their assembly. As regards BEAST, we considered the stars with a first-epoch observations taken before June 9th, 2019: several stars with a first epoch after this date are yet to be analyzed, possibly skewing the statistical validity of the resulting companion distribution; conversely, almost all the selected stars have already been scrutinized with a second epoch, ensuring that the results are fully representative of the whole sample. 36 stars, including HIP 79098, comply with this criterion. Within detection limits, 18 systems were not found to host companions; 17 stars were found to possess exactly one secure[2] companion, and one star hosts 2 companions. For the SHINE subsample, we started from the subsample already analyzed by Vigan et al. (2021), which includes stars with a first epoch taken until February 2017, and complemented it with the subset of the stellar companion sample presented in Bonavita et al. (2022b) that satisfies the same first-epoch requirement. Out of 187 stars, 41 systems are binary, 8 are triple and one has four companions.

By design, the BEAST sample was constructed by excluding known intermediate-separation binaries ($0.1'' \lesssim s \lesssim 6.0''$) not to negatively affect the performances of SPHERE (Section 2.1). The exclusion of binaries was even more harsh in SHINE where, unlike in BEAST, known binary systems with $s < 0.1''$ (either interferometric, eclipsing or spectroscopic) were removed. For our purposes, we decided to focus on companions with projected separations 1 au $\lesssim s \lesssim$ 1000 au. 5 additional companions – 4 in SHINE, 1 in BEAST – with projected separation $<$ 1000 au but falling outside the IRDIS field of view were recovered from Gaia DR3. In order to evaluate and to partially account

[1] Albeit not exactly equal: a $2-5\%$ excess of equal-mass binaries is observed in Gaia binaries with $600 \lesssim a \lesssim 5000$ au; moreover, the q distribution of the remaining stars is somewhat more leaning to larger q values than expected, perhaps due to the higher binding energy of more massive systems (El-Badry et al. 2019).

[2] We do not include μ^2 Scorpii's CC0 in the following discussion.

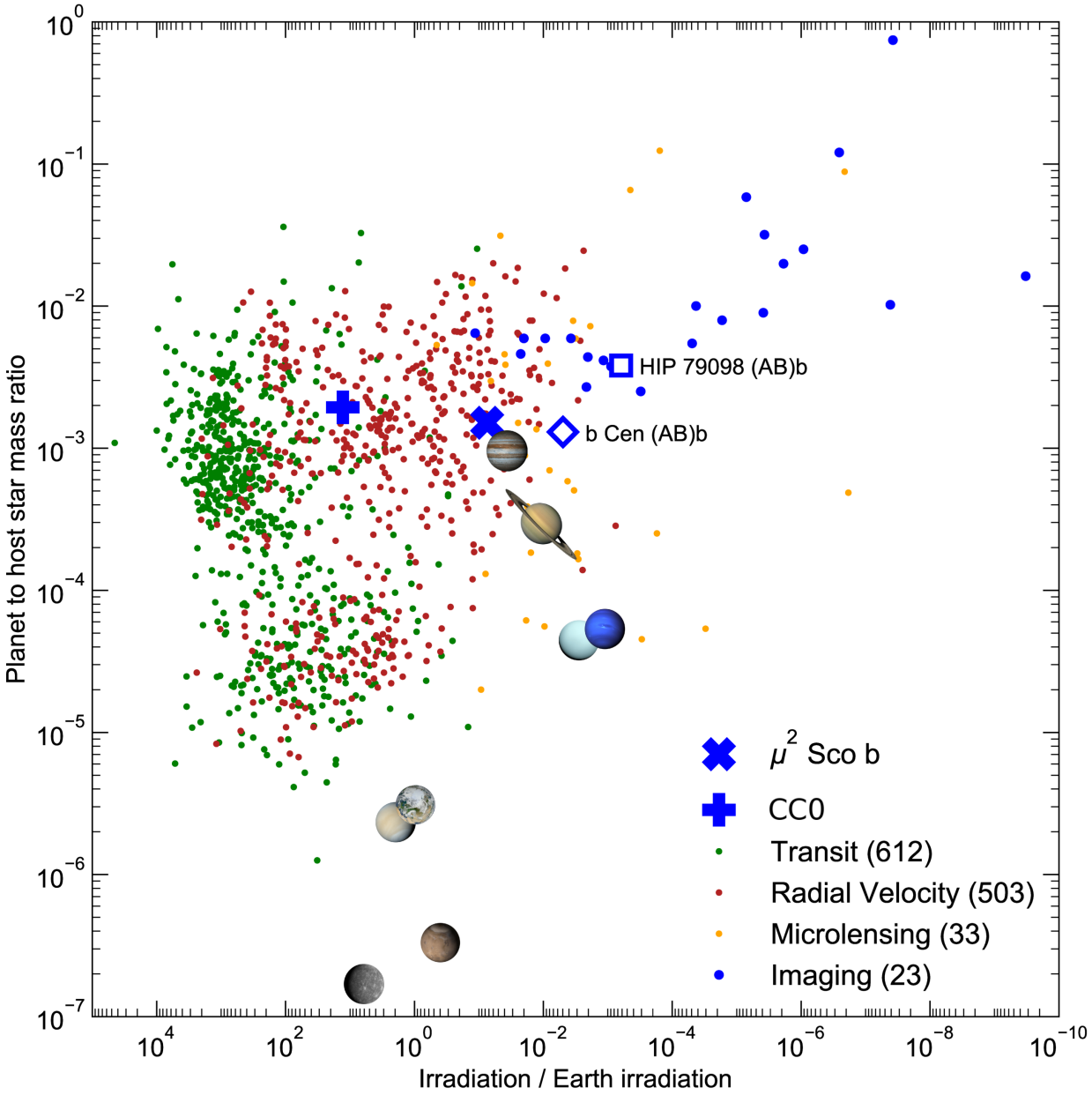

Figure 6.1: Mass ratio vs irradiation for known exoplanets. Only exoplanets whose stellar host mass is known to a precision of at least 30% are shown. Each planet is labeled according to its detection method: transits in green, radial velocity in red, microlensing in orange and direct imaging in blue. BEAST discoveries are overplotted with larger blue symbols, and circular orbits with radius equal to the observed projected distance are assumed; Solar System planets (images from NASA) are also shown for reference. μ^2 Sco b can be considered a Jupiter analog both in terms of irradiation and mass ratio, while the irradiation received by probable CC0 is similar to Mercury's. Sources: NASA Exoplanet Archive (https://exoplanetarchive.ipac.caltech.edu/), the Extrasolar Planets Encyclopaedia (http://exoplanet.eu/).

for the selection bias against binaries, we finally completed our sample with a group of stars that could have been observed in SHINE and BEAST *if they were not known* to be binaries. For SHINE, we started from the initial roster of target candidates and applied all the selection criteria described in Desidera et al. (2021) but the one of binarity. We recovered 470 stars. Under the assumption that these stars would have been divided in priority classes in the same way as the 1224 stars that were actually selected, that is, that the figure of merit distribution of the two samples would have been the same, we randomly added to our sample 53 stars with 59 known companions that would have been detected by SPHERE. As concerns the masses of these primaries and companions, we strictly opted for the following priority order: 1) dynamical masses from the literature, if available; 2) new estimates through MADYS using Gaia DR3 data, if individual components were therein resolved; 3) new estimates through MADYS using the contrasts measured by the instrument that resolved the components. Stellar ages, based on a variety of methods such as the membership to moving groups or associations, lithium depletion, activity and rotation, were retrieved from Desidera et al. (2021). For BEAST, we started from the initial list by Rizzuto et al. (2011) whence the initial candidate roster was extracted, and we recovered the 40 B-type stars complying with all the requirements listed in Section 2.1.1 but the one concerning known binarity. The final SHINE masses were obtained as the average between estimates from BHAC15, PARSEC and MIST isochrones (Table 3.3). In a similar fashion, the masses of BEAST stellar companions[3] were re-evaluated to ensure uniformity; the masses of SHINE binaries were not recomputed, as they already based on MADYS.

In order to compare the derived secondary mass distribution with an empirical IMF that is adequate for Sco-Cen, we recovered the full sample of US members assembled by Miret-Roig et al. (2022). The comparison with our SPHERE sample is shown in Figure 6.2: as confirmed by a Kolmogorov-Smirnov test with level $\alpha = 0.01$, the two distributions are significantly different, even when the SPHERE sample is restricted to companions with a projected separation > 500 au. In particular, the SPHERE distribution is bimodal, and no companions is seen in the mass range $50M_{\rm J} < M < 100M_{\rm J}$. Under the assumption of the US IMF, the probability of having no companions in this mass range is $\sim 10^{-6}$, and even the probability of having less than five such companions is as low as $\sim 2 \cdot 10^{-3}$. The presence of such a dry *brown dwarf desert* is unexpected, and is in tension with the observation that RV companions to FGK stars with periods larger than 80 days are uniformly distributed from $15M_{\rm J}$ to $0.5M_{\odot}$ (Kiefer et al. 2019). As the median, 16th and 84 percentiles of companion-hosting SHINE stars in our sample are $1.17M_{\odot}$, $0.81M_{\odot}$ and $1.76M_{\odot}$, respectively, the primary mass distribution is directly comparable to that of the RV study. In any case, no dependence of this BD desert on mass is observed, as the result holds for the entire SPHERE sample. Indeed, the mass distribution of the BEAST and SHINE subsamples – restricted to $M_p < 1M_{\odot}$ due to SHINE's primary mass distribution – is consistent from being drawn from the same parent distribution according to a Kolmogorov-Smirnov test with level $\alpha = 0.01$.

The projected separation of SPHERE companions is shown in Figures 6.3-6.4 as a function of companion mass and mass ratio, respectively. Overplotted are detection sensitivity contours for the BEAST survey, computed as in Section 2.4.3. If seen in term of the absolute mass, BEAST substellar companions are found in the surroundings of several SHINE sources and might be regarded as low-

[3]The masses of BEAST primaries were instead left as in Table 2.2 due to the presence of several unresolved binaries. A constant 10% uncertainty was assumed. The same method of Table 2.2 was used for the companions of stars excluded from BEAST due to binarity. In a single case (HIP 76600), the parallax of a BEAST star was recomputed, for severe inconsistencies between the spectral type and the absolute magnitudes, on the one hand, and among Gaia and the two Hipparcos reductions, on the other hand, were noted. Assuming $q = 1$ (the star is a double-lined spectroscopic binary), and adjusting the parallax to obtain magnitudes consistent with the observed $J - H$ and $H - K$ colors, we derived $\varpi = 6.84 \pm 0.50$ mas.

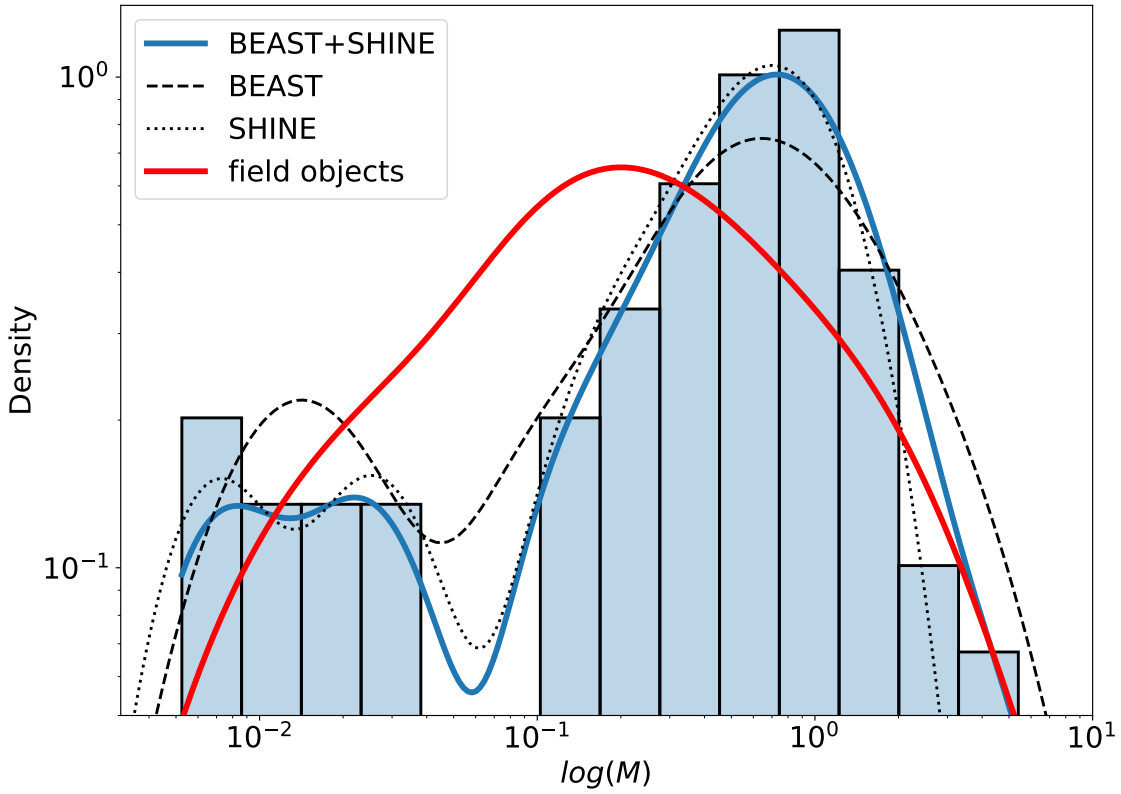

Figure 6.2: Mass distribution of SPHERE companions, showed both with histograms and a KDE (blue line), compared with the US IMF (red line). KDE for the BEAST and SHINE subsamples are shown with a dashed and a dotted line, respectively.

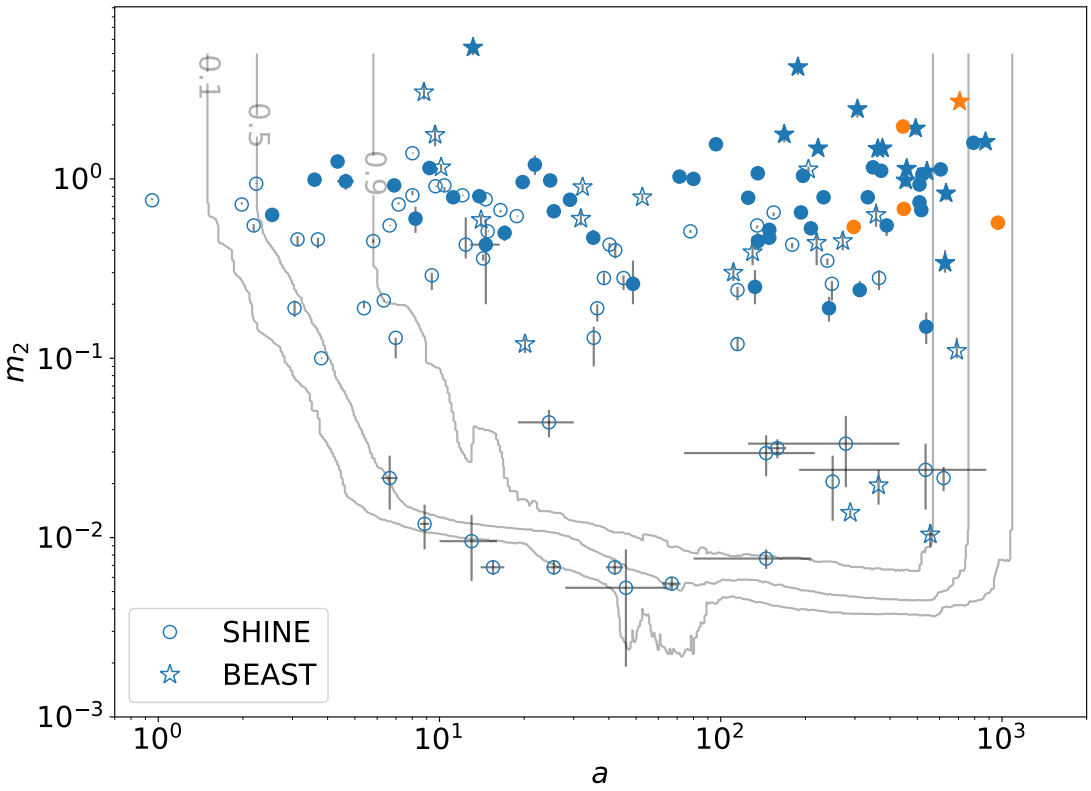

Figure 6.3: Mass vs separation for SPHERE companions (SHINE: dots; BEAST: stars). Filled symbols indicate the companions found around stars excluded from the surveys due to known binarity. Orange symbols indicate companion detected through Gaia. 10%, 50% and 90% detection efficiency contours for the BEAST are overplotted as gray lines.

mass brown dwarfs. Conversely, with respect to their mass ratio, b Centauri b and μ^2 Scorpii b are found to follow a "planet-like" sequence characterized by an anticorrelation between q and a. While this trend might be a mere consequence of survey incompleteness, it is interesting to notice that the same anticorrelation – albeit with a larger scatter – is tentatively seen in the stellar subsample which is virtually complete. The latter trend is qualitatively in agreement with the predictions of a disk fragmentation scenario (Tokovinin & Moe 2020), and corroborates the hypothesis that most SPHERE companions are born within a circumstellar disk.

We point out that most of these last considerations should be regarded as purely indicative, and a full statistical analysis of the entire surveys is needed to draw definitive conclusions on the interplay between different star formation mechanism. Nevertheless, the observed hiatus between a planet-like and a star-like companion population is grounded on solid foundations, and will constitute the focus of the next Section.

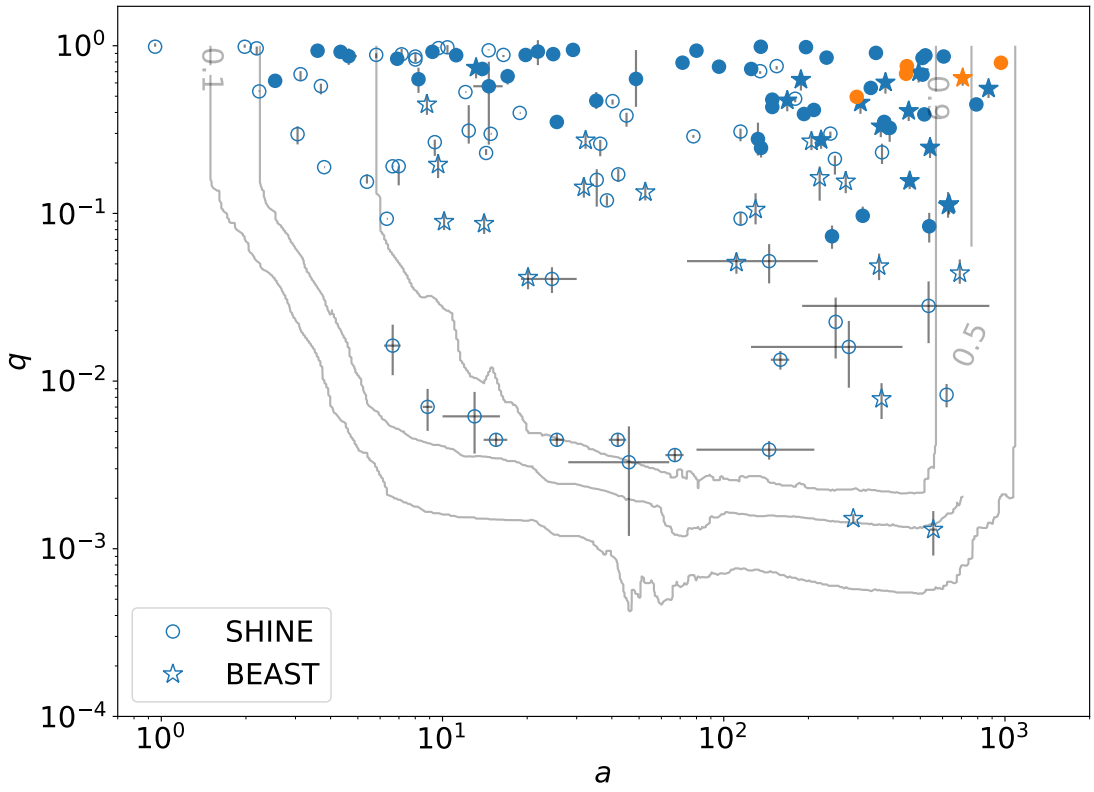

Figure 6.4: Mass ratio vs separation for SPHERE companions (SHINE: dots; BEAST: stars). Filled symbols indicate the companions found around stars excluded from the surveys due to known binarity. Orange symbols indicate companion detected through Gaia. 10%, 50% and 90% detection efficiency contours for the BEAST are overplotted as gray lines.

6.3 A new definition of planet?

Substellar companions with $1 M_{\rm J} \lesssim M \lesssim 40 M_{\rm J}$, populating the low-mass peak of the companion mass distribution shown in Figure 6.2, are more frequently found around more massive hosts both in radial velocity (Reffert et al. 2015; Wolthoff et al. 2022) and direct imaging[4] studies (Bowler 2016; Nielsen et al. 2019; Vigan et al. 2021). As mentioned in Chapter 1, radial velocity studies indicate a turnover in this trend at about 2 $M_{\odot}$; but the increasing separation of the snow line – beyond which most giant planets are thought to form – with stellar mass (Kennedy & Kenyon 2008), coupled with the scarce sensitivity of RV to separations larger than a few au, did not allow before BEAST to argue whether a wide-orbit population around more massive stars existed or not.

We must ask ourselves what we exactly mean by "planet" and "planetary system", and if the μ^2 Sco system should be seen as a planetary system or rather as a multiple stellar system composed of a massive star and one or two brown dwarfs. Just as the transition from substellar to stellar objects at 75˘80 $M_{\rm J}$ is determined by the possibility to ignite hydrogen in their core, the transition from giant planets to brown dwarfs is often set to $\sim 13\ M_{\rm J}$, the so-called deuterium-burning limit (DBL). According to this definition, the μ^2 Sco system should be considered a multiple stellar system, while b Cen b would be a (circumbinary) giant planet. Nevertheless, the clear similarities between the two systems, shown in the previous Section, highlight how a distinction based uniquely on a physical process happening in the core might not be adequate in every circumstance, and certainly not always corresponding to different formation pathways.

A second distinction can be operated between objects being formed "on their own", that is through turbulent core fragmentation, and objects being formed within a circumstellar disk. It is here that the mass ratio, in turn connected to the initial reservoir of the protoplanetary disk (Equation 1.17), comes into play. On the one hand, a few known giant planet companions to very low-mass primary stars or brown dwarfs are likely the outcome of turbulent fragmentation within the natal molecular cloud (e.g., Fontanive et al. 2020). On the other hand, the two brown dwarfs companions ($M \sin i = 22\ M_{\rm J}$ and $25\ M_{\rm J}$) to the evolved $2.7\ M_{\odot}$ star ν Oph show a 6:1 mean motion resonance of their orbits, a clue of a formation within a protoplanetary disk. As we have seen in Section 6.2, substellar companions to B stars – characterized by even smaller mass ratios – most probably belong to this latter group.

This issue has been recently discussed within the IAU Commission F2, and led to a revised version of the definition of planets: although no explicit distinction based on the formation pathway (which is not easily related to physical properties) was set, an upper limit was established to the planet-to-star mass ratio of $q < 0.04$ in addition to the DBL mass limit at $M < 13 M_{\rm J}$ (Lecavelier des Etangs & Lissauer 2022). While this revision is appropriate for systems around low-mass stars, one could also expect that more massive stars —- originally surrounded by more massive protoplanetary disks -— can form companions within a disk that are more massive than the deuterium-burning limit. We notice that the mass ratios q of μ^2 Sco b, the candidate CC0 and b Cen b are consistent with one another and – within a factor two – with that of Jupiter to the Sun (Figure 6.1); the mass ratios are smaller than those in the ν Oph system and the recently adopted revised IAU definition of planet. In this sense, μ^2 Sco b and b Cen b should both be considered as planets.

[4]Mass and separation ranges are highly varying across different direct imaging studies. See Table 3 from Vigan et al. (2021) for a comprehensive comparison of the cited studies.

6.4 The formation mechanism of B-star exoplanets

Adopting, for simplicity, the definition of "B-star exoplanets" for the three (or four, including the probable CC0) substellar companions discovered by BEAST, we should now discuss whether any of the known pathways for giant planet formation might be able to form objects similar to those observed. As mentioned in the Introduction (Section 1.5), neither core accretion or gravitational instability models have been until now designed to cope with stellar hosts as massive as BEAST targets. Indeed, one of the long-term goals of the survey consists in driving theoretical efforts toward the modeling of B-star protoplanetary disks.

For the moment being, it might be useful to address the issue from a semi-empirical standpoint. Giant planets around less massive stars than μ^2 Sco show a bottom-up mass distribution, that is, a larger occurrence of less massive planets; this is not true for stellar companions, which instead show a top-down distribution that favors larger values of q. This stellar companion population, by construction, encompasses every possible pathway for multiple star formation, including disk-borne GI. One might wonder if objects like μ^2 Sco b and b Cen b constitute the high-mass tail of the bottom-up planet-like population (PP), or rather the low-mass tail of the top-down star-like population (SP).

A tentative comparison between a SP and a PP – based in turn on previous multiplicity and direct imaging studies, respectively – can be made in a similar way as in Janson et al. (2021a): for the SP, we adopt a log-normal separation distribution as in (De Rosa et al. 2014) – suited for A stars – and a mass ratio distribution as in Reggiani & Meyer (2013):

$$\frac{\partial^2 N}{\partial \log_{10}(a)\partial q} \propto \frac{(\log_{10}(a[au]) - 2.59)^2}{2 \cdot 0.79^2} \cdot q^{0.25}, \tag{6.6}$$

normalizing it to the median frequency of $1 - 75$ $M_{\rm J}$ companions at [5-300] AU for BA hosts taken from Vigan et al. (2021). For the PP, we adopt the parametric model from Vigan et al. (2021) and Meyer et al. (2021) with the set of parameters referring to BA stars:

$$\frac{\partial^2 N}{\partial \log_{10}(a)\partial q} \propto \frac{(\log_{10}(a[au]) - 0.79)^2}{2 \cdot 0.77^2} \cdot q^{-1.31}. \tag{6.7}$$

The expected number of companions around one star with $a \in [100, 1000]$ au, $q \in [0.0005, 0.0030]$ is $1.4 \cdot 10^{-4}$ for the SP scenario, $9.0 \cdot 10^{-3}$ for the PP scenario. Taking into account that we have observed 39 targets in the survey, the probability of finding at least one companion within these ranges is $5.4 \cdot 10^{-3}$ for the SP scenario and 0.30 for the PP scenario. If we further assume that – as suggested for stars with $M < 2.5 M_{\odot}$ (Vigan et al. 2021) – the peak of the orbital distribution shifts to larger separations with stellar mass, and we employ irradiation levels as our scaling factor, the probability under the PP scenario rises to 0.91. In this last case, the probability of finding at least two companions – as μ^2 Sco b and b Cen b – is fairly high too (0.68). We stress that the comparison is based on a naive extrapolation of the known frequencies of planetary and stellar companions from A stars to ~ 9 $M_{\odot}$ stars, and that a companion mass ratio distribution getting steeper at larger separations (De Rosa et al. 2014; Moe & Di Stefano 2017) might mitigate – at least partially – such a strong prevalence for the PP scenario.

From a formation standpoint, the bottom-up PP distribution is naturally associated with CA. CA assembles giant planets by building a solid core from dust present in the protoplanetary disk; as the core attains a critical mass (~ 10 $M_{\oplus}$), it rapidly starts accreting hydrogen and helium to become a gas giant (Pollack et al. 1996). The shift of the orbital peak of the PP distribution would

be a natural consequence of the wider distance of the snow line, and the increased reservoir of gas and dust in the protoplanetary disk would make it possible to form an object as massive as μ^2 Sco b; in other words, the PP scenario would explain the similarity of q ratio and irradiation with CA planets like Jupiter.

On the other hand, CA requires a few million years to operate, a timescale comparable to the disk lifetime around low-mass stars (Gorti et al. 2009; Gorti & Hollenbach 2009). The survival of a protoplanetary disk is mainly dictated by the strength of ultraviolet (FUV: 6 eV $< h\nu <$ 13.6 eV; EUV: 13.6 eV $< h\nu <$ 0.1 keV) and X-ray (0.1 keV $< h\nu <$ 2 keV) irradiation from the central star. While disk lifetimes do not vary much for stellar masses in the range 0.3-3 $M_\odot$, more massive stars (> 7 $M_\odot$) are expected to lose their disks rapidly (in $\sim 10^5$ years) due to extremely high EUV and FUV fields (Gorti & Hollenbach 2009). Indeed, only very feeble disk remnants have been observed around O stars, while disks around B stars survive for a few hundred thousand years, leaving not enough time for CA to operate (Gorti et al. 2009).

In this regard, it is interesting to qualitatively compare the disk survival timescales of the binary b Cen ($M_A \sim 5.5$ $M_\odot$, $M_B \sim 3.5$ $M_\odot$) and the single μ^2 Sco ($M \sim 9.1$ $M_\odot$). While a naive comparison between b Cen A – expected to emit nearly all the X and UV flux in the b Cen system and treated thus as a single star – and μ^2 Sco would yield a three times shorter disk lifetime around μ^2 Sco (see eq. 7 by Gorti & Hollenbach 2009), the actual ratio should be much larger due to an initial disk mass for b Cen related to the total system mass, hence comparable to that of μ^2 Sco. Combining Eq. (11) from Cesaroni et al. (2007) for the photoevaporation outflow rate with the expected ionizing photon flux Φ for the three stars, the ratio[5] between the two disk survival timescales should be around ~ 20. While the impact of this on planet formation is difficult to be properly assessed, the presence of (at least) a companion with $q \sim 0.002$ around μ^2 Sco looks much more challenging than that around b Cen in the framework of a CA scenario. Recent updates of the classical CA model, such as pebble accretion, have been indicated as a possible solution to the conundrum (Lambrechts & Johansen 2012)[6]

According to our parametric model, GI should be considered as one of the top-down processes underlying the disfavoured SP scenario. While not likely to be responsible for most planets observed around solar-type stars, this extremely rapid ($\sim 10^4$ yr) mechanism might be considered for stars much more massive than the Sun; GI preferentially produces massive planets in wide orbits, although rapid migration can force some of them to move much closer to the star (Malik et al. 2015). In this regard, it is interesting to notice that our orbital analysis shows a preference for large eccentricities for both the confirmed μ^2 Sco b and the probable CC0. A recent analysis of 27 directly imaged giant planets and brown dwarfs in the separation range 5-100 au around a wide range of stellar hosts ($0.2 - 2.8$ $M_\odot$) has hinted at an interesting eccentricity dichotomy between the two populations: while the former usually has low eccentricity values ($e = 0.13^{+0.12}_{-0.08}$), the latter is characterized by a flat distribution over the range $0 < e < 1$ (Bowler et al. 2020). If this dichotomy continues at larger separations and stellar masses, it might favor an in-situ GI scenario for μ^2 Sco b and CC0 (as regards b Cen b, only indications that $e < 0.4$ exists); alternatively, the large eccentricities might

[5]We interpolate between $\log \Phi_{\rm EUV}$ values for $M = 3$ $M_\odot$ and $M = 7$ $M_\odot$ (see Table 2 by Gorti & Hollenbach 2009) and ϕ_i values for $M = 16.8$ $M_\odot$, $M = 25.6$ $M_\odot$ and $M = 65$ $M_\odot$ (Hollenbach et al. 1994), deriving the empirical relation $\log \Phi = -5.9705 \log M + 21.553 \log M + 30.1$. The b Cen photoevaporation outflow rate is the sum of the individual contributions of b Cen A and b Cen B.

[6]Alternatively, the problem might be alleviated if μ^2 Sco were actually formed by the merging of two nearly equal mass stars, which is possibly not an exotic case (de Mink et al. 2014). On this respect, it is notable that μ^2 Sco appears to be a slow rotator (see Appendix 5.3.B); in fact it has been argued recently that post-mergers should appear as slow rotators Schneider et al. (2019); Wang et al. (2022). On the other hand, the same studies suggest that mergers might have strong magnetic fields, but there is no evidence for this in μ^2 Sco (see Appendix 5.3.B).

be simply a result of a strong dynamical evolution after formation, possibly causing the migration of μ^2 Sco b and CC0 into their current orbits (bringing a CA scenario back into the game; see, e.g., Marleau et al. 2019a).

It is instructive to estimate whether an in-situ formation at the position of CC0 is possible according to current GI models. With a best-fit semimajor axis of about 20 au, the mean irradiation level of CC0 is comparable to that of Mercury, preventing the presence of ice grains which are fundamental in a CA scenario (Mordasini et al. 2012a). Whether the same argument applies to GI is not clear, crucially depending on the values of Toomre's Q parameter and the cooling time, which determine if the protoplanetary disk can fragment or not at this position. Fragmentation occurs if Toomre's Q parameter, defined as:

$$Q = \frac{\Omega^* c_s}{\pi G \Sigma}, \tag{6.8}$$

is less than unity. Here Ω^* is the epicyclic frequency, c_s is the sound speed, G is the gravitational constant and Σ is the surface density. Since the radial dependencies of Ω^* and Σ are similar ($\propto r^{-3/2}$), the radial variation of Q depends on that of c_s, and the treatment can be simplified. Recalling that a full modeling of GI around stars as massive as μ^2 Sco is still lacking, we might start from simple scaling laws from the results obtained for solar hosts. The relevant proportionalities in Q are given by: $\Omega^* \propto M_*^{1/2}$, $c_s \propto T_{gas}^{1/2}$, $\Sigma \propto M_{\rm disk}$. As regards the disk mass, we conservatively assume a linear proportionality between $M_{\rm disk}$ and M_*. For the gas temperature, we might start from our best-fit estimates for stellar radius and $T_{\rm eff}$ to derive the effect due to stellar irradiation at 20 au (Eq. 4, 96) that is $T_{irr} = 690 \pm 50$ K, supposing a flared disk in vertical hydrostatic equilibrium. The onset of fragmentation for $0.1 M_\odot$ disks around $1 M_\odot$ stars in theoretical simulations occurs for $T \lesssim 50$ K (Helled et al. 2014), so we may write:

$$Q_c = \frac{\sqrt{\frac{M_*}{1M_\odot}}\sqrt{\frac{T_{irr}}{50K}}}{\left(\frac{M_{\rm disk}}{0.1M_\odot}\right)} \sim 1.23. \tag{6.9}$$

Since fragmentation happens if $Q_c < 1$, a formation from GI would not be possible at the location of CC0. However, if $M_{\rm disk}/M_*$ increases by more than 20% than expected from the linear proportionality in the mass range of B stars, as assumed above, in situ fragmentation at the position of CC0 becomes possible. Indeed, indications exist that – at least for $M < 2M_\odot$ – $M_{\rm disk} \propto M^q$ with $q = 1.3-2.0$ (Pascucci et al. 2016): assuming that $q > 1.1$ for B stars, the value of Q_c would become lower than 1. Also, a warmer disk reduces the cooling time, favoring the onset of fragmentation at fixed Q. On the other hand, given the much lower irradiation temperature at the distance of μ^2 Sco b, μ^2 Sco b could have easily formed in situ via GI: not only the Toomre parameter is likely much smaller than unity in the approximations considered above; but also, more importantly, the conditions in protoplanetary disks at $R > 50$ au are most favorable to fragmentation since gas, even in a massive disk, is expected to be optically thin, thus leading to short cooling timescales (Boley et al. 2010).

An interesting consequence of this scenario would be that disks around stars similar to μ^2 Sco might be unstable at some phase of their evolution over a wide range of separations. However, the formation of planet-like objects such as the companions of b Cen and μ^2 Sco rather than more massive (even stellar) objects is difficult to reconcile with a GI scenario, preferentially producing massive BD and low-mass stars (Kratter et al. 2010). Extensive population synthesis efforts, taking into account migration and N-body interactions, have found that 90-95% of the surviving objects have masses above the DBL already around stars with $0.8 - 1.2 M_\odot$ (Forgan & Rice 2013; Forgan

et al. 2018). The corresponding typical mass ratio $q = 0.01 - 0.1$ is one or two orders of magnitude larger than that of b Cen b and μ^2 Sco b and CC0, implying an unusually low conversion efficiency of disk mass into companion mass for BEAST companions. Hence, the presence of B-star exoplanets is not expected; according to recent 3D radiative magneto-hydrodynamic simulations, though, the presence of a magnetic field can reduce the fragmentation scale by 1-2 orders of magnitude, possibly turning GI into a viable formation path for Jupiter-analogs around B stars (Boley et al. 2010; Deng et al. 2021). It is currently not clear whether also the brown dwarf desert observed in the SPHERE sample might be reproduced under this modified scenario.

We stress that any definitive conclusion on this problem cannot be reached without a follow-up of the detected system, the completion of the BEAST survey and, finally, the development of theoretical model tuned to B-type stars.

6.5 Summary and future perspectives

This Thesis has been devoted to the quest for giant planets around young B-type stars with the purpose of probing the frontiers of planetary formation models. After illustrating why direct imaging is the best-suited planet-hunting technique for this specific science case (Chapter 1), we have introduced the BEAST survey and its main features. Crucially, we introduced an indirect method for age determination for its stellar sample (Chapter 2). We have presented a tool initially designed to this particular scope and later extended to a whole range of possible scientific applications (Chapter 3). Thanks to MADYS we have explored the kinematic structure of the Upper Scorpius association, gaining new insights on its star formation history (Chapter 4). The early results of BEAST, consisting in the discovery of three substellar companions with peculiar properties, have been reported in Chapter 5 and discussed in the present Chapter.
We summarize here the main results presented throughout this dissertation:

- an indirect method for age determination of young stars was devised. Exploiting the kinematic structure of the Scorpius-Centaurus association, we were able to identify groups of comoving stars to BEAST targets and to constrain this key parameter for direct imaging compaigns (Janson et al. 2021b);
- we created a versatile Python tool, MADYS, for the determination of stellar and substellar parameters, notably age and mass, and applied it to individual substellar companions, to isolated stars, to groups of comoving stars and even to the entire Upper Scorpius association (Squicciarini & Bonavita 2022);
- we discovered a network of substructures in the Upper Scorpius association, finding a correlation between its current velocity structure and its star formation history (Squicciarini et al. 2021);
- we discovered and analyzed the outstanding μ^2 Scorpii system, composed of a robustly detected $14.4 \pm 0.8 M_{\rm J}$ companion and possibly of a second closer $\sim 20 M_{\rm J}$ object. The first planet-like system around a star massive enough to end up its life as a supernova, μ^2 Scorpii is expect to elicit – together with its sibling b Centauri – a vibrant discussion in the exoplanet community (Squicciarini et al. 2022).

While the main question at the root of this Thesis (*"can planet formation occur around B-type stars?"*) eventually found a positive answer, an entire kaleidoscope of consequent questions was born out of that response:

- if B-star environments are scaled-up versions of our Solar System, how can the shorter disk survival around more massive stars be reconciled with the slow growth of solid cores required by core accretion?
- if instead the responsible mechanism is gravitational instability, why does the observed mass distribution deviate from expectations?
- is there any physical difference between bound and free-floating substellar objects?

Future work, including atmospheric characterization of B-star exoplanets through high-resolution spectroscopy, interferometric and astrometric follow-up aimed at refining their orbital elements, dedicated searches for circumplanetary disks in the near-infrared and mid-infrared range, will help us connect the dots and ascertain their still elusive origin. Besides that, the completion of BEAST and, perhaps, the commencement of similar surveys, combined with demographic studies that will be carried on by ground-based and space-borne facilities – such as the Extremely Large Telescope (Gilmozzi & Spyromilio 2007) and the James Webb Space Telescope (Gardner et al. 2006) –, will enable a comprehensive analysis of the substellar companion population across a range of primary masses wider than ever before, and pave the way to a new suite of planet formation models dedicated to intermediate and massive stars.

List of Figures

List of Tables

Bibliography

Abt, H. A. & Morrell, N. I. 1995, ApJS, 99, 135

Ahumada, R., Prieto, C. A., Almeida, A., et al. 2020, ApJS, 249, 3

Albareti, F. D., Allende Prieto, C., Almeida, A., et al. 2017, ApJS, 233, 25

Alecian, E., Tkachenko, A., Neiner, C., Folsom, C. P., & Leroy, B. 2016, A&A, 589, A47

Alibert, Y., Mordasini, C., & Benz, W. 2011, A&A, 526, A63

Allard, F. 2016, in SF2A-2016: Proceedings of the Annual meeting of the French Society of Astronomy and Astrophysics, ed. C. Reylé, J. Richard, L. Cambrésy, M. Deleuil, E. Pécontal, L. Tresse, & I. Vauglin, 223–227

Allard, F., Hauschildt, P. H., Alexander, D. R., Tamanai, A., & Schweitzer, A. 2001, ApJ, 556, 357

Allard, F., Homeier, D., & Freytag, B. 2011, in Astronomical Society of the Pacific Conference Series, Vol. 448, 16th Cambridge Workshop on Cool Stars, Stellar Systems, and the Sun, ed. C. Johns-Krull, M. K. Browning, & A. A. West, 91

Amard, L., Palacios, A., Charbonnel, C., et al. 2019, A&A, 631, A77

Ambartsumian, V. A. 1954, in Liege International Astrophysical Colloquia, Vol. 5, Liege International Astrophysical Colloquia, 293

Andrews, J. J., Breivik, K., & Chatterjee, S. 2019, ApJ, 886, 68

Andrews, S. M., Huang, J., Pérez, L. M., et al. 2018, ApJ, 869, L41

Andrews, S. M., Rosenfeld, K. A., Kraus, A. L., & Wilner, D. J. 2013, ApJ, 771, 129

Angus, R., Morton, T., & Foreman-Mackey, D. 2019, The Journal of Open Source Software, 4, 1469

Armitage, P. J. 2020, Astrophysics of Planet Formation, 2nd edn. (Cambridge University Press)

Arzoumanian, D., André, P., Könyves, V., et al. 2019, A&A, 621, A42

Asensio-Torres, R., Currie, T., Janson, M., et al. 2019, A&A, 622, A42

Astropy Collaboration, Robitaille, T. P., Tollerud, E. J., et al. 2013, A&A, 558, A33

Backus, I. & Quinn, T. 2016, MNRAS, 463, 2480

Baillié, K., Marques, J., & Piau, L. 2019, A&A, 624, A93

Baines, E. K., White, R. J., Huber, D., et al. 2012, ApJ, 761, 57

Balona, L. A. 1984, MNRAS, 211, 973

Balona, L. A. 1994, MNRAS, 268, 119

Baraffe, I., Homeier, D., Allard, F., & Chabrier, G. 2015, A&A, 577, A42

Barnes, A. T., Longmore, S. N., Dale, J. E., et al. 2020, MNRAS, 498, 4906

Barnes, S. A. 2007, ApJ, 669, 1167

Barrado, D. 2016, in EAS Publications Series, Vol. 80-81, EAS Publications Series, 115–175

Baruteau, C., Crida, A., Paardekooper, S. J., et al. 2014, in Protostars and Planets VI, ed. H. Beuther, R. S. Klessen, C. P. Dullemond, & T. Henning, 667

Basri, G. & Brown, M. E. 2006, Annual Review of Earth and Planetary Sciences, 34, 193

Batalha, N. M., Rowe, J. F., Bryson, S. T., et al. 2013, ApJS, 204, 24

Bate, M. R., Bonnell, I. A., & Bromm, V. 2002, MNRAS, 336, 705

Beckwith, S. V. W., Sargent, A. I., Chini, R. S., & Guesten, R. 1990, AJ, 99, 924

Bell, C. P. M., Mamajek, E. E., & Naylor, T. 2015, MNRAS, 454, 593

Bell, C. P. M., Naylor, T., Mayne, N. J., Jeffries, R. D., & Littlefair, S. P. 2013, MNRAS, 434, 806

Benisty, M., Bae, J., Facchini, S., et al. 2021, ApJ, 916, L2

Berger, T. A., Huber, D., van Saders, J. L., et al. 2020, AJ, 159, 280

Berghoefer, T. W., Schmitt, J. H. M. M., & Cassinelli, J. P. 1996, A&AS, 118, 481

Beuzit, J. L., Demailly, L., Gendron, E., et al. 1997, Experimental Astronomy, 7, 285

Beuzit, J. L., Vigan, A., Mouillet, D., et al. 2019, A&A, 631, A155

Birnstiel, T., Ormel, C. W., & Dullemond, C. P. 2011, A&A, 525, A11

Blaauw, A. 1946, Publications of the Kapteyn Astronomical Laboratory Groningen, 52, 1

Blaauw, A. 1964, ARA&A, 2, 213

Blaauw, A. 1978, Internal Motions and Age of the Sub-Association Upper Scorpio (Mirzoyan, L. V.), 101

Blair, A. M. 1990, Journal of the History of Ideas, 51, 405

Blunt, S., Wang, J. J., Angelo, I., et al. 2020, AJ, 159, 89

Boccaletti, A., Di Folco, E., Pantin, E., et al. 2020, A&A, 637, L5

Bodenheimer, P. & Pollack, J. B. 1986, Icarus, 67, 391

Boley, A. C., Hayfield, T., Mayer, L., & Durisen, R. H. 2010, Icarus, 207, 509

Bonavita, M. 2020, Exo-DMC: Exoplanet Detection Map Calculator

Bonavita, M., Fontanive, C., Gratton, R., et al. 2022a, MNRAS, 513, 5588

Bonavita, M., Gratton, R., Desidera, S., et al. 2022b, A&A, 663, A144

Bond, I. A., Udalski, A., Jaroszyński, M., et al. 2004, ApJ, 606, L155

Bonnefoy, M., Zurlo, A., Baudino, J. L., et al. 2016, A&A, 587, A58

Borucki, W. J., Koch, D., Basri, G., et al. 2010, Science, 327, 977

Boss, A. P. 1997, Science, 276, 1836

Bowler, B. P. 2016, PASP, 128, 102001

Bowler, B. P., Blunt, S. C., & Nielsen, E. L. 2020, AJ, 159, 63

Boyajian, T. S., McAlister, H. A., van Belle, G., et al. 2012a, ApJ, 746, 101

Boyajian, T. S., von Braun, K., van Belle, G., et al. 2012b, ApJ, 757, 112

Brandt, G. M., Brandt, T. D., Dupuy, T. J., Li, Y., & Michalik, D. 2021a, AJ, 161, 179

Brandt, G. M., Brandt, T. D., Dupuy, T. J., Michalik, D., & Marleau, G.-D. 2021b, ApJ, 915, L16

Brandt, T. D., Dupuy, T. J., & Bowler, B. P. 2019, AJ, 158, 140

Brown, A. G. A., Dekker, G., & de Zeeuw, P. T. 1997, MNRAS, 285, 479

Brown, A. G. A. & Verschueren, W. 1997, A&A, 319, 811

Bryan, M. L., Knutson, H. A., Howard, A. W., et al. 2016, ApJ, 821, 89

Budding, E., Butland, R., & Blackford, M. 2015, MNRAS, 448, 3784

Buder, S., Sharma, S., Kos, J., et al. 2021, MNRAS, 506, 150

Burrows, A., Hubbard, W. B., Lunine, J. I., & Liebert, J. 2001, Reviews of Modern Physics, 73, 719

Burrows, A., Marley, M., Hubbard, W. B., et al. 1997, ApJ, 491, 856

Busso, G., Cacciari, C., Bellazzini, M., et al. 2021, Gaia EDR3 documentation Chapter 5: Photometric data, Gaia EDR3 documentation

Cadman, J., Rice, K., Hall, C., Haworth, T. J., & Biller, B. 2020, MNRAS, 492, 5041

Cameron, A. G. W. 1978, Moon and Planets, 18, 5

Campbell, B., Walker, G. A. H., & Yang, S. 1988, ApJ, 331, 902

Cánovas, H., Cantero, C., Cieza, L., et al. 2019, A&A, 626, A80

Cantat-Gaudin, T., Jordi, C., Vallenari, A., et al. 2018, A&A, 618, A93

Cantat-Gaudin, T., Jordi, C., Wright, N. J., et al. 2019a, A&A, 626, A17

Cantat-Gaudin, T., Krone-Martins, A., Sedaghat, N., et al. 2019b, A&A, 624, A126

Carbillet, M., Bendjoya, P., Abe, L., et al. 2011, Experimental Astronomy, 30, 39

Cardiel, N., Zamorano, J., Bará, S., et al. 2021, MNRAS, 504, 3730

Carpenter, J. M., Mamajek, E. E., Hillenbrand, L. A., & Meyer, M. R. 2006, ApJ, 651, L49

Carpenter, J. M., Mamajek, E. E., Hillenbrand, L. A., & Meyer, M. R. 2009, ApJ, 705, 1646

Carson, J., Thalmann, C., Janson, M., et al. 2013, ApJ, 763, L32

Casertano, S., Lattanzi, M. G., Sozzetti, A., et al. 2008, A&A, 482, 699

Castelli, F. 1991, A&A, 251, 106

Castelli, F. & Kurucz, R. L. 2003, in Modelling of Stellar Atmospheres, ed. N. Piskunov, W. W. Weiss, & D. F. Gray, Vol. 210, A20

Ceppi, S., Cuello, N., Lodato, G., et al. 2022, MNRAS, 514, 906

Cesaroni, R., Galli, D., Lodato, G., Walmsley, C. M., & Zhang, Q. 2007, in Protostars and Planets V, ed. B. Reipurth, D. Jewitt, & K. Keil, 197

Cesaroni, R., Neri, R., Olmi, L., et al. 2005, A&A, 434, 1039

Chabrier, G. 2003, PASP, 115, 763

Chabrier, G., Johansen, A., Janson, M., & Rafikov, R. 2014, in Protostars and Planets VI, ed. H. Beuther, R. S. Klessen, C. P. Dullemond, & T. Henning, 619

Chambers, K. C., Magnier, E. A., Metcalfe, N., et al. 2016, arXiv e-prints, arXiv:1612.05560

Chao, K.-H., deGraffenried, R., Lach, M., et al. 2021, Chemie der Erde / Geochemistry, 81, 125735

Charbonneau, D., Brown, T. M., Latham, D. W., & Mayor, M. 2000, ApJ, 529, L45

Chauvin, G., Lagrange, A. M., Dumas, C., et al. 2004, A&A, 425, L29

Cheetham, A., Bonnefoy, M., Desidera, S., et al. 2018, A&A, 615, A160

Chen, C. H., Pecaut, M., Mamajek, E. E., Su, K. Y. L., & Bitner, M. 2012, ApJ, 756, 133

Chini, R., Hoffmeister, V. H., Nasseri, A., Stahl, O., & Zinnecker, H. 2012, MNRAS, 424, 1925

Choi, J., Dotter, A., Conroy, C., et al. 2016, ApJ, 823, 102

Clarke, C. J. 2009, MNRAS, 396, 1066

Clarke, C. J., Gendrin, A., & Sotomayor, M. 2001, MNRAS, 328, 485

Claudi, R. U., Turatto, M., Gratton, R. G., et al. 2008, in Society of Photo-Optical Instrumentation Engineers (SPIE) Conference Series, Vol. 7014, Ground-based and Airborne Instrumentation for Astronomy II, ed. I. S. McLean & M. M. Casali, 70143E

Cody, A. M. & Hillenbrand, L. A. 2018, AJ, 156, 71

Cossins, P., Lodato, G., & Clarke, C. J. 2009, MNRAS, 393, 1157

Currie, T. & Hansen, B. 2007, ApJ, 666, 1232

Cutri, R. M., Skrutskie, M. F., van Dyk, S., et al. 2003, VizieR Online Data Catalog, II/246

Cutri, R. M., Wright, E. L., Conrow, T., et al. 2012, Explanatory Supplement to the WISE All-Sky Data Release Products, Explanatory Supplement to the WISE All-Sky Data Release Products

Cutri, R. M., Wright, E. L., Conrow, T., et al. 2021, VizieR Online Data Catalog, II/328

Czekaj, M. A., Robin, A. C., Figueras, F., Luri, X., & Haywood, M. 2014, A&A, 564, A102

Daffern-Powell, E. C., Parker, R. J., & Quanz, S. P. 2022, MNRAS, 514, 920

Dahm, S. E. & Carpenter, J. M. 2009, AJ, 137, 4024

Damiani, F., Prisinzano, L., Jeffries, R. D., et al. 2017, A&A, 602, L1

Damiani, F., Prisinzano, L., Pillitteri, I., Micela, G., & Sciortino, S. 2019, A&A, 623, A112

David, T. J. & Hillenbrand, L. A. 2015, ApJ, 804, 146

David, T. J., Hillenbrand, L. A., Gillen, E., et al. 2019, ApJ, 872, 161

Davis, J., Tango, W. J., Booth, A. J., et al. 1999, MNRAS, 303, 773

de Geus, E. J., de Zeeuw, P. T., & Lub, J. 1989, A&A, 216, 44

de Mink, S. E., Sana, H., Langer, N., Izzard, R. G., & Schneider, F. R. N. 2014, ApJ, 782, 7

De Rosa, R. J., Patience, J., Wilson, P. A., et al. 2014, MNRAS, 437, 1216

de Zeeuw, P. T., Hoogerwerf, R., de Bruijne, J. H. J., Brown, A. G. A., & Blaauw, A. 1999, AJ, 117, 354

Deeg, H. J. & Belmonte, J. A. 2018, Handbook of Exoplanets (Springer Cham)

Deng, H., Mayer, L., & Helled, R. 2021, Nature Astronomy, 5, 440

Desidera, S., Chauvin, G., Bonavita, M., et al. 2021, A&A, 651, A70

Dodson-Robinson, S. E., Veras, D., Ford, E. B., & Beichman, C. A. 2009, ApJ, 707, 79

Dohlen, K., Langlois, M., Saisse, M., et al. 2008, in Society of Photo-Optical Instrumentation Engineers (SPIE) Conference Series, Vol. 7014, Ground-based and Airborne Instrumentation for Astronomy II, ed. I. S. McLean & M. M. Casali, 70143L

Dominik, C., Blum, J., Cuzzi, J. N., & Wurm, G. 2007, in Protostars and Planets V, ed. B. Reipurth, D. Jewitt, & K. Keil, 783

Donaldson, J. K., Weinberger, A. J., Gagné, J., Boss, A. P., & Keiser, S. A. 2017, ApJ, 850, 11

Donati, J. F., Catala, C., Landstreet, J. D., & Petit, P. 2006, in Astronomical Society of the Pacific Conference Series, Vol. 358, Solar Polarization 4, ed. R. Casini & B. W. Lites, 362

Donati, J. F., Semel, M., Carter, B. D., Rees, D. E., & Collier Cameron, A. 1997, MNRAS, 291, 658

Dones, L. & Tremaine, S. 1993, Icarus, 103, 67

D'Orazi, V., Biazzo, K., & Randich, S. 2011, A&A, 526, A103

Dotter, A. 2016, ApJS, 222, 8

Doyon, R., Lafrenière, D., Artigau, E., Malo, L., & Marois, C. 2010, in In the Spirit of Lyot 2010, ed. A. Boccaletti, E42

Duchêne, G. & Kraus, A. 2013, ARA&A, 51, 269

Ducourant, C., Teixeira, R., Galli, P. A. B., et al. 2014, A&A, 563, A121

Ducourant, C., Teixeira, R., Krone-Martins, A., et al. 2017, A&A, 597, A90

Duffell, P. C., D'Orazio, D., Derdzinski, A., et al. 2020, ApJ, 901, 25

Dullemond, C. P. & Dominik, C. 2005, A&A, 434, 971

Duncan, M., Quinn, T., & Tremaine, S. 1988, ApJ, 328, L69

Duquennoy, A. & Mayor, M. 1991, A&A, 248, 485

Ekström, S., Georgy, C., Eggenberger, P., et al. 2012, A&A, 537, A146

El-Badry, K., Rix, H.-W., Tian, H., Duchêne, G., & Moe, M. 2019, MNRAS, 489, 5822

Elmegreen, B. G. & Elmegreen, D. M. 2001, AJ, 121, 1507

Emsenhuber, A., Mordasini, C., Burn, R., et al. 2021, A&A, 656, A69

Epstein, C. R. & Pinsonneault, M. H. 2014, ApJ, 780, 159

Erickson, K. L., Wilking, B. A., Meyer, M. R., Robinson, J. G., & Stephenson, L. N. 2011, AJ, 142, 140

Espaillat, C., Ingleby, L., Hernández, J., et al. 2012, ApJ, 747, 103

Esplin, T. L., Luhman, K. L., Miller, E. B., & Mamajek, E. E. 2018, AJ, 156, 75

Essick, R. & Weinberg, N. N. 2016, ApJ, 816, 18

Evans, D. W., Riello, M., De Angeli, F., et al. 2018, A&A, 616, A4

Evans, J. 1998, The history & practice of ancient astronomy (Oxford University Press)

Everitt, B., Landau, S., Leese, M., & Stahl, D. 2011, Cluster analysis, 5th edn. (Wiley)

Fabricius, C., Luri, X., Arenou, F., et al. 2021, A&A, 649, A5

Faherty, J. K., Riedel, A. R., Cruz, K. L., et al. 2016, ApJS, 225, 10

Falgarone, E., Phillips, T. G., & Walker, C. K. 1991, ApJ, 378, 186

Fang, Q., Herczeg, G. J., & Rizzuto, A. 2017, ApJ, 842, 123

Fedele, D., Carney, M., Hogerheijde, M. R., et al. 2017, A&A, 600, A72

Fedele, D., van den Ancker, M. E., Henning, T., Jayawardhana, R., & Oliveira, J. M. 2010, A&A, 510, A72

Feiden, G. A. 2016a, A&A, 593, A99

Feiden, G. A. 2016b, in Young Stars & Planets Near the Sun, ed. J. H. Kastner, B. Stelzer, & S. A. Metchev, Vol. 314, 79–84

Feiden, G. A. & Chaboyer, B. 2012, ApJ, 761, 30

Fernandes, R. B., Mulders, G. D., Pascucci, I., Mordasini, C., & Emsenhuber, A. 2019, ApJ, 874, 81

Fernandez, J. A. 1980, MNRAS, 192, 481

Fiorucci, M. & Munari, U. 2003, A&A, 401, 781

Fitzpatrick, E. L. & Massa, D. 2005, AJ, 129, 1642

Flasseur, O., Denis, L., Thiébaut, É., & Langlois, M. 2018, A&A, 618, A138

Flasseur, O., Denis, L., Thiébaut, É., & Langlois, M. 2020, A&A, 637, A9

Fontanive, C., Allers, K. N., Pantoja, B., et al. 2020, ApJ, 905, L14

Forgan, D. & Rice, K. 2011, MNRAS, 417, 1928

Forgan, D. & Rice, K. 2013, MNRAS, 432, 3168

Forgan, D. H., Hall, C., Meru, F., & Rice, W. K. M. 2018, MNRAS, 474, 5036

Fulton, B. J., Rosenthal, L. J., Hirsch, L. A., et al. 2021, ApJS, 255, 14

Gagné, J., Lafrenière, D., Doyon, R., Malo, L., & Artigau, É. 2014, ApJ, 783, 121

Gagné, J., Mamajek, E. E., Malo, L., et al. 2018, ApJ, 856, 23

Gaia Collaboration, Babusiaux, C., van Leeuwen, F., et al. 2018a, A&A, 616, A10

Gaia Collaboration, Brown, A. G. A., Vallenari, A., et al. 2018b, A&A, 616, A1

Gaia Collaboration, Brown, A. G. A., Vallenari, A., et al. 2021, A&A, 649, A1

Gaia Collaboration, Prusti, T., de Bruijne, J. H. J., et al. 2016, A&A, 595, A1

Gaia Collaboration, Vallenari, A., Brown, A. G. A., et al. 2022, arXiv e-prints, arXiv:2208.00211

Galicher, R., Boccaletti, A., Mesa, D., et al. 2018, A&A, 615, A92

Galicher, R., Marois, C., Macintosh, B., et al. 2016, A&A, 594, A63

Gallet, F. & Bouvier, J. 2013, A&A, 556, A36

Galli, P. A. B., Joncour, I., & Moraux, E. 2018, MNRAS, 477, L50

Gammie, C. F. 2001, ApJ, 553, 174

Garaud, P. & Lin, D. N. C. 2007, ApJ, 654, 606

Gardner, J. P., Mather, J. C., Clampin, M., et al. 2006, Space Sci. Rev., 123, 485

Gaudi, B. S., Meyer, M., & Christiansen, J. 2021, in ExoFrontiers; Big Questions in Exoplanetary Science, ed. N. Madhusudhan, 2–1

Gilmozzi, R. & Spyromilio, J. 2007, The Messenger, 127, 11

Gizis, J. E., Allers, K. N., Liu, M. C., et al. 2015, ApJ, 799, 203

Gladman, B. 1993, Icarus, 106, 247

Goldman, B., Schilbach, E., Röser, S., et al. 2018, in Proceedings of the International Astronomical Union, Vol. 330, Astrometry and Astrophysics in the Gaia Sky, ed. A. Recio-Blanco, P. de Laverny, A. G. A. Brown, & T. Prusti, 214–215

Goldreich, P. & Ward, W. R. 1973, ApJ, 183, 1051

Gontcharov, G. A. 2006, Astronomy Letters, 32, 759

González, M., Joncour, I., Buckner, A. S. M., et al. 2021, A&A, 647, A14

Goodwin, S. P. & Whitworth, A. P. 2004, A&A, 413, 929

Gordon, K. D., Misselt, K. A., Bouwman, J., et al. 2021, ApJ, 916, 33

Gorti, U., Dullemond, C. P., & Hollenbach, D. 2009, ApJ, 705, 1237

Gorti, U. & Hollenbach, D. 2009, ApJ, 690, 1539

Goździewski, K. & Migaszewski, C. 2020, ApJ, 902, L40

Grasser, N., Ratzenböck, S., Alves, J., et al. 2021, A&A, 652, A2

Gray, D. F. 1997, Nature, 385, 795

Grigsby, J. A., Morrison, N. D., & Anderson, L. S. 1992, ApJS, 78, 205

Güdel, M. 2020, Space Sci. Rev., 216, 143

Guerri, G., Daban, J.-B., Robbe-Dubois, S., et al. 2011, Experimental Astronomy, 30, 59

Guo, Y., Li, J., Xiong, J., et al. 2022, Research in Astronomy and Astrophysics, 22, 025009

Gutermuth, R. A., Myers, P. C., Megeath, S. T., et al. 2008, ApJ, 674, 336

Gutierrez-Moreno, A. & Moreno, H. 1968, ApJS, 15, 459

Güttler, C., Blum, J., Zsom, A., Ormel, C. W., & Dullemond, C. P. 2010, A&A, 513, A56

Hacar, A., Tafalla, M., Forbrich, J., et al. 2018, A&A, 610, A77

Hacar, A., Tafalla, M., Kauffmann, J., & Kovács, A. 2013, A&A, 554, A55

Haemmerlé, L., Eggenberger, P., Ekström, S., et al. 2019, A&A, 624, A137

Haisch, Karl E., J., Lada, E. A., & Lada, C. J. 2001, ApJ, 553, L153

Hall, C., Forgan, D., & Rice, K. 2017, MNRAS, 470, 2517

Hartmann, L. 1998, Accretion Processes in Star Formation (Cambridge University Press)

Hauck, B. & Mermilliod, M. 1997, VizieR Online Data Catalog, II/215

Hauschildt, P. H., Allard, F., Ferguson, J., Baron, E., & Alexander, D. R. 1999, ApJ, 525, 871

Hayashi, C. 1981a, in Fundamental Problems in the Theory of Stellar Evolution, ed. D. Sugimoto, D. Q. Lamb, & D. N. Schramm, Vol. 93, 113–126

Hayashi, C. 1981b, Progress of Theoretical Physics Supplement, 70, 35

Hayashi, C., Nakazawa, K., & Nakagawa, Y. 1985, in Protostars and Planets II, ed. D. C. Black & M. S. Matthews, 1100–1153

Helled, R., Bodenheimer, P., Podolak, M., et al. 2014, in Protostars and Planets VI, ed. H. Beuther, R. S. Klessen, C. P. Dullemond, & T. Henning, 643

Henry, G. W., Marcy, G. W., Butler, R. P., & Vogt, S. S. 2000, ApJ, 529, L41

Herman, M. K., Zhu, W., & Wu, Y. 2019, AJ, 157, 248

Hillenbrand, L. A., Bauermeister, A., & White, R. J. 2008, in Astronomical Society of the Pacific Conference Series, Vol. 384, 14th Cambridge Workshop on Cool Stars, Stellar Systems, and the Sun, ed. G. van Belle, 200

Hiltner, W. A., Garrison, R. F., & Schild, R. E. 1969, ApJ, 157, 313

Hobbs, L. M. 1978, ApJ, 222, 491

Hoemann, E., Heigl, S., & Burkert, A. 2021, MNRAS, 507, 3486

Holl, B., Perryman, M., Lindegren, L., Segransan, D., & Raimbault, M. 2022, A&A, 661, A151

Hollenbach, D., Johnstone, D., Lizano, S., & Shu, F. 1994, ApJ, 428, 654

Houk, N. 1982, Michigan Catalogue of Two-dimensional Spectral Types for the HD stars. Volume_3. Declinations -40_f0 to -26_f0. (Ann Arbor: Dept. of Astronomy, University of Michigan)

Howes, L. M., Lindegren, L., Feltzing, S., Church, R. P., & Bensby, T. 2019, A&A, 622, A27

Hsu, D. C., Ford, E. B., Ragozzine, D., & Ashby, K. 2019, AJ, 158, 109

Hubeny, I. & Lanz, T. 2011, TLUSTY: Stellar Atmospheres, Accretion Disks, and Spectroscopic Diagnostics

Huber, D., Bryson, S. T., Haas, M. R., et al. 2016, ApJS, 224, 2

Huber, D., Ireland, M. J., Bedding, T. R., et al. 2012, ApJ, 760, 32

Ida, S. & Lin, D. N. C. 2005, ApJ, 626, 1045

Janson, M., Asensio-Torres, R., André, D., et al. 2019, A&A, 626, A99

Janson, M., Bergfors, C., Brandner, W., et al. 2014, ApJ, 789, 102

Janson, M., Bonavita, M., Klahr, H., et al. 2011, ApJ, 736, 89

Janson, M., Gratton, R., Rodet, L., et al. 2021a, Nature, 600, 231

Janson, M., Hormuth, F., Bergfors, C., et al. 2012, ApJ, 754, 44

Janson, M., Lafrenière, D., Jayawardhana, R., et al. 2013, ApJ, 773, 170

Janson, M., Squicciarini, V., Delorme, P., et al. 2021b, A&A, 646, A164

Jeffries, R. D., Jackson, R. J., Cottaar, M., et al. 2014, A&A, 563, A94

Jewitt, D. & Luu, J. 1993, Nature, 362, 730

Johansen, A. & Lacerda, P. 2010, MNRAS, 404, 475

Johansen, A., Oishi, J. S., Mac Low, M.-M., et al. 2007, Nature, 448, 1022

Johnson, H. L. & Morgan, W. W. 1953, ApJ, 117, 313

Kapoor, R. 2013, Indian journal of history of science, 48, 405

Kaufer, A., Stahl, O., Tubbesing, S., et al. 1999, The Messenger, 95, 8

Kennedy, G. M. & Kenyon, S. J. 2008, ApJ, 673, 502

Kerr, M., Johnston, S., Hobbs, G., & Shannon, R. M. 2015, ApJ, 809, L11

Kerr, R. M. P., Rizzuto, A. C., Kraus, A. L., & Offner, S. S. R. 2021, ApJ, 917, 23

Kervella, P., Arenou, F., Mignard, F., & Thévenin, F. 2019, A&A, 623, A72

Kharchenko, N. V. & Roeser, S. 2009, VizieR Online Data Catalog, I/280B

Kiefer, F., Hébrard, G., Sahlmann, J., et al. 2019, A&A, 631, A125

Kim, J., Chevance, M., Kruijssen, J. M. D., et al. 2021, MNRAS, 504, 487

Kirkpatrick, J. D., Martin, E. C., Smart, R. L., et al. 2019, ApJS, 240, 19

Koestler, A. & Butterfield, H. 1968, The Sleepwalkers, Danube edition (Macmillan)

Kokubo, E. & Ida, S. 1996, Icarus, 123, 180

Kokubo, E. & Ida, S. 2000, Icarus, 143, 15

Kouwenhoven, M. B. N., Brown, A. G. A., & Kaper, L. 2007a, A&A, 464, 581

Kouwenhoven, M. B. N., Brown, A. G. A., Portegies Zwart, S. F., & Kaper, L. 2007b, A&A, 474, 77

Kouwenhoven, M. B. N., Brown, A. G. A., Zinnecker, H., Kaper, L., & Portegies Zwart, S. F. 2005, A&A, 430, 137

Kratter, K. & Lodato, G. 2016, ARA&A, 54, 271

Kratter, K. M., Murray-Clay, R. A., & Youdin, A. N. 2010, ApJ, 710, 1375

Kraus, A. L., Herczeg, G. J., Rizzuto, A. C., et al. 2017, ApJ, 838, 150

Krolikowski, D. M., Kraus, A. L., & Rizzuto, A. C. 2021, AJ, 162, 110

Kroupa, P., Aarseth, S., & Hurley, J. 2001, MNRAS, 321, 699

Krumholz, M. R. 2014, Phys. Rep., 539, 49

Kuhn, M. A., Hillenbrand, L. A., Sills, A., Feigelson, E. D., & Getman, K. V. 2019, ApJ, 870, 32

Kuiper, G. P. 1951, Proceedings of the National Academy of Science, 37, 1

Kuruwita, R. L., Ireland, M., Rizzuto, A., Bento, J., & Federrath, C. 2018, MNRAS, 480, 5099

Kuzuhara, M., Currie, T., Takarada, T., et al. 2022, ApJ, 934, L19

Lada, C. J. & Lada, E. A. 2003, ARA&A, 41, 57

Lada, C. J., Muench, A. A., Luhman, K. L., et al. 2006, AJ, 131, 1574

Lada, C. J. & Wilking, B. A. 1984, ApJ, 287, 610

Ladjelate, B., André, P., Könyves, V., et al. 2020, A&A, 638, A74

Lafrenière, D., Jayawardhana, R., Janson, M., et al. 2011, ApJ, 730, 42

Lafrenière, D., Jayawardhana, R., van Kerkwijk, M. H., Brandeker, A., & Janson, M. 2014, ApJ, 785, 47

Lafrenière, D., Marois, C., Doyon, R., Nadeau, D., & Artigau, É. 2007, ApJ, 660, 770

Lallement, R., Babusiaux, C., Vergely, J. L., et al. 2019, A&A, 625, A135

Lallement, R., Capitanio, L., Ruiz-Dern, L., et al. 2018, A&A, 616, A132

Lambrechts, M. & Johansen, A. 2012, A&A, 544, A32

Lamers, H. J. G. L. M., Gieles, M., Bastian, N., et al. 2005, A&A, 441, 117

Larson, R. B. 1981, MNRAS, 194, 809

Larson, R. B. 2002, in Astronomical Society of the Pacific Conference Series, Vol. 285, Modes of Star Formation and the Origin of Field Populations, ed. E. K. Grebel & W. Brandner, 442

Lecavelier Des Etangs, A., Ehrenreich, D., Vidal-Madjar, A., et al. 2010, A&A, 514, A72

Lecavelier des Etangs, A. & Lissauer, J. J. 2022, New A Rev., 94, 101641

Leike, R. H., Glatzle, M., & Enßlin, T. A. 2020, A&A, 639, A138

Lenz, D., Hensley, B. S., & Doré, O. 2017, ApJ, 846, 38

Levato, H., Malaroda, S., Morrell, N., & Solivella, G. 1987, ApJS, 64, 487

Lin, D. N. C., Bodenheimer, P., & Richardson, D. C. 1996, Nature, 380, 606

Lindegren, L., Hernández, J., Bombrun, A., et al. 2018, A&A, 616, A2

Lindegren, L., Klioner, S. A., Hernández, J., et al. 2021, A&A, 649, A2

Linder, E. F., Mordasini, C., Mollière, P., et al. 2019, A&A, 623, A85

Liu, M. C., Magnier, E. A., Deacon, N. R., et al. 2013, ApJ, 777, L20

Lodieu, N. 2013, MNRAS, 431, 3222

Luger, R., Sestovic, M., Kruse, E., et al. 2017, Nature Astronomy, 1, 0129

Luhman, K. L. & Esplin, T. L. 2020, AJ, 160, 44

Luhman, K. L. & Mamajek, E. E. 2012, ApJ, 758, 31

Luhman, K. L., Mamajek, E. E., Shukla, S. J., & Loutrel, N. P. 2017, AJ, 153, 46

Luhman, K. L. & Rieke, G. H. 1999, ApJ, 525, 440

Lynden-Bell, D. 1967, Monthly Notices of the Royal Astronomical Society, 136, 101

Lynden-Bell, D. & Pringle, J. E. 1974, MNRAS, 168, 603

Ma, B. & Ge, J. 2014, MNRAS, 439, 2781

Mackereth, J. T., Miglio, A., Elsworth, Y., et al. 2021, MNRAS, 502, 1947

Maire, A.-L., Langlois, M., Dohlen, K., et al. 2016, in Society of Photo-Optical Instrumentation Engineers (SPIE) Conference Series, Vol. 9908, Ground-based and Airborne Instrumentation for Astronomy VI, ed. C. J. Evans, L. Simard, & H. Takami, 990834

Males, J. R. & Guyon, O. 2018, Journal of Astronomical Telescopes, Instruments, and Systems, 4, 019001

Malik, M., Meru, F., Mayer, L., & Meyer, M. 2015, ApJ, 802, 56

Malkov, O. Y., Oblak, E., Snegireva, E. A., & Torra, J. 2006, A&A, 446, 785

Malmberg, D., de Angeli, F., Davies, M. B., et al. 2007, MNRAS, 378, 1207

Mamajek, E. E. 2009, in American Institute of Physics Conference Series, Vol. 1158, Exoplanets and Disks: Their Formation and Diversity, ed. T. Usuda, M. Tamura, & M. Ishii, 3–10

Mamajek, E. E. & Hillenbrand, L. A. 2008, ApJ, 687, 1264

Mamajek, E. E., Meyer, M. R., & Liebert, J. W. 2002, in American Astronomical Society Meeting Abstracts, Vol. 200, American Astronomical Society Meeting Abstracts #200, 71.14

Marigo, P., Girardi, L., Bressan, A., et al. 2017, ApJ, 835, 77

Marleau, G.-D., Coleman, G. A. L., Leleu, A., & Mordasini, C. 2019a, A&A, 624, A20

Marleau, G. D. & Cumming, A. 2014, MNRAS, 437, 1378

Marleau, G.-D., Mordasini, C., & Kuiper, R. 2019b, ApJ, 881, 144

Marley, M. S., Saumon, D., Visscher, C., et al. 2021, ApJ, 920, 85

Marois, C., Lafrenière, D., Doyon, R., Macintosh, B., & Nadeau, D. 2006, ApJ, 641, 556

Marois, C., Macintosh, B., Barman, T., et al. 2008, Science, 322, 1348

Marrese, P. M., Marinoni, S., Fabrizio, M., & Altavilla, G. 2019, A&A, 621, A144

Martig, M., Fouesneau, M., Rix, H.-W., et al. 2016, MNRAS, 456, 3655

Mathews, G. S., Williams, J. P., Ménard, F., et al. 2012, ApJ, 745, 23

Mawet, D., Milli, J., Wahhaj, Z., et al. 2014, ApJ, 792, 97

Maxted, P. F. L., Serenelli, A. M., & Southworth, J. 2015, A&A, 575, A36

Mayne, N. J. & Naylor, T. 2008, MNRAS, 386, 261

Mayor, M., Pepe, F., Queloz, D., et al. 2003, The Messenger, 114, 20

Mayor, M. & Queloz, D. 1995, Nature, 378, 355

McCall, M. L. 2004, AJ, 128, 2144

Meingast, S., Alves, J., & Fürnkranz, V. 2019, A&A, 622, L13

Mermilliod, J. C. 2006, VizieR Online Data Catalog, II/168

Meru, F. 2015, MNRAS, 454, 2529

Meru, F., Juhász, A., Ilee, J. D., et al. 2017, ApJ, 839, L24

Mesa, D., Gratton, R., Zurlo, A., et al. 2015, A&A, 576, A121

Meyer, M., Calissendorff, P., & Amara, A. 2021, submitted on A&A

Miret-Roig, N., Bouy, H., Raymond, S. N., et al. 2022, Nature Astronomy, 6, 89

Mizuno, H. 1980, Progress of Theoretical Physics, 64, 544

Moe, M. & Di Stefano, R. 2017, ApJS, 230, 15

Moraux, E. 2016, in EAS Publications Series, Vol. 80-81, EAS Publications Series, 73–114

Mordasini, C., Alibert, Y., Benz, W., Klahr, H., & Henning, T. 2012a, A&A, 541, A97

Mordasini, C., Alibert, Y., Klahr, H., & Henning, T. 2012b, A&A, 547, A111

Mordasini, C., Dittkrist, K.-M., Alibert, Y., et al. 2011, in The Astrophysics of Planetary Systems: Formation, Structure, and Dynamical Evolution, ed. A. Sozzetti, M. G. Lattanzi, & A. P. Boss, Vol. 276, 72–75

Morton, T. D. 2015, isochrones: Stellar model grid package, Astrophysics Source Code Library, record ascl:1503.010

Nakazawa, K. & Nakagawa, Y. 1981, Progress of Theoretical Physics Supplement, 70, 11

Naoz, S. 2016, ARA&A, 54, 441

Napiwotzki, R., Schoenberner, D., & Wenske, V. 1993, A&A, 268, 653

Naylor, T. 2009, MNRAS, 399, 432

Nguyen, M. M., De Rosa, R. J., & Kalas, P. 2021, AJ, 161, 22

Nielsen, E. L., De Rosa, R. J., Macintosh, B., et al. 2019, AJ, 158, 13

Nielsen, E. L., Liu, M. C., Wahhaj, Z., et al. 2013, ApJ, 776, 4

Nielsen, E. L., Rosa, R. J. D., Rameau, J., et al. 2017, AJ, 154, 218

Niemczura, E. 2003, A&A, 404, 689

Nieva, M. F. 2013, A&A, 550, A26

Nomoto, K. 1984, ApJ, 277, 791

Nomoto, K. & Leung, S.-C. 2017, in Handbook of Supernovae, ed. A. W. Alsabti & P. Murdin, 483

Norris, J. 1971, ApJS, 23, 213

Nutter, D., Ward-Thompson, D., & André, P. 2006, MNRAS, 368, 1833

Ochsenbein, F., Bauer, P., & Marcout, J. 2000, A&AS, 143, 23

Offner, S. S. R., Dunham, M. M., Lee, K. I., Arce, H. G., & Fielding, D. B. 2016, ApJ, 827, L11

Offner, S. S. R., Kratter, K. M., Matzner, C. D., Krumholz, M. R., & Klein, R. I. 2010, ApJ, 725, 1485

Ohnaka, K., Hofmann, K. H., Schertl, D., et al. 2013, A&A, 555, A24

Paczynski, B. 1978, Acta Astron., 28, 91

Pang, X., Tang, S.-Y., Li, Y., et al. 2022, ApJ, 931, 156

Parker, R. J. 2014, MNRAS, 445, 4037

Parker, R. J. & Daffern-Powell, E. C. 2022, MNRAS, 516, L91

Pascucci, I., Testi, L., Herczeg, G. J., et al. 2016, ApJ, 831, 125

Pecaut, M. J. & Mamajek, E. E. 2013, ApJS, 208, 9

Pecaut, M. J. & Mamajek, E. E. 2016, MNRAS, 461, 794

Pecaut, M. J., Mamajek, E. E., & Bubar, E. J. 2012, ApJ, 746, 154

Perryman, M., Hartman, J., Bakos, G. Á., & Lindegren, L. 2014, ApJ, 797, 14

Perryman, M. A. C., Lindegren, L., Kovalevsky, J., et al. 1997, A&A, 323, L49

Peter, D., Feldt, M., Henning, T., & Hormuth, F. 2012, A&A, 538, A74

Phillips, M. W., Tremblin, P., Baraffe, I., et al. 2020, A&A, 637, A38

Pillitteri, I., Wolk, S. J., Chen, H. H., & Goodman, A. 2016, A&A, 592, A88

Piskunov, N., Snik, F., Dolgopolov, A., et al. 2011, The Messenger, 143, 7

Planck Collaboration, Aghanim, N., Akrami, Y., et al. 2020, A&A, 641, A1

Pollack, J. B. 1984, ARA&A, 22, 389

Pollack, J. B., Hubickyj, O., Bodenheimer, P., et al. 1996, Icarus, 124, 62

Poppenhaeger, K. & Wolk, S. J. 2014, A&A, 565, L1

Pourbaix, D., Tokovinin, A. A., Batten, A. H., et al. 2004, A&A, 424, 727

Poznanski, D., Prochaska, J. X., & Bloom, J. S. 2012, MNRAS, 426, 1465

Prada Moroni, P. G., Valle, G., Dell'Omodarme, M., & Degl'Innocenti, S. 2016, Astronomische Nachrichten, 337, 819

Preibisch, T., Brown, A. G. A., Bridges, T., Guenther, E., & Zinnecker, H. 2002, AJ, 124, 404

Preibisch, T. & Zinnecker, H. 1999, AJ, 117, 2381

Proctor, R. A. 1869, Proceedings of the Royal Society of London Series I, 18, 169

Pueyo, L. 2016, ApJ, 824, 117

Quiroga, C., Torres, A. F., & Cidale, L. S. 2010, A&A, 521, A75

Rafikov, R. R. 2003, AJ, 125, 942

Rafikov, R. R. 2004, AJ, 128, 1348

Rafikov, R. R. 2005, ApJ, 621, L69

Rafikov, R. R. 2009, ApJ, 704, 281

Rafikov, R. R. 2011, ApJ, 727, 86

Raghavan, D., McAlister, H. A., Henry, T. J., et al. 2010, ApJS, 190, 1

Raymond, S. N., Quinn, T., & Lunine, J. I. 2006, Icarus, 183, 265

Reffert, S., Bergmann, C., Quirrenbach, A., Trifonov, T., & Künstler, A. 2015, A&A, 574, A116

Reggiani, M. & Meyer, M. R. 2013, A&A, 553, A124

Reggiani, M. M. & Meyer, M. R. 2011, ApJ, 738, 60

Ribas, Á., Bouy, H., & Merín, B. 2015, A&A, 576, A52

Ribas, Á., Merín, B., Bouy, H., & Maud, L. T. 2014, A&A, 561, A54

Rice, K., Lopez, E., Forgan, D., & Biller, B. 2015, MNRAS, 454, 1940

Rice, W. K. M., Armitage, P. J., Mamatsashvili, G. R., Lodato, G., & Clarke, C. J. 2011, MNRAS, 418, 1356

Rice, W. K. M., Mayo, J. H., & Armitage, P. J. 2010, MNRAS, 402, 1740

Richert, A. J. W., Getman, K. V., Feigelson, E. D., et al. 2018, MNRAS, 477, 5191

Ricker, G. R., Winn, J. N., Vanderspek, R., et al. 2015, Journal of Astronomical Telescopes, Instruments, and Systems, 1, 014003

Riello, M., De Angeli, F., Evans, D. W., et al. 2018, A&A, 616, A3

Riello, M., De Angeli, F., Evans, D. W., et al. 2021, A&A, 649, A3

Rigliaco, E., Wilking, B., Meyer, M. R., et al. 2016, A&A, 588, A123

Rizzuto, A. C., Ireland, M. J., Dupuy, T. J., & Kraus, A. L. 2016, ApJ, 817, 164

Rizzuto, A. C., Ireland, M. J., & Kraus, A. L. 2015, MNRAS, 448, 2737

Rizzuto, A. C., Ireland, M. J., & Robertson, J. G. 2011, MNRAS, 416, 3108

Rizzuto, A. C., Ireland, M. J., Robertson, J. G., et al. 2013, MNRAS, 436, 1694

Roccatagliata, V., Franciosini, E., Sacco, G. G., Randich, S., & Sicilia-Aguilar, A. 2020, A&A, 638, A85

Rodrigo, C. & Solano, E. 2020, in XIV.0 Scientific Meeting (virtual) of the Spanish Astronomical Society, 182

Rodrigo, C., Solano, E., & Bayo, A. 2012, SVO Filter Profile Service Version 1.0, IVOA Working Draft 15 October 2012

Rodrigues, T. S., Bossini, D., Miglio, A., et al. 2017, MNRAS, 467, 1433

Rodrigues, T. S., Girardi, L., Miglio, A., et al. 2014, MNRAS, 445, 2758

Röser, S., Schilbach, E., Goldman, B., et al. 2018, A&A, 614, A81

Rousset, G., Lacombe, F., Puget, P., et al. 2003, in Society of Photo-Optical Instrumentation Engineers (SPIE) Conference Series, Vol. 4839, Adaptive Optical System Technologies II, ed. P. L. Wizinowich & D. Bonaccini, 140–149

Russell, J. L. 1964, The British Journal for the History of Science, 2, 1

Sacco, G. G., Jeffries, R. D., Randich, S., et al. 2015, A&A, 574, L7

Safronov, V. S. 1972, Evolution of the protoplanetary cloud and formation of the earth and planets. (Keter Publishing House)

Sambursky, S. 1962, Isis, 53, 460

Samland, M., Bouwman, J., Hogg, D. W., et al. 2021, A&A, 646, A24

Savage, B. D. & Panek, R. J. 1974, ApJ, 191, 659

Scally, A. & Clarke, C. 2002, MNRAS, 334, 156

Schlichting, H. E. 2014, ApJ, 795, L15

Schneider, F. R. N., Ohlmann, S. T., Podsiadlowski, P., et al. 2019, Nature, 574, 211

Schöller, M., Correia, S., Hubrig, S., & Ageorges, N. 2010, A&A, 522, A85

Schreyer, K., Semenov, D., Henning, T., & Forbrich, J. 2006, ApJ, 637, L129

Sepulveda, A. G. & Bowler, B. P. 2022, AJ, 163, 52

Shakura, N. I. & Sunyaev, R. A. 1973, A&A, 24, 337

Shatsky, N. & Tokovinin, A. 2002, A&A, 382, 92

Sheehan, P. D. & Eisner, J. A. 2017, ApJ, 851, 45

Shepherd, D. S., Claussen, M. J., & Kurtz, S. E. 2001, Science, 292, 1513

Shepherd, D. S., Nürnberger, D. E. A., & Bronfman, L. 2004, ApJ, 602, 850

Shobbrook, R. R. 1983, MNRAS, 205, 1215

Skrutskie, M. F., Cutri, R. M., Stiening, R., et al. 2006, AJ, 131, 1163

Smith, B. A. & Terrile, R. J. 1984, Science, 226, 1421

Soderblom, D. R. 2010, ARA&A, 48, 581

Soderblom, D. R., Hillenbrand, L. A., Jeffries, R. D., Mamajek, E. E., & Naylor, T. 2014, in Protostars and Planets VI, ed. H. Beuther, R. S. Klessen, C. P. Dullemond, & T. Henning, 219

Somers, G., Cao, L., & Pinsonneault, M. H. 2020, ApJ, 891, 29

Soummer, R., Ferrari, A., Aime, C., & Jolissaint, L. 2007, ApJ, 669, 642

Soummer, R., Pueyo, L., & Larkin, J. 2012, ApJ, 755, L28

Spada, F., Demarque, P., Kim, Y. C., Boyajian, T. S., & Brewer, J. M. 2017, ApJ, 838, 161

Spiegel, D. S. & Burrows, A. 2012, ApJ, 745, 174

Squicciarini, V. & Bonavita, M. 2022, arXiv e-prints, arXiv:2206.02446

Squicciarini, V., Gratton, R., Bonavita, M., & Mesa, D. 2021, MNRAS, 507, 1381

Squicciarini, V., Gratton, R., Janson, M., et al. 2022, A&A, 664, A9

Stamatellos, D., Whitworth, A. P., & Hubber, D. A. 2011, ApJ, 730, 32

Stassun, K. G., Collins, K. A., & Gaudi, B. S. 2017, AJ, 153, 136

Stassun, K. G., Corsaro, E., Pepper, J. A., & Gaudi, B. S. 2018, AJ, 155, 22

Steiman-Cameron, T. Y., Durisen, R. H., Boley, A. C., Michael, S., & McConnell, C. R. 2013, ApJ, 768, 192

Stetson, P. B. 2000, PASP, 112, 925

Strom, K. M., Strom, S. E., Edwards, S., Cabrit, S., & Skrutskie, M. F. 1989, AJ, 97, 1451

Struve, O. 1952, The Observatory, 72, 199

Sullivan, K. & Kraus, A. L. 2021, ApJ, 912, 137

Suri, S., Beuther, H., Gieser, C., et al. 2021, A&A, 655, A84

Symposium, I. A. U., de Grijs, R., Lépine, J., & Union, I. A. 2010, Star Clusters (IAU S266): Basic Galactic Building Blocks Throughout Time and Space, IAU symposium and colloquium proceedings series (Cambridge University Press)

Tetzlaff, N., Neuhäuser, R., & Hohle, M. M. 2011, MNRAS, 410, 190

Tobin, J. J., Hartmann, L., Fűrész, G., Hsu, W.-H., & Mateo, M. 2015, AJ, 149, 119

Tobin, J. J., Kratter, K. M., Persson, M. V., et al. 2016, Nature, 538, 483

Tokovinin, A. & Briceño, C. 2018, AJ, 156, 138

Tokovinin, A. & Briceño, C. 2020, AJ, 159, 15

Tokovinin, A. & Moe, M. 2020, MNRAS, 491, 5158

Tokunaga, A. T., Simons, D. A., & Vacca, W. D. 2002, PASP, 114, 180

Toomre, A. 1964, ApJ, 139, 1217

Torres, C. A. O., Quast, G. R., Melo, C. H. F., & Sterzik, M. F. 2008, in Handbook of Star Forming Regions, Volume II, ed. B. Reipurth, Vol. 5 (Astronomical Society of the Pacific), 757

Udry, S. & Santos, N. C. 2007, ARA&A, 45, 397

Van Cleve, J. E., Howell, S. B., Smith, J. C., et al. 2016, PASP, 128, 075002

van Leeuwen, F. 2007, A&A, 474, 653

Verde, L. 2010, in Lecture Notes in Physics, Berlin Springer Verlag, ed. G. Wolschin, Vol. 800, 147–177

Vigan, A., Bonavita, M., Biller, B., et al. 2017, A&A, 603, A3

Vigan, A., Fontanive, C., Meyer, M., et al. 2021, A&A, 651, A72

Vines, J. I. & Jenkins, J. S. 2022, MNRAS[arXiv:2204.03769]

Vorobyov, E. I. 2011, ApJ, 729, 146

Vorobyov, E. I., Zakhozhay, O. V., & Dunham, M. M. 2013, MNRAS, 433, 3256

Wade, G. A., Neiner, C., Alecian, E., et al. 2016, MNRAS, 456, 2

Wang, C., Langer, N., Schootemeijer, A., et al. 2022, Nature Astronomy [arXiv:2202.05552]

Wang, J. J., Graham, J. R., Dawson, R., et al. 2018, AJ, 156, 192

Wang, S. & Chen, X. 2019, ApJ, 877, 116

Weber, E. J. & Davis, Leverett, J. 1967, ApJ, 148, 217

Weidenschilling, S. J. 1977, Ap&SS, 51, 153

Weidenschilling, S. J. & Marzari, F. 1996, Nature, 384, 619

Wenger, M., Ochsenbein, F., Egret, D., et al. 2000, A&AS, 143, 9

Wetherill, G. W. 1990, Icarus, 88, 336

Wilking, B. A., Gagné, M., & Allen, L. E. 2008, Star Formation in the ρ Ophiuchi Molecular Cloud, Vol. 5 (Reipurth, B.), 351

Wilking, B. A. & Lada, C. J. 1983, ApJ, 274, 698

Williams, I. P. & Cremin, A. W. 1968, QJRAS, 9, 40

Williams, J. P. & Cieza, L. A. 2011, ARA&A, 49, 67

Wilner, D. J., MacGregor, M. A., Andrews, S. M., et al. 2018, ApJ, 855, 56

Winn, J. N. & Fabrycky, D. C. 2015, ARA&A, 53, 409

Winn, J. N., Howard, A. W., Johnson, J. A., et al. 2009, ApJ, 703, 2091

Winters, J. G., Henry, T. J., Jao, W.-C., et al. 2019, AJ, 157, 216

Wolff, S. C. 1990, AJ, 100, 1994

Wolff, S. C., Strom, S. E., Dror, D., & Venn, K. 2007, AJ, 133, 1092

Wolszczan, A. 1994, Science, 264, 538

Wolszczan, A. & Frail, D. A. 1992, Nature, 355, 145

Wolthoff, V., Reffert, S., Quirrenbach, A., et al. 2022, A&A, 661, A63

Woolfson, M. 2000, Astronomy and Geophysics, 41, 12

Wootten, A. & Thompson, A. R. 2009, IEEE Proceedings, 97, 1463

Worley, C. C., de Laverny, P., Recio-Blanco, A., et al. 2012, A&A, 542, A48

Wright, E. L., Eisenhardt, P. R. M., Mainzer, A. K., et al. 2010, AJ, 140, 1868

Wright, N. J., Bouy, H., Drew, J. E., et al. 2016, MNRAS, 460, 2593

Wright, N. J. & Mamajek, E. E. 2018, MNRAS, 476, 381

Wu, Y. & Lithwick, Y. 2011, ApJ, 735, 109

Zhang, J., Zhao, J., Oswalt, T. D., et al. 2021, ApJ, 908, 207

Zsom, A., Ormel, C. W., Güttler, C., Blum, J., & Dullemond, C. P. 2010, A&A, 513, A57

Zuckerman, B. & Song, I. 2004, ARA&A, 42, 685

Zurlo, A., Goździewski, K., & Lazzoni, C. 2022, submitted on A&A

Zurlo, A., Vigan, A., Galicher, R., et al. 2016, A&A, 587, A57

Zurlo, A., Vigan, A., Mesa, D., et al. 2014, A&A, 572, A85